University of Catania

Doctor of Philosophy in Physics - XXVIII Cycle

Experimental measurements and Monte Carlo simulations of a transport beamline for laser-driven proton beams

Antonella Tramontana

PhD Thesis

PhD coordinator:
Prof. F. Riggi

Tutor:
Prof. S. Albergo

Supervisors:
Dott. G. Cuttone
Dott. F. Romano

December 9, 2015

Dedicated to my family and to Armando

Maestro, spostare delle pietre è una cosa, questo e' del tutto diverso!
No, non diverso. Solo diverso in tua mente. Devi disimparare cio' che hai imparato.
D'accordo, ci provero'.
No! Provare no. Fare! O non fare. Non c'e' provare.

The Empire Strikes Back

Abstract

In the last few decades, ion optical acceleration represented one of the most attractive topics in the relativistic laser-plasma interaction research, opening the possibility to investigate innovative regimes and different potential applications. In particular, it is becoming evident that, in the next future, laser-driven acceleration could represent an effective alternative to conventional particle accelerators. Indeed, laser-matter interaction could lead to more compact and less expensive acceleration systems and, consequently, to a larger availability of high-energy ion beams around the world. Up to now, optically accelerated ion beams are characterised by extreme features, not suitable for many applications and of course also for the hadrontherapy applications, that are the most demanding in terms of beam transport, handling, control and reliability.

Significant effort, at laser/target level as well as by means of customised transport beamlines, is currently ongoing in several facilities world wide in order to demonstrate the possible clinical application of laser-driven beams. Also pre-clinical studies, as the experiment reported in the thesis, were performed to try to improve the knowledge on the biological effectiveness of laser-driven beams in respect to the conventional ones, but in most of cases the uncertainties arising from the beam handling and transport do not allow to achieve undeniable results. Therefore, to reach the required accuracy for radiobiology experiments, it is desirable to better handle and control the transported beam.

According to this requirement, new prototypes for the beam transport and handling have been designed and realised at INFN-LNS in Catania. They can be properly combined in a modular system composing a prototype beamline for the beam collection and energy selection. On the basis of these prototypes, the final transport elements will be realised and assembled within 2017 for the ELIMAIA beamline, at the ELI-Beamlines facility in Prague (Cz).

In addiction to a precise description of the transport beamline prototypes, results from their tests will be reported in the thesis, together with different simulative studies. Monte Carlo simulations have been initially performed to support the design procedure and, at a later stage, to study the particle transport and dose distributions along the beamline. In particular, the Geant4 (GEometry ANd Tracking) Monte Carlo toolkit has been used at this aim.

After the characterisations of each single beamline element with both conventional and laser-driven beams and after the Monte Carlo code validation (performed using the experimental data as reference), the attention was focused on the possibility to study a possible configuration of the whole prototype beamline, properly coupling the two main elements composing that. At this aim, experimental campaigns could be planned for the next months.

To realistically reproduce the configuration to be used in the future experimental campaigns, Monte Carlo simulations of the whole transport beamline prototype were performed and finalised to the realisation of a proof-of-principle radiobiological experiment, that, as will be demonstrate, could be carried out with high dose-rate, small energy spread and well controlled dose distributions.

Summarising, thanks to the experimental and simulative studies reported in this thesis, the control of laser-driven beams with the realised transport beamline prototypes is demonstrated. Even if the obtained results are not sufficient yet for an extended feasibility study related to hadrontherapy

applications, they represent an important step towards future and more systematic studies.

Contents

Introduction

≪*Experimental measurements and Monte Carlo simulations of a transport beamline for laser-driven proton beams*≫: in this thesis I will present an innovative beamline solution for the transport and the handling of laser accelerated protons with energies up to 30 MeV. The main task is to obtain controlled and reliable beam features, in terms of energetic and angular distribution, for multidisciplinary and medical applications. Many efforts of different researchers are currently dedicated to this task. The common issue is represented by the extreme characteristics of optically accelerated beams.

In this thesis the treated novelty is represented by the laser-driven acceleration of ion beams as possible alternative to the conventional acceleration methods. The interest in this field has been greatly boosted since 2000, when three experiments reported on the observation of collimated proton beams with multi-MeV energies from the rear (non-irradiated) side of solid targets. At present available laser intensities up to 10^{21} W/cm^2, the dominant mechanism for ion acceleration from thin foils is referred to the TNSA, Target Normal Sheet Acceleration. In this regime, thin solid targets (of the order of tens or hundreds of μm) are irradiated with ultraintense (10^{18} W/cm^2) short-pulse (30 fsec - 10 ps) lasers. Consequently, high-energy electrons are generated at the foil front side. Thanks to their mean free-path, larger than the target thickness, they can cross the target producing an intense electrostatic field (of the order of TV /m). The ion acceleration is therefore due to the charge imbalance between positive ions at rest on the target and the electron sheath expanding at its rear surface, in the laser incidence direction.
Protons generated in this regime are commonly characterised by non-conventional and extreme features, such as a high intensity per pulse of the order of kA (from 10^{9-10} up to 10^{13} particles per shot) and a very low shot-to-shot reproducibility. Their energy spectrum is typically broadband, exponential shaped, from a minimum of few keV up to a cut-off energy E_{Max}, that is linearly dependent on I$^{1/2}$, with I the laser intensity. Several research groups world wide have experimentally demonstrated the generation of protons with energies up to 70 MeV and heavier ions with energies up to 7 AMeV.
Moreover, on average these beams are characterised by a very wide energy-dependent angular distribution up to $\pm$ 20 deg: more energetic particles are emitted in a narrower angular range respect to lower energetic particles. Beams accelerated in TNSA regime have also a rather small transverse and longitudinal emittance: the transverse emittance, although the wide angular distribution, gets a very small value, thanks to the very small laser spot size on the target (few tens of μm); on the other hand, the longitudinal emittance is depending on the very short temporal duration of the laser pulse ($<$ 1 ps).
Considering the reported beam features, the research on developing a high-quality, controllable, reproducible, laser-driven protons source gained incredible interest. The field of applications for this kind of beams is very wide, it goes indeed from the plasma physics to interdisciplinary areas, such as proton radiography and imaging, nuclear reactions and fast ignition. In this thesis the

hadrontherapy application has been chosen as demonstration-case. Medical applications are indeed the most demanding in terms of beam characteristics and performances, i. e. beam delivering system, advanced diagnostics and precise dosimetry.

At present only 42 hadrontherapy centres operate around the world. A wide implementation of hadrontherapy is indeed difficult because it requires an ion accelerator (e.g., cyclotron or synchrotron) and a system for the ion beam transportation and manipulation. These technically sophisticated elements cost from 100 to 200 million euros in the case of a therapeutic centre with four treatment rooms. Considering this background, investigations are currently being undertaken, aiming at the development of more compact and less expensive technologies. The idea of a laser ion accelerator was indeed identified as a possible *compact, flexible and cost-effective* solution. Thanks to the relatively small-size of laser ion accelerator together with the associated cost-reduction expected with the future technological progress, high-energy proton and heavier ion beams could be much more accessible for patients treatment. There are at least two possible ways of using a laser accelerator. In the simplest one, it replaces a conventional accelerator, still maintaining the transport beamline. In the other one, which appears to be much more attractive, instead of devices comprising bulky and heavy magnets required for the deflection of high energy ion beams (rigidity), it is proposed to use an all-optical system, which bends and rotates laser beams, arranging their interaction with a target in such a process that generates fast ions directly in the treatment room. Both laser acceleration solutions are very attractive, but for a possible medical application the laser-driven beam parameters, i. e. energy, stability and quality, must satisfy the same requirements as established in conventional hadrontherapy.

Currently, the energy of beams accelerated in the laser plasma experiments is approaching the value at which protons can be considered for therapeutic applications. However, some beam properties have not yet reached the necessary level or are not sufficiently well controllable. Progress is being made to improve these aspects with structured targets or exploring new acceleration regimes, but up to now it is not sufficient, yet.

In this background the necessity to realise a dedicated transport beamline seems to be one of the main possible solutions (chapter 1).

Naturally for the hadrontherapy applications, there is also the issue to understand the difference in terms of radiobiological effectiveness of high-energy ions accelerated by laser radiation, in comparison with ions generated by conventional accelerators. First of all, such a distinction, if it exists, may be due to the very short duration of the laser-accelerated ion beams. The *'instantaneous'* intensity of the laser-generated beams is indeed several orders of magnitude larger than the intensity of conventionally accelerated ion beams (10^{9-10} Gy/s *vs* 1-10 Gy/min). There are indications regarding that, in the high-intensity interaction of fast ions with DNA molecules, clusters can be formed, increasing the probability of the double strand break and, accordingly, the probability of killing the cancer cells. However, at the same time there are papers reporting the possibility to have no biological effect variation if laser-driven beams are used. Therefore, in order to better understand this actually unsolved question, radiobiology experiments using laser-accelerated protons have to be performed. Several experimental campaigns have been already carried out as the one performed at LULI laboratories in Paris, reported in chapter 3. During this campaign, protons

produced within the TNSA regime by irradiating 25 and 50 μm thick Au foil targets with a 5×10^{19} W/cm^2, short-pulse (1.3 ps) laser, were used to irradiate Human Umbilical Vein Endothelial Cells (HUVEC). Thanks to the delivery and transport system based on a dipole and on a drift sector, the broadband energy spectrum of the input proton beam was spatially separated. The beam features on the cells plane, i. e. dose distribution, beam uniformity and energy versus dispersion curve, were then measured and obtained data successfully compared with simulation outputs, performed using the Geant4 toolkit. Finally the investigation of the clonogenic assay and of the sublethal cytogenetic damage was performed using protons of 6, 9 and 14 MeV with an energetic spread of $\pm$ 9% and dose of about 4.5 $\pm$ 0.8, 1.8$\pm$ 0.5 and 0.6$\pm$ 0.2 Gy, respectively. The irradiation was characterised by a dose rate of about 3×10^9 Gy/sec per shot.

The analysis of the above reported biological end-points showed only few differences with respect to the corresponding measurements performed with conventional beams, but the significant energy spread, dose uncertainty and beam uniformity do not allow to be too confident in the obtained radiobiological results, demonstrating that the irradiation conditions need to be improved. Therefore, to reach the required accuracy for radiobiology experiments, it is desirable to better handle and control the transported beam.

Considering this background, providing beams with controlled energy and angular distribution, not too far from the requirements established for conventional treatments, becomes a crucial requirement. Therefore several research groups started to demonstrate more efficient and better controlled ion acceleration mechanisms, with the use of tailored targets and, moreover, with the improvement of the laser technology, they also tried to develop beamlines based on magnetic devices for the beam transport and handling.

In this context, the idea of the transport beamline presented in this thesis was born, as prototype of the future ELIMAIA (ELI Muldisciplinary Applications of laser-Ion Acceleration) beamline, that will be installed at the ELI-Beamlines in Prague.

The beam transport line prototype has been designed for proton beams with energy up to 30 MeV. As described in chapter 4, it is based mainly on the combined use of a modular system for the beam collection followed by an energy selection system (ESS), for the final energy refinement. In particular the collection prototype consists of two long permanent magnet quadrupoles (PMQs), 80 mm in length, and two short PMQs of 40 mm, both characterised by an active bore of 20 mm with a 1 mm thick shielding pipe placed inside the bore for shielding from the input beam. The maximum field gradient values are of about 114 T/m and 100 T/m, respectively. The fourth quadrupole has been added to the triplet configuration in order to better manage the lower energies of the operation energy range of the system that goes from 1 up to 30 MeV.

Regarding the energy selector system, it consists of a sequence of four dipole magnets with alternating polarity. In each dipole, particles are deflected thanks to a magnetic field of about 0.8 T on a 10×104 mm^2 gap. The overall effect of the dipole sequence coupled to a central collimator is to select particles in a given energy range.

Both prototypes have been tested with conventional proton beams at INFN-LNS in Catania and at INFN-LNL in Legnaro (see chapter 4).

As shown in chapter 5, the ESS has been also tested with laser-driven protons at the Centre for

Plasma Physics of the Queen's University in Belfast (UK), where there is the TARANIS (Terawatt Apparatus for Relativistic And Nonlinear Interdisciplinary Sciences) laser system. Several simulation sets have been simultaneously performed and obtained outputs compared with the corresponding experimental data.

Indeed both systems, PMQs and ESS, have been simulated using the Geant4 Monte Carlo toolkit in order to provide preliminary predictions to support the design of the beamline elements and to study the particle transport, fluences and doses along the beamline.

The developed code, described in chapter 2, has been also added to the official *hadrontherapy advanced example* and freely released in the Geant4 toolkit, since the version 10.1.

Considering the purpose to have a reliable and realistic code, each element has been treated with its real sizes and magnetic properties, described using detailed field grids obtained by COMSOL and Opera simulations. However a code to be completely reliable has to be validated using the experimental data as reference. The correct beamline elements implementation was indeed confirmed by the good agreement obtained from the comparison between simulation outputs and experimental data, coming from the PMQs and ESS tests, performed with conventional and non-conventional beams.

Having a reliable code, a simulation study of the whole transport beamline has been performed, as preliminary step for a future controlled radiobiological test. In particular, as described in chapter 6, in order to simulate the beam shot-to-shot instabilities, a typical laser-driven proton beam with different angular distributions was implemented. The performed simulation study was very useful to plan the next experimental test and to show how only the optimised use of the collection system with the energy selector allows to obtain a controlled and reliable output beam, mainly considering the simulated input fluctuations. Using the generated beam, as input, a proof-of-principle radiobiological experiment was then finally reproduced with the simulations (see chapter 6).

In the next chapters, there will be a detailed description of the experimental and simulative work performed to gradually fulfil the main task and subtasks of this thesis, above briefly reported.

Chapter 1

Laser-target interaction and possible applications in the medical field

The 20th century brought with itself the scientific revolutions of quantum mechanics and relativity, followed by a technologic rapid improvement. The discovery of the atom and of its positively charged core resulted in a scientific interest towards the study of its structure and properties, which led to the construction of the first particle accelerators based on linear structures, such as early Cockroft-Waltons and Van-de-Graafs, as well as cyclic structures, such as fixed magnetic field cyclotrons and variable magnetic field synchrotrons.

Within 70 years after the Lawrence's discovery of the cyclotron (1930-32), impressive advances had been achieved in the accelerators field thanks to the growing interest in a wide range of applications. However tens of years have been also dedicated to reach the level of reliability, control and maturity needed for every day applications, e.g. in industry and in medical applications. It is also important to realise that the evolution has not resulted in one particular design but in a variety of tools best suited to specific applications, such as high-energy physics, nuclear and reactor physics, industry and clinical medicine. The lesson to be learned is that initial breakthroughs in novel concepts must be followed up by dedicated efforts in order to render this novel technology suitable for specific applications.

In this thesis the treated novel concept is represented by the laser-driven acceleration of ion beams as possible alternative to the conventional acceleration methods. The interest in this field has been greatly boosted since the year 2000 when three experiments reported on the observation of collimated proton beams with multi-MeV energies from the rear (non-irradiated) side of solid targets. Those experiments are described in:

- Maksimchuk et al., 2000 - I_L=3$\times$ 10^{18} Wcm^{-2}, $N_p \geq 10^9$ and E_p = 1.5 MeV [1];
- Clark et al., 2000 - I_L = 5$\times$ 10^{19} W cm^{-2} N_p 10^{12} and E_p = 18 MeV [2];
- Snavely et al., 2000 - I_L = 3$\times$ 10^{20} W cm^{-2} N_p 2 $\times$ 10^{13} and E_p = 58 MeV [3].

where I_L, N_p and E_p are laser intensities, number of protons and maximum observed value of ion energy, respectively [4].
After this initial period, laser driven acceleration became more and more interesting, mainly considering the different potential applications, such as nuclear reactions, warm dense matter and fast ignition. One of these promising applications is represented by the cancer treatment.
Currently, the mechanisms of laser driven acceleration are being improved, and energies could reach up to hundreds of AMeV. However, considering the currently extreme features of these unconventional accelerated ion beams, many efforts are dedicated to the development of dedicated beam transport lines or to the improvement at the laser-target interaction level and to the realisation of suitable detectors [5].
In the next future, new generation of lasers should allow to achieve more controlled and suitable beams with respect to the present ones, thus opening the way towards future applications.
In this chapter, the theoretical description of the laser-target interaction is presented, with a focus on the Target Normal Sheath Acceleration regime. An overview of the obtained beam parameters together with the historical evolution of the laser technology are reported as well. Finally the feasibility of the hadrontherapy application is described, through a comparison between conventional acceleration method and innovative, laser-based one. This application has been chosen as demonstration case, considering that is the most demanding in terms of beam parameters, control and reproducibility.

1.1 High power laser interaction with solid targets

Although typically reported as laser-accelerated ions, they cannot efficiently be accelerated with today's lasers because of their high mass value. Therefore, when speaking of laser-driven ion acceleration, always a two-stage acceleration process is implied, starting with electrons directly accelerated by the laser that, then, drives the ion acceleration via charge separation. Therefore, in order to understand the ion acceleration processes, a brief introduction has to be dedicated to the laser-electron interaction.
Considering a simplistic approach, the target ionization is obtained if the laser intensity is high enough to balance the binding energy of a given electron in its atom. For instance, considering that the laser intensity needed to ionize an hydrogen atom is $I_H = 3.51 \times 10^{16}$ W/cm^2, if $I_0 > I_H$ at least a partial ionization for any target material (hydrogen is always presents, at least as contaminant) is guaranteed, though this can occur well below this threshold ($\approx 10^{10}$ W/cm^2). In fact an electron can be ejected from an atom if it receives enough energy by absorbing a single photon with right frequency, as in the photoelectric effect, or absorbing several photons of lower frequency. Latter process is called *multiphoton ionization* (MPI) and depends strongly on the light intensity, or, that is the same, on the photon density. However, if the laser electric field becomes strong enough it can distort the electric field felt by the electron. In this case the Coulomb barrier will be change in a finite height barrier and the electron can escape from the atom via tunnelling ionization. Moreover, if the electric field intensity is very high, it can suppress the Coulomb barrier. In this case we can talk of *barrier suppression ionization* (BSI), as a variant of tunnelling ionization regime.

Therefore, considering a real laser-target interaction, at the beginning, when the laser pre-pulse impinges on the target, because of its low intensity, multiphoton ionization dominates. When the main pulse arrives tunnelling effect dominates [6–8]. The situation seems to be simple. Actually it is more complicated.

As a consequence of high intensity laser interaction with matter, plasma is produced. Before a brief description of the laser-electron interaction, few parameters have to be introduced. One of the most relevant is the electron density, which determines the plasma oscillation frequency ω_p. The equality between the electron and the critical density (n_e and n_c respectively) is equivalent to the equality between the laser and plasma frequencies ω_L, ω_p. The equations for n_c and ω_p are:

$$\omega_L = \omega_p \Leftrightarrow \frac{2\pi c}{\lambda} = \sqrt{\frac{4\pi n_e e^2}{m_e}} \Rightarrow n_e = \frac{m_e \omega_L^2}{4\pi e^2} = n_c \tag{1.1}$$

According to the relation between electron and critical density of the plasma, we can divide the environement in two regions with two different values of the refractive index. The refractive index η is bounded with densities or frequencies through this simple relation:

$$\eta = \sqrt{1 - \omega_p^2/\omega^2} = \sqrt{1 - n_e^2/n_c^2} \tag{1.2}$$

If $n_e > n_c$, we are in an *overdense* region with imaginary values of η. This means that the laser pulse cannot propagate into the plasma. On the other hand, if $n_e < n_c$ or $n_e \approx n_c$, the refractive index has real values and all the plasma interactions occurs. In this case we are in an *underdense* region. The relativistic case is not so simple, because the refractive index η is non-linear. From [4] we can write:

$$\eta_{relatistic} = \sqrt{1 + < \overrightarrow{a}^2 >} \tag{1.3}$$

where $\overrightarrow{a}$ is ratio between electromagnetic energy and electron rest mass energy ($\overrightarrow{a} = e\overrightarrow{A}/m_e c^2$) and the brackets mean the average value over the oscillation period.

In this case, the process of plasma penetration by laser is quite complicated, because of non-linearity in the wave equation and of the variation of the plasma density profile as a result of radiation pressure [9–11]. Luckily, this problem can be solved via ponderomotive force as it is discussed in [4], where it is defined as: ≪*the slowly-varying, effective force describing the cycle averaged motion of the "oscillation centre" of a charged particle in an oscillating non-uniform field, over a time scale longer than the oscillation period.*≫

1.1.1 The single-electron in an electromagnetic field

When laser impinges on a target, the interaction with electrons occurs. Considering no collective effects, the motion of an electron in an electro-magnetic field **E** and **B** of the laser can be described using the Lorentz equation together with the energy equation:

$$\frac{d\mathbf{p}}{dt} = -e(\mathbf{E} + \mathbf{v} \times \mathbf{B}); \qquad \frac{d}{dt}(\gamma m_e c^2) = -e(\mathbf{v} \cdot \mathbf{B}) \tag{1.4}$$

with e the electron charge, m_e the electron rest mass, c the speed of light, $\mathbf{v}$ the velocity vector, $\mathbf{p} = \gamma m_e \mathbf{v}$ the relativistic impulse vector and $\gamma = \sqrt{(1 - v^2/c^2)}$ the relativistic factor [10]. The laser, for simplicity assumed as a linear polarized electro-magnetic plain wave with the perpendicular and transverse fields $\mathbf{E}$ and $\mathbf{B}$ propagating along the z direction, is described by:

$$\mathbf{E}(x, y, z, t) = E_0(t) e^{i(\omega_L t - kz)} \mathbf{e}_x; \qquad \mathbf{B}(x, y, z, t) = B_0(t) e^{i(\omega_L t - kz)} \mathbf{e}_y \tag{1.5}$$

with E_0 and B_0 the field amplitudes, ω_L the laser frequency and k the wave number. In the non-relativistic case (v≪c), the $\mathbf{B}$ field can be neglected and the electron just oscillates transversely due to the electric field amplitude and to the laser frequency ω_L. The oscillation velocity v_{osc} is given by:

$$v_{osc} = \frac{eE_0}{m_e \omega_L} \tag{1.6}$$

After the laser pulse solicitation, the electron is again at rest at its initial position. With increasing the field amplitude, the velocity v_{osc} eventually approaches c and, when E_0 is of the order of 10^{12} V/m, the relativistic effects cannot be neglected further on, i.e. the magnetic field is not negligible anymore.

Therefore, additional to the transverse oscillation a notable longitudinal motion in laser propagation direction appears, due to the magnetic field component.

As long as a plain wave is assumed for the laser pulse, no net energy gain is observed for the electron. It changes its position due to the drift motion, but it is again at rest after the laser pulse (Lawson-Woodward theorem [12])

In order to describe the relativistic limit in practical quantities, a useful relation between laser intensity and electrical field amplitude is given by:

$$E_0 = \sqrt{(2I_0/\epsilon_0 c)} \tag{1.7}$$

with ϵ_0 the electric constant. This reveals the limit for entering in the relativistic regime at a laser intensity of $I_0 \approx 10^{18}$ W/cm^2.

Another quantity is the dimensionless electric field amplitude a_0. If $a_0 > 1$, relativistic laser-electron interactions occur. It is defined as the relation between the parallel and the transverse component of the Lorentz force and can also be expressed via the laser intensity I_0 and the laser wavelength λ_L:

$$a_0 = \frac{eE_0}{m_e \omega_L c} = \sqrt{\frac{I_0[W/cm^2]\lambda_L^2[\mu m^2]}{1.37 \times 10^{18} W/cm^2 \mu m^2}} \tag{1.8}$$

It can be also described as the peak value of the laser potential vector normalized with respect to the electron rest mass [13–15].

1.2 The ponderomotive force

For realistic high-intensity laser pulses, the temporal and spatial laser profile has to be taken into account, as it significantly differs from the plain wave approximation (uniform in space and slowly varying in time) assumed above. Actually, the laser is strongly focused and it is characterised by pulse duration of only 10s to 100s of femtoseconds. The resulting - typically Gaussian-like - electric field spatial distribution causes the occurrence of an additional force, named the *ponderomotive force*, that leads to charge separation and (permanent) electrons heating [14].
The *ponderomotive force* concept was introduced in the 19th century [16] and it is nowadays widely used in the relativistic laser matter interaction field.
In the non-relativistic limit (v $\ll$ c), the equation of motion obtained from the Lorentz force is:

$$\frac{\delta v_x}{\delta t} = -\frac{e}{m_e} E_x(\mathbf{r}) \tag{1.9}$$

The EM wave is considered as propagating in z direction with the electric field oscillating in x direction and characterised by a radial intensity dependency. Using the Taylor expansion of the electric field:

$$E_x(\mathbf{r}) = E_0(x) cos(\omega_L t - kx) + x\frac{\delta E_0(x)}{\delta x} cos(\omega_L t - kx) \tag{1.10}$$

We have:

$$\frac{\delta v_x(2)}{\delta t} = -\frac{e^2}{m_e^2 \omega_L^2} E_0 \frac{\delta E_0(x)}{\delta x} cos^2(\omega_L t - kx) \tag{1.11}$$

Multiplying by m_e and taking the cycle-average yields, the ponderomotive force f_p on the given electron is:

$$f_p = -\frac{e^2}{4 m_e \omega_L^2} \frac{\delta E_0^2}{\delta x} \tag{1.12}$$

This force can be expressed as the spatial derivative of a potential $f_p = -\nabla \Phi_p$, the *ponderomotive potential* of the laser field $\Phi_p = \frac{m_e c^2}{4\gamma^2} a_0^2$. From the obtained relation between f_p and m_e, it is clear how the ponderomotive force mainly acts on electrons. If we consider m_i instead of m_e, where m_i and m_e are respectively the ion and electron masses, the ponderomotive force becomes negligible. As already reported, at the beginning indeed only electrons are accelerated and then, via charge separation, they drive the ions acceleration [10, 17].
This non-relativistic calculation still ignores the magnetic field and the electron is consequently pushed out of the laser focus under 90 deg to the laser propagation direction. An additional forward push is inserted when taking into account the magnetic field component and moving towards relativistic intensities. In order to obtain the ponderomotive force in the relativistic case, the Lorentz force can be written in terms of potential vector $\mathbf{A}$ and the motion of electron can be divided in two parts, considering the different temporal scale (p_s and p_f are the slow and fast components of the electron momentum). The relativistically correct solution is:

$$f_p = -m_e c^2 \nabla \bar{\gamma} \tag{1.13}$$

with $\bar{\gamma} = \sqrt{1 + p_s^2/m^2c^2 + a_0^2/2}$ the time-averaged (over one laser cycle) relativistic factor for linear polarized light; the solution for circularly polarized light is similar, only with just a_0^2 instead of $a_0^2/2$.

Figure 1.1 shows the ponderomotive force effect on the electron motion, due to the laser beam, in the relativistic case. In this case, solving the equation of motion for the electron is only pos-

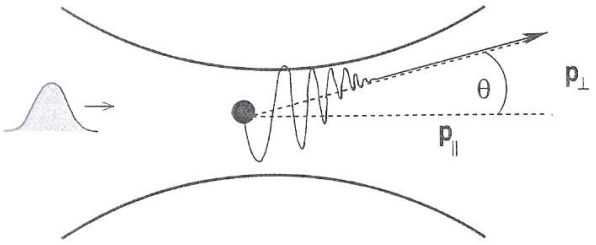

FIGURE 1.1: Relativistic electrons motion in the laser focus [17].

sible numerically, but the final kinetic energy W_p and propagation angle θ (relative to the laser propagation direction) can be calculated, as:

$$W_p = (\bar{\gamma} - 1)m_e c^2; \qquad tan^2(\theta) = \frac{2}{\bar{\gamma} - 1} \tag{1.14}$$

These relations show a direct relationship between electron angle and ejection energy and were confirmed by experimental results reported in Moore et al. (1995), Meyerhofer (1997) e Malka et al. (1997) [18]. It is now important to study the laser energy absorption mechanisms and the resulting collective effects.

1.3 Absorption mechanisms of the laser energy

When an electromagnetic wave with optical or near infrared frequency ω_L is focused on a gas, the produced plasma has an electron density n_e less than critical density n_c. Hence the plasma is called underdense and the wave can propagates through it.

Interaction with a solid target is radically different, in fact the electromagnetic wave promptly ionizes the target forming an overdense plasma with $n_e > n_c$. The laser pulse can then only penetrate in the skin layer $l_{sd} = c/\omega_c = (\lambda/2\pi)\sqrt{n_c/n_e}$ and the interaction is then a surface interaction. Since the laser pulse cannot penetrate into solid density regions, the absorbed energy is there transported mostly by energetic (fast) electrons which may be generated during the laser interaction by several mechanisms [6, 18].

Absorption mechanism can be most globally described via the solution of Vlasov-Maxwell system, which contains all the effects leading to the absorption. Vlasov-Maxwell system of equations is a description of interactive system consisting of charged particles in plasma, which create a self-consistent collective field.

Several interesting processes have been studied in literature together with their relations with respect to the density profile or size of the pre-plasma, to the laser pre-pulse effects as well as to

non-normal laser incidence [15, 19–22]. Here only few mechanisms are briefly reported: the *inverse Bremsstrahlung* and the *resonance absorption* [6, 18].
If the inverse Bremsstrahlung dominates for $I_L\lambda^2 < 10^{15}W\mu m^2/cm^2$, the resonance absorption becomes crucial for $I_\lambda^2 > 10^{15}W\mu m^2/cm^2$, where I e λ are respectively the laser intensity and wavelength.
In both processes, the laser energy is transferred to the plasma as heat energy, that increases therefore the target ionisation degree.

1.3.1 Inverse bremsstrahlung

Inverse bremsstrahlung decreases when the laser intensity grows in contrast to the *resonance absorption*. This process is based on laser energy transfer to plasma via Columbian interactions (usually ion-electron collisions) that heat locally the plasma. In other words, electrons oscillate as a response to the electromagnetic field of the laser beam and then collide with ions, transferring electromagnetic energy to the plasma. A simple model to describe these collisions can be obtained, imagining that the direction of motion of each electron is random, i. e. at each collision, the oscillation energy become thermalized. According to this model, the contribution of this energy to the thermal energy of the plasma is:

$$\Delta E = \frac{1}{2}m_e v_{osc}^2 \tag{1.15}$$

where m_e is the electron mass and v_{osc} the oscillation amplitude. This process can be characterised by the absorption coefficient σ_{IB} typical. For a radiation of frequency v, it is:

$$\sigma_{IB}[cm^{-1}] = 3.7 \times 10^8 \frac{Z^2 n_i^2}{T_e^{1/2} v_e^3}\left(1 - e^{-\frac{hv}{k_B T_e}}\right) \tag{1.16}$$

with Z the ion state of charge, n_i its density in cm^3 and T_e the electron temperature in eV.
As one can see, the efficiency of the inverse bremsstrahlung increases with the radiation frequency as well as with the ionization degree that increases spontaneously with the plasma temperature, as a consequence of the energy absorption.

1.3.2 Resonance absorption

The laser radiation can also be absorbed by a collisionless process, the so-called *resonance absorption*. In this mechanism the electromagnetic field excites a large amplitude plasma wave, which is then damped, transferring energy to the plasma. The dispersion relation for an electromagnetic wave propagating through a plasma is:

$$\omega_L^2 = \omega_P^2 + k^2 c^2 \tag{1.17}$$

where ω_L is the incident radiation frequency, ω_P the plasma frequency, k the wave vector and c the light speed.
If $\omega_L < \omega_P$ the electromagnetic wave ceases to propagate and decades exponentially, but if $\omega_L > \omega_P$

the electromagnetic wave propagates without attenuation, i.e. the plasma becomes transparent. When the laser beam propagates into the plasma, the local value of ω_P increases as the wave penetrates to higher density plasma regions until $\omega_P = \omega_L$. The surface at which this condition is satisfied is called *critical surface* and it occurs at the critical density. In this condition, when electromagnetic and plasma frequencies are identical, the electromagnetic frequency resonantly excites a plasma wave, that then transfers energy to the plasma. At higher densities, k indeed becomes imaginary and the wave decays evanescently. This apparently simple absorption mechanism is however more complicated. Indeed, if the electromagnetic wave enters the plasma at normal incidence, its electric field is tangential to the critical surface and it cannot excite a plasma wave. A plasma wave is excited only if the electromagnetic wave enters the plasma obliquely and with the correct polarization.

Provided that the polarization and angle of incidence conditions are met, a plasma wave grows at the critical surface. Because the plasma wave is excited from resonance, it continues to grow until some damping process starts, allowing the energy transfer to the plasma, in particular to a relatively small number of energetic electrons. Instead of raising the temperature of all the electrons close to the critical surface, the resonance absorption produces indeed a small number of very hot electrons, which then, because of their long mean free path, move freely through the target, depositing uniformly their energy. Frequently this hot electron component is described using a Maxwell distribution characterised by $T_h \gg T_e$. The total electron distribution can be therefore treated with two Maxwell distributions, as shown in figure 1.2, where a simulation output is reported.

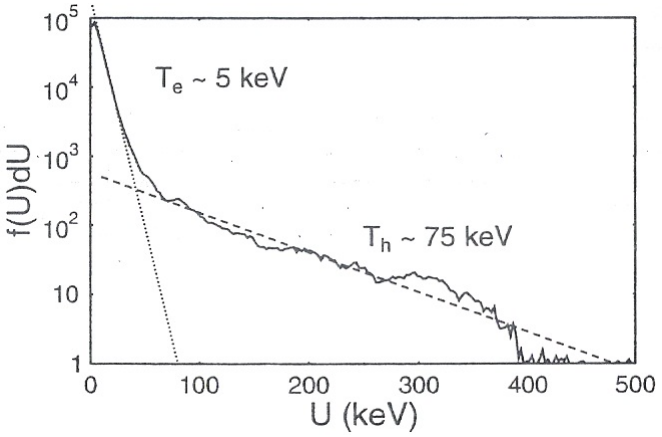

FIGURE 1.2: Typical bi-Maxwell electron distributions due to the collisionless heating. The plot reports a 2D-PIC simulation output (I=5 $\times 10^{16}$ Wμm^2/cm^2, laser incidence angle of 45 deg, n_e/n_c=3) [6].

1.4 Main acceleration mechanisms

Up to now, the ions dynamics has been neglected, as they are much heavier than the electrons and therefore not able to contribute within short time scales. Ions indeed respond to slowly varying electric fields.

Roughly ion acceleration mechanisms can be divided into two groups, according to the target side

from which ions are accelerated: *Rear surface acceleration* and *Front surface acceleration* [4, 10]. Figure 1.3 shows these two acceleration groups.

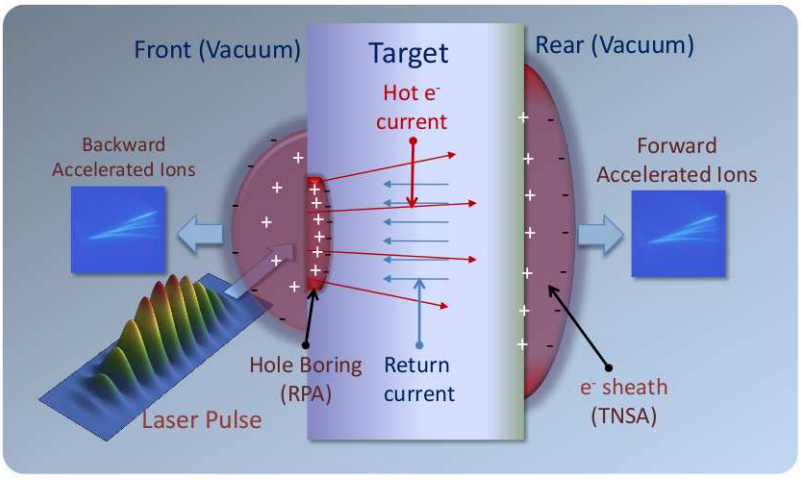

FIGURE 1.3: Figure shows some of the possible acceleration mechanisms in the interaction with a thick solid target, including TNSA at the rear side and hole boring RPA at the front side. The hot electron flow leading to sheath formation and expansion at the rear side together with the associated return current are also reported [4].

- **Rear surface acceleration**: a very intense current of high energy hot electrons may be generated at the front side of the target and eventually reach the rear side. There, as the hot electrons cross the rear side boundary and attempt to escape in vacuum at the rear side, a charge unbalance is generated and consequently also a sheath field E_s, normal to the rear surface. Since E_s must take back electrons with typical temperature T_h, we can describe the distance L_s of the sheath from the target via the relation:

$$eE_s \approx \frac{T_h}{L_s} \tag{1.18}$$

where e is elementary charge and L_s can be approximated with the Debye length of the hot electrons λ_{Dh}. This approximation comes directly from the definition of Debye length that is the distance within which a significant charge separation can occur. Considering n_h the density of hot electron, we have:

$$L_s \approx \lambda_{Dh} = \left(\frac{T_h}{4\pi e^2 n_h}\right)^2 \tag{1.19}$$

For typical experimental data, electric field values of about 10^{10-11} V/cm can be calculated. This huge field will backhold most of the escaping electrons, ionize atoms at the rear surface and start to accelerate ions. As a rough estimate, a test ion crossing the sheath would acquire the energy $E_i \approx ZeE_sL_s = ZT_h$, resulting in a $I^{1/2}$ scaling (see equation 1.7).
Since the target can contain hydrogen impurities on its surface, protons can be easily accelerated from this layer (target rear side). In fact they are faster than other ions thanks to their higher charge-to-mass ratio.
This mechanism is commonly known as Target Normal Sheath Acceleration (TNSA). As

discussed also in section 1.4.1, TNSA has become the reference framework to interpret observations of multi-MeV protons from the target rear side.

- **Front surface acceleration**: starting from the first measurements, the possibility of a contribution originating at the front surface of the target was also observed and therefore investigated. The main idea is that the intense radiation pressure of the laser pulse pushes an overdense target inwards, which causes a sharp growth in density profile and changes the shape of its surface. This process is known as *hole boring*, that is a part of the Radiation Pressure Acceleration (RPA) scheme.
  In this acceleration mechanism, the approximate relation for the plasma surface velocity v_{hb} is obtained from balancing electromagnetic and mass momentum flows:

$$I_L/c \approx n_i(m_i v_{hb})v_{hb} \tag{1.20}$$

  with n_i the ion density. This corresponds to an energy per nucleon of

$$E_i = \frac{1}{2}m_p v_{hb}^2 \approx I_L/(An_i c) \tag{1.21}$$

  As one can see, the scaling law of the ions energy with respect to the laser intensity is now I_L, more favourable than the $I_L^{1/2}$, typical of the TNSA regime. This aspect suggests RPA effects will become more important for higher laser intensities.

In table 1.1 a short description of the main features, advantages and drawbacks of TNSA and RPA regimes is reported. We have to remember that TNSA regime dominate for $I_L < 10^{21} W/cm^2$, while RPA for $I_L > 10^{22} W/cm^2$ Considering that all the experiments reported in this thesis have been performed in the TNSA regime, only this mechanism will be treated in more detail.

1.4.1 Target Normal Sheath Acceleration - TNSA

At present available laser intensities up to 10^{21} W/cm^2 the dominant mechanism for ion acceleration from thin foils is referred to the TNSA [23]. Several international groups have experimentally demonstrated the generation of protons with energies up to 70 MeV and heavier ions with energies up to 7 AMeV [4, 24, 25].
In figure 1.4, the detailed scheme of this regime is reported [15]. As shown and as confirmed form the experimental results, the pre-pulse of the laser is intense enough to create a pre-plasma before the main pulse arrives. Relativistic electrons, then generated by the main pulse in the laser focus, start to propagate through the target. Measurements of the optical self-emission (transition radiation) of the electrons leaving the target rear side have resulted in a divergent electron transport inside the target. The electron distribution is broadened by multiple small-angle scattering with the target material in the cold solid region. The full-cone angle was determined at intensities around 10^{19} W/cm^2 for rather thick targets (> 40 μm) to about 30 deg and for thinner targets (< 10 μm) up to about 150 deg [15, 26, 27].

TABLE 1.1: Main features, advantages and drawbacks of TNSA and RPA regimes [Courtesy of D. Margarone]

TNSA
- Large generated proton number: 10^{10-13}ppb
- Relatively high proton energies: scale with $I_L^{1/2}$ (I_L is the laser intensity)
- Short bunch duration at the source: few ps
- Very high Beam Currents: few kA
- Small Beam Size: source radius of a few microns
- Very low emittance: $5 \times 10^{-3}\pi$mmmrad (in convent. RF LINAC is ≈ 0.5 πmmmrad)
- High Beam Divergence: energy dependent distribution up to $\approx \pm 20$ deg
- High energy spread: several tens of %
- Low shot-to-shot reproducibility
RPA
- The electromagnetic wave is directly converted into ion energy via the space-charge force related to the displacement of all electrons in a thin foil
- Particle bunch propagates in a ballistic way and gains more energy directly from the laser beam: scale with I_L
- All particles have approximately the same velocity: quasi-monochromatic energy spectrum
- Possible production of GeV-scale proton beams in case of extremely high intensity lasers
- Ultrahigh laser intensities are required: $>10^{22}$ W/cm^2
- Ultrahigh laser contrast is required
- Circularly polarized laser pulses are required
- Ultrathin targets are required: nm scale

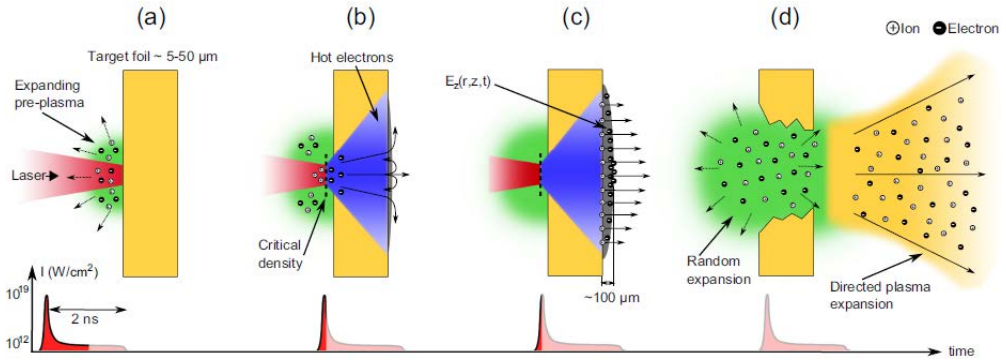

FIGURE 1.4: TNSA-mechanism scheme: the laser pulse coming from the left is focused into the preplasma on the target front side generated by amplified spontaneous emission of the laser system (a). The main pulse interacts with the plasma at the critical surface and accelerates hot electrons into the target material (b). The electrons are transported under a divergence angle through the target, leave the rear side and form a dense electron sheath. The strong electric field of the order of TV/m generated by the charge separation is able to ionize atoms at the rear side (c). They are accelerated over a few μm along the target normal direction. After the acceleration process is over and the target disrupted (ns), the ions leave the target in a quasi-neutral cloud together with comoving electrons (d)[1, 15].

Electrons involved in this regime can be described as part of two different populations. The first is the hot (or fast) electron component, directly created by the laser pulse in the plasma plume at the front surface of the target. Its density is of the critical density order ($n_h \approx 10^{20-21} cm^{-3}$) and its temperature is of the ponderomotive potential order ($T_h \approx MeV$). The free motion of this hot electron beam through the target require the presence of a return current that locally compensates the flow of the hot electrons. In metallic target this current is provided by the second component

of conduction (or cold) electrons that are put in motion by the electric field of fast electrons. The second electron component density is of the solid density order, that is, much bigger than fast component, so the required velocity for current neutralization is small and their temperature is much lower than hot electrons [8].
Therefore if the cold electrons component is trapped in the target, the hot electrons are transported up to the rear side, where, escaping, generate an electron sheath. This sheath can only extend over a thin layer before it is completely shielded. The characteristic distance is called the Debye length and typically is of the order of 10s of μm.
Thanks to this charge separation, that gives rise to an extremely intense longitudinal electric fields $\approx TV/m$, the ion acceleration is finally obtained. As already reported, the acceleration is most effective on protons, which can be present either in the form of surface contaminants or among the constituents of the solid target, as in plastic foils. The heaviest ion populations provide a positive charge with much more inertia, thus creating the charge separation, which generates the accelerating field. Part of the heavy population can be also effectively accelerated, on a longer time scale, if the proton number is not high enough to balance the charge of the escaping hot electrons, and especially if impurity protons are removed before the interaction, for example by pre-heating the target [15].
Several theoretical models have been proposed in order to describe the TNSA regime, but the most efficient in predicting the energy cut-off, thanks to the realistic modelling of the electrons motion, is the one proposed by Passoni [28]. Despite of the strong assumption, this model successfully describes the scaling law of the proton acceleration in TNSA regime, compatible with the experimental results that show a linear dependence of $E_{cut-off}$ with $I^{1/2}$.
Simultaneously to the theoretical studies, several experiments have been indeed performed in order to investigate the properties of the TNSA ion beams. Their energy spectrum is typically broadband, exponential shaped, up to a cut-off energy, i. e. it can be roughly approximated by a quasi-thermal distribution with a sharp cut-off at a maximum energy [4, 29]. Many experiments have reported spectral observations for a wide range of laser and target parameters. A number of experimental studies have been also devoted to the investigation of the angular characteristics of the emitted beams, closely dependent on the electron sheath spatial distribution, and consequently on the target properties (resistivity, surface roughness, etc) affecting the electron propagation.
On average they are characterised by a very wide energy-dependent angular distribution up to $\pm$ 20 deg: more energetic particles are emitted in a narrower angular range respect to lower energetic particles. Figure 1.5 reported a typical energetic spectrum and angular distribution obtained in TNSA regime.

1.5 Scaling law for laser-driven proton beams

Acceleration regimes have been deeply investigated in a very large number of experiments, performed in many laser facilities all over the world. The maximum observed value of the ion energy E_{max} has been probably the most characterising parameter of such experiments together with the shape of the energy spectrum. All these efforts resulted in an extensive collection of experimental

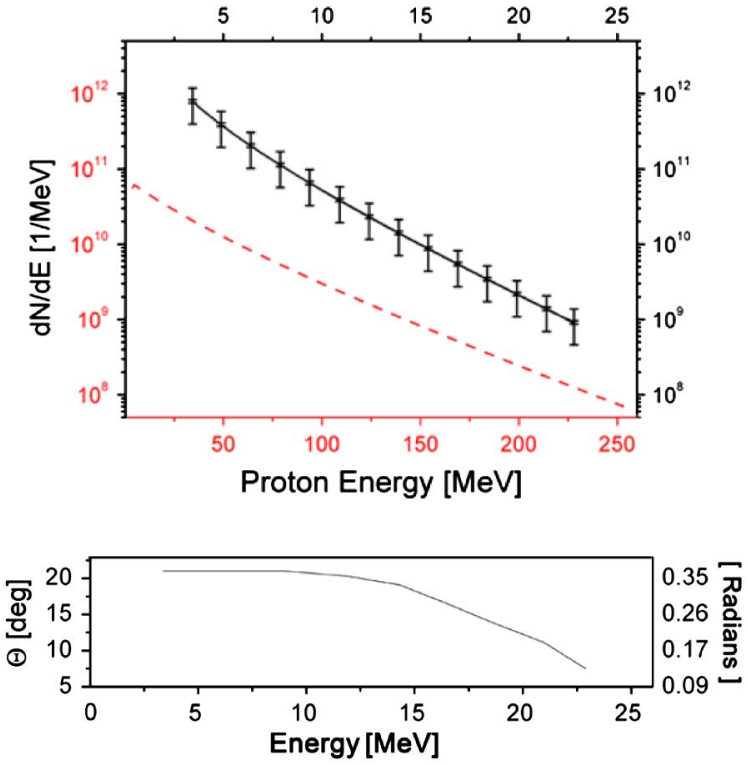

FIGURE 1.5: TNSA regime: typical beam features. Top an experimental energetic spectrum (black solid curve) along with a scaled predicted TNSA spectrum with maximum energy of 250 MeV (red dashed curve). Bottom: Maximum beam divergence as a function of proton energy.[30].

data, useful to understand the basic acceleration mechanisms and, in particular, to provide sufficiently reliable scaling laws, which may give directions for further developments.

In detail, great effort has been put in properly addressing the correlation among the maximum energy value and the main laser and target parameters. Due to the importance of the laser irradiance, in literature it has become common to report the maximum proton energy E_{max} as a function of this parameter. Figure 1.6 shows a collection of experimental data for E_{max} with respect to the laser intensity together with the two trend lines corresponding to a $I^{1/2}$ and I dependences, already described in section 1.4. It is also interesting to study the proton-beam maximum energy and the energy-conversion efficiency varying one parameter at a time, either laser intensity (I), laser energy (E), laser pulse duration (τ_{laser}) or target thickness (d), in order to obtain useful scaling laws [29, 31–33].

For instance, figure 1.7 reports how solid targets thickness changes the maximum energy of laser-accelerated protons as well as the laser-proton energy-conversion efficiency. As shown, when the target thickness decreases, the maximum proton energy and the energy-conversion efficiency grow, but if the target is too thin (8 μm for parameters of the reported example) the proton energy drops down because of the surface disruption before the main laser pulse arrival.

The shown experimental data have been compared in [29] with a simple self-similar, isothermal, time-limited fluid model using a single free parameter, the effective acceleration time (or limit time) t_{acc}. For this model, the maximum (cut-off) energy that can be gained by the accelerated ions is:

$$E_{max} = 2T_h \left[ln \left(t_p + \sqrt{t_p^2 + 1} \right) \right]^2 \tag{1.22}$$

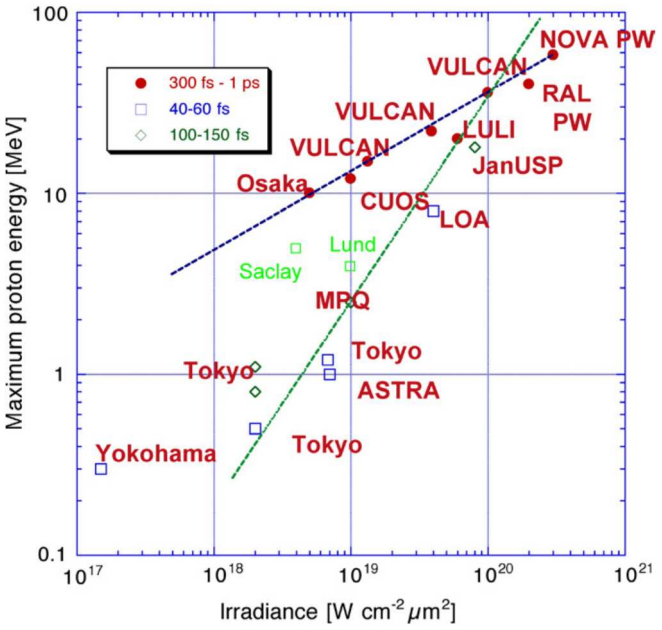

FIGURE 1.6: Maximum proton energy from laser irradiated solid targets as a function of the laser irradiance and for three ranges of pulse durations, and with additional data (labels Lund and Saclay) reporting later experiments up to 2008. Two trend lines are overlaid, the shallower one corresponding to a $I^{1/2}$ dependence, and the steeper one to a scaling proportional to I [4].

where $t_p = \omega_p t_{acc}/\sqrt{2exp(1)}$ is the normalized acceleration time with the plasma frequency defined as $\omega_p = \sqrt{Z_i e^2 n_{e0}/(m_i \epsilon_0)}$, e the elementary charge, t_{acc} the acceleration time, ϵ_0 the electric permittivity, m_i the particle mass, Z_i its state of charge (for protons $m_i = m_p$ and $Z_i = 1$) and n_{e0} and T_h the density and the temperature of hot electrons, respectively [11]. As shown in figure this model fits well with experimental data, if $t_{acc} = 1.3 \times \tau_{laser}$. Data reported in figure 1.7 are referred to Aluminium targets. Other conductor targets (for example, gold) give similar proton-beam results, on the other hand insulator targets show unsatisfactory filamentary proton beams [29].

1.6 Scaling law for lasers

Laser-plasma based accelerators have the potential to deliver accelerating gradients values more than 1000 times higher than in conventional accelerator technology. This large increase in accelerating gradient together with the reduced shielding requirements for the laser technology have represented crucial elements in the comparison with conventional accelerators, considering also the associated possibility size and cost reduction.

It should be emphasised that many of the applications, currently performed with conventional accelerators, have been demonstrated on very large lasers as proof of principle and will soon be carried out on the new generation of compact scale high-intensity, high repetition rate lasers [5].

After the invention of the laser technology in 1960, the power of lasers has increased dramatically over the years and recent advances have led to the development of multi-terawatt and petawatt

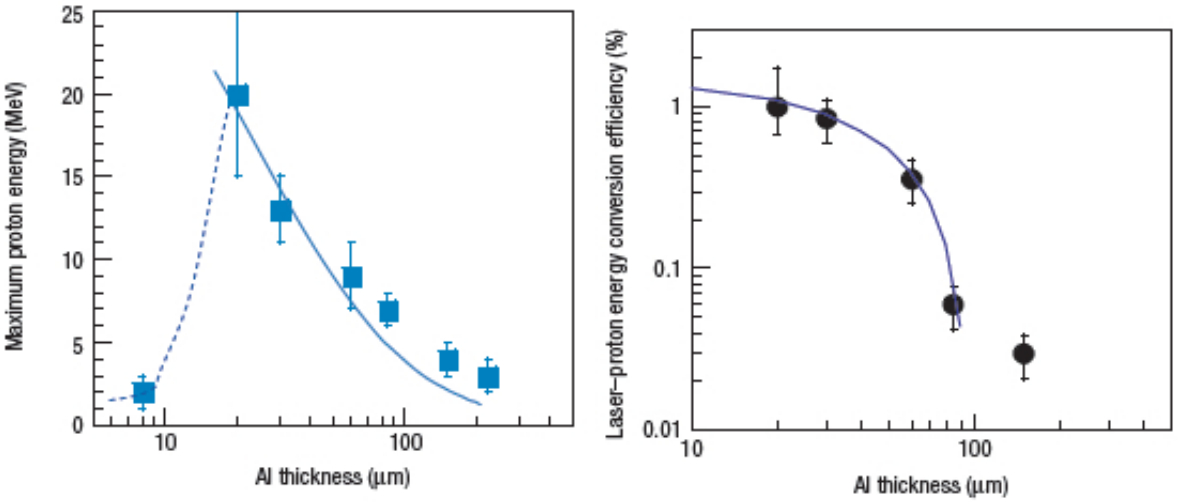

FIGURE 1.7: On the left, the maximum proton energy, and on the right, the laser-proton energy-conversion (calculated for protons with energy >4 MeV) for similar laser conditions (τ_{laser} =320 fs and I ~4 × 10^{19} Wcm^{-2}) and various Al foil thicknesses. Data points represent experimental data and solid lines calculations using the fluid model with the same laser parameters. The dashed line is a guide for the eye. Error bars on the proton energy represent the shot-to-shot fluctuation cumulated with the simulated measurement uncertainty in the detector. Error bars on the energy conversion efficiency are standard deviation, and take into account the maximum energy error bar, the error in the laser energy and the uncertainty in the calibration of the detector that induces uncertainties in the absolute proton number. More details are reported in [29].

pulsed laser systems in many worldwide laboratories. Figure 1.8 illustrates the increase in achievable laser intensity since 1960. As shown, the greatest advance was made in the mid-1980s with the

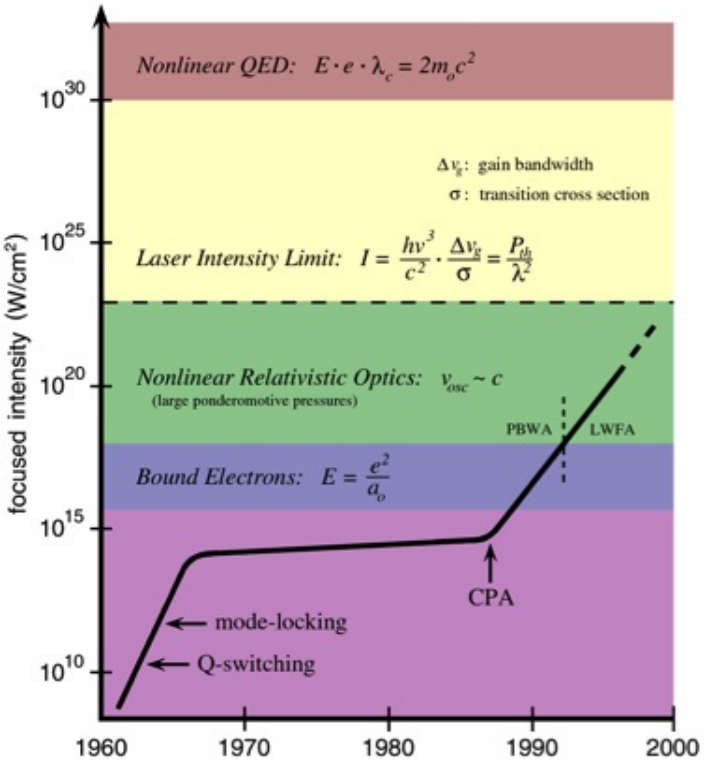

FIGURE 1.8: Scaling of the maximum laser intensity due to the technologic improvements, as a function of the time.

introduction of chirped pulse amplification (CPA) by Strickland and Mourou [34]. In CPA, a laser pulse of the order of femtoseconds or picoseconds is temporally stretched by three to four orders of magnitude using dispersive gratings, thus preventing damage to the laser-amplifying medium. After amplification, these laser pulses are recompressed to deliver about 10^{18-21} Wcm^{-2} on the target. Several techniques promise to continue to extend the boundaries of laser science in the foreseeable future [5].

In this field the pioneer was the Lawrence Livermore National Laboratory (LLNL) where a series of high-power lasers have been built since the 1970s up till the present time, when ultimately the National Ignition Facility (NIF) is delivering a total laser energy of 1.8 MJ divided on several laser beams, up to 192. A number of large-scale facilities like NIF have been or are being built, such as at the Institute of Laser Engineering at Osaka University in Japan (FIREX project) and at the Rutherford Appleton Laboratory in the UK (VULCAN laser).

Alternatively to the large-scale facilities, it is expected that the compact, high repetition rate, table-top lasers with comparable intensity parameters will define the future for laser-driven nuclear and particle phenomena [35]. With respect to compact table top lasers, there already exist a large number around the world in the 10-200 TW power regime yielding laser intensities between 10^{19-20} Wcm^{-2}, such as the 100TW JanUSP laser of the Lawrence Livermore Laboratory with 10 J at 100 fs and intensities of 10^{20} Wcm^{-2} [36]; the 10 Hz, 100TW high-intensity laser, with 2.5 J at 25 fs, 6×10^{19} Wcm^{-2} at the Laboratoire d'Optique Appliquee, LOA [37] and the 100TW laser at the Laboratoire pour l'Utilisation des Lasers Intense, LULI with 30 J at 300 fs and intensities of 6×10^{19} Wcm^{-2} [38]. In 2004, HERCULES, a laser facility at the University of Michigan, claimed the world record in laser intensity of about 0.7×10^{22} Wcm^{-2} (27 fs, 1.2 J) [39].

As one can argue from this historical overview, the improvement at the laser level is very promising. The possibility to increase the laser intensity represents indeed a crucial parameter, considering that it is strictly related to the possibility to reach higher energy for the optically accelerated ion beams and therefore to fulfil one the main requirements for their application in several fields.

1.7 A demonstration case: the hadrontherapy application

Since the first experiments reporting multi-MeV proton acceleration from laser-irradiated foils, the research on developing a high-quality, controllable, laser-driven proton source gained incredible interest. The field of applications for this kind of beams is indeed very wide, it goes from the plasma physics to interdisciplinary areas, such as proton radiography and imaging, nuclear reactions and fast ignition. In this thesis as well as in the project in which it is developed, the hadrontherapy application has been chosen as demonstration-case. Medical applications are indeed the most demanding in terms of beam characteristics and performances, i. e. beam delivering system, advanced diagnostics and precise dosimetry.

Hadrontherapy is a kind of radiation therapy, which uses high energetic carbons and protons to irradiate cancer tumours. It is characterised by a number of advantages in respect to radiation therapy with gamma-rays, thanks to the lower integral dose received by healthy tissue together with the well localized maximum of the released dose limited to the ion stopping point (Bragg peak).

Also the biological effectiveness is higher for charged radiation in respect to photons, thanks to the higher ionization density. This aspect allows to enhance the probability of DNA double strand break and therefore the therapeutic strength [40–42]. Figure 1.9 sums up the reported advantages. In detail, proton therapy has been successfully used for the treatment of different types of tumours,

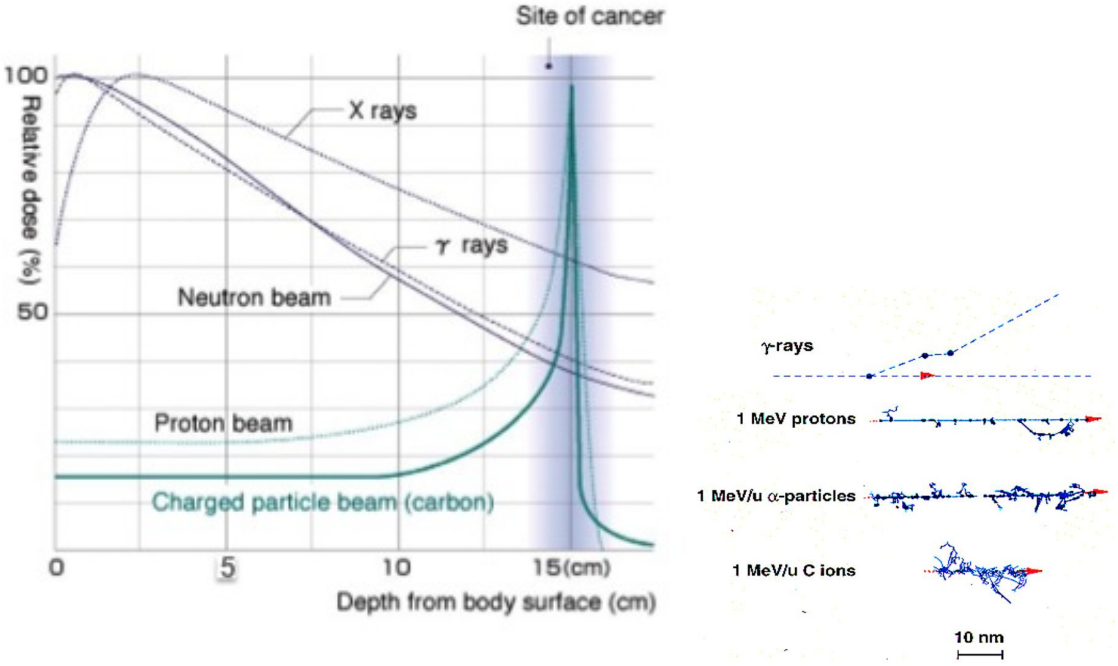

FIGURE 1.9: The main advantages of hadrontherapy with respect to conventional radiotherapy. On the left the physical advantage: different relative dose distributions as a function on the depth (ballistic property of proton/ion beams). On the right the biological advantage: different secondary electrons densities along the primary particle path.

such as eye tumour using relatively low-energy particles and various paediatric tumours or cervical and prostate tumours, with high-energy protons. On the other side, heavier ions (carbon ions) have additional clinical advantages due to lower scattering effect and greater biological effectiveness in the target, if compared to X-, gamma-rays and protons. The main disadvantage of use carbon beams is associated with the exposure of tissues located just behind the Bragg peak. This is due to the projectiles fragments created in the inelastic nuclear collisions of carbons with the atomic nuclei of the body tissue. Up to now, carbon ions have been utilised mainly in the treatment of malignant tumours occurring in cervical spine, salivary glands, lungs, prostate, liver and soft tissues [43].
The therapeutic use of proton/ion beams for cancer treatment was proposed for the first time by R R Wilson in 1946 at the Lawrence Berkeley Laboratory (LBL) in Berkeley, USA [44]. Few years later, the first clinical application was performed. John Lawrence used protons from the LBL cyclotron for pituitary hormone suppression in patients with metastatic breast carcinoma [45]. Right after, several treatments have been performed in the United States (Harvard), in Sweden (Uppsala) and in the USSR (Moscow and Dubna). Since then, about 110 thousand cancer patients have undergone hadrontherapy (90% with the use of protons, and 10% with heavier ions, mainly carbons) [46].

After more than 50 years from the first proton treatment, several clinical centres are being constructed and designed for proton radiation therapy treatment even though they are not enough, yet, to satisfy the requests [47].

1.7.1 Conventional acceleration and beam requirements

Unlike research institutes wherein the era of hadrontherapy was originated, all new centres are equipped with dedicated medical ion accelerators, from which the beams are transported to 3-5 treatment rooms.
At present only 42 hadrontherapy centres operate around the world, although up to 30% of cancer patients need this form of treatment. A wide implementation of hadrontherapy is indeed difficult because it requires an ion accelerator (e.g., a quite large cyclotron or synchrotron) and a system for the ion beam transportation and manipulation. These technically sophisticated elements cost from 100 to 200 million euros in the case of a therapeutic centre with four treatment rooms.
Considering this background, investigations are currently being undertaken, aiming at the development of more compact and less expensive technologies. Several companies are indeed working on compact medical ion accelerators, exploiting technologies known in the field of conventional particle accelerators, such as superconducting cyclotrons, synchrocyclotrons or compact linacs [48, 49]. Although these possible improvements, one of the most expensive element is still necessary, without an alternative candidate. It is the GANTRY system, which is a device intended for the multifield (from different directions) irradiation of the laying patient. The gantry allows indeed to have different incident angles of the ion beams around the patient, providing tumor irradiation from all needed directions, as shown in figure 1.10 [40, 50].

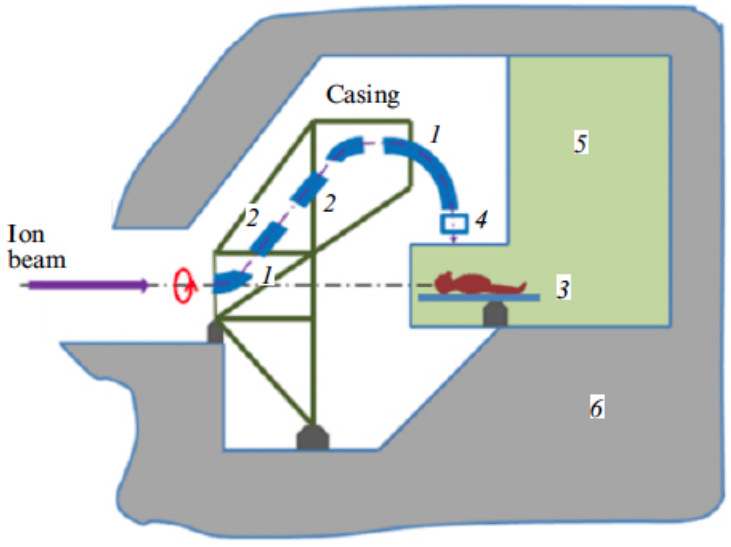

FIGURE 1.10: Classical setup of a gantry: (1) bending magnets, (2) quadrupole lenses, (3) positioner, (4) system of dose formation and dose monitoring, (5) treatment room and (6) concrete protection. The casing with the elements mounted on it can be rotated up to 180 deg [40].

Currently, the majority of hadrontherapy centres apply the methods of passive beam broadening. Schematic of the corresponding instrumentation to control the ion beam parameters is shown in figure 1.11.

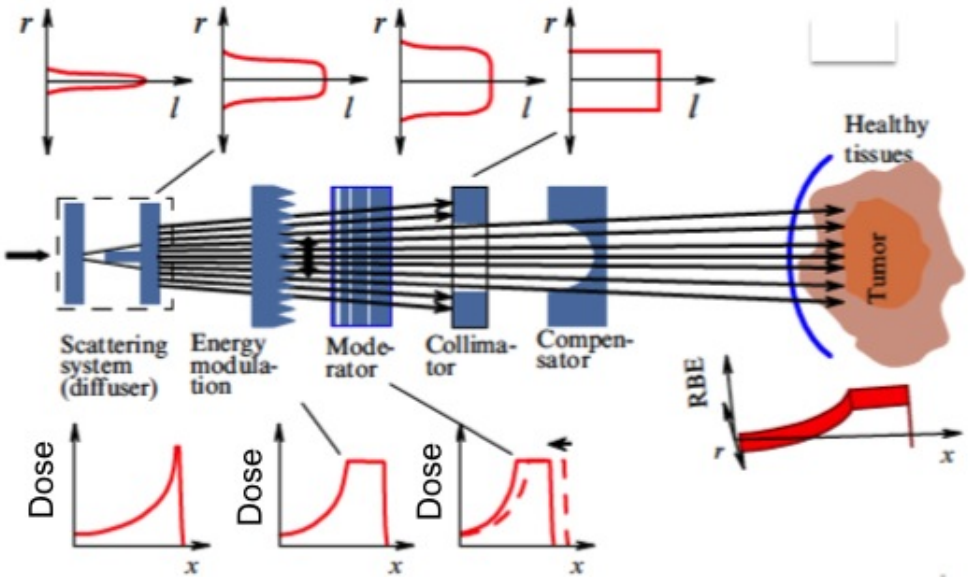

FIGURE 1.11: Schematics of a passive formation of the dose field [51].

The monoenergetic collimated beam is broadened in the transverse direction by a diffuser (a foil with a certain thickness), which makes the distribution of particles uniform over a larger diameter. Then, passing through holes whose shape corresponds to the shape of the tumour, the beam is shaped according to the specific target. The beam particles pass also through thickness-modulated decelerating filters. Since the energy loss is proportional to the thickness of the filter, different parts of the beam lose different energies. In this way, the beam energy spectrum is modified obtaining a uniform dose distribution on the target area (SOBP) [40].

The second used method for the dose delivering is the active target irradiation, based on the transverse deflection of ions by a magnetic field. It was first implemented for proton beams at the Paul Scherrer Institute (PSI) in Villingen (Switzerland) [52]. The principle of active irradiation of a tumour is illustrated in figure 1.12 [40]. The volume of the target is divided into a sequence of

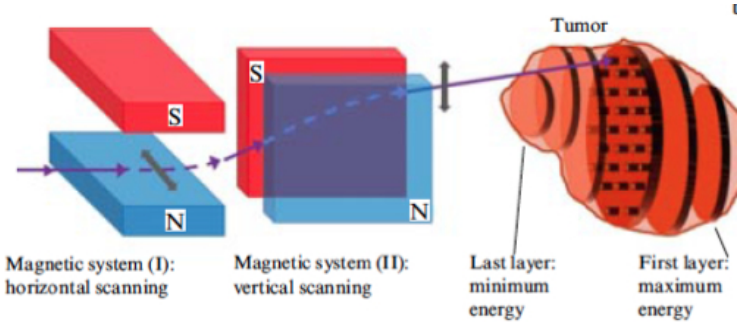

FIGURE 1.12: Active target scanning [53].

layers, which can be reached by particles having different energy. Using two fast-varying magnets

deflecting pencil ion beams in the vertical and horizontal directions, the target is scanned voxel-by-voxel, starting with the outermost layer. After the complete scanning of a layer, the beam energy is decreased, and the next layer is scanned.

The basic parameters required in an ion beam for the medical application are easily reached with conventional accelerator technology. They essentially depend on whether the chosen method of a target irradiation is passive or active. In all cases, however, the maximum energy should be equal to 250 MeV for protons, and to 430 MeV/n in the case of carbon ions. The beam intensity must be equal to about 5×10^{10} particle/s for protons and to 10^9 particle/s for carbons. There is also the requirement of a 'quasi' monoenergetic beam with $\Delta E/E = 10^{-2}$, together with a system duty, i.e., the fraction of the time of during which the beam can be used, that must be not smaller than 0.3. Moreover, an absolute dosimetry, with an uncertainty less than 3 % is of crucial importance for a successful treatment [40, 54, 55].

1.7.2 Optical acceleration

An approach fundamentally different is based on the idea of a laser ion accelerator, defined as a ≪*compact, flexible and cost-effective*≫ solution [56]. Thanks to the relatively small-size of laser ion accelerator together with the associated cost-reduction expected with the future technological progress, high-energy proton and heavier ion beams could be much more accessible for patients treatment. There are at least two possible ways of using a laser accelerator. In the simplest one, it replaces a conventional accelerator, still maintaining the transport beamline. In the other one, which appears to be much more attractive, instead of devices comprising bulky and heavy magnets required for the beam deflection, it is proposed to use an *all-optical* system, which bends and rotates laser beams, arranging their interaction with a target in such a process that generates fast ions directly in the treatment room and not outside it, as shown in figure 1.13. This can simplify the technical problems related to the generation and the transport of ion beams, substantially reducing the costs [40, 50].

Another positive aspect in the laser acceleration choice in respect to the conventional one, in a future perspective, is related to the possible introduction of innovative treatment modalities based on hybrid treatment (protons, ions, electrons, gamma-rays, neutrons) [4, 40]. During the laser-target interaction different particles are indeed produced.
On the other side, for the implementation of laser accelerators in hadrontherapy, the parameters of accelerated ion beams, in terms of energy, stability and quality, must satisfy the same requirements as established in conventional hadrontherapy.
Currently, the energy of beams accelerated in the laser plasma experiments is approaching the value at which protons can be considered for therapeutic applications. However, some beam properties have not yet reached the necessary level or are not sufficiently well controllable. Regarding the energetic spectrum, proton pulses obtained from the laser-target interaction are far from being monochromatic. Usual energy spread is about 100%, with only a small fraction of the total flux at

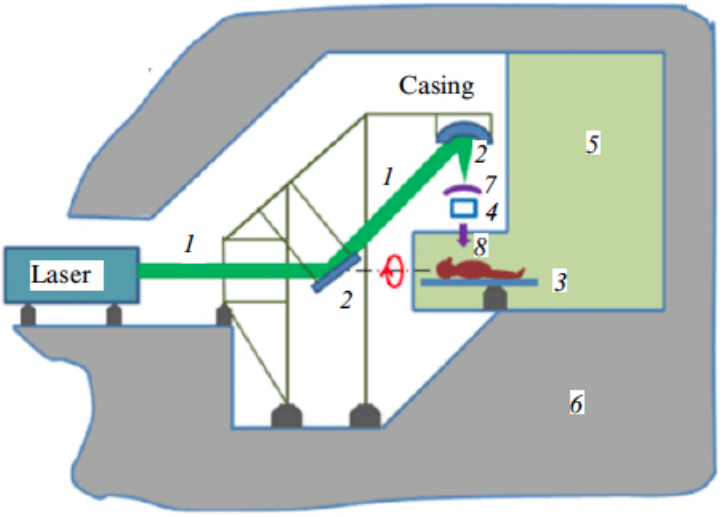

FIGURE 1.13: Optical setup equivalent to the conventional gantry: (1) laser beam, (2) optical system of transportation and focusing of the laser pulse, (3) positioner, (4) dose monitoring system, (5) treatment room, (6) concrete protection, (7) target and (8) ion beam. The casing with the elements mounted on it can be rotated up to 180 deg [40].

the highest energy [37]. Moreover, laser-driven protons emerge from a spot size of about 1 μm in diameter and are characterised by an angular distribution ranging up to approximately $\pm$ 20 deg. Progress is being made to improve these aspects with shaped targets or exploring new acceleration regimes [4, 57], but up to now it is not sufficient yet. Another challenge is also represented by the extremely high particle fluxes per shot, which imply the development of novel detectors for diagnostics and dosimetry. A further complication is also given by the presence of the electromagnetic pulse, which is an issue for on-line detectors.

Several problems are also related to the possibility to reach the required number of particles per second that should be solved using optimised targets and improving the laser systems. On the way towards this challenging improvement, it is necessary to solve a number of sophisticated technical problems, among which extremely important are the enhancement of laser pulse stability and repetition rate, in connection with an increase in average laser power [29, 58].

For the hadrontherapy application, an open issue is represented by the relative biological effectiveness of high-energy ions accelerated by laser radiation, in comparison with ions generated by conventional accelerators. Several groups have indeed started preliminary work on the methodology and viability of using laser-driven ion sources for cell irradiation experiments, a mandatory step in view of any future therapeutic use. The main aim of these investigations is to establish a procedure for cell handling, irradiation and dosimetry compatible with a laser-plasma interaction environment [59, 60]. In detail, as regarding the cell irradiation, the biological effects of laser-driven protons emitted in bursts of picosecond duration at the source and therefore characterised by ultra-high dose rates, are up to now virtually unknown and need to be carefully assessed prior to any possible therapeutic use.

Summing up, laser-driven accelerators represent a possible alternative to conventional ones, but many efforts have to be dedicated on the laser technology development, on the laser-target interaction optimisation as well as on the realisation of dedicated transport beamlines and dosimetric

detectors in order to envisage possible future medical applications. The main tasks are to obtain a reproducible and controlled beam with approximately monoenergetic spectrum and narrow angular distribution, to have the knowledge of their biological effectiveness and to realise precise dosimetric detectors.

Chapter 2

Monte Carlo simulation of a transport beamline

Monte Carlo methods are widely used in several fields. In this thesis, they were used to simulate the response and to perform the preliminary studies of a transport beamline dedicated to laser-driven beams. The beamline prototypes, developed to control the laser accelerated proton beams up to 30 MeV, will be described in chapter 4.
In detail, the Geant4 toolkit has been used to developed the simulation code. Each element has been simulated with its real sizes and magnetic properties. Also the non-conventional energetic and angular distributions of a typical laser-driven beam have been implemented.
The development of this Monte Carlo tool was guided by two main goals: provide preliminary predictions in order to support the design of the beamline elements and study the particle transport, fluences and doses along the beamline in order to optimise the beamline configuration considering the necessity.
In this chapter, after an introduction on the Monte Carlo methods and on the Geant4 toolkit, the code used for all the simulations reported in the thesis is presented. It has been also added to the official *hadrontherapy* advanced example, freely released in the Geant4 toolkit, since the version 10.1.

2.1 The Monte Carlo method

Monte Carlo (MC) is a technique used in scientific computing, which can provide approximate solution to complex problems. The key feature of MC method is the usage of random numbers: the problem is handled by producing random-generated repetitions of the experiment, according to the appropriate probability distributions, and deriving the average and the other statistical properties [61]. MC method plays a major role in the various research fields including the particle therapy and transport with a consequently relevance in the clinical applications.
Although there were a number of isolated and undeveloped applications of Monte Carlo simulation

principles at earlier dates, modern application of Monte Carlo methods dates from the 1940s, when the term *Monte Carlo* was coined by physicists working on nuclear weapon projects at the Los Alamos National Laboratory. They were investigating the radiation shielding and the distance that neutrons would likely travel through various materials. Despite they had most of the necessary data, such as the average distance a neutron would travel in a substance before it collided with an atomic nucleus, the problem could not be solved by theoretical calculations. John von Neumann and Stanislaw Ulam suggested that modelling the experiment on a computer, by using a probability, could solve the problem. Their secret code was named 'Monte Carlo' from Von Neumann [62]. The name is a reference to the Monte Carlo casinó in Monaco, where Ulam's uncle would borrow money to gamble and, more in general, it is related to the random characters of the games of chance, such as the roulette.

Mathematician Stanislaw Ulam said: ≪ *The first thoughts and attempts I made to practice [the Monte Carlo method] were suggested by a question which occurred to me in 1946 as I was convalescing from an illness and playing solitaires. The question was what are the chances that a Canfield solitaire laid out with 52 cards will come out successfully? After spending a lot of time trying to estimate them by pure combinatorial calculations, I wondered whether a more practical method than 'abstract thinking' might not be to lay it out say one hundred times and simply observe and count the number of successful plays. This was already possible to envisage with the beginning of the new era of fast computers, and I immediately thought of problems of neutron diffusion and other questions of mathematical physics, and more generally how to change processes described by certain differential equations into an equivalent form interpretable as a succession of random operations. Later [in 1946] I described the idea to John von Neumann, and we began to plan actual calculations.*≫ [63]

After this first application, in 1950s, MC methods were used for the development of the hydrogen bomb. Nowadays they are widely used in several fields in Physics as well as in Chemistry, following different approaches. However, these approaches tend to follow a fixed scheme: define a domain of possible inputs, generate inputs randomly from the domain using a specified probability distribution, perform a deterministic computation using these inputs and aggregate the results of the individual computations into the final result. Thus, the reliability computation is heavily dependent on the goodness of the random numbers, which are required in large amounts to achieve good statistics. Therefore long chain of random numbers has to be 'created' with the so called *pseudorandom* numbers generators, i. e. algorithms for the generation of a sequence of numbers that approximately have the properties of random numbers, even if they are completely determined by an initial state, named *seed* [64, 65].

2.2 The Geant4 toolkit

Several Monte Carlo codes have been recently developed for different applications in physics, such as Geant4, EGS [66], PENELOPE [67] and MCNP [68]. From the historical point of view, the development of Monte Carlo codes in Physics is coming in particular from the nuclear and high energy physics, because of the ever-increasing demand for large-scale and accurate simulations of complex particle detectors. However, similar requirements also arise from other fields, from the

nuclear medicine to the space science.
The Geant4 (GEometry ANd Tracking) [69, 70] toolkit, which the simulation reported in this thesis are based upon, is one of the most widely used Monte Carlo codes. It is currently used in several fields, from high energy to medical physics and space science, thanks to its advanced functionalities in the geometry description and to a wide and well-tested set of physics models.
The first version of a code devoted to particle-tracking of high-energy physics has been released in 1974 at CERN (Geneva, CH) in order to simulate the interaction of high-energy elementary particles with detectors. This first version was limited in the number of transported particles and detector geometries. In 1982 the initial code evolved through Geant3, written in Fortran language. It allowed to simulate very big experimental setups together with the transport of high-energy beams. The limit of this language relied on the huge number of lines strictly linked to each other, difficult to understand and manage for external users. An important year that has signed a great change in the code evolution was the 1998. Indeed, during this year a new generation of MC code, named Geant4, is released. It is written in C++ language and it takes advantage from the object oriented software technology, which allows writing a clearer and more partitioned code. Geant4 is currently developed and managed by an international collaboration constituted approximately by one hundred members from Europe, North America and Japan. Usually, two updated versions of Geant4 are release every year [71].
Geant4 is a toolkit, i. e. a collection of libraries written in C++, with no ready-to-use default program. Indeed, the Geant4 source code consists of a kernel containing all libraries and tools that the user has to include, according to the specific requirements of his application. Moreover, the user must derive the concrete classes constituting the application from the virtual interfaces included in the kernel. The object-oriented language allows the development of distinct classes according to the different aspects of real experiments, as for instance the geometry and material description, the source modelling, the physics processes and so on. As all Monte Carlo radiation transport codes, Geant4 follows specific procedures of computation:

- define a set of possible inputs and restraints for a system;
- randomly generate inputs into the system and perform computation;
- aggregate the results of the individual computations into the final results.

Till the Geant4 version 9.6, the code has been written in a sequential mode and the simulation run was managed by one thread at a given time. This could slow down the simulation, due to high computation time, especially when high statistics was required. In order to overcome computation time issues, the multi-thread mode has been implemented in the toolkit since the version 10.0 and included in the official release. It consists in the event parallelism i.e. each thread simulates one or more events independently and at the same time [72, 73]. Only the master thread controls the overall data flux, distributes the events to the workers threads and produces the final results. The thread parallelism significantly accelerates the data processing, still guaranteeing affordable results. The possibility to run in the sequential mode the simulation was, however, still maintained.

2.3 Main features of the Geant4 toolkit

The Geant4 toolkit has been built as the basis for specific simulation components, therefore it was required to have interfaces with other components and to provide parts to be used with other components. During the design phase, modularity and flexibility are recognised as crucial requirements, but coupled to the possibility to implement physics models that has to be transparent and open to user validation. A modular and hierarchical structure for the toolkit has been therefore developed, with sub-domains linked by an uni-directional flow of dependencies.
The main domains for the simulation of the particle passage through matter are:
- geometry and materials;
- particle interaction in matter;
- tracking management;
- event and track management;
- visualization and visualization framework;
- user interface.

These domains led to the creation of corresponding class categories that are used to create logical units. Class categories are defined as ≪ *clusters of classes that are themselves cohesive, but are loosely coupled relative to other clusters*≫. This means that a category contains classes, which have a close relationship. However, relationships between classes which belong to different class categories are weak, i.e., only limited classes of these have *uses* relations. The class categories and their relations are presented in figure 2.1 by a class category diagram. Each box in the figure represents a class category, and a *uses* relation by a straight line. The circle at an end of a straight-line means the class category which has this circle uses the other category. As shown in figure 2.1, there is an unidirectional flow of dependencies. Categories at the bottom of the diagram are used virtually by all higher categories and provide the foundation of the toolkit. There is the *global* category that covers the system of units, numeric constants and random number handling, the *materials*, *particles*, *graphical representations and geometry* categories dedicated for the detector description and the navigation in the geometry model, and finally the *intercoms* which provides both a means of interacting with Geant4 through the user interface and also a way of communication between modules that should not otherwise depend on each another.
The other categories displayed on figure 2.1 are required to describe the particles tracking and the physical processes they undergo. In particular, the *track* category contains classes for tracks and steps, used by the *processes* which contain implementations of physics interactions models. Additionally, one such process, *transportation*, handles the transport of particles in the geometry. All processes may be invoked by the tracking package, which manages their contribution to the evolution of a track state and provides information from *hits* in the sensitive volumes (i.e. energy deposition, generation of secondary particles, etc.), and *digitisation* (model of the detector response). Over these, the *event* package manages the single event and the *run* one the collections of events, that share a common experimental configuration. The *readout* package allows handling the description of the electronics and the readout associated to the experimental set-up. Finally, the *visualisation*, *persistency* and *user interface* packages use all of the above packages, connecting

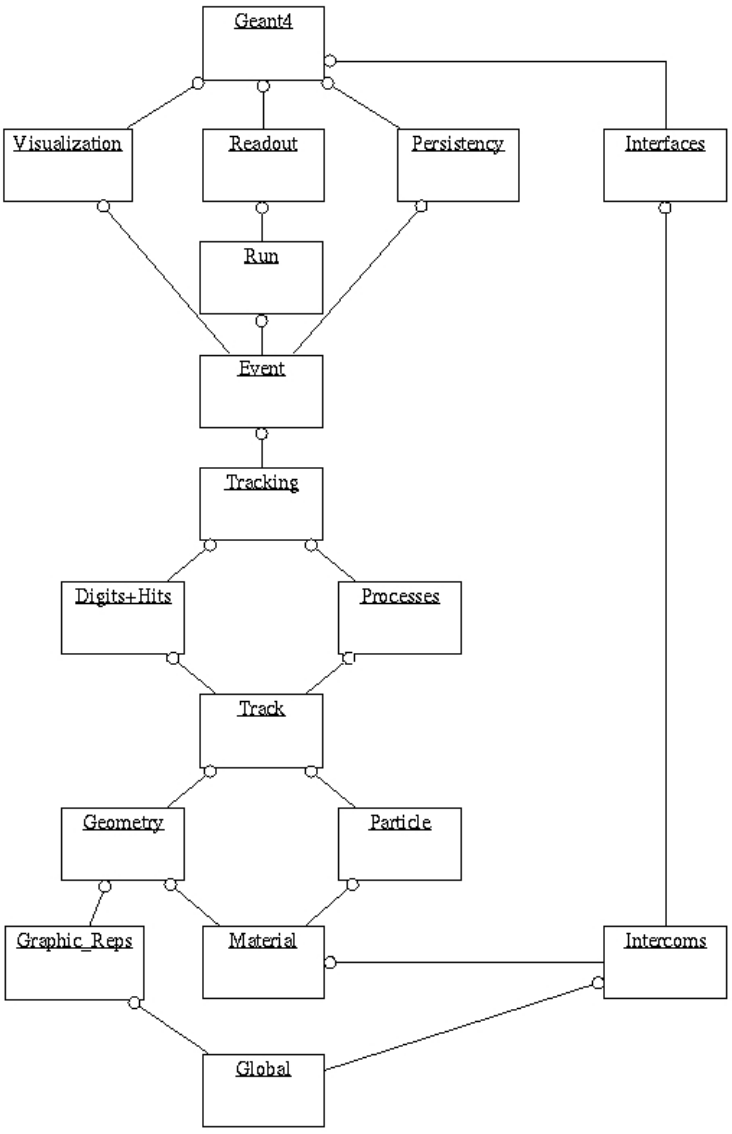

FIGURE 2.1: The top level category diagram of the Geant4 toolkit. The open circle on the joining lines represents a using relationship; the category at the circle end uses the adjoined category.

the whole application with the user.

Summarising up, Geant4 is one of the most used Monte Carlo code because it provides comprehensive detector and physics modelling capabilities. It is possible to model the experimental set-up in terms of geometry and materials and to define the particles involved and their physics interactions. The user can track particles in matter and describe the response of the detector. Moreover, Geant4 provides interfaces to enable users to interact with their simulation application and to store their results in analysis objects (histograms, ntuples, etc.). Visualisation drivers and graphical user interfaces are also provided.

The main advantage of using Geant4 is provided by its wide offer of complementary and alternative physics models describing both the electromagnetic and hadronic interactions of particles with matter.

In order to better show the main features of the most important packages of the Geant4 toolkit, a

more detailed description is reported below.

2.3.1 Geometry and materials

The *geometry* package allows to describe a geometrical structure and to propagate particles through it. A component of the experimental set-up is defined geometrically, through three layers:

- Solid: the shape and the size of a geometrical component are defined.
- Logical volume: the attributes (material, sensitivity, presence of electromagnetic fields, etc.) of the component are defined.
- Physical volume: the placement of the volume with respect to the enclosing mother volume is defined.

The experimental set-up of a generic Geant4 simulation is modelled with a hierarchical tree structure, each volume containing smaller volumes. The largest volume which has to contain each else defined volume is the $World$ volume.
The *materials* category reflects what exists in nature. Materials are made of single element or of a mixture of elements. Similarly elements are made of single isotope or of a mixture of isotopes. Characteristics like radiation and interaction length, excitation energy loss, coefficients in the Bethe-Bloch formula etc. are computed for each material. A ready-to-use table containing all the elements and materials that can be implemented is already provided in the Geant4 kernel and it is invoked through the instance of the $G4NistManager$ class. This table is derived by the NIST (National Institute of Standards and Technology) database of elements and isotope composition [64, 65, 74, 75].

2.3.2 Detector and Hit

The *Detector* package manages the detector components of the experimental set-up. A Geant4 detector is created when the *sensitivity* attribute of the associated geometrical component is set at the level of the logical volume. There can be more detectors within the same Geant4 experimental set-up. If a volume is defined *sensitive*, several information can be stored by using a collection of Hit, such as the energy deposition, the particle momentum, time or position. The Hit, derived by the $G4VHit$ class, is a snapshot of a physical interaction of a track in the sensitive region of the detector. Then, at the end of each event or run, the collected information can be stored in an output file. A *digit* represents a detector output.

2.3.3 Primary particle

The *primary particle* component manages the modelling of the radiation field of interest. Particles are based on the $G4ParticleDefinition$ and $G4PrimaryParticle$ classes, which store the basic

static properties of particles, like type, energy, vertex and momentum, and allow particles to carry the list of processes to which they are sensitive. The primary particles can be generated mainly by means of the *G4ParticleGun* or *G4GeneralParticleSource* (GPS). Their potentialities are essentially equivalent, however only the GPS allows to easily configure the input properties via UI commands. Moreover, using GPS it is possible to directly use user commands for:

1. particles definition;
2. spatial sampling: simple 2D or 3D surfaces such as discs or spheres and squares or boxes;
3. pre-defined angular distributions: unidirectional, isotropic, cosine-law, beam or point focused;
4. pre-defined energetic spectrum: linear, exponential, power-law, Gaussian, blackbody or user-defined.

When the input features cannot be described using the default GPS functionalities, the ParticleGun represents a more versatile, although less user-friendly, alternative method. Also for this method, there are some basic ready-to-use control commands that allow to set particle type, energy, momentum direction, starting position, initial time, number of particles shooting at one time and polarization, without having to edit the code. However, unlike the GPS, no pre-defined distributions are handled and no ready-to-use randomization is provided.

2.3.4 Tracking

The *Tracking* package manages the tracking of the particles in the experimental set-up, i. e. the sequence of steps for a given particle. The step, managed by the *G4Step* class, is defined as the distance between two subsequent interaction points. At the level of the step it is possible to retrieve information about the particle, e.g. its kinetic energy at begin and at the end of the step, its energy deposition during the step (associated with the beginning of the step) or the undertaken physics process.
Each particle is moved step by step with a tolerance that permits to optimise the execution performance, preserving at the same time the required tracking precision. The smallest step length is chosen between these two following options: the *maximum allowed step* (user selected) and the *step* proposed by the action of all attached processes, including the geometrical limits. The tracking scans all physics processes and actions for a given particle, and then decided for the one which returns the smallest step value.
Charged particles are tracked to the end of their range. However, for CPU performance, a process may, optionally, choose to suppress the secondary particles production, if their range is less than a user-defined value, called *range cut*. In this case the process considers the energy of the non-generated particle to the local energy deposited during the step in order to enforce the energy conservation.

2.3.5 Event and Run

The *event* is the main unit of the simulation. It is managed by the *G4Event* class. It starts when one or more primary particles are generated and it ends when all the primary and secondary particles are fully tracked in the experimental set-up. As regarding the *run* (*G4Run* class), it is a collection of events that share the same conditions. The configuration of geometry, detectors and physics processes cannot be altered during a run.

2.3.6 Physics

The *Physics* category manages all physics processes participating in the particle-matter interactions. The abstract interface of physics processes allows multiple implementations of physics models per interaction or per channel. Models can be selected by energy range, particle type, material, etc. Geant4 offers a wide set of alternative and complementary electromagnetic and hadronic physics models together with several physics processes for the particles-matter interaction, that cover the physics of photons, electrons, muons, ions and hadrons from 250 eV up to several PeV.
For a particle interaction, it is crucial the difference between the *process*, a particular initial and final state with a defined cross-section and mean-life, and the *model* that implements the production of secondary particles. The Geant4 toolkit offers multiple models for the same process.
In general the user can construct a *physics list* by hand, using the physics models contained in the Geant4 kernel or directly using a reference physics list, already containing a set of well-tested physics components. For instance, the QGSP-BIC and the QGSP-BERT reference physics lists, contain the electromagnetic, hadronic, decay and neutron physics models.
In the Geant4 toolkit, there are seven major categories of processes (*G4Process* class): *electromagnetic*, *hadronic*, *transportation*, *decay*, *photolepton_hadron* and *parameterisation*. Moreover, three *pure* types of processes are defined: well-located in space (*PostStep* i. e. *discrete*), distributed in space (*AlongStep* i. e. *continuos*), well-located in time (*AtRest*).
A type of process can be pure *discrete*, *continuous* or *atRest* or can be a combination of different types. Examples of combination of continuous and discrete processes are the ionisation and the bremsstrahlung interactions. In the case of ionisation, the energy loss is continuous and the production of secondary particles is discrete. In the case of bremsstrahlung, the energy loss due to soft photons is continuous and the hard photon emission is discrete. In both cases, the production threshold separates the continuous and the discrete parts of the process.
Finally each process has two main methods: *GetPhysicalInteractionLength*() and *DoIt*(). The first one determines the interaction length of the specific process, required for the particle tracking, and the second one generates the final state (energy, momentum of particle, generation of secondaries, etc).

2.3.7 Interfaces and visualizations

Interactivity and visualisation span the related packages: *intercoms*, *interfaces* and *visualisation*. The user can define interactive commands to type in an interactive session during the simulation, in order to customise its configuration. This strategy increases, on one side, the efficiency of the work, as the same code can be used in multiple studies, and, on the other side, the quality of the work, since the same simulation code would be validated by different users, in different experimental set-ups.
The user is also able to visualise the experimental set-up and the particles tracks. By default, the tracks of the particles are coloured on the basis of their charge: neutral particles such as photons, are coloured in green, negatively and positively charged particles, such as electrons and positrons, have red and blue tracks, respectively. As regarding the experimental set-up, the visualisation attributes of the geometrical components are user defined at the level of the logical volumes.
Geant4 offers several drivers for different graphic systems, such as OpenGL, DAWN, WRML, WIRED and RayTracer that can be in parallel instantiated in the same simulation.

2.4 A generic Geant4 application

Although in Geant4 no default main program is provided, in a typical user application it has to be provided in order to link the classes to each other. The *main*() program has the mandate to instate the two toolkit classes named *G4RunManager* and *G4UImanager*, which together manage the whole simulation.
In particular, the G4RunManager class has to be instantiated at the beginning of the main program and supervises the simulation, controlling the configuration during each run through the methods *SetUserInitialization*() and *SetUserAction*(). These methods deal with the setting and the instance within the main program of the Initialization and Action classes, respectively. Indeed, in any Geant4-based application it is possible to distinguish the User Initialization classes, which are called at the beginning of the simulation, and the User Action classes, which are called by the *G4RunManager* for each run.
In the Multi-thread mode, the Initialization classes are instantiated directly in the main program, while the Action classes are instantiated through the *ActionInitialization* intermediary class which, in turn, is initialized in the main program.
Table 2.1 shows the class type classification as typically done for a Geant4 application.

The *DetectorConstruction* and the *PhysicsList* classes are mandatory and describe respectively the geometry/materials of the setting and the physics models/processes used for the particle tracking in the matter. They inherit all mandatory methods from the correspondent purely-virtual classes *G4VUserDetectorConstruction* and *G4VUserPhysicsList* and are initialized in the main program through the *SetUserInitialization* method.
The *ActionInitialization* class is also initialized by the *SetUserInitialization* method of the *G4RunManager* class in the *main* program of the application, and in turn contains the instances

TABLE 2.1: Main classes of a generic Geant4 application.

Class Type	User Class	Role
Initialization class	DetectorConstruction	Mandatory
	PhysicsList	Mandatory
	ActionInitialization	Mandatory
Action class	PrimaryGeneratorAction	Mandatory
	RunAction	Optional
	TrackingAction	Optional
	StackingAction	Optional
	SteppingAction	Optional

(through the *SetUserAction* method) of all the action classes of the application. In particular, the *PrimaryGeneratorAction* class describes the characteristics of the input source. The *RunAction* allows to gain control of the simulation at the beginning and at the end of the run, as for the retrieving of the total number of events for the run, or the total energy deposition in a detector, at the end of the run. The *TrackingAction* may be used to retrieve information from the particles at the track level as the type, energy and vertex of generated secondary particles. The *StackingAction* allows the customisation of the stacking mechanism of the particle tracks, as for the killing of the particles tracks in specific regions of the experimental set-up. Finally, the *SteppingAction* allows the retrieval of information at the step level, as the energy loss during the step or the kinetic energy of a given particle at the end of the step.

2.5 The transport beamline for laser-driven proton beams

The National Institute of Nuclear Physics (INFN) is officially part of the international Geant4 collaboration since the beginning and it is actively involved in the development of the code. In detail, the INFN-LNS group in Catania is contributing to the low energy electromagnetic and hadronic models development and validation as well as to the maintenance of the advanced examples and to the development of two examples, currently distributed in the public release of the code, named *gammaknife* and *hadrontherapy*.

The *gammaknife* application simulates a Gamma Knife device for Stereotactic Radiosurgery. It reproduces the cobalt sources displacement inside the unit and allows a comparison with the Treatment Planning System used for the dose computation.

The *hadrontherapy* advanced example uses proton and ion beams for therapeutic purposes. In this application, the CATANA beamline of INFN-LNS for eye melanoma treatment is fully simulated. Recently, a module dedicated to the computation of the dose-average linear energy transfer has been included [76, 77]. During the last year, as a result of this thesis, a new module has been also implemented, reproducing a typical beamline for the transport and the handling of laser-driven beams.

As reported in chapter 1, during the last years, the interest in particle acceleration driven from ultra-intense lasers is strongly growing, thanks to the huge number of potential applications and to

the possibility to investigate new physical regimes. It could bring to more compact and less expensive acceleration systems and, consequently, to a larger availability of radiation beams around the world. However, current available laser-driven charged particle beams are characterised by non-conventional and sometimes extreme features, such as a wide divergence and a 100% energy spread. In this framework the capability to accelerate laser-driven beams in a controlled and reproducible manner for their use in any potential downstream application represents one of the main objective. The ELIMED (MEDical and multidisciplinary application at ELI-beamlines) project was born and a transport beamline prototype dedicated to laser-driven beams has been recently realised. This beamline has been simulated using the Geant4 toolkit. It was based on the *hadrontherapy* advanced example, where a specific module for the laser-driven beamline was recently added and publicly released within the 10.1 Geant4 distribution.

The Monte Carlo approach was very successful, because it allowed to optimise the beamline prototypes design and to study the output beam features as a function of the input characteristics. As shown in figure 2.2 two main devices compose the beamline: a collection system and an energy selector. The first element (set of quadrupoles), placed few cm downstream the source point, collects, focuses and pre-selects the accelerated particles in angle and energy. The final beam energy refinement is obtained by means of the energy selection system (ESS), composed of two collimators, four permanent dipole magnets with alternating polarity and a central slit. A detailed description of the different prototypes is reported in chapter 4.

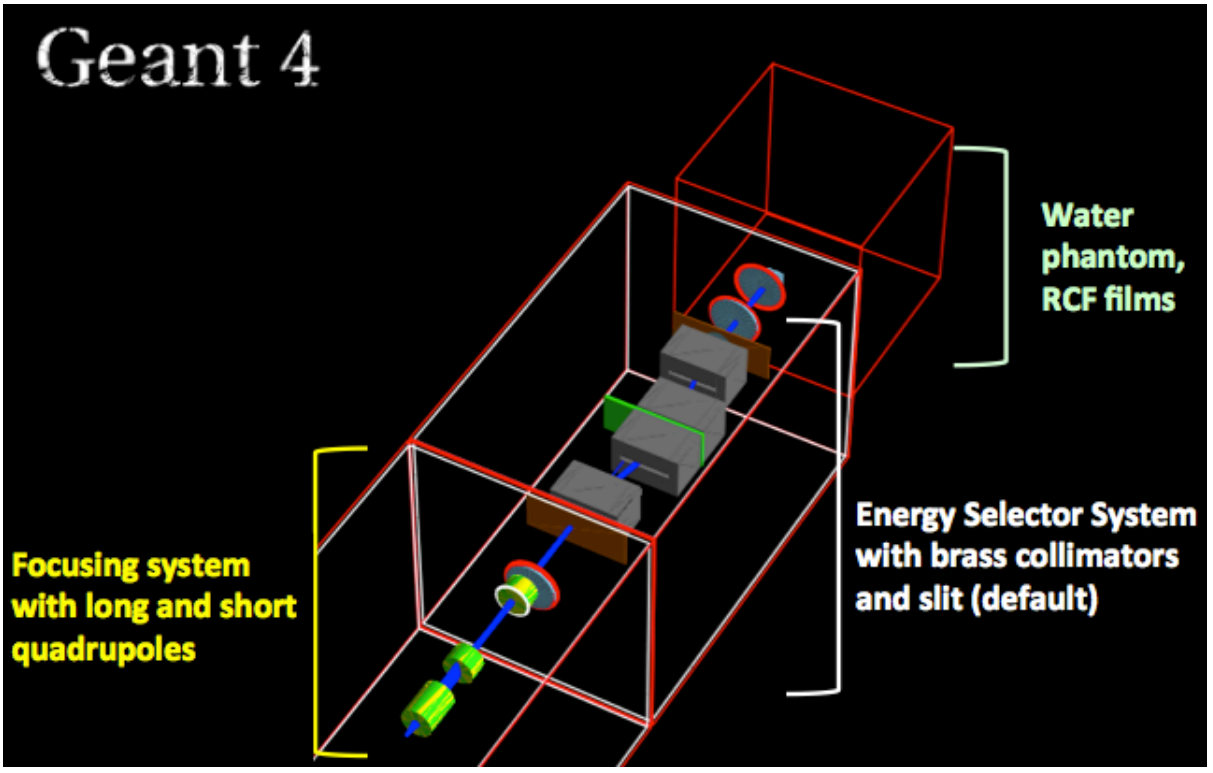

FIGURE 2.2: The transport beamline dedicated to laser-driven beams simulated with the Geant4 toolkit as an optional line of the *hadrotherapy* advanced example.

At the end of the beamline, there is a third section, dedicated to the dose evaluation. It is based on the use of the *water phantom*, already implemented in the *hadrontherapy* application, or on

the simulation of Gaf Chromic films.
Each element was simulated in detail, considering the specific materials and implementing the electromagnetic fields, where necessary. Several UI commands have been also implemented in order to change some geometrical parameters at run-time.
The development of this Monte Carlo tool was driven from two main goals: provide preliminary predictions in order to support the design of the beamline elements and study the particle transport, fluences and doses along the beamline.

2.6 Main requirements of the beamline

According to the specific goals of the beamline simulation, the tool has been designed and realised to fulfil the following requirements:

- to accurately simulate the particle source, considering the proton energy spectrum and the angular distribution obtained from the experimental data, in order to reproduce in a realistic way the expected laser-target interactions products;
- to implement the different magnetic elements of the transport beamline, by including detailed field grids, obtained by means of the COMSOL and Opera tools [78, 79];
- to provide easy ways to retrieve different kinds of information, as the energy spectrum, the angular, spatial and dose distribution and the shape of the beam at different distances from the target (for instance, before the quadrupoles system, before and after the energy selector system and at the exit point).

The secondary radiation, due to the interaction of the charged particles with the devices composing the beamline, was an interesting topic, however this is not treated in this thesis.

2.6.1 Input beam

Due to the laser-accelerated ion beams peculiarities, several input modalities have been considered in order to implement the most realistic features. In particular, the angular and energy distributions of the input beam have been derived from the experimental data and modelled using parameterized functions. Hereafter the final choice is described.
The input source characteristics were defined in the $PrimaryGeneratorAction$ class and the primary input was generated invoking the $GeneratePrimaryVertex()$ mandatory method. Preliminarily to the calling of this method, in the $Construct()$ function, the $G4GeneralParticleSource$ (GPS) was initialized. The input beam features have been finally implemented using several UI commands, defined in the *laserDrivenBeamline.mac* macro file of the official *hadrontherapy* application.
In detail, the spatial distribution has been defined using the following commands in order to reproduce the laser spot size on the target surface.

```
->  /gps/pos/shape Circle
-> /gps/pos/radius num
```

→ *Sets the source shape type. For a planar source (used option), this can be circle, annulus, ellipse, square or rectangle.*
→ *Sets the radius of the source.*
As regarding the energy-dependent angular distribution implementation, the input beam has been treated as the sum of several sub-beams, defined in different energy ranges. Indeed, in the TNSA regime, the energy spectrum is exponential shaped and the energy-dependent angular distribution is shell-like, as in the representative example reported in figure 2.3.

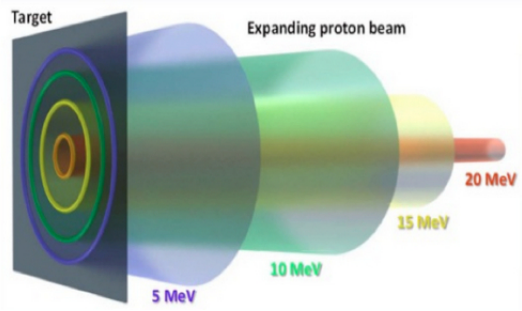

FIGURE 2.3: Plot showing a typical energy-dependent angular distribution of a laser-driven proton beam.

Each beam was characterised by an isotropic dispersion limited in an angular range, from 0 up to a *thetaM* value, obtained from the experimental data or from the parameterized functions. As concerns the energy distribution, it has been implemented using a user-defined histogram, whose data were also interpolated with a decreasing exponential function, in order to best reproduce the experimental data. The used commands are:

```
-> /gps/ang/type iso
-> /gps/ang/mintheta 0 deg
   /gps/ang/maxtheta thetaM
```

→ *Sets the angular distribution type: isotropic (used option), cosine-law, user-defined, ...*
→ *Sets a minimum and maximum value for the angle distribution.*

```
-> /gps/ene/type Arb
```

→ *Sets the energy distribution type: mono-energetic, linear, power-law, exponential, Gaussian, point-wise spectrum(used option), ...*

```
-> /gps/hist/type arb
-> /gps/hist/point Em Weight
```

→ *Sets the histogram type: point-wise is the used option.*

→ *Specify one entry (with contents Weight) in a histogram (where Em is the abscissa value).*

```
-> /gps/hist/inter Exp
```

→ *Sets the interpolation type: linear, logarithmic, exponential (used option) and cubic spline for point-wise spectra.*

As example, figure 2.4 reports the simulated energy-dependent angular distribution together with the energy spectrum, obtained starting from the experimental data measured at the Queen's University of Belfast (UK). See chapter 5 for more details. This beam is implemented in the *laserDrivenBeamline.mac* macro file of the official *hadrontherapy* application.

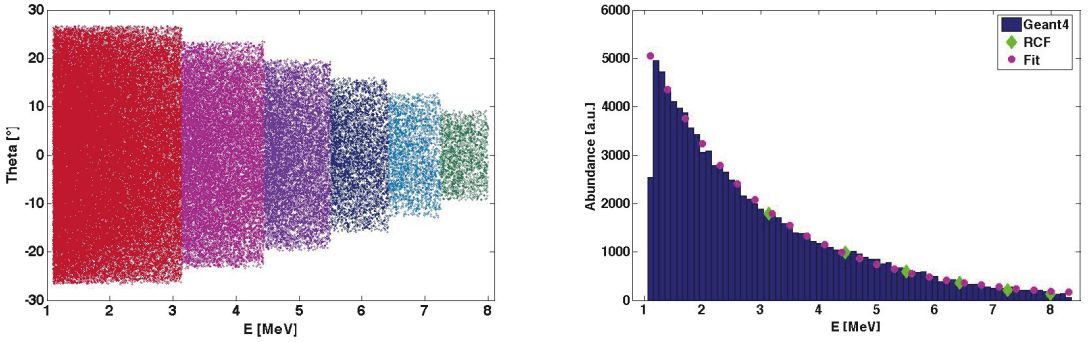

FIGURE 2.4: Plots showing a energy-dependent angular distribution (on the left) and an energy spectrum (on the right), obtained starting from the experimental data, using the GPS ready-to-use commands reported in the *laserDrivenBeamline.mac* macro file of the official *hadrontherapy* application.

2.6.2 Geometry set-up and magnetic field implementation

The geometry setup of the whole beamline was described in a dedicated class, named *LaserDrivenBeamLine*. This class implements the geometrical set-up, which it is fixed for each run of the simulation. Anyway, it is possible to change the geometrical configuration by line commands, without modifying the default geometry in the code. It is possible to modify the default sizes of an object or its placement within the mother volume and to activate and deactivate a solid. The instance of the new customised commands are contained in the $LaserDrivenBeamLineMessenger$ user class, strictly linked with the $LaserDrivenBeamLine$ class. In particular, the most important implemented commands allow to change the relative distance between quadrupoles in order to modify the beam focusing or the slit position of the ESS in the transversal direction with respect to the beam axis in order to vary the selected output energy.

Each element of the beamline has been simulated according to the real sizes, materials and properties. In particular, the implementation of the magnetic fields represents a key point in the beamline simulation, because particle transport is strongly dependent on the accuracy of the map reproduction. In principle the beam transport could be performed with some dedicated codes, like OPERA,

but they do not take into account physical interactions. Geant4 gives the possibility to solve the electromagnetic field equations and, at the same time, also to evaluate the particle interactions with matter and track the secondary particles. With Geant4 it is possible to describe a variety of fields: magnetic, electric and electromagnetic fields, uniform or non-uniform, that can be specified in a generic setup. As regards the propagation of a particle inside a field, the equation of motion is numerically solved. In general, the Runge-Kutta method, with a user-defined accuracy, was used for the integration of the ordinary differential equations. However, in specific cases, other solvers can be also used. The field implementation was performed following these five main steps:

1. create the magnetic field. The uniform fields were implemented using the $G4UniformMagField$ class, similarly, the $G4MagneticField$ class allows to initialize a non-uniform field;
2. create a $G4FieldManager$ object. Generally it could be associated with the *world* (global field) or with any *logical volume* (local field), in order to define the field only in the desired region;
3. choose the appropriate integration stepper. The Runge-Kutta method was the chosen one (for smooth field other methods are also available);
4. set the precision parameters, i. e. an acceptable level of numerical precision in order to get performant simulation with acceptable errors. Requiring very high precision can, indeed, cause a large number of steps;
5. working in multithread mode, the field class object (both global or local) must be thread-local. Therefore, it must be assigned to G4FieldManager by the $ConstructDandField()$, invoked at thread-local level.

In the transport beamline simulation, there were different kinds of fields, quasi-uniform and non-uniform. In particular, the collection system, with its quadrupoles, is characterised by a non-uniform field; therefore it has to be described by using realistic maps. On the other hand the energy selector system could be treated as composed by four separated regions, each one characterised by a uniform field value, as +B0 and -B0 for the two external and two internal regions, respectively. This approximation for the energy selector system field could miss the optic distortion effects due to the field gradients that unavoidably exist between the different regions and near the edge. Therefore, in order to guarantee the best accuracy for particle transport, the map implementation has been considered also for the energy selector.
Practically, as concerns the code implementation, the different magnetic fields were initialized in the $LaserDrivenBeamLine$ class, in particular, in the $ConstructSDandField()$ method, and by means of several grid maps, obtained by COMSOL and OPERA simulations. A file (with extension .TABLE) with the three field components defined on a 3D spatial grid, was coupled to each magnetic field and imported through a dedicated class, named $HadrontherapyMagneticField3D$. Each grid map was also shifted respect to the global coordinates of the associated element, in order to match the electromagnetic property with the associated physical volume. For instance, a typical magnetic field initialization is as follows:

```
G4MagneticField* FirstMagneticField=
new HadrontherapyMagneticField3D("field/MapFileName.TABLE", xOffset, yOffset, zOffset);
```

where $xOffset$, $yOffset$ and $zOffset$ represents the coordinates of the element coupled to MapFileName.TABLE grid map, defined in a global reference system.
As concerns the field evaluation at each particle step during the transport inside a field region, a linear interpolation of the grid map was implemented in a dedicated method of the *HadrontherapyMagneticField3D* class, named $GetFieldValue()$.
Different benchmarks have been performed for each magnetic element, in order to check and set simulation parameters for the best compromise between accuracy and CPU time. Particle tracking and beam emittance have been therefore compared with three reference codes outputs: COMSOL [78], OPERA [79] & TraceWin [80]. The agreement of the simulation outputs with respect to the experimental data, coming from the energy selector and the collection system tests, has finally confirmed the correct Geant4 implementation of each element of the transport beamline (see chapter 4 and 5).

2.7 Evaluated outputs

The scoring registration of physical quantities, such as the energy or the angular distribution of particles, is one of the most critical aspects of a Monte Carlo simulation. Geant4 does not provide a direct and automatic data retrieving, but user has to implement the code to obtain and store the required output. In the treated case, the main requirements concerning the output data along the transport beamline are related to the energy and angular spread as well as the shape and the uniformity of the primary beam together with the computation of the released dose and its spatial distribution at different points along the beamline and at the exit point.
In general, there are several ways to interact with the Geant4 kernel and obtain relevant information along the particle tracks. The used way was to implement some functions in the *SteppingAction* class. In detail, by means of the methods of the *G4StepPoint* class, it was possible to retrieve several kinds of information, such as the energy, the angular and the spatial distribution of the beam along the line.
Dedicated functions was used, as:
- GetKineticEnergy()→ to get the particle energy value;
- GetTotalEnergyDeposit() →to get the deposited energy value of the particle in a given volume;
- GetMomentumDirection() →to get the particle x, y and z momentum direction value;
- GetPosition()→ to get the particle x, y and z coordinate value.

As regarding the dose evaluation, the already existing *water phantom* has been used but, in parallel, the scorer tool at the same measurement point was also implemented to directly obtain the absolute dose in a faster way. The scorer is a native Geant4 tool. It is derived from the *G4VPrimitiveSensitivity* virtual class and allows the generation of one hit collection per event and scoring one kind of physical quantity, like the energy loss, the dose or the fluence. It consists in a sort of 3D map divided in voxels with user-defined dimensions. The specific physical quantity

is then registered for each voxel and an ASCII file is generated at the end of the run.
The scorer was activated in the main program through the *G4ScoringManager* class, as follows:

```
G4ScoringManager * scManager = G4ScoringManager::GetScoringManager();
```

Then it was called for the specific simulation directly by UI commands, defined in a macro file.
As regarding the Radio chromic films, their features were implemented in terms of real geometry and materials (described in appendix A) and the dose retrieved by means of the scorer tool. The RCF implementation was very useful in order to check the correct development of the different analisys tools, used to obtain the input beam features starting from the experimental data.
MC simulations were widely used in this thesis as support for the setup optimisation of the different experimental campaigns. Thanks to the developed code, dose and beam angular and energy distributions were preliminary investigated and then, for the code validation, compared with the experimental data. The correct beamline elements implementation was indeed confirmed by the good agreement obtained from the comparison between simulation outputs and experimental data, coming from the tests performed with conventional and non-conventional beams (see chapters 3, 4 and 5). Having a reliable code, this simulation tool was finally used to perform a study of the whole transport beamline, as preliminary step for a future radiobiological experimental run (chapter 6).

Chapter 3

First experimental campaign for preliminary radiobiological measurements @ LULI facility

Cancer rank is the second biggest cause of death in developed countries, behind cardiovascular diseases. It is estimated that one-third of the population will develop a tumour within their lifetime [47]. These statistics single out cancer prevention and treatment as one of the major societal challenges worldwide, and motivate research into novel, more effective ways of fighting cancer.
Radiotherapy is a broadly used approach for the cancer treatment. However, although energetic photons are widely used, ion beams are much more effective thanks to their physical dose deposition pattern. The tumour control probabilities are indeed comparable to, or exceed, those achieved with conventional radiotherapy, moreover the side effects are considerably reduced [81], which makes this type of treatment particularly suitable for pediatric tumours.
As already described in chapter 1, unfortunately only about 42 centres have been already realised worldwide to perform treatments with protons and heavier ions (i.e. carbon) [82]. The large cost of the accelerators (synchrotron, cyclotron or linac) installations represents indeed the main limiting factor for a wider availability of this kind of treatment, when compared for example with X-ray radiotherapy, virtually available in any large hospital. The idea of future facilities based on laser-driven ion accelerators has been proposed as a way of reducing complexity and cost [37, 83, 84]. Significant effort, at laser/target level as well as by means of customised transport beamlines, is therefore ongoing in order to demonstrate their possible clinical application.
Several groups have also started preliminary work on the methodology and viability of using laser-driven ion sources for cell irradiation experiments, a mandatory step in view of any future therapeutic use. One of main aims of these investigations is to establish a procedure for cell handling, irradiation and dosimetry compatible with a laser-plasma interaction environment [60].
Also the biological effects of laser-driven protons, emitted in bursts of picosecond duration at the source, and therefore characterised by ultra-high dose rates, are virtually unknown and need to be carefully assessed prior to any medical use.

Kreipl et al. in [85] reports a simulative study, performed using the biophysical Monte Carlo code PARTRAC. In particular, the impact of intertrack effects (spatial and temporal proximity of ion tracks) on water radiolysis and on the yield of different types of DNA lesions is shown and the results imply that, up to the end of the chemical stage, the yield of DNA lesions should not change for picosecond ion pulses, compared to ion beams with longer dose delivery times.
Experimental activities in this field have been also carried out. Lethal effects on cells have been investigated using pulsed beams at ultra-high dose rate [86], as well as laser-driven protons. In particular in this case the biological end-points are measured accumulating dose over several laser shots [87–89], but also isolating effects associated to a single short burst deposition [90–93]. From the experimental results seems that the survival fraction curves of conventional and ultra-high dose rate beams do not differ significantly. However, several cellular models as well as other biological end-points should be still investigated with more controlled irradiations. In this background, the results obtained in the experiment carried out at LULI (Laboratoire pour l'Utilisation des Lasers Intenses) laboratories in Paris are presented here.
The proton source was produced within the TNSA regime by irradiating 25 and 50 μm thick Au foil targets with a high-power, short-pulse laser.
Using the beam accelerated from the non-irradiated target surface, as input, Human Umbilical Vein Endothelial Cells (HUVEC) were irradiated with protons of 6, 9 and 14 MeV and dose of about 4.5, 1.8 and 0.6 Gy, respectively, in order to investigate the clonogenic assay and the sublethal cytogenetic damage. Several simulation sets have been also performed and obtained outputs were compared with the experimental data.
In this chapter the experiment is carefully described together with the simulation study.

3.1 Laser system

The experimental run was performed at the LULI laboratories of the Ecole Polytechnique (Paris, Fr) and in particular at the LULI2000 facility [94]. It is an unique facility in Europe thanks to the possibility to couple on target high-energy pulses of ns and ps durations as well as auxiliary beams. An outline of its spaces, the laser hall and the two experimental areas, is given in figure 3.1.

The LULI2000 hall contains 2 main laser chains, named NANO2000 and PICO2000, with two additional, synchronized chains of smaller energies, in the *ns/ps* regime, dedicated for diagnostic purposes (Thomson scattering, X-ray, etc.). In particular:

- NANO2000, the nanosecond version of LULI2000, consists in two Nd:Glass laser chains, 200 mm in diameter, delivering each 1 kJ in nanosecond pulses at ω=1053 nm wavelength. A fibre oscillator allows also to shape the pulse duration from 0.5 to 20 ns. The repetition rate is limited to a shot every 90 minutes (between 4 and 6 shots "full energy" per day). A 10 Hz laser allows quick alignment diagnostics;

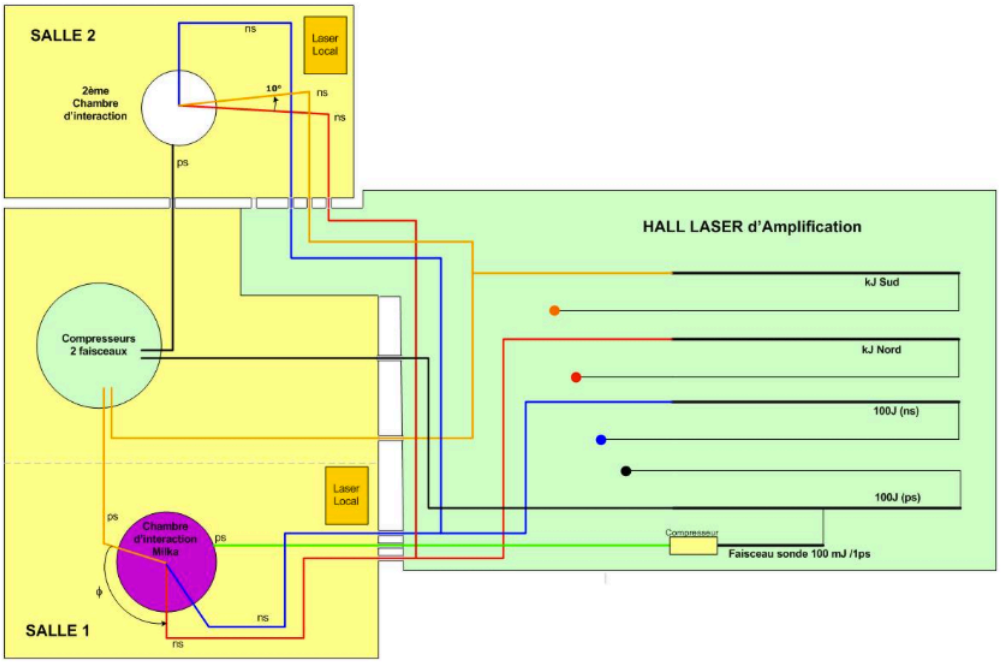

FIGURE 3.1: LULI2000 facility: laser hall and experimental areas [94].

- PICO2000 is obtained thanks to the implementation of the chirped pulse amplification technique at one NANO2000 laser chain. It is able to deliver 150 J in 1 ps at ω=1053 nm (150TW).

During the experimental run, the PICO2000 laser beam at ω=1053 nm was redirected in the Milka vacuum chamber (*salle 1*). Thanks to a $F/4$ off-axis parabola (OAP), characterised by a focal length of 800 mm, the beam was focused on the target surface with an incident angle of $\sim$22.5°. Figure 3.2 reports the laser focal spot. From the image analysis, a FWHM of about 9μm has been measured.

On average, the pulse duration and the laser beam energy at the entrance of the compressor were of about 1.3 ps and 100$\pm$10 J, respectively. Therefore, considering the compressor efficiency of 65%, the mean laser intensity, during the experimental campaign, was roughly 5×10^{19} W/cm^2.

3.2 Experimental set-up

In order to expose the cells only to particles within a selected narrow energy range, a beam transport and delivery system capable to separate protons with different energies was installed inside the target chamber. A draft of the experimental chamber arrangement is shown in figure 3.3, together with a lateral view of the beam transport and irradiation system with detailed information of the relative distances.

As regarding the target holder, it was placed at the nominal chamber centre, on the permanent Milka motorized target stage. The ion beam transport and delivery system was installed inside the

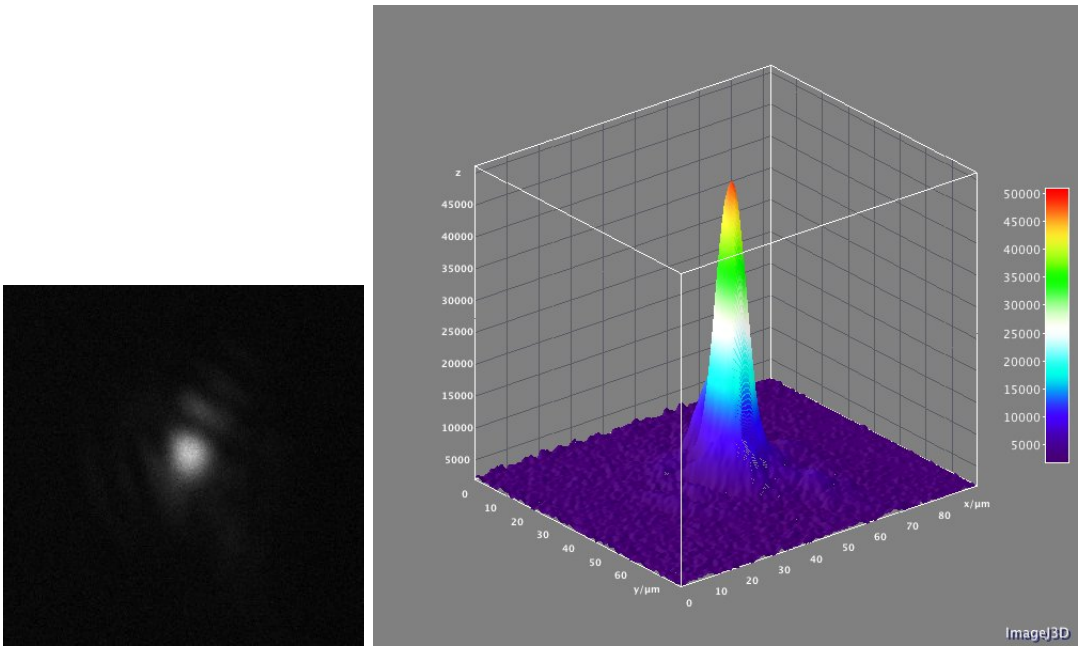

FIGURE 3.2: Focal spot of the PICO2000 laser beam during the experimental run (on the left) together with its profile obtained using an ImageJ script (on the right).

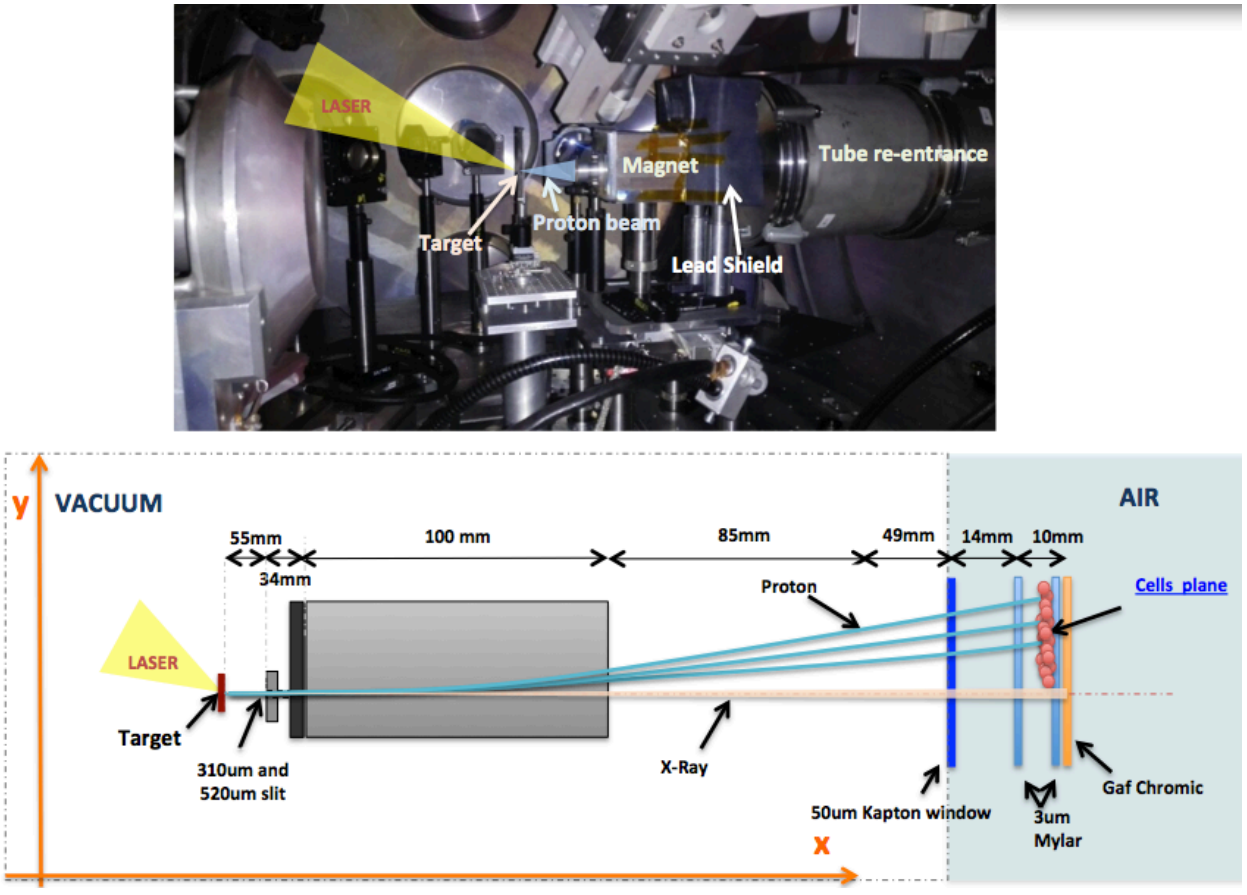

FIGURE 3.3: Image of the experimental set-up (top) and draft with the detailed information of the relative distances (bottom). Protons were deflected according to their energy while x-rays contribution going through the slit was undeflected.

main chamber, along the target normal axis, with the system entrance slit placed at 55 mm from the target holder. Two different slit widths were used, respectively of 310 and 520 μm, in order to change the final beam features. During the run the chamber pressure was of 10^{-4} mbar.
As concerns the mounted transport system, it was made of a 100 mm permanent magnet, characterised by an approximately constant magnetic field of about 0.92 T on a 50 mm $\times$ 4 mm gap. Figure 3.4 reports the experimental magnetic field values as a function of x and y axis, for the central plane of the gap, measured using an Hall probe.

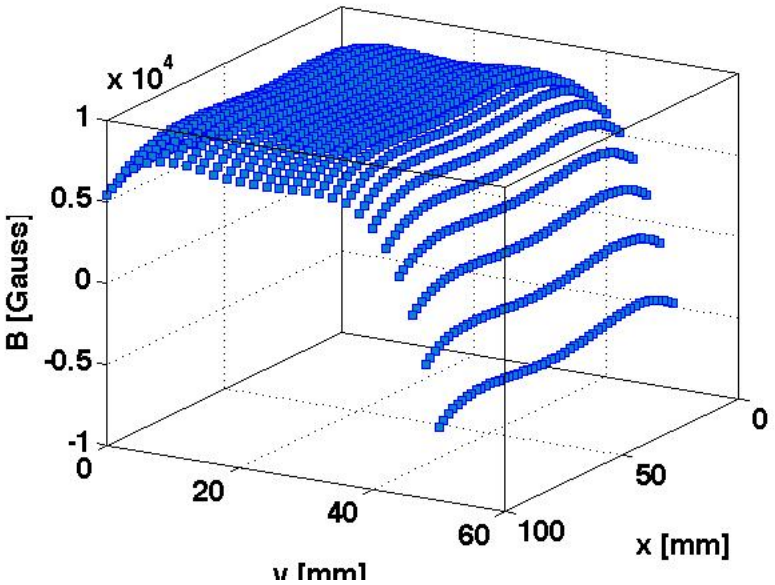

FIGURE 3.4: Experimental magnetic field values as a function of x and y axis, for the central plane of the gap, obtained using an Hall probe.

Thanks to this dipole, protons were deflected according to their energies. Obviously also heavier ions were deflected, but with a different angular dispersion due to their higher mass values. Regarding the parasitic X-ray radiation, produced in the intense laser-target interaction, it was partially suppressed by suitable lead shielding placed into the chamber; only the contribution of the X-rays going through the slit reached the sample plane. However they are indeflected, therefore spatially separated from protons, as shown in figure 3.3.
For the irradiation section, cells were deposited on a Mylar, 3 μm thick film attached on a customised dish. To avoid mixing of the cells irradiated with different doses, samples were deposited on the foil in small dots of about 3$\times$5 mm^2 in size and at specific positions. Typically we have deposited 3 separated dots on the same dish for simultaneous exposure to about 5, 10 and 15 MeV protons in the same laser shot.
The customised designed dishes have been equipped with an automated syringe system to quickly remove and re-inject the physiological medium where cells need to be immersed, to preserve their integrity prior to and after irradiation. These dishes were placed outside the target chamber, inside an in air re-entrance, immediately behind a 50 μm Kapton window, as shown in figure 3.5. The in air tube extension was required in order to place the sample at close distance from the beam transport and delivery system exit point, therefore to reduce the overall distance from the target

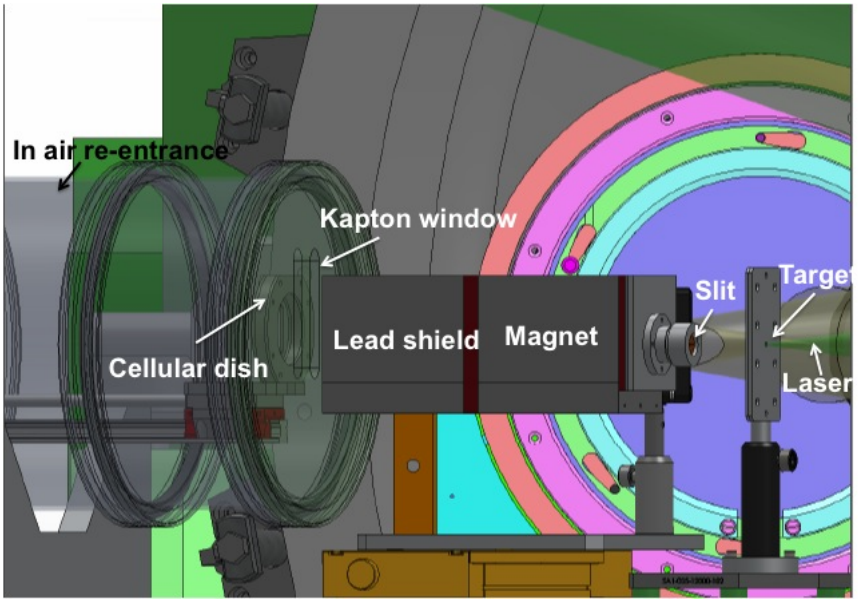

FIGURE 3.5: Draft of the used setup, realised using the CAD software. The customised cellular dish is placed just behind the Kapton window, inside an in air re-entrance.

and maximize the irradiation dose onto the cells. To facilitate the positioning and removal of the samples before and after each shot, the dishes were mounted on a sliding bar system to insert and extract the dish into and from the tube.

3.2.1 Beam detectors

During the experimental run three main detectors have been used for the protons beam detection: gaf chromic films, image plates and CR-39s. For a description of the dectors, see appendix A.
In detail, stacks of low-sensitivity, HD-V2 radiochromic films were employed inside the main chamber at few cm from the proton source, in order to spatially and spectrally characterise the beam generated from the laser-target interaction. High-sensitivity EBT3 radiochromic films were, instead, placed outside the interaction chamber, just behind the biological sample to provide a shot-to-shot characterisation of the irradiation dose. Both these kinds of gafchromic models have been preliminary calibrated with clinical proton beam at INFN-LNS, as reported in appendix A.
Image plates (IP) and nuclear track detectors (CR-39), thanks to their high sensitivity, have been also used. They have been placed just behind the RCF films, in order to study the proton dispersion, due to the magnetic field effect. A scheme of the used setup is reported in figure 3.6.

Different Al filter of 0, 250 μm, 500 μm and 1 mm in thickness have been placed between the RCF film and the IP/CR-39 detectors. Using these filters, 5.6, 8.6, 10.6 and 14.5 MeV protons are stopped and, from the IP/CR-39 outputs analysis, their positions on the dispersion axis (y) were obtained. In particular, for the IPs, the type BAS-TR 2025 from Fuji Photo Film Co. Ltd and a scanner FUJI FILM FLA-7000, as reader, were used. Since the signal obtained from the IP decreases with time, they were always scanned right after the exposure.

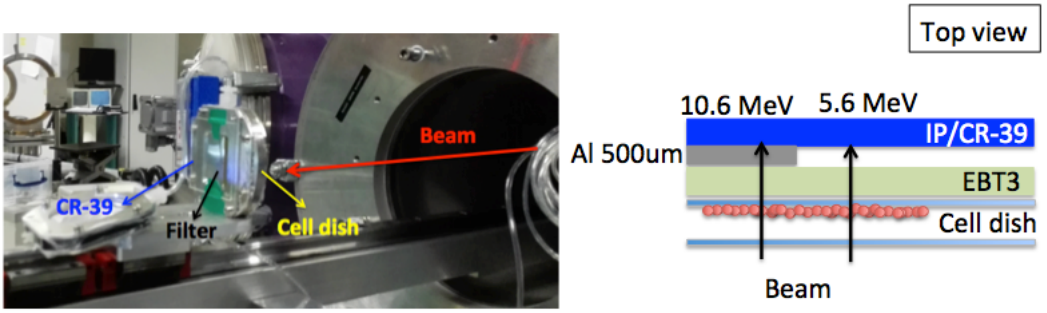

FIGURE 3.6: Image and scheme of the used setup for the detectors irradiation.

As regarding the biological samples, they could be considered as detectors with unknown response, which give information on the biological effects of the laser-driven beam characteristics. The biological outcome of radiation exposure is, indeed, determined by the amount and complexity of DNA damage. However, more detailed information can be obtained by observing the complexity of the damage. In detail, Human Umbilical Vein Endothelial Cells (HUVEC) were used and the investigated radiobiological end-points were:

- Clonogenic assay: DNA damage results are correlated to cell survival (which is the gold standard assay for radiobiology and represents the basis for radiotherapy treatment planning). The PICO2000 beamline has allowed to perform this study at dose rates of about 10^9Gy/sec.
- Sublethal cytogenetic damage: some cell types may develop sub-lethal damage, as the Stress-Induced Premature Senescence (SIPS). SIPS may have clinically relevant long-term consequences by compromising organ function and/or integrity and increasing the risk of secondary cancer in radiotherapy patients [95, 96]. The physiological senescence is inevitable for normal cells, which stop proliferating after a finite number of cell divisions. However, SIPS represents a response that can be triggered by a variety of stimuli, including the ionizing radiation [97].

In order to judge the biological effectiveness of these non-conventional beams in respect to conventional ones, both end-points have been investigated using conventional accelerated proton beams and the clonogenic assay also with X-rays.

3.3 Targets, input energy spectra and angular distributions

During the experimental run, the PICO2000 CPA beam was focused onto several gold targets of different thickness, chosen in order to optimise the proton energy, the irradiation dose value and the beam uniformity onto the biological samples. Gold (Au, atomic number 79) has been chosen because, based on previous experience with similar targets and similar laser beam parameters, it has shown the best performances in terms of the proton beam spatial homogeneity, respect to other materials.

Preliminary to the cell irradiation, we have studied the features of the proton beam generated by

the laser-target interaction in order to choose two different targets. Indeed it is crucial to achieve the optimal irradiation conditions, i. e. to irradiate the cells samples with energy up to 15 MeV, with different dose values and with the higher available homogeneity.
The input proton beam energy spectrum has been therefore measured by means of HD-V2 stacks placed few cms downstream the target and wrapped in a 12 μm thick, Al foil in order to reduce the electron, heavy ion and photon contributions on the detector signal.
Figure 3.7 reports, as an example, a RCF stack composed of 27 layers, obtained shooting on a 25 μm, Au target. The labelled beam energy at each layer is given by the Stopping Range of Ions in Matter (SRIM) software package.

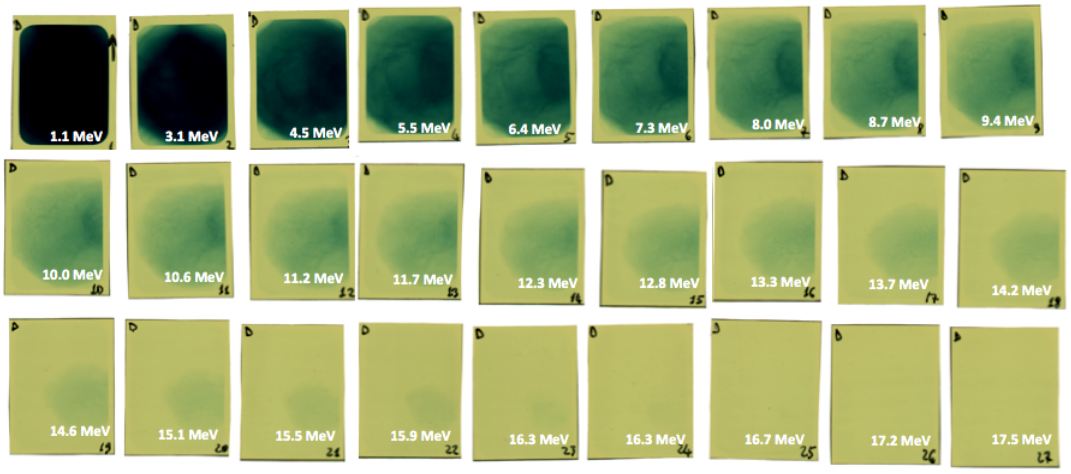

FIGURE 3.7: RCF stack obtained irradiating the 25 μm Au target. Proton energies at each layer are labelled (SRIM calculations).

Applying the spectroscopic method, briefly explained in appendix A, the proton spectrum has been calculated. Figure 3.8 reports the energetic distributions obtained for 10, 25 and 50 μm, Au targets (thicknesses of interest for the purpose of the experiment).

The energetic spectrum corresponding to the 50 μm Au target is characterised by a lower proton flux and energy cut-off value respect to the other cases.
As concerns the energetic distributions resulting from the laser interaction with the 10 and 25 μm thick targets, they are substantially equivalent for energies lower than 15 MeV, even though shot-to-shot fluctuations are present. However the spatial homogeneity of the generated proton beams are not so similar. As an example, figure 3.9 reports the 10th layer of two stacks (10 μm thick target on the left and 25 μm thick target on the right side), corresponding to 10 MeV protons contribution, together with their 3D beam profiles, obtained using ImageJ. As shown, the beam profiles are both Gaussian-like, higher flux is recorded in the centre of the beam and decreases towards the periphery. However there are some filamentous structures in the beam generated using the 10 μm thick target.

Summing up, 25 and 50 μm thick Au targets have been chosen in order to irradiate the samples with different dose values. The 10 μm thick Au target has been discarded because of the poor beam homogeneity.

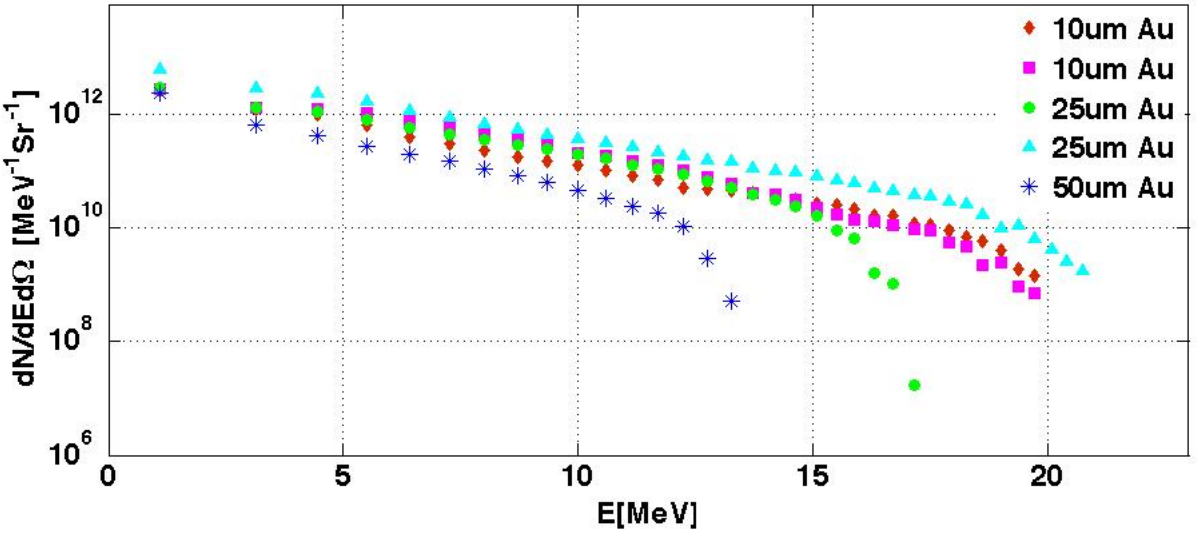

FIGURE 3.8: Energetic distributions of the proton beams generated from the laser interaction with 10, 25 and 50 μm thick, Au targets.

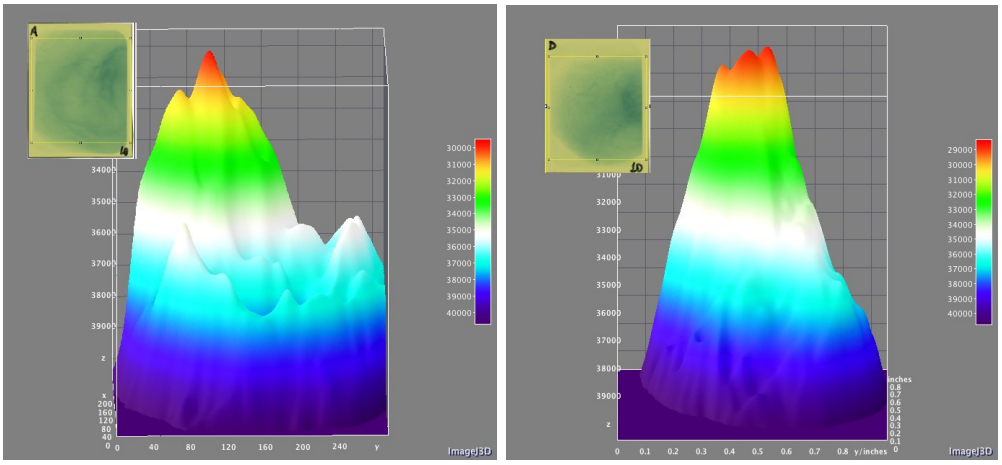

FIGURE 3.9: 3D beam profiles of the selected ROIs (yellow rectangle) in the 10th films of the stacks irradiated using the 10 μm (left) and 25 μm (right) thick targets.This plot are obtained using ImageJ.

3.4 Output

The delivery and transport system aimed to spatially separate the broadband energy spectrum of the generated proton beam. The working principle was based on the use of a dipole with a magnetic field oriented perpendicular to the beam propagation direction. Inside the dipole, protons are deflected by the Lorentz force component perpendicular to the magnetic field B. Considering the setup of figure 3.10 with L the dipole length and D the drift lenght, y deflection on the detector plane, function of the particle Energy E_{kin}, is obtained:

$$y_D = \frac{qBL(D + L/2)}{\sqrt{2mE_{kin}}} \tag{3.1}$$

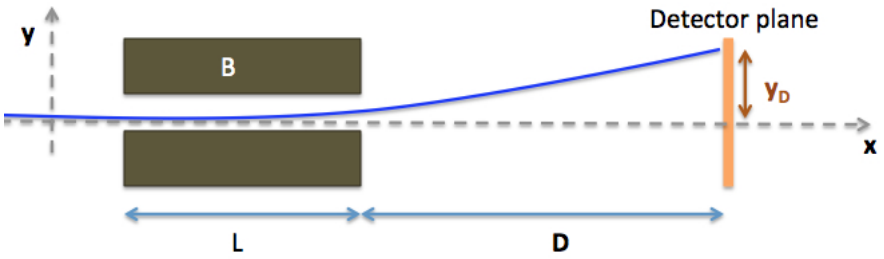

FIGURE 3.10: Magnetic deflection due to the Lorentz force: basic principle of the used experimental setup.

where q is the ion charge and m its mass value. Basing on this principle and in order to characterise the transport system, the Energy vs y function has been experimentally measured with IP and CR-39 detectors (section 3.4.2). Section 3.4.3 reports the obtained results related to the cell samples and the measured radiobiological end-points.
However as first step, the energy vs y curve as well as the expected dose distribution on the cells plane have been also investigated by means of a set of Monte Carlo simulations (section 3.4.1).

3.4.1 Simulated data

After a preliminary simulation study for the setup optimization, a set of Monte Carlo simulations has been performed using as input the proton beam features measured with the RCF stacks when the irradiated target was 25 μm thick (green circles and blue triangles of figure 3.8). The distances and sizes have been accurately implemented, together with the magnetic field. In particular the implemented field grid map has been obtained applying a polynomial interpolation to the experimental data.
The cells have been considered as a 10 μm thick layer made of water, as described in [98].
During the run, we have assumed that cells were irradiated only with protons. Although in the laser-target interaction a multi species beam is generated, ions heavier than protons are less deflected and partially stopped by the Kapton window. Simulations output has confirmed that unwanted contributions don't reach the cellular dots, if we have deposited them for a simultaneous exposure to 5, 10 and 15 MeV protons.
Hereafter the E vs y curve, the energy spectrum and the dose distributions on the cells plane are presented, considering as input only the proton contribution. The reported data have been evaluated for the two different entrance slit characterised by a width of 310 and 520 μm, using, as input, the two energetic spectra, corresponding to the green circles and to the blue triangles of figure 3.8. They will be hereafter named '1°' and '2°'.
Fixing the input exponential trend (fitting procedure on the '1°' experimental data) and the number of simulated particles, the output energy spectrum together with the E vs y curve were studied, as shown in figure 3.11.

As expected, with a bigger slit aperture an higher number of protons reaches the exit point of the beamline. However the energy resolution becomes worse.

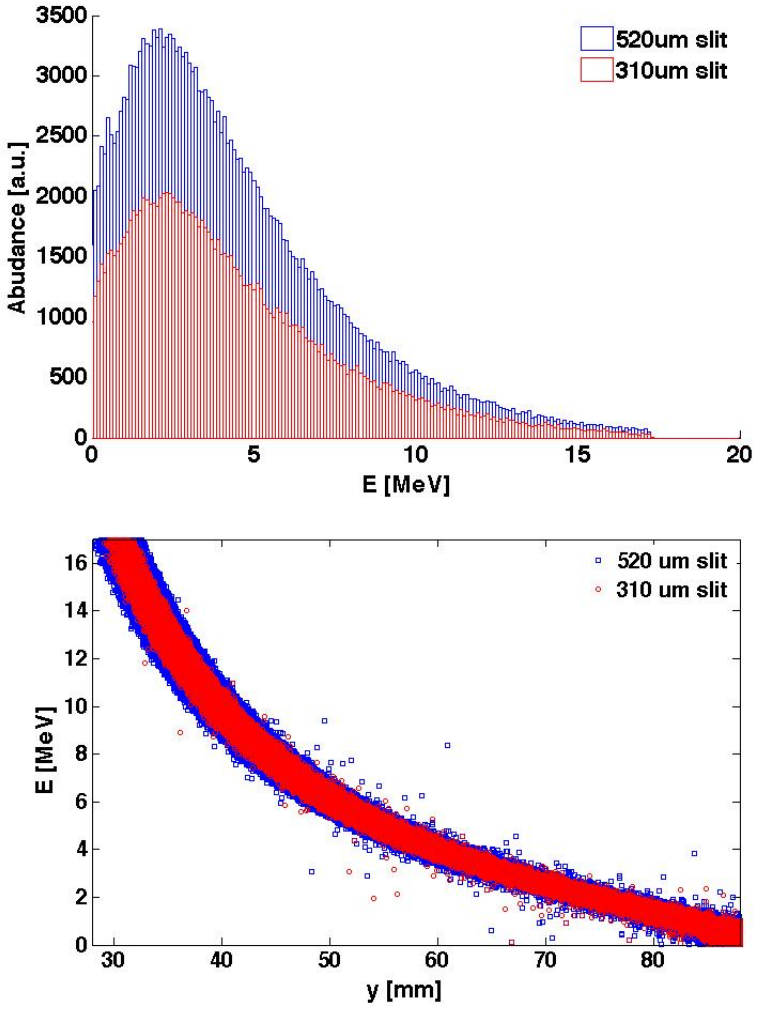

FIGURE 3.11: Energy spectra (top) and E vs y curves (bottom) obtained using 310 and 520 μm entrance slit apertures. The '1°' input exponential trend and a fixed number of simulated particles were used.

Indeed, a bigger solid angle is covered using a bigger entrance slit and the spatial mixing effects, due to the input beam divergence, are therefore more evident. In other words, a given energy value has not a univocal y position, but it is characterised by a Δy whose width depends on the slit aperture. This effect could be easily evaluated considering the thickness of the E vs y curves. In detail these thicknesses are about 2.2 mm and 3.4 mm for the 310 and 520 μm entrance slits cases, respectively. These values have been calculated as the FWHM of the curve profile.
In table 3.1, the energy spreads associated to the three cellular dots are listed, considering that, during the experimental run, they are approximately deposited at the y coordinates corresponding to 6, 9 and 14 MeV protons.
In particular, the energy spreads have been calculated as the FWHM values of the energy spectra, evaluated on a 3 mm (y)$\times$ 5 mm (z) area centred in y=50.5, 41.5 and 33.5 mm, respectively corresponding to the a above mentioned energies.

As reported, the energy spreads are almost constant for a given setup and become bigger for wider entrance slit.

TABLE 3.1: Energy spreads evaluated on a 3 mm (y)× 5 mm (z) area approximately centred in the three cells dots position.

y[mm]	E[MeV] ±ΔE[MeV] 310μm slit	E[MeV] ±Δ E[MeV] 520μm slit
50.5	5.9 ±0.4 (7%)	5.9±0.6 (10.2%)
41.5	9.0 ±0.7 (7.8%)	9.0±0.9 (10%)
33.5	13.9 ±1.2 (8.4%)	13.7±1.5 (11%)

A set of simulations has been also performed to evaluate the dose distributions on the cells plane, using as input the two available energy spectra, in order to consider the shot-to-shot input beam fluctuations. Figures 3.12 and 3.13 report the output data for the two slit apertures. Left and right sides correspond to '1°' and '2°' input proton beam, respectively.

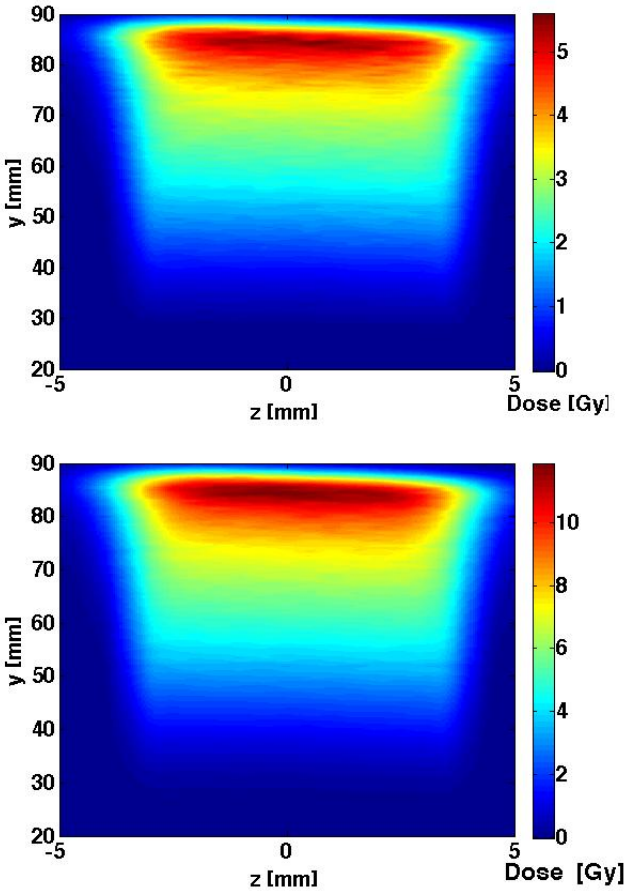

FIGURE 3.12: Dose distributions on the cells plane obtained with the 310 μm entrance slit and with the two input beams of figure 3.8: left corresponds to the '1°' (green circles) and right to '2°' (blue triangles).

As shown, the dose distributions are almost independent from the input, because they reflect the exponential trend of the implemented energetic spectra. However, the proton flux differences between the '1°' and '2°' input beam produce different absolute dose values.
In tables 3.2 and 3.3 the mean doses evaluated for the two entrance slits, on a 3 mm (y) × 5 mm (z) area centred at the above reported y coordinates, are listed. As expected, fixing the input energy

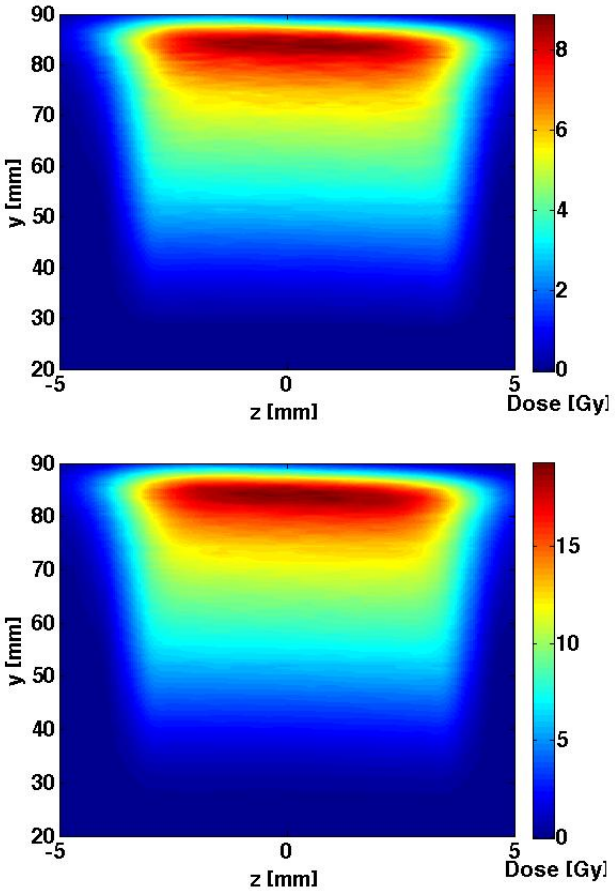

FIGURE 3.13: Dose distributions on the cells plane obtained with the 520 μm entrance slit and with the two input beams of figure 3.8: left corresponds to the '1°' (green circles) and right to '2°' (blue triangles).

TABLE 3.2: Dose values evaluated on a 3 mm (y)× 5 mm (z) area approximately centred in the three cells dots position. Data are obtained using the 310 μm entrance slit.

	y=50.5 mm	y=41.5 mm	y=33.5 mm
	Dose [Gy]	Dose [Gy]	Dose [Gy]
1°	1,8 ± 0,1 (5,8%)	0,9± 0,1 (9,5%)	0,3± 0,1 (17,8%)
2°	3,7 ± 0,2 (6,0%)	1,9± 0,2 (9,7%)	0,7± 0,1 (18,4%)

TABLE 3.3: Dose values evaluated on a 3 mm (y)× 5 mm (z) area approximately centred in the three cells dots position. Data are obtained using the 520 μm entrance slit.

	y=50.5 mm	y=41.5 mm	y=33.5 mm
	Dose [Gy]	Dose [Gy]	Dose [Gy]
1°	3,0 ± 0,2 (6,0%)	1,6± 0,2 (9,6%)	0,6± 0,1 (16,8%)
2°	6,2± 0,4 (6,0%)	3,2± 0,3(9,7%)	1,1± 0,2 (18,4%)

distribution, the dose values increase for the bigger entrance slit as well as for higher y positions, i. e. for lower energies. Moreover, for a given y position, fluctuations corresponding to the input shot-to-shot instabilities are not negligible.

3.4.2 Experimental data

The performed experimental run has two main aims: the measurement of the Energy vs y curve and the cellular irradiation contemporary to the dose evaluation.
For the Energy vs y curve measurement, CR-39 and IP detectors have been arranged as shown in figure 3.6. The used setupd are:

- EBT3 in order to stop 5.6 MeV protons
- EBT3 + 250 μm Al foil in order to stop 8.6 MeV protons
- EBT3 + 500 μm Al foil in order to stop 10.6 MeV protons
- EBT3 + 1 mm Al foil in order to stop 14.5 MeV protons

For the analysis, the IP image-file created by the scanner has been converted, thanks to an already developed ImageJ tool, in a 32-bit image with the pixel value replaced with the PSL signal intensity. This signal was therefore studied as a function of y, in order to obtain the positions corresponding to the different energy cuts.
For the CR-39, the etching procedure has been performed with a 6.25 M NaOH solution at 70°C temperature for 2 hours while the analysis was done with an inverted microscope using a 40x magnification (calibration factor 864px=100μm). In detail, for each CR-39 two purposes were fulfilled:

- fixing the z position, we have registered pictures along the y axis, with a step of 300 μm. From the particles counts, i. e. the fluence, as a function of y, the positions corresponding to the different energy cuts have been measured (Figure 3.14, a);
- a matrix of pictures has been registered in the central area, in order to evaluated the beam homogeneity along the z direction (Figure 3.14, b).

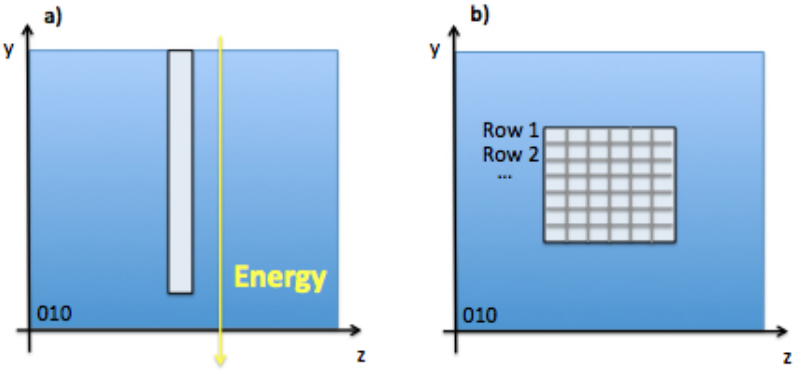

FIGURE 3.14: Schemes used in the CR-39 analysis to obtain a) the position of the energy cut and b) the beam homogeneity.

For all measurements y=0 corresponds to the target position, as in figure 3.3.
As an example, the performed data analysis is here shown for the CR-39 and IP detectors, irradiated using the 310 μm entrance slit and the filters setup to stop 8.6 MeV protons. In figure 3.15, on the

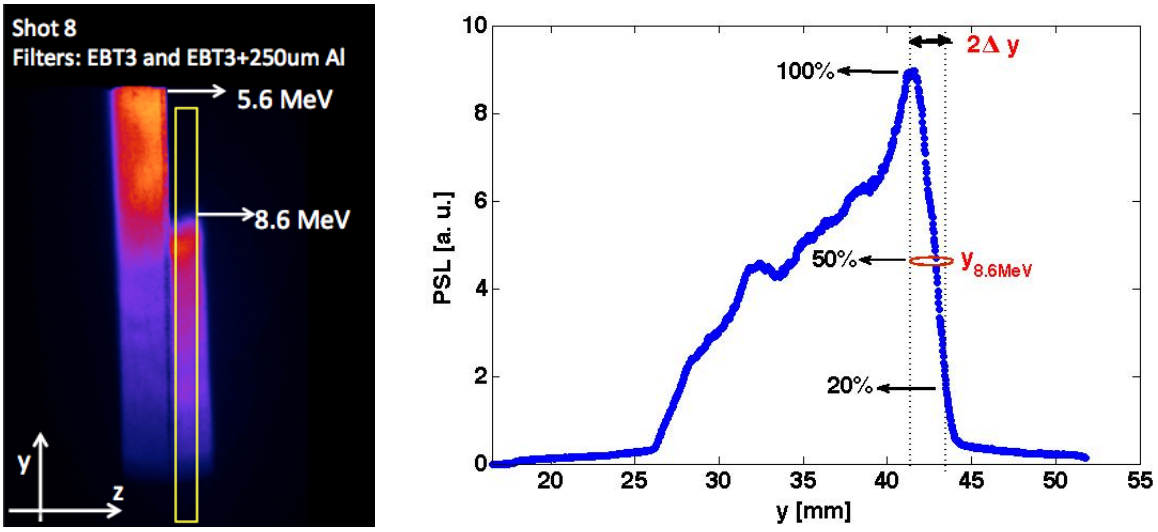

FIGURE 3.15: IP irradiated with the filter setup to stop 5.6 and 8.6 MeV protons. On the left, the IP signal, and on the right, the beam profile of the selected ROI (yellow rectangle).

left, the IP signal is reported. As shown there are two steps corresponding to two different energy cuts, 5.6 and 8.6 MeV. Now we want to focus our attention on the 8.6 MeV energy cut. On the right, indeed, the beam profile of the selected ROI (yellow rectangle) is reported. For the analysis we have considered the sharp step located between 40 and 45 mm. In particular the positions corresponding to 100%, 50% and 20% of the IP signal have been measured. The 50% value of the maximum has been considered as the y position corresponding to the 8.6 MeV cut and the half distance between the two extreme values has been considered as error:

$$y_{8.6MeV} \pm \Delta y = 42.7 \pm 1.1 \; mm \tag{3.2}$$

The y error is an index of the spatial mixing effect, in other words it is related with the thickness of the Energy vs y curve, as studied in the simulations section (see figure 3.11).
The y error can be also compared with the geometrical projection of the entrance slit that represents the minimum spatial resolution of our system. In order to measure this value, an IP wrapped in 12 μm Al foil, in order to avoid the signal saturation, has been placed on the detector plane. The X-rays, produced in the laser target interaction, passed, indeed, through the entrance slit of our transport system and reached indeflected this plane. Figure 3.16 shows the projection of the 310 μm slit, coupled to the ROI (yellow rectangle) profile. A value of 2.2 mm is obtained as signal width at the 20% of the maximum, after the background contribution subtraction. This value can be also useful to evaluate the magnification factor of out system, that is of about 7.1.

The correspondent analysis has been performed also for the CR-39s.
Figure 3.17 reports the fluence [p/cm^2] as a function of y [mm], after 2 hours as etching time.

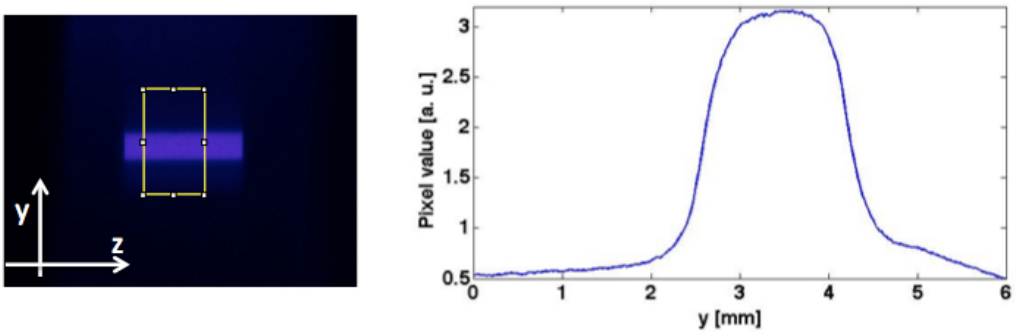

FIGURE 3.16: IP irradiated in order to know the slit projection dimension (left) together with the signal profile of the selected ROI (right).

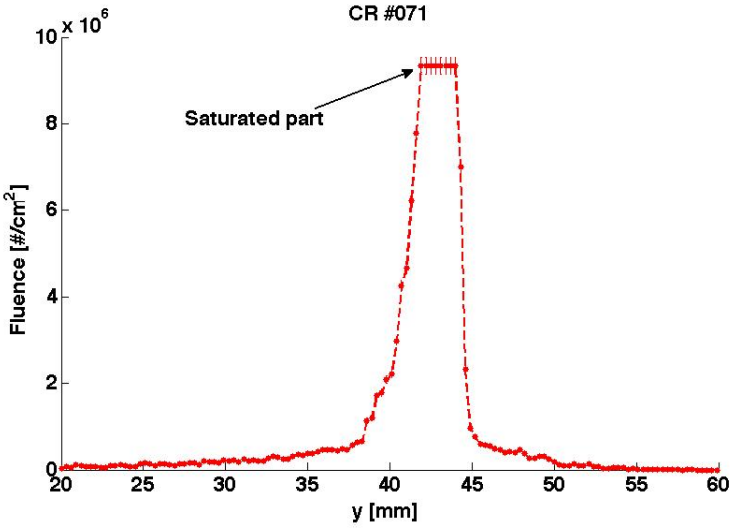

FIGURE 3.17: Fluence distribution [p/cm^2] as a function of y [mm] for the CR-39 irradiated using the filters setup to stop 8.6 MeV protons.

As shown, the trend of the fluence distribution is not the same of figure 3.15. We have, indeed, a saturated region corresponding to the lower energetic particles together with an underestimated fluence part corresponding to the higher energetic protons. We cannot see, indeed, higher energetic particles with only 2 hours of etching.
Szydlowski et al. in [99] reports the CR-39 calibration curve obtained using a NaOH 6.25 M solution at a temperature of 70°C.

As it is shown in figure 3.18, after an etching time of 2h, only protons with energy up to 1.5 MeV have a significant diameter. For this reason, we have decided to increase the etching time up to 8h for some detectors, obtaining a wider saturated region.
Increasing the etching time the track diameter as well as the visible energy range increases, but the threshold from which particle tracks are overlapping decreases, as reported in figure 3.19 [100].

In order to evaluate the y position corresponding to the energy cut with the lower uncertainty, we have therefore chosen to analyse the fluence distribution obtained after 2 hours of etching time. In particular we have considered the central point and the half width of the saturated region as

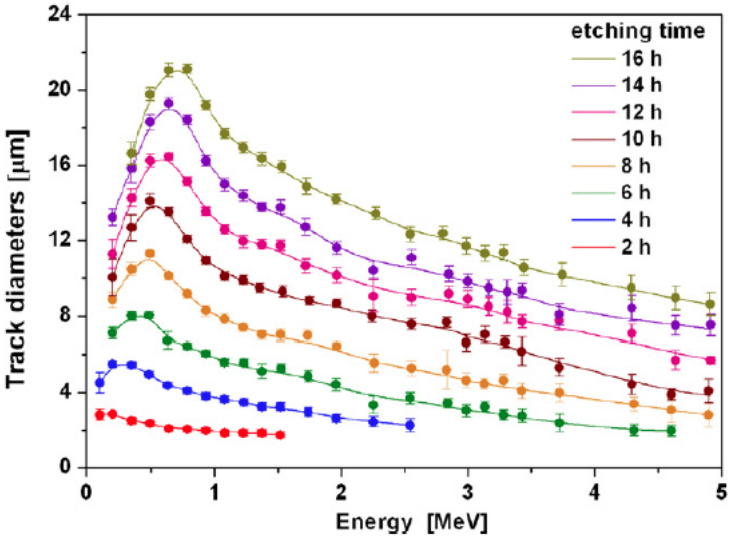

FIGURE 3.18: Calibration curves of the CR-39 detector which present the track diameters as a function of proton energy and etching time [99]

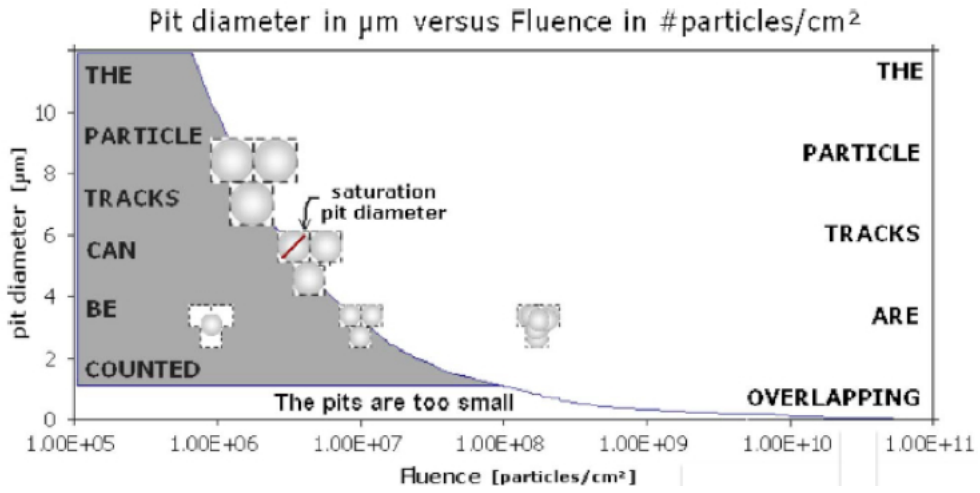

FIGURE 3.19: This graph shows, as a function of track diameter vs fluence, when tracks are separated, and can therefore be individually counted, or when they are overlapping [100].

$y_{8.6MeV}$ and Δy, respectively

$$y_{8.6MeV} \pm \Delta y = 42.5 \pm 1.1 \; mm \tag{3.3}$$

We want to stress that increasing the etching the time, Δy value increases and $y_{8.6MeV}$ decreases. CR39 were also used for the evaluation of the beam homogeneity. Figure 3.20 reports the particles counts, for the above considered CR-39, as a function of z, for y=38.4, 36.4, 32.4 and 29.4 mm.

The obtained mean beam homogeneity evaluated for z in [16-21] mm (5 mm is the cell dot width) is of about 88.2%.In table 3.4 the beam homogeneity values for the different CR-39 detectors are listed. This parameter is on average higher than 85%. However, with this measurements we can understimated the beam inhomogeneity on the cells dots, considering that their hight is 3 mm.

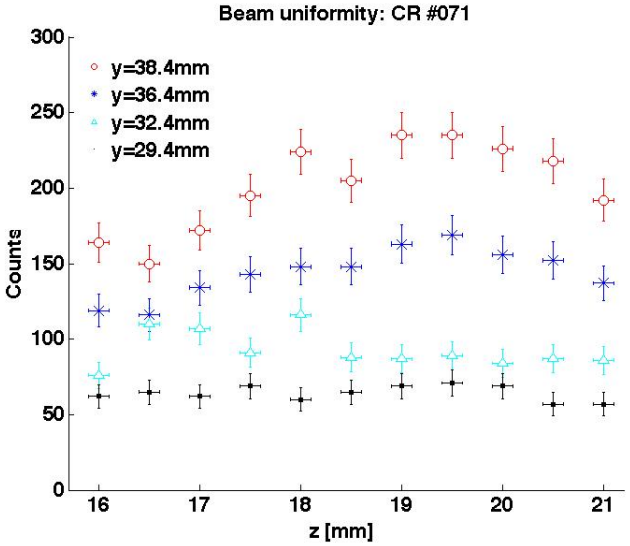

FIGURE 3.20: Counts distribution as a function of z [mm] for the CR-39 irradiated using the filters setup to stop 8.6 MeV. The y positions corresponding to the different curves are 38.4,36.4,32.4 and 29.4mm.

TABLE 3.4: Uniformity percentage for the different CR-39 detectors evaluated for z in the range [16-21] mm (5 mm is the cell dot width).

CR-39	Uniformity [%]
num.71	88.2
num.16	84.8
num.30	89.6
num.10	86.4
num.03	85.8

The above described procedure has been performed for all irradiated detectors. Data related to the different energy cut positions measured by means of CR-39s/IPs and evaluated from the simulations are reported in table 3.5.

TABLE 3.5: Energy cut positions obtained from the simulations and from the CR-39s/IPs analysis, using the 310 and 520 μm entrance slits.

	310 μm slit			520 μm slit		
E [MeV]	y_{Sim}[mm]	y_{IP}[mm]	y_{CR-39}[mm]	y_{Sim}[mm]	y_{IP}[mm]	y_{CR-39}[mm]
5.6	52.2±1.2	51.4±1.1	-	52.2±1.7	55.1±1.7	-
8.6	42.7±1.1	42.7±1.1	42.5±1.1	42.7±1.7	45.7±1.7	42.5±1.8
10.6	38.6±1.1	37.7 ±1	39.2 ± 1.	38.7±1.7	40.5±1.7	41.3±1.7
14.5	33.0±1.1	32.9±1.1	damaged	33.0±1.7	33.6±1.7	35±1.7

As shown, there is a good agreement within the uncertainties between the experimental and the simulated data. Higher discrepancies between simulation and experimental data have been found for the 520 μm entrance slit. In this case, as confirmed from a simulation set not reported here, the slit was not mounted exactly on the axis normal to the target, at laser focus position, but with a displacement of few hundreds μm on the y axis. This value can be roughly evaluated also

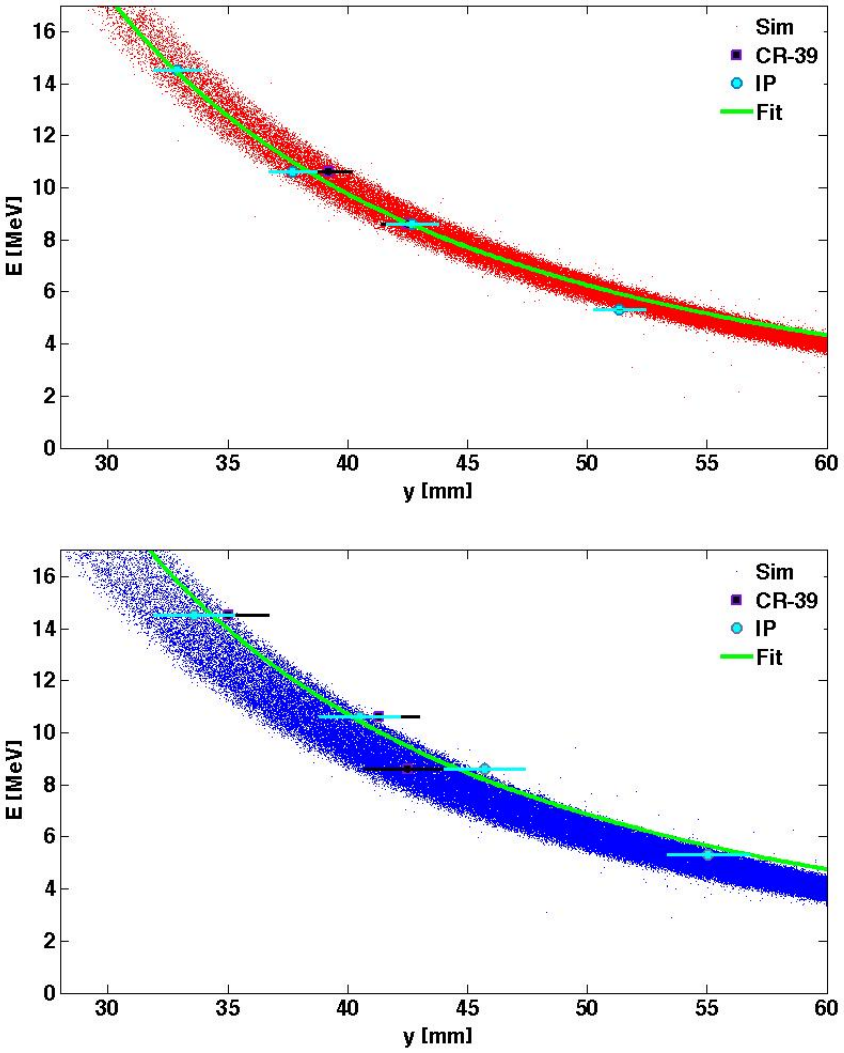

FIGURE 3.21: Energy vs y curve: simulation and experimental data obtained using the 310μm (top) and 520μm (bottom) entrance slit.

considering that the magnification factor of our system is of about 7.1.
Figure 3.21 shows data reported in table 3.5, together with their fits, realised using a A/y^b function, as in 3.1. Obtained parameters values are:

- 310 μm slit $\rightarrow$ A= 1.56 $\times$ 10^4, b=2 (R^2=0.99)
- 520 μm slit $\rightarrow$ A= 1.71 $\times$ 10^4, b=2 (R^2=0.97)

Knowing the Energy vs y experimental curves for the two entrance slits, we have evaluated the mean energy corresponding to the y coordinates of the three cells dots. Obtained values are listed in table 3.6.

The dose measurements were performed by means of EBT-3 films, placed immediately behind the cell plane. Figure 3.22 reports a typical RCF signal obtained during the experimental run, together with the signal profile associated to the selected ROI (yellow rectangle).
As shown, the signal is almost uniform on the cellular dots. We have, indeed, a inhomogeneity

TABLE 3.6: Energy values corresponding to the three cells dots, irradiated using the two entrance slits.

Num. dot	y [mm]	E [MeV] 310 μm slit	E [MeV] 520 μm slit
1	52.5	5.7	6.2
2	42.5	8.6	9.4
3	34.5	13.1	14.3

pixel value lower than 12%, if only the central region corresponding to the cell dot width (5 mm), is considered.

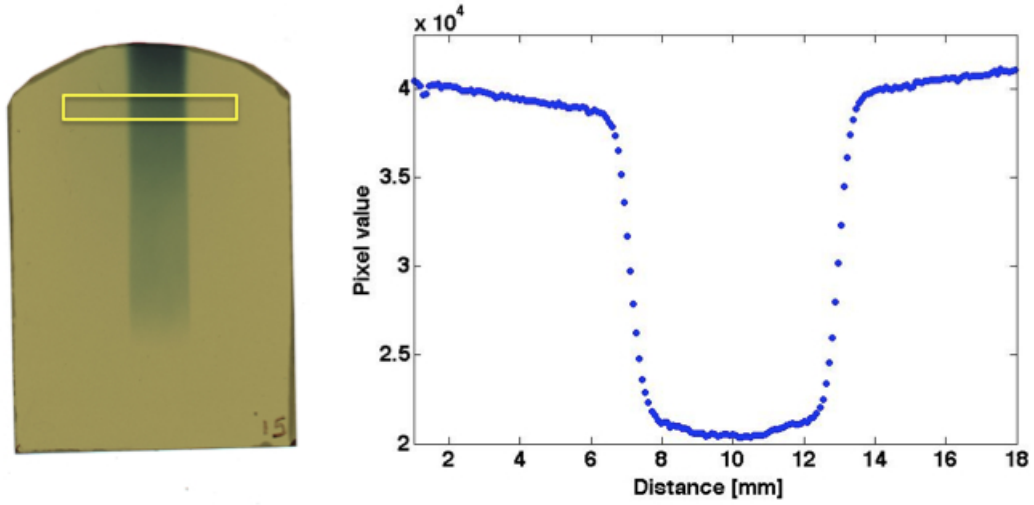

FIGURE 3.22: Typical RCF signal (left) together with the profile of the selected ROI (right).

Using the EBT-3 calibration curve (see appendix A), the mean dose values with the related standard deviations have been measured on a 3 mm × 5 mm area (dots area) centred in y = 52.5, 42.5 and 34.5 mm (dots positions). Table 3.7 and 3.8 report these values for each dot and for the different shots, together with the investigated radiobiological end-points.

TABLE 3.7: Dose values and investigated radiobiological end-points for the three cells dots, obtained using the 310 μm entrance sit.

Shot number	Target	1° Dot Dose [Gy]	2° Dot Dose [Gy]	3° Dot Dose [Gy]	Rad. end-point
1	25 μm Au	4.4 ±0.9 (23.5%)	1.6±0.2 (14.6%)	0.7±0.1 (19.0%)	Senescence
2	25 μm Au	4.5 ±0.8 (18.0%)	1.1±0.1 (8.5%)	0.9±0.1 (12.9%)	Senescence
3	25 μm Au	4.2 ±0.7 (16.6%)	1.5±0.2 (14.0%)	0.7±0.1 (14.1%)	Senescence
4	25 μm Au	4.2 ±0.6 (14.4%)	1.5±0.2 (13.0%)	0.5±0.07 (14.6%)	Senescence
5	25 μm Au	4.8 ±0.8 (17.1%)	1.4±0.2 (17.0%)	0.47±0.07 (14.3%)	Survival
6	50 μm Au	2.1 ±0.4 (17.6%)	1.1±0.2 (15.0%)	0.68±0.08 (11.5%)	Survival

As reported, for the 25 μm Au target, obtained measurements are in a quite good agreement in respect to the simulated data, reported in section 3.4.1. However, in the experimental data, no significant variation was found in the dose value delivered to the dots when different entrance slit are

TABLE 3.8: Dose values and investigated radiobiological end-points for the three cells dots, obtained using the 520 μm entrance sit.

Shot number	Target	1° Dot Dose [Gy]	2° Dot Dose [Gy]	3° Dot Dose [Gy]	Rad. end-point
1	25 μm Au	3.4 ±0.3 (8.9%)	2.7±0.4 (13.1%)	0.73±0.09 (12.3%)	Survival
2	25 μm Au	3.8 ±0.5 (12.5%)	2.1±0.3 (13.0%)	0.5±0.1 (20.4%)	Senescence
3	25 μm Au	4.1 ±0.7 (17.1%)	3.1±0.4 (12.6%)	0.6±0.1 (23.4%)	Senescence
4	25 μm Au	6.3 ±0.8 (12.8%)	2.6 ±0.2 (6.0%)	0.7±0.2 (23.5%)	Senescence
5	50 μm Au	4.3 ±0.6 (13.8%)	1.8±0.3 (17.6%)	0.7±0.1 (16.7%)	Survival

used. This could be due to the laser-target interaction instability, to the target inhomogeneity and to the laser beam fluctuations. Therefore, focusing our attention only to the irradiations addressed to the senescence evaluation, we can assess that the three dots are irradiated with 4.5 ± 0.8, 1.8 ± 0.5 and 0.6 ± 0.2 Gy, respectively. Considering all the cellular samples, a mean dose rate value of about 3×10^9 Gy/s has been also calculated. The retrieved dose rate is crucial because it represents the main difference of laser-driven beams in respect to conventional accelerated ones in the hadrontherapy field [101].

3.4.3 Measured radiobiological end-points

Even if the dose represents one of the main parameters for the quantitative evaluation of macroscopic biological effects of ionization radiations, there are enormous fluctuations at microscopic scale, due to the different pattern of energy deposition events. Charged particles beams produce local higher ionization events respect to X-rays. For this reason, equal dose values of different radiation qualities, as X-ray and charged particles, does not produce the same biological damage. Therefore, in order to correlate the biological effects to the energetic deposition in terms of ionization density the Linear Energy Transfer (LET) has to be considered. This quantity, as shown in 3.4, is the local energy value dE released in a unit of length dl for a given material. It is common used in keV/μm, where the material is water.

$$LET = \frac{dE}{dl} \tag{3.4}$$

Considering the different energy deposition of X-ray and charged particles, we have $LET_{X-Ray} < LET_{Ions}$.

In order to evaluate also the different biological effects generated from radiations with different LET values, the Relative Biological Effectiveness (RBE) can be defined. This quantity is:

$$RBE = \frac{DoseX}{DoseT\,_{Isoeffect}} \tag{3.5}$$

where $DoseX$ and $DoseT$ are, respectively, the needed absorbed doses of a given radiation, usually X-Ray, and of the tested radiation in order to produce the same biological effect on the considered target. On average, for the RBE calculation the dose-clonogenic assay curves are measured, in terms of cellular surviving fraction as a function of the absorbed dose value. For instance, figure

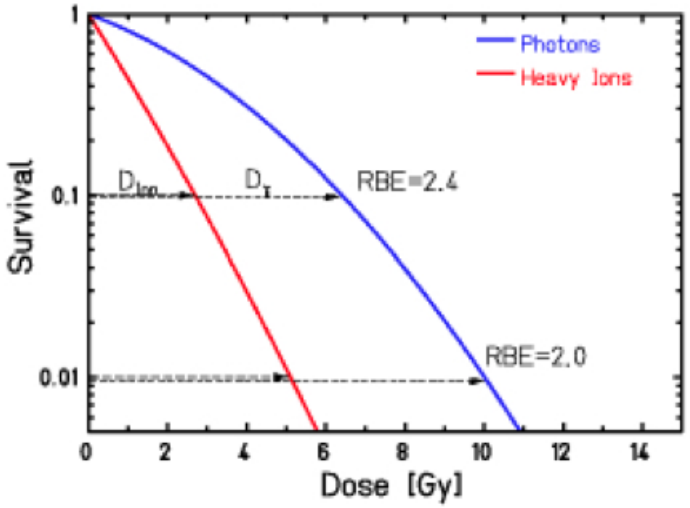

FIGURE 3.23: Typical survival-dose curves for mammalian cells irradiated with X-rays (reference radiation) and charged particles (tested radiation), together with the RBE values evaluated at 1 % and 10 % of the survival fraction.

3.23 reports typical dose-effect curves for photon (low LET) and ions (high LET), where the survival fraction is reported on the y axis in log scale, as a function of the dose. As shown, the RBE value depends on the considered biological effect. It changes, indeed, if we consider the 1% or 10% of the measured survival effect. Moreover, fixing the biological effect, it will also change for different cellular models because of the different intrisic radiosensibility.

Generally the dose-effect curves have some peculiarities that depend on the used radiation beam. If X-rays (low LET) are used, the curve is characterised by a 'shoulder' at low dose values: there is a lower lethal biological effect with a contemporary enhancement in reparable sublethal effects (linear-quadratic model). In other words, if low LET radiations are used, there is a 'huge' spatio-temporal distance between two ionization events if the delivered dose is < 2 Gy and, therefore, the cellular systems are able to repair the radioinduced damage with, as result, an higher cellular survival.

On the other hand, if high LET radiations are used, the dose-effect curve becomes steeper and the shoulder is reduced: the biological effect increases linearly with the absorbed dose. This is due to the distance between two ionization events, that is of the same order of the DNA diameter (1.8 nm).

Contemporary to the irradiation for the carcer treatment, there is also the unavoidable irradiation of the healty cells that are located near the tumour. One of the many possible consequences is the Stress Induced Premature Senescence (SIPS). This effect, that appears on normal cells as well as on cancer ones, is dose dependent. It could be defined as Senescence - Like Growth Arrest (SLGA), i. e. a proliferation stop. However, if the SLGA is a planned physiological effect, the SIPS is only induced from the irradiation or other factors [95].

Up to now, the biological effects obtained using conventional X-rays and proton beams are well known and an increasing interest in studying them at extremely high dose-rate (10^9 Gy/s) was born. For this reason the experimental run at LULI has been crucial, because it allowed to investigate the clonogenic assay as well as the senescence on Human Umbilical Vein Endothelial Cells

(HUVEC) model using laser-driven protons at about 3×10^9 Gy/s.
The HUVEC cellular model has been chosen because it represents one of the most used model for in-vitro studies on endothelial tissue. Moreover it shows an high reproducible pattern for the cellular growth and maintenance, useful for senescence investigation.
The same biological end-points have been also measured using X-rays (250kV-peak) and conventional proton beams, both at $\sim$ 1 Gy/min as dose-rate. In particular the irradiations have been performed, respectively, at the University Federico II of Naples (Italy) and at the clinical CATANA facility of INFN-LNS (Catania, Italy) [102].
Figure 3.24 shows the survival fraction curves obtained with these three input beams, together with their fit curves, performed using the linear-quadratic model:

$$SurvivalFraction \rightarrow SF = e^{-(\alpha D + \beta D^2)} \tag{3.6}$$

where D is the dose value in Gy, α a constant related to the single event killing (number of cells killed per Gy-linear component) and β a constant related to two events killing (number of cells killed per Gy^2-quadratic component). Data related to laser-driven protons take into account the total contribution of the three cellular dots, even if they are irradiated with different energies, i. e. with different LET values (about 3, 5 and 7 keV/μm). Indeed, as reported in [103] and confirmed by experimental measurements, for protons the survival fraction is, indeed, almost not dependent from the LET fluctuations, if values lower than 28 keV/μm are considered.

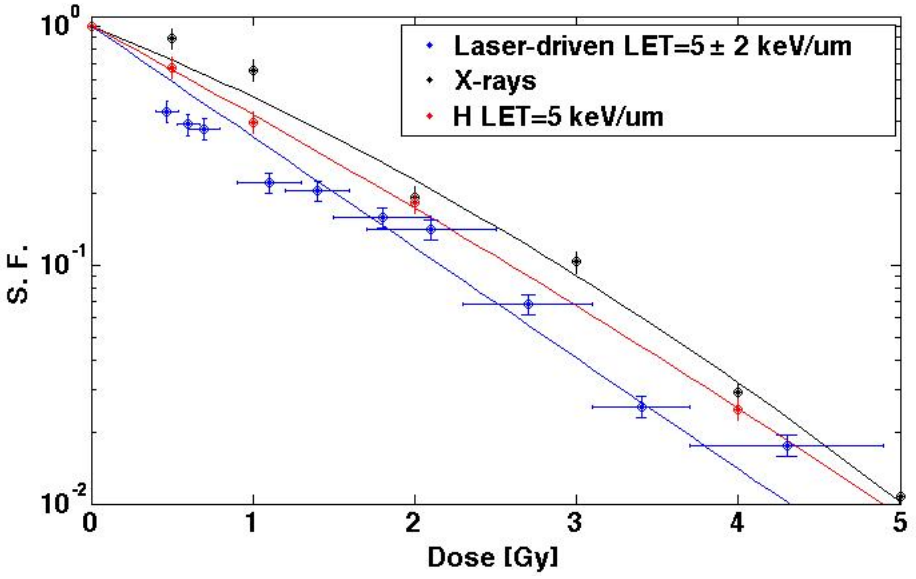

FIGURE 3.24: Experimental survival-dose curves obtained irradiating HUVEC cells with X-rays, conventional protons and laser-driven protons beams.

The obtained RBE value at 10% of surviving fraction are 1.3 $\pm$ 0.2 and 1.1 $\pm$ 0.1 for laser-driven and conventional beams, respectively, both calculated respect to the X-rays. These two values have a no-significant difference considering the evaluated uncertainties. Moreover they are in a good agreement with data reported in literature and obtained for laser-driven beams.

As regarding the senescence, investigated at 1, 7, 14 and 28 days from the experiment, figure 3.25 reports the measured data for one of the three cellular dots.

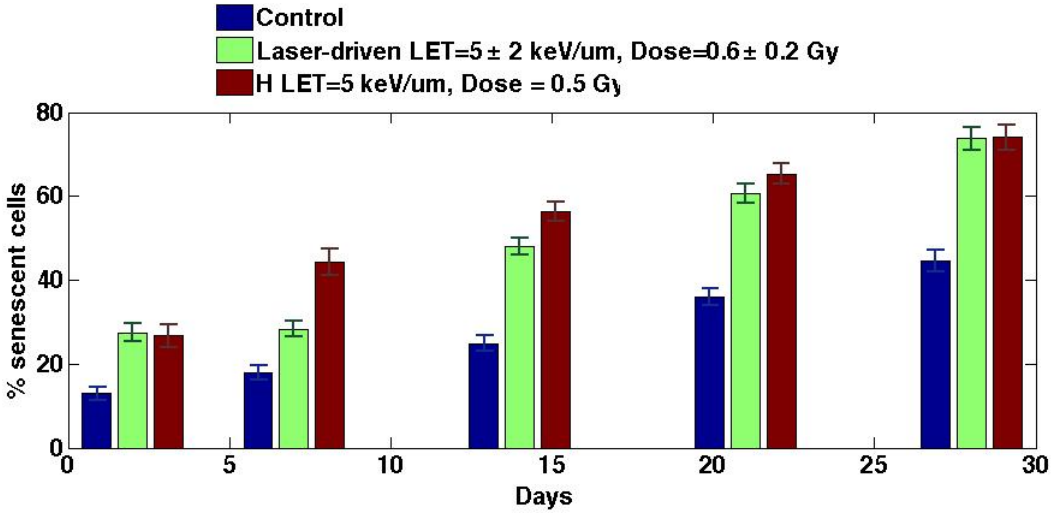

FIGURE 3.25: Experimental percentage of senescence cells evaluated at 1, 7, 14 and 28 days from the irradiation, performed with conventional and laser-driven protons beams.

As shown, for this dot, the senescence trend is the same for the different kinds of radiations and in particular, laser-driven beams seems to less induce the premature senescence. However the cellular response is different for the other dots.

The few differences that we have found could perhaps be related to the ultrashort nature of the deposition: possible alterations of the radical production (oxygen depletion effect) [104], spatio-temporal overlap of independent tracks resulting in collective effects [105] or poor interaction between direct (caused promptly by direct DNA-ion and secondary electron interaction) and indirect (caused by radicals, with diffusion time up to 10 μs) DNA lesions [85]. However, considering the significant energy spreads and dose uncertainty that characterised the test, the obtained results have demonstrated that the irradiation conditions need to be improved. Therefore, to reach the required accuracy for radiobiology experiments, it is desirable to better handle and control the transported beam.

New experimental runs with controlled proton beams should be therefore performed, in order to completely understand the relation between laser-driven beams ad radiobiological end-points.

Chapter 4

Laser-driven beams for multidisciplinary applications

In the majority of theoretical and experimental studies devoted to the ion acceleration in laser plasmas, hadron therapy has been indicated as one of the most important applications. As described in chapter 1, several papers [83, 106] formulate a concept in which a laser ion accelerator could replace a standard accelerator (or even the injector), still maintaining systems of ion delivery and target irradiation [107]. In a most promising version, envisaged in a future perspective, traditional accelerators and magnetic systems for the ion beam delivery will be completely removed and replaced by an all-optical system. On the way towards these challenges, it is necessary to solve several technical problems, such as the enhancement of laser pulse stability and repetition rate, in connection with an increase in the average laser power [40]. Moreover for possible hadrontherapy application, the relative biological effectiveness of high-energy ions accelerated by laser radiation, in comparison with ions generated by conventional accelerators, is still matter of discussion and needs furhter studies. As already reported in chapter 3, such a distinction, if existing, may arise from the very short duration of the laser-accelerated ion bunches. The *'instantaneous'* intensity of the laser-generated beams is indeed several orders of magnitude larger than the intensity of conventionally accelerated ion beams. There are indications on this concern suggesting that, in the high-intensity interaction of laser-driven ions with DNA molecules, clusters can be formed, increasing the probability of the double strand break and, as a consequence, the probability of killing the cancer cells [41, 104, 105]. However, on the other hand there are papers reporting the possibility to have no biological effect variation if laser-driven beams are used, at least for some specific end-points [85].
Therefore, in order to better answer this question, futher experiments in the cancer cell irradiation field using laser-accelerated protons have to be performed, exploiting different irradiation conditions. In particular, the dependence of biological effectiveness on the duration of the beam pulse, on the dose and on the beam energy, i. e. on the linear energy transfer, should be accurately investigated. Several campaigns [60, 87–91, 93, 108] as well as the experiment reported in chapter 3, have been performed to try to improve the knowledge on this concern, but in most of cases the uncertainties arising from the beam handling and transport do not allow to achieve undeniable

results.
For hadrontherapy as well as for almost all considered applications of laser accelerators, including injectors [109] and controlled laser nuclear fusion [110], the quality of the proton beam is indeed of key importance. The currently used energetic spectra are unacceptable for any possible medical application. They do not provide an optimal shape of the Bragg curve, leading to unacceptably high damage of healthy tissues surrounding the tumour. For this reason, the question of how to provide beams with controlled energy and angular distribution arises.
In this context, several world wide research centres have started developing the required technology, as the Japan Atomic Energy Agency in Kizugawa, the Munich Centre for Advanced Photonics (MAP) in Munich, Germany, the Institute of Physics of Czech Academy of Sciences in Prague within the framework of the ELI-Beamlines project, the University of Catania together with the INFN Laboratori Nazionali del Sud in Catania, Italy, the Institute for Heavy Ion Research in Darmstadt, Germany, the OncoRay-National Center for Radiation Research in Oncology in Dresden, Germany, the Laboratoire d'Optique Appliquée-LOA in Palaiseau, France and the Queen's University of Belfast, UK.
The main progresses in this scientific area are associated with:

- the demonstration of more efficient and better controlled ion acceleration mechanisms, with the use of tailored targets and with the improvement of the laser technology for the generation of more powerful and stable high-quality electromagnetic pulses;
- the development of transport beamlines based on magnetic devices for the appropriate control of the accelerated ion beams.

In this chapter, the status of the main progresses recently carried out on this concern are reported. Then, the main features of new beam transport elements will be discussed. They are the prototypes of the ones composing the future ELIMAIA (ELI Multidisciplinary Applications of laser-Ion Acceleration) beamline, that will be installed at ELI-Beamlines, as briefly reported in section 4.2. Also the experimental characterisation of each beamline element, performed using conventional proton beams, is reported in detail.

4.1 State of the art

A promising approach to control accelerated ion beams is associated with the ability to implement special targets. The main aims from this point of view are the energy cut-off enhancement and the source spectrum manipulation. For instance, Mackinnon et al. in [111] studied the dependence of the ion acceleration on the target thickness, with the aim of addressing the role played by the electron temporal dynamics and its effect on the formation of the sheath accelerating electric field. The experimental results showed an increase in the peak proton energy from 6.5 to 24 MeV when the thickness of the Al foil targets was decreased from 100 to 3 μm. These data clearly indicate that an increase in the target thickness imply a lower mean density of the hot electrons at the

surface and a consequent lowering of the peak proton energy. Experimental studies have been also performed changing the material of the target, as reported in [29]. Moreover, recently, an energy cut-off increase up to 67.5 MeV has been demonstrated by Gaillard et al. in [112] using special targets, namely at-top hollow microcone targets [113]. In general, the use of structured targets has been investigated to increase the ion maximum energy, e.g. double layer targets [114] and more recently also nanowire-covered targets [115].

Various approaches have been also proposed in order to manipulate the TNSA spectrum of protons and ions, in most cases with the aim to obtain narrow band peaks but also to enhance proton numbers throughout the whole spectrum or in some spectral bands, as required by specific applications. For instance, spectral peaks appear, as a consequence of multispecies plasma expansion, in experiments employing high-Z metallic targets where a plastic layer (0.5 μm PMMA) was coated as a dot on the rear surface of a 5 μm Ti foil [116]. Also the possibility to focus the accelerated beams has been investigated. For this purpose, specially shaped targets have been used as thin-wall concave shell targets [117] or thick-wall foils with a cavity [118].

From hereafter we will focus our attention on the beam control performed by means of elements placed just behind the target holder. There are many different approaches with the same task: 'cut' the generated energy spectrum into beamlets with a narrow energy distribution.

Toncian et al. in [119, 120] shows how a laser triggered micro-lens can focus and partially energy select laser generated MeV proton and ion beams. This all-optical system uses a transient electric field, that is excited at the inner surface of a metal cylinder (700 μm in diameter and 3 mm in length) irradiated on the outer surface by a high-intensity laser pulse while a laser-driven proton beam transits through it. As the field is transient, typically lasting for 10 ps, it affects only the component transiting through the cylinder within this time window, affecting, therefore only protons within a narrow energy band and leading to a spike in the energy spectrum. With this kind of system a 0.2 MeV band at about 6 MeV was obtained. Obviously, by varying the optical delay between the main laser beam, interacting with the target, and the second laser beam, used to irradiate the hollow cylinder, the location of this peak on the energy axis can be tuned selectively, thereby allowing to tailor the energy distribution of the transmitted beam. However in the output beam, together with the main peak, there are significant contamination components at higher and lower energy components. They indeed pass through the cylinder before and after the field generation, respectively.

Beyond this all-optical solutions, several groups have implemented more conventional techniques for energy selection and transport of laser-accelerated protons, in view of possible applications. In this context the range of explored options includes the use of magnetic chicanes, as in [89, 121, 122], whose efficiency is strongly limited by the wide divergence of the input beam. Also pulsed solenoids have been investigated, as reported in [30, 123–126]. In this case the obtained output beams were characterised by a main peak with significant contaminations at higher and lower energies, due to two main reasons. Because of the co-moving electrons forced from the field on the solenoid axis, the plasma quasi-neutrality is lost and it generates an electrostatic lens inside the magnet. This is assumed as the reason for the enhanced focusing capability of the ion beam, especially if compared to the numerical simulations outputs. Moreover, the interaction of ions (or plasma) with the inner

wall of the solenoid causes local surface discharges that influence the magnetic field.
The alternative of one or two quadrupole magnets has been also explored with several simulative and experimental studies. For instance, Ter-Avetizyan et al. in [127] show how a permanent magnetic lens system acts as a tunable band pass filter, collecting and focusing protons with the same energy. Using two 50 mm quadrupoles characterised by 1.3 T as magnetic field value at the maximal useable diameter, an increase of the output proton density in the (3.7 $\pm$ 0.3) MeV energy band to a factor of $\sim$30 has been observed respect to a non-handled beam. However, even if the obtained output beam has an approximately flat profile with a size of 40 $\times$ 40 mm^2, it cannot be considered parallel as well as monoenergetic. Indeed it has characterised by a divergence of about 1.2 deg and by energy contributions down to 1 MeV. Similar studies have been conducted and reported in [128, 129].
The main difference between the last two options is the operational energy range: for MeV or sub-MeV energies, solenoids are a convenient approach, whereas quadrupoles have more advantages at higher energies, also without pulsed magnet or superconducting technologies [130]. As reported in [57], the number of protons selected using quadrupoles system is lower of almost one order of magnitude but, in contrast to the solenoid, no low energy peaks are present. Finally, as regarding the co-moving electrons, always present in the laser acceleration, they are strongly focused toward the solenoid axis with significant consequent contamination in the output beam. In a system of quadrupoles, instead, they are defocused with probably small effect in the quality of the output beam. The main issue could be indeed related to the increase of the beam trasversal dimension, due to the propagation of the charged particles without the co-moving electrons component [127].
A transport solution composed of many elements, i. e. permanent quadrupole magnets, a radio-frequency phase rotation cavity and a tunable monochromator, has been considered and tested in a beamline operating at 1 Hz repetition with a view to future biomedical applications. An output beam centred at 1.9 MeV with a 5% spread and a transmission efficiency of about 10% has been demonstrated [131]. For all these approaches, as reported in literature, the crucial common parameters are the acceptance angle of the transport system, which limits the number of output particles especially considering the wide input divergence, the downstream beam shape and the output energy spectrum.
In this framework, the features of the beam transport prototypes of the future ELIMAIA beamline were defined. The ELIMAIA beamline will be installed within 2017 at the ELI-Beamlines in Prague (Cz) with the aim of studying multidisciplinary applications with well controlled beams.

4.2 ELI-Beamlines and the ELIMED project

Extreme Light Infrastructure (ELI) is a new Research Infrastructure part of the European ESFRI Roadmap. ELI aims to host the most world wide intense lasers and to develop new interdisciplinary research opportunities based on these lasers and on the secondary radiations derived from them, finally making them available to an international scientific user community. In particular there will be accomplished and implemented research projects covering the interaction of light with matter at intensity being 10 times higher than currently achievable values. Ultra-short laser pulses of a

few femtoseconds (10-15 fs) duration with performance up to 10 PW will be installed.
The ELI facility will be based on four sites. Three of them are presently being implemented in the Czech Republic, Hungary and Romania with complementary scientific profiles. The place of the fourth infrastructure is under discussion.

- In Dolni Brezhany, near Prague, Czech Republic, the ELI-Beamlines facility will mainly focus on the development of short-pulse secondary sources of radiation and particles, and on their multidisciplinary applications in molecular, biomedical and material sciences, physics of dense plasmas, warm dense matter and laboratory astrophysics. In addition, the pillar will utilise its high-power, high-repetition-rate laser for high-field physics experiments with focused intensities of about 10^{23} W/cm^2, investigating exotic plasma physics and non-linear QED effects.

- The ELI Attosecond Light Pulse Source (ELI-ALPS) in Szeged, Hungary is establishing a unique facility which provides light sources between THz (10^{12} Hz) and x-ray (10^{18-19} Hz) frequency range in the form of ultrashort pulses with high repetition rate. ELI-ALPS will be dedicated to extremely fast dynamics by taking snap-shots in the attosecond scale of the electron dynamics in atoms, molecules, plasmas and solids. It will also pursue research with ultrahigh intensity lasers.

- In Magurele, Romania, the ELI Nuclear Physics (ELI-NP) facility will focus on laser-based nuclear physics. It will host two machines: a very high intensity laser and a conventional linear accelerator. In particular, in terms of available beams, there will be two 10 PW lasers beams coherently added to get intensities of the order of 10^{23}-10^{24} W/cm^2, and a very intense, brilliant gamma beam, obtained by incoherent Compton back scattering of a laser light off a brilliant conventional accelerated electron beam. Applications will include nuclear physics experiments to characterise laser-target interaction, photonuclear reactions, exotic nuclear physics and astrophysics.

From hereafter I will focus on the ELI-Beamlines pillar. Because of its applications, the presented thesis has been developed in the framework of this project. Figure 4.1 shows an artistic view of the future ELI-Beamlines building together with the separation in experimental, laser and offices areas. A draft of the experimental areas is shown in figure 4.2, together with the detailed view of the ELIMAIA (ELI Multidisciplinary Applications of laser-Ion Acceleration) beamline, representing the ELI-Beamlines areas specifically dedicated to the ion acceleration and their applications.

ELIMAIA is planned to be realised in four phases:

- preparatory phase: during this phase the building of the ELI-Beamlines facility will be realised; even if no laser beams will be available, this phase is of fundamental importance for the final design of the transport beamline, from the target to the irradiation point. The design of a beamline prototype is planned, together with a preliminary dosimetric system.

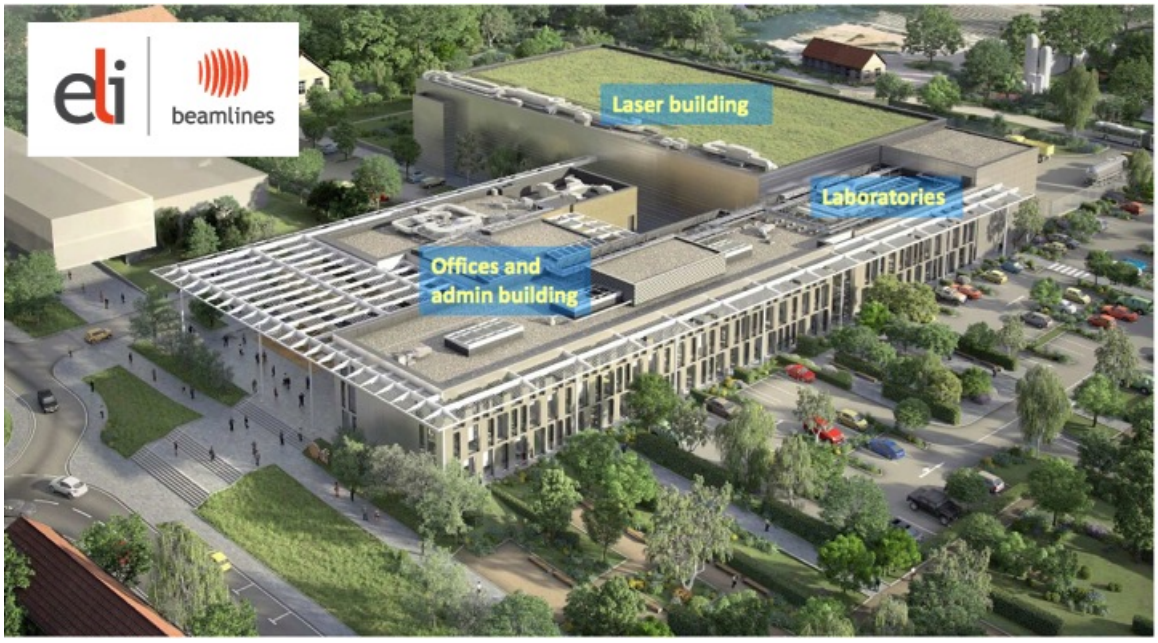

FIGURE 4.1: View of the ELI-Beamlines build

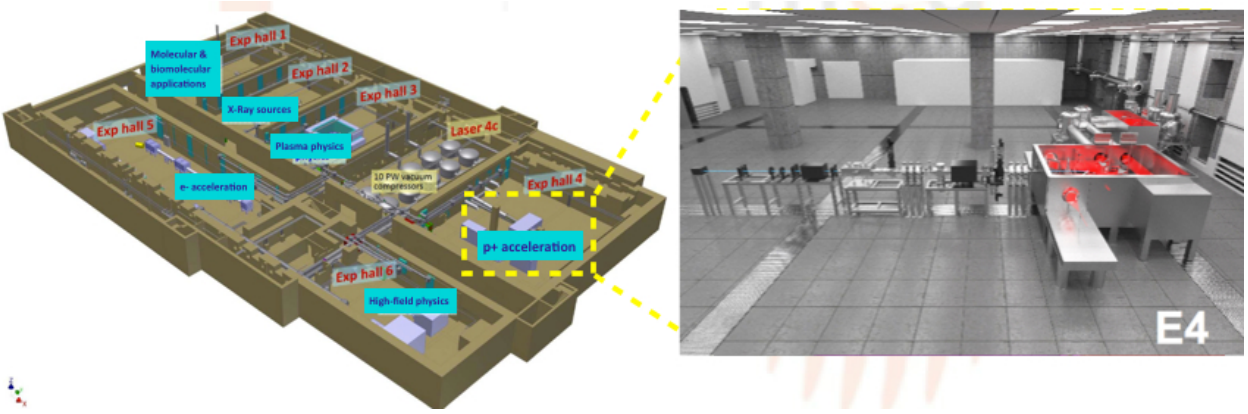

FIGURE 4.2: Plan of the experimental halls in ELI-Beamlines with the detail of the ELIMAIA area.

- First phase: the first laser beams will be available inside the ELIMAIA hall and preliminary tests will be carried out.
- Second phase: proton beams with energy up to 60 MeV will be produced.
- Third phase: proton beams with energy up to 100 MeV will be produced. All the final selection and diagnostic systems will be working at their maximum performances. The transport-line and the dosimetric systems will be installed and the final radiobiological study of the beam will be realised.

Preliminary to the first phase, prototypes of the future ELIMED beamline had to be designed and realised in order to study the possible criticality of the different elements. The beamline prototypes that are presented in this thesis, are the result of a collaboration, launched in 2012, between the INFN-LNS (Nuclear Physics Laboratory, Catania, Italy) and ASCR-FZU (Institute of Physics of

the Czech Academy of Science), responsible for the ELI-Beamlines facility implementation. The main aim of this collaboration, named ELIMED (ELI-Beamlines MEDical applications), was to investigate the feasibility of the design and the realisation of a complete beam transport line for optically accelerated beams dedicated for multidisciplinary and medical applications. The study and the development of new detectors for absolute and relative dosimetry with innovative radiobiological investigations was also foreseen.
In 2012, an INFN founded project, named ELIMED/PLASMAMED (Proton LAser-drive beam transport, diagnostic and Multidisciplinary Applications), has been also established with these purposes.

4.3 The ELIMAIA transport beamline prototypes

As already pointed out, the main goal of the ELIMED project is the realisation of a complete beam transport line, from the laser interaction point to the final sample irradiation point, coupled to the development of new detectors for dosimetry.
Optically accelerated ion beams are characterised by high intensities, several species with multiple charge states, broad energy spectra and energy-dependent angular distributions. Therefore, in order to make these beams suitable for multidisciplinary purposes, the main scope of the beam transport line will be to control the beam energy and angular distributions as well as the reproducibility of the delivered beam spot size and dose distributions, in order to perform accurate dosimetric measurements and radiobiological irradiations for pre-clinical studies.
The proposed technical solution is based on a modular system for the beam capture followed by the final energy selection. In figure 4.3 is reported a draft of the prototypes assembled in a possible proposed configuration including a target interaction chamber and, downstream, the irradiation point.

It starts close to the production point of the charged particles and it is divided into two sections: the collection part and the energy selector. The aim of the first section is to collect the largest fraction of particles so that to reduce the beam angular divergence, as well. The device must be quite compact since it has to be placed inside the scattering chamber, as close as possible to the target. To fulfil such requirements, solenoid magnets producing pulsed high magnetic field are widely used. Indeed, a solenoid has a large acceptance and ensures focusing on both transverse planes. Moreover, considering that the focal point of a solenoid depends on the particle energies, this system also provides a very preliminary selection in energy: it is done by placing a collimator at a certain distance from the solenoid. However the particles passing through the solenoid-collimator system are not well selected in energy since part of low and the high-energy components are transported together with the selected one. This is due to several reasons, as reported in section 4.1.
As alternative to the above system, the capturing phase can be done by means of quadrupole lens. In this case, that is our choice, a set of quadrupoles based on permanent magnets can be placed into the interaction chamber. Moreover, a mechanical system for the quadrupoles relative distance variation can be used in order to modify the focal point position of the desired energy component.

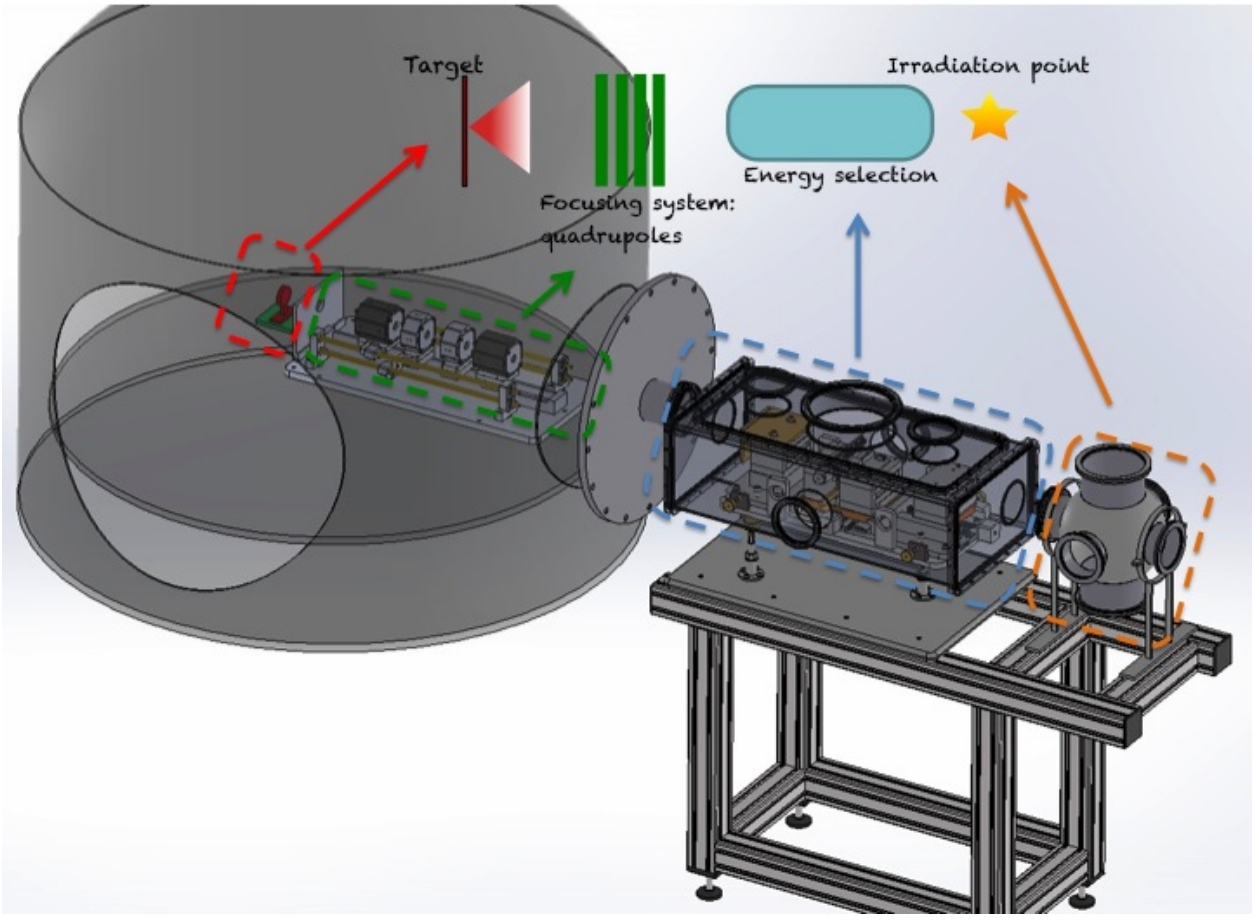

FIGURE 4.3: Draft of thedeveloped prototypes assembled in a possible proposed configuration. On the basis of these prototypes the final elements of the ELIMAIA beamline is being realised, maintaining some of the developed ideas.

This option, as already reported, is characterised by a lower transmission efficiency, however it implies also more reliability and less costs in terms of design and construction.
As regarding the second beamline section, since the beam coming from the capturing system could be even affected by unwanted energy component, an energy selector device providing the final energy refinement was considered.
In the next subsections a detailed description of the two prototypes is reported, together with their characterisations with conventional accelerated protons.

4.3.1 The collection system

A lens is defined as an element in which a charged particle, traversing into it, experiences a bend toward or away from the optic axis, with the angle of bending proportional to the distance of the particle from the optic axis. In this system, the x and y components of the magnetic flux density $\mathbf{B}$, assuming z as the beam axis, increase linearly with the distance from the straight optic axis. Such system is a quadrupole lens that consists of four hyperbolically shaped pole faces or electrodes. Hereafter I will focus my attention on the magnetic case that was chosen in the beamline prototype. In figure 4.4 the magnetic field configuration together with the generated force on a generic charged

particle are shown. The beam is supposed to travel in the z direction, perpendicular to the plane

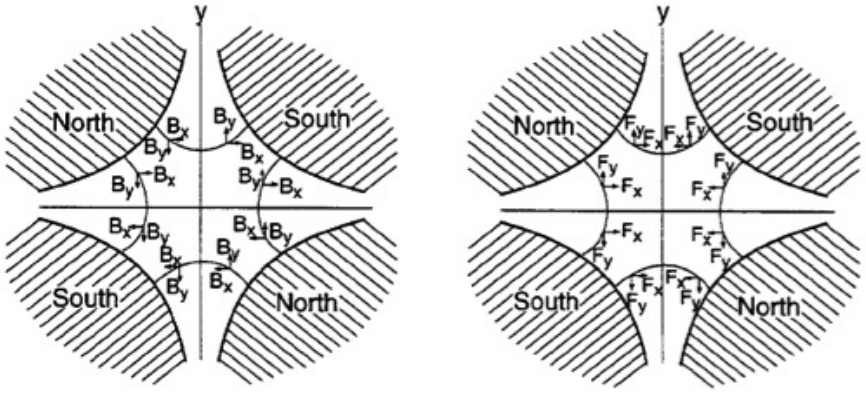

FIGURE 4.4: Magnetic lens features: on the right, the field configuration and, on the left, the generated force on a generic charged particle.

of this paper. It is seen that B_x changes sign upon traversal of the $x0y$ plane, whereas B_y change sign passing through the $y0x$ plane. In order to quantitatively evaluate the field distribution, the Laplace's equation $\nabla^2 V = 0$ with the given boundary conditions has to be solved. If the four poles are equilateral hyperbolas, we find:

$$V = -gxy \tag{4.1}$$

where g is a structural parameter, typical for each quadrupole. Considering that $\overrightarrow{\nabla} \times \overrightarrow{B} = 0$, the magnetic field can be described as $\overrightarrow{B} = -\overrightarrow{\nabla} V$, therefore:

$$B_x = -\frac{\delta V}{\delta x} = gy \qquad B_y = -\frac{\delta V}{\delta y} = gx \tag{4.2}$$

The above structural parameter g is none other than the field gradient of the vertical component in the horizontal direction (or equivalently, the field gradient of the horizontal component in the vertical direction).

With $B_z = 0$, the equations of motion for particles of mass m, charge ze and velocity v, with the transverse velocity components very small if compared to the longitudinal one, are:

$$m\ddot{x} = -(ze)vB_y \qquad m\ddot{y} = (ze)vB_x \tag{4.3}$$

Considering for the x component $\ddot{x} = d^2x/dt^2 = (d^2z/dt^2)(d^2x/dz^2) = v^2(d^2x/dz^2)$ and for the y component $\ddot{y} = d^2y/dt^2 = (d^2z/dt^2)(d^2y/dz^2) = v^2(d^2y/dz^2)$, we have:

$$\frac{d^2x}{dz^2} + \frac{(ze)g}{mv}x = 0 \qquad \frac{d^2y}{dz^2} - \frac{(ze)g}{mv}y = 0 \tag{4.4}$$

Putting $k^2 = (ze)g/mv = (ze)g/p = g/Br$, where p is the relativistic momentum of the particle and Br its magnetic rigidity, the solution of 4.4 can be written in the form:

$$x = a\ cos\ kz + b\ sin\ kz \qquad y = c\ cosh\ kz + d\ sinh\ kz \tag{4.5}$$

with a, b, c and d as coefficients.

From the motion equation solution, we can deduce that quadrupole lenses are able to focus in one plane and defocus in the perpendicular one. Thus, several quadrupoles must be normally combined for a useful lens system.

In particular in the developed prototype a triplet configuration has been chosen. Although the doublet achieves a significant improvement with respect to a single quadrupole, and although its construction is inherently simpler than that of a three-lens system, the latter system is often preferred. In order to get the beam focusing on both transversal planes at least two quadrupoles are indeed foreseen to be used. However adding a third quadrupole, the matching of the focal point on vertical and horizontal directions is obtained, so that a common waist is achieved after the focusing [132, 133].

Considering the different problems related to the high electromagnetic pollution of the laser-interaction environment, permanent magnet quadrupoles have been designed. They are based on a hybrid Halbach cylindrical array with 8 sectors, as shown in figure 4.5, where also the magnetic flux density of one element of the collection system is presented. The poles are set at 45°, with respect to the horizontal axis, and are attached to four iron sections, almost saturated, used as supporting structure as well as magnetic flux guides. The poles have a rectangular main body (13×14 mm^2) with two smaller pieces close to the bore, which allow to increase the field and, hence, the gradient inside the bore itself. The T-like magnets between two poles are modelled as three independent squared pieces (10×10 mm^2). The magnetic features of each quadrupole section depend from the BH curve of the used materials, considering that NdFeB N50 is the material of the magnets and iron XC10 of the other four parts. Each magnet has its own direction for the permanent magnetization.

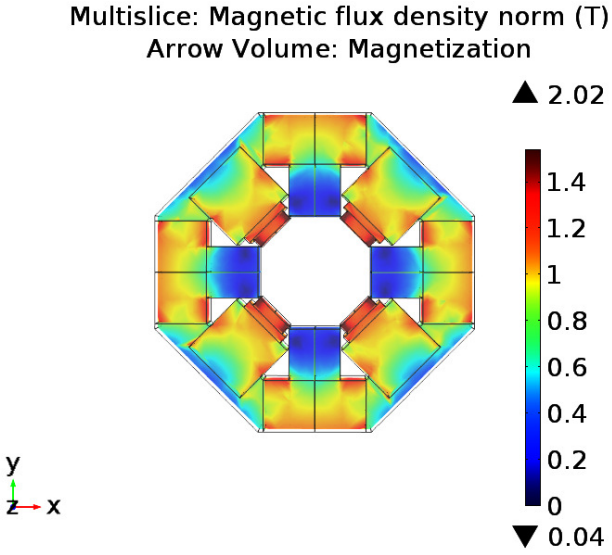

FIGURE 4.5: Magnetic flux density of the 40 mm quadrupole.

The collection system prototype has been already realised with the aim to improve the transmission and selection efficiencies of the magnetic energy selector prototype, placed downstream.

In particular it consists of two long permanent magnet quadrupoles (PMQs), 80 mm in length, and

two short PMQs of 40 mm, both characterised by an active bore of 20 mm with a 1 mm thick shielding pipe placed inside the bore for the shielding from the input beam. The maximum field gradient values are of about 114 T/m and 100 T/m, respectively. The fourth quadrupole has been added to the triplet configuration in order to better manage the lower energies of the operation range of the system, that goes from 1 up to 30 MeV.
Figures 4.6 and 4.7 show the short and long quadrupoles together with their y magnetic field components measured by the manufacturer along the x axis in [-4:4] mm, in their middle planes.

From a more extended study, reported in [134], and from the measurements performed by the

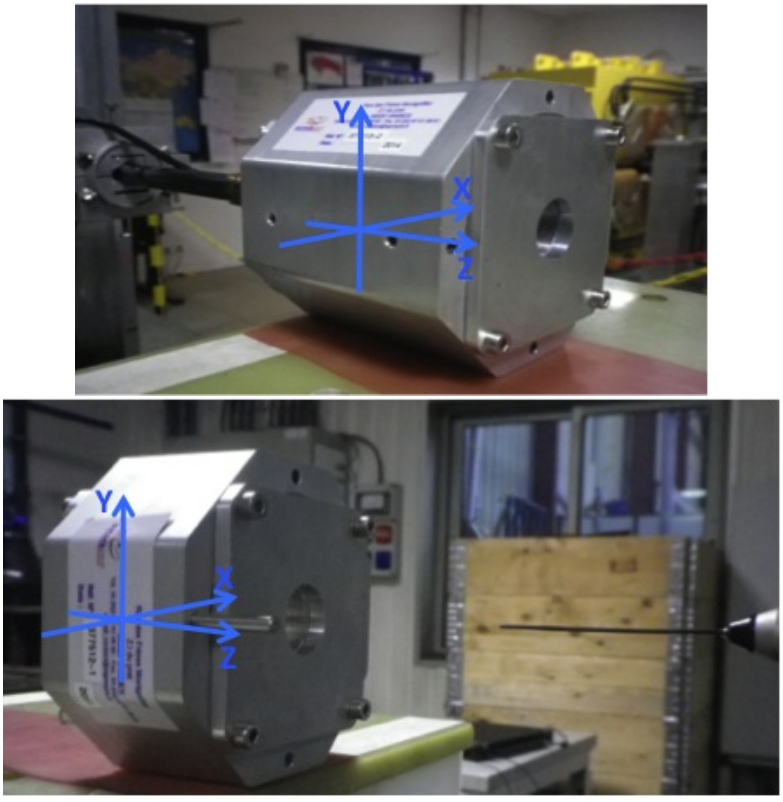

FIGURE 4.6: Long (80 mm) and short (40 mm) quadrupoles.

manufacturer, it was deduced that only for r < 6 mm the variation of the field gradient is less than 2%. Therefore only in the central region of the bore the gradient can be considered uniform.

4.3.1.1 Test with conventional proton beams: experimental vs simulation data

The collection system (PMQs) is able to focus and collect protons up to 30 MeV, although, according to the simulation results, the best performances can be achieved at energies lower than 20 MeV. Recently the PMQs prototype has been preliminary tested with a 10 MeV proton beam, delivered by the TANDEM accelerator at INFN-LNS in Catania. The used setup was made of the collection system with two upstream collimators, used to make the input beam parallel. The collimators were 1 mm in diameter and have been mounted with a relative distance of 700 mm. The second collimator was placed 1465 mm upstream the collection system. The different PMQs have been mounted with a relative distance of 20 cm, alternating the long to the short one (beam view). To

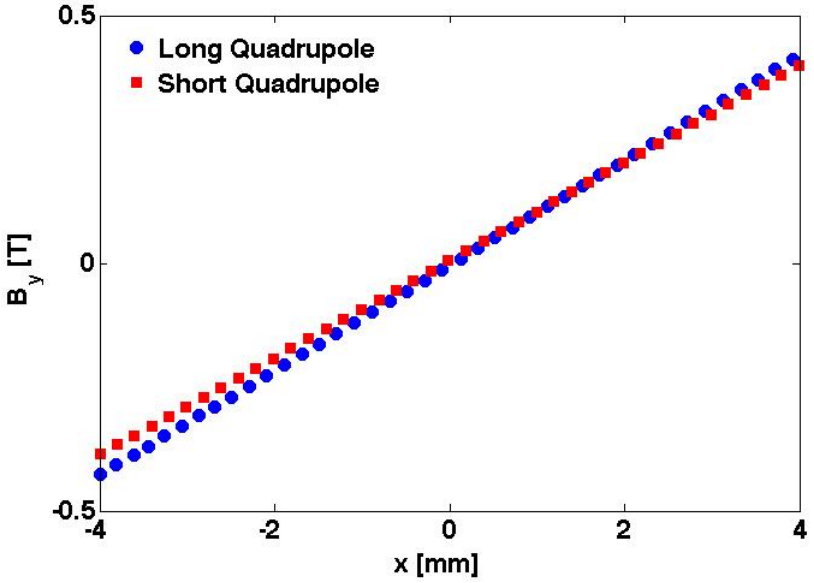

FIGURE 4.7: Measured y magnetic field components along the x axis in the middle planes of the long and short quadrupoles.

characterise and measure the beam shape, Gafchromic films, EBT-3 type, have been placed at the exit plane of each quadrupole.

Figure 4.8 shows the input beam shape, evaluated at the first quadrupole entrance, and the output data obtained at the third quadrupole input plane.

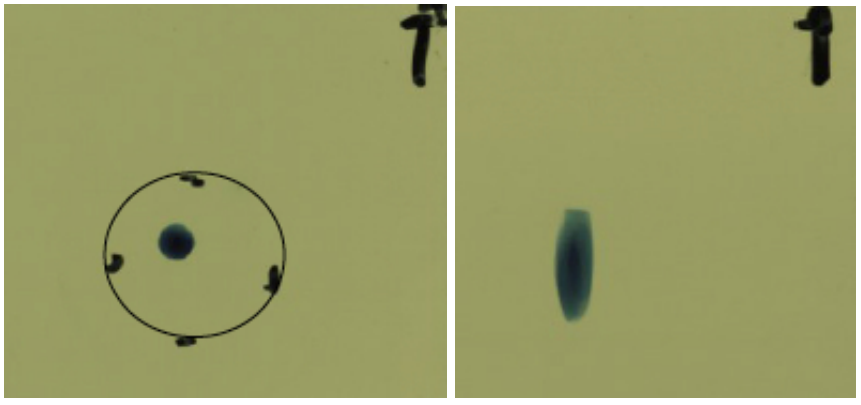

FIGURE 4.8: Measured beam profile at the first (input beam) and third quadrupole entrances.

The input beam has a diameter of about 4.6 mm (FWHM) and its axis is not perfectly aligned to the quadrupoles one. The distance between these two axis is about 2.3 mm along the y direction and 2.4 mm along the z direction.

The output beam has been analysed, as well. It is elliptic shaped, with 4 mm and 13.5 mm as y and z spot dimensions, respectively, evaluated at the 50 % of the maximum intensity value. On the upper part, the beam spot is cut by the quadrupole internal shielding.

The simulation of the experimental setup has been also performed. In figure 4.9 the input and output beam features are reported. From a quantitative analysis of the beam spot dimensions, performed at the 50 % of the maximum intensity value, a quite good agreement is obtained respect

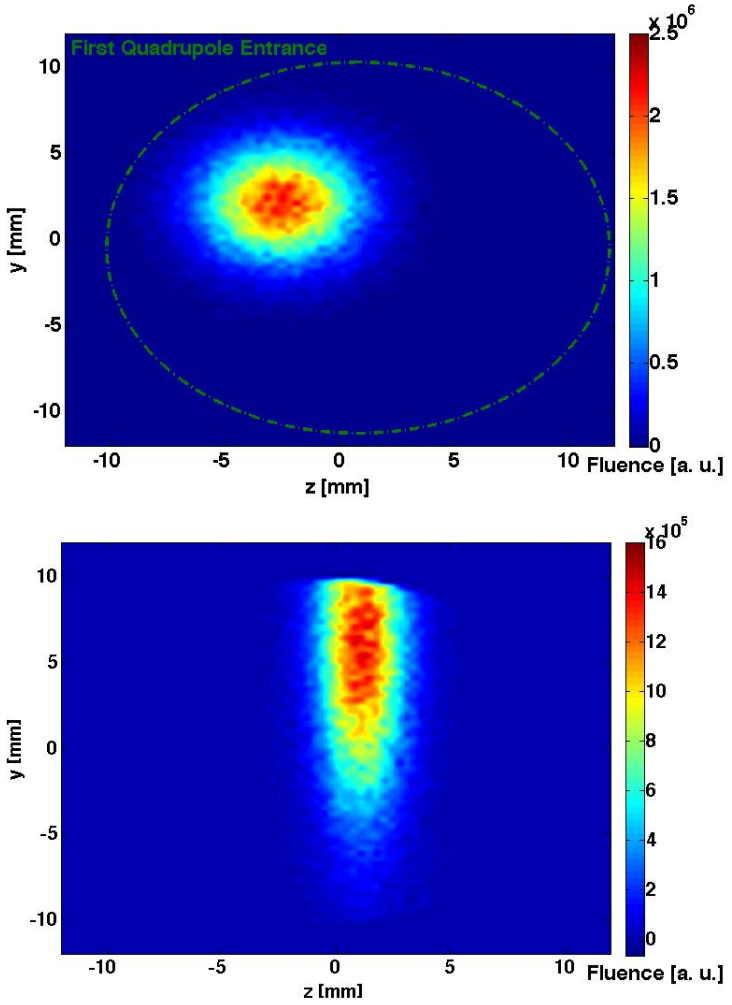

FIGURE 4.9: Simulated beam profile at the first (input beam) and third quadrupole entrances.

to the experimental data. Output beam dimensions of 3.8 mm (y) and 12.7 mm (z) are indeed obtained.

More precise investigations, especially using microbeam or input divergent beams, have to be performed in order to study the quadrupole features, when the beam pass in the field region characterised by a gradient variation higher than 2 %.

4.3.2 The energy selector system

The Energy Selector System (ESS) prototype, as reported in [121, 135–137], consists of a sequence of four dipole magnets with alternating polarity, similar to a bunch compressor [138, 139]. In each dipole, particles are deflected thanks to the magnetic field, i. e. to the Lorentz force. However, the overall effect of the dipole sequence coupled to a central collimator is to select particles in a given energy range.

As shown in figure 4.10, the dipole sequence separates protons of different energies, getting rid of plasma electrons that have reached the ESS.

In particular, the proton beam enters into the first two dipoles and is spectrally dispersed in the

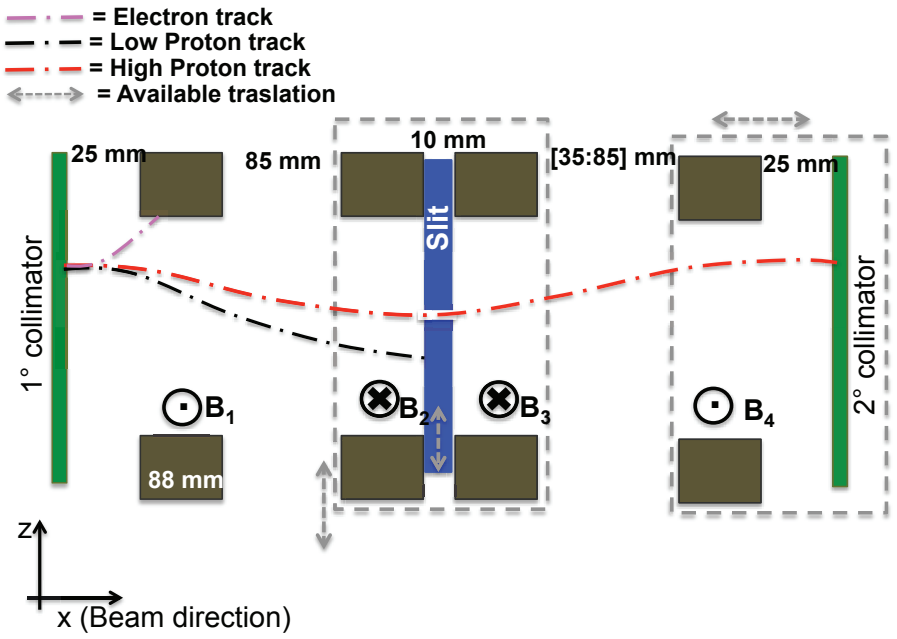

FIGURE 4.10: Schematic diagram of the Energy Selector system. The particles bunch is produced on the left, before the first collimator, and is travel from the left to the right.

radial plane. In this way it is possible to achieve, at the exit of the second dipole, a quite good separation between the particles trajectories as a function of their energies: high energetic particles are less deflected than low energetic ones. A movable central *slit* is used to let particles within a narrow energy range enter the next deflecting sector and to stop all the others. Therefore particles passing through the slit collimator are then refocused by the opposite gradient of the third and fourth dipole magnetic fields.

The already realised ESS prototype, whose CAD draft together with its dedicated vacuum chamber are reported in figure 4.11, is about 600 mm long, considering also the two collimators, placed 25 mm upstream and downstream the first and the fourth dipole, respectively. Their diameters have been properly chosen in order to limit the particles spatial mixing, due to the particle wide angular distribution, typical of a laser-driven proton beam. Particles with different energy may have, indeed, the same radial position on the selection plane (*slit*), as it will be shown in chapter 5.

Each ESS dipole is composed by soft iron yoke and permanent NdFeB magnets that provide a maximum magnetic field of about 0.8 T on a 10 (y) $\times$ 104 (z) mm^2 gap. The experimental magnetic field in the gap central axis is shown in figure 4.12. A detailed magnetic field measurement of each dipole, including the fringing field, has been performed with steps of 2 and 6 mm along y and z directions, respectively. The experimental values were affected by an error of $\pm$ 50 gauss, due to the uncertainty in the probe positioning during the measurement.

Obtained data have been then used to correct the field implemented in the Geant4 simulation. Starting from a field grid obtained with software OPERA, experimental data have been indeed fitted using polynomial functions and obtained scale factors have been then used to rescale the magnetic field grid that was implemented in the Geant4 simulations.

These measurements have been also useful to evaluate the field inhomogeneity between the extreme

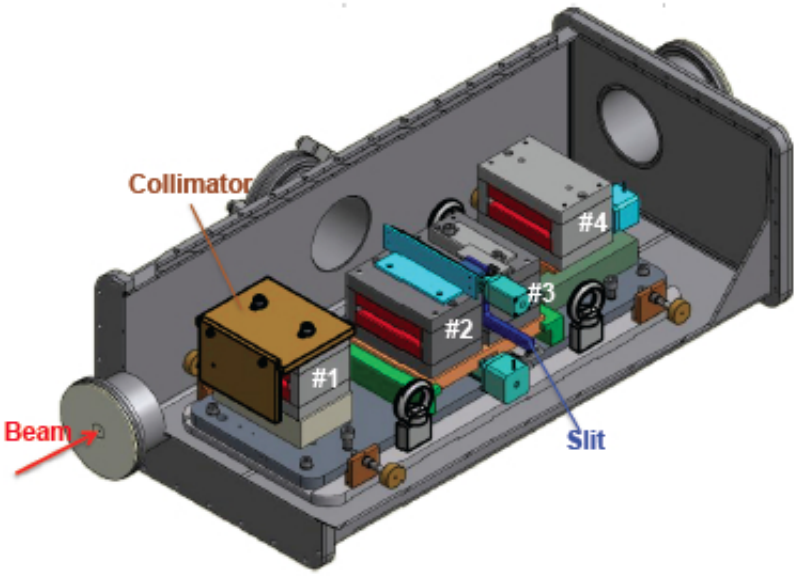

FIGURE 4.11: AutoCad scheme of the Energy Selector system in its dedicated chamber.

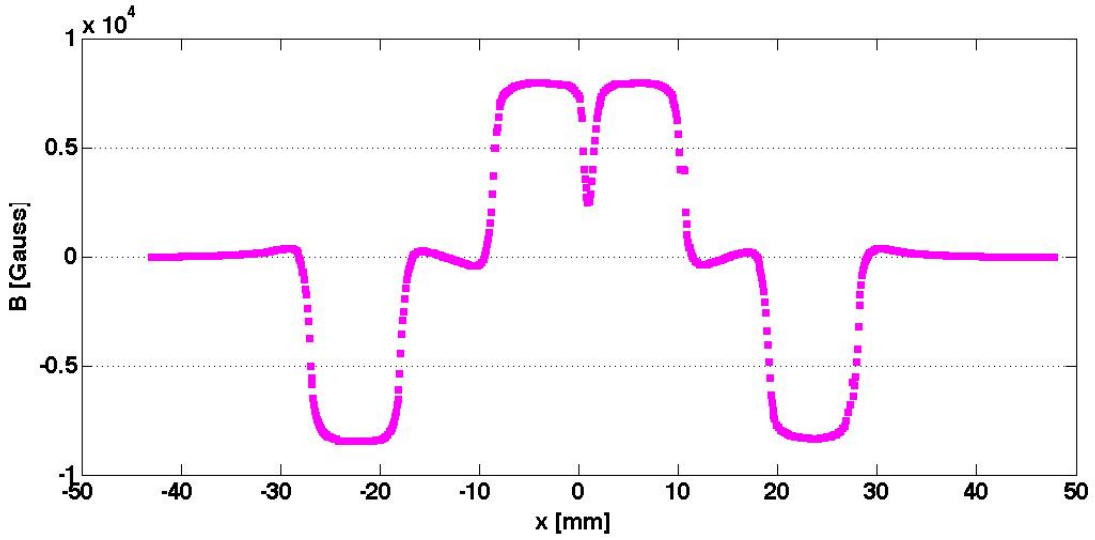

FIGURE 4.12: Magnetic field profile measured along the central axis. An error of ± 50 gauss has to be considered for each point.

parts of each gap (upper vs lower and right vs left). The higher inhomogeneity values is of about 15 %, however, considering the central gap region of 4 (y) × 84 (z) mm^2, the inhomogeneity is less than 5 %.

During the design phase of the ESS, a remote control for the slit movement has been also foreseen, in order to allow the energy variation of the output beam without break the vacuum. The central twin magnets can be also remotely moved, in the transversal direction, of 50 mm by means a roller guide system. In such a way, the device is able to select protons within the energy range of [1:60] MeV and desired particles can pass through the central region of the gap, where the magnetic field is almost uniform.

Finally, the last dipole can shift 50 mm back and forth along the longitudinal direction in order to

compensate the asymmetry of the magnetic field. This movement permits the beam to leave the selector system maintaining the straight direction and minimizing the angular spread as shown in figure 4.13 and as also studied in [122, 140]. All remoted controls have a precision of 100 μm.

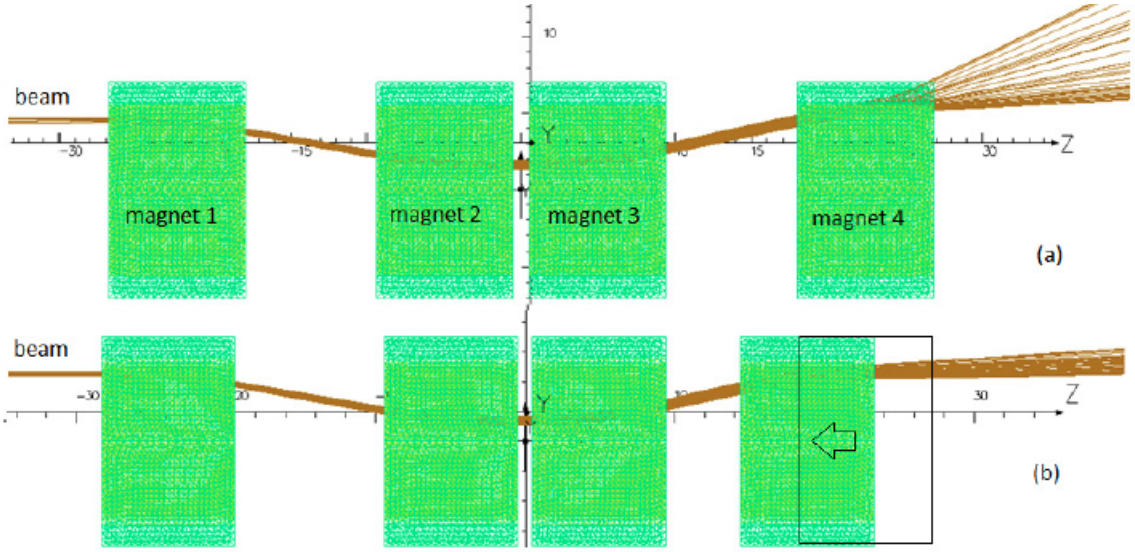

FIGURE 4.13: The figure represents the comparison between two configurations of the magnetic energy selector system. With a symmetric arrangement of the magnets, the monochromatic beam coming from left side leaves the device with a wide angular spread. To minimize such effect, the 4th magnet may be shifted few cm upstream.

Preliminary to any experimental run, a verification of the correct ESS implementation in the Geant4 simulations has been performed. As it has been discussed before, different energy spectrum components can be selected within the [1-60] MeV energy interval by varying the position of the slit aperture. Therefore as first test of the ESS simulation, the energies selected using an analytical calculation have been compared with the results of the MC simulations, performed implementing a point-like source with a uniform spectrum with energies ranging from 1 up to 60 MeV and no angular divergence, as input. Figure 4.14 shows the very good agreement between the obtained energy vs slit positions (z_{slit}) curves.

Deriving these distributions, the ESS energetic resolution curve can be calculated, as shown for the experimental data in section 4.3.2.1.
These preliminary Geant4 simulations have been also useful to study some ESS features. For instance, fixing a specific slit aperture, the relative energy spread of selected particles increases for higher energies, thus affecting the energetic resolution. This is evident in Figure 4.15, where the uniform proton beam [1-60] MeV, with no divergence, has been sent at the entrance of the ESS. The simulations have been carried out for several slit positions; in figure only two cases relative to two selected energies are shown: 4.22 MeV and 45.9 MeV with 4 and 11 % as spread values, respectively.

The energy spread affecting the beam passing through the slit depends also on the slit aperture size. For a given energy, it can be reduced by decreasing the slit aperture size although a smaller

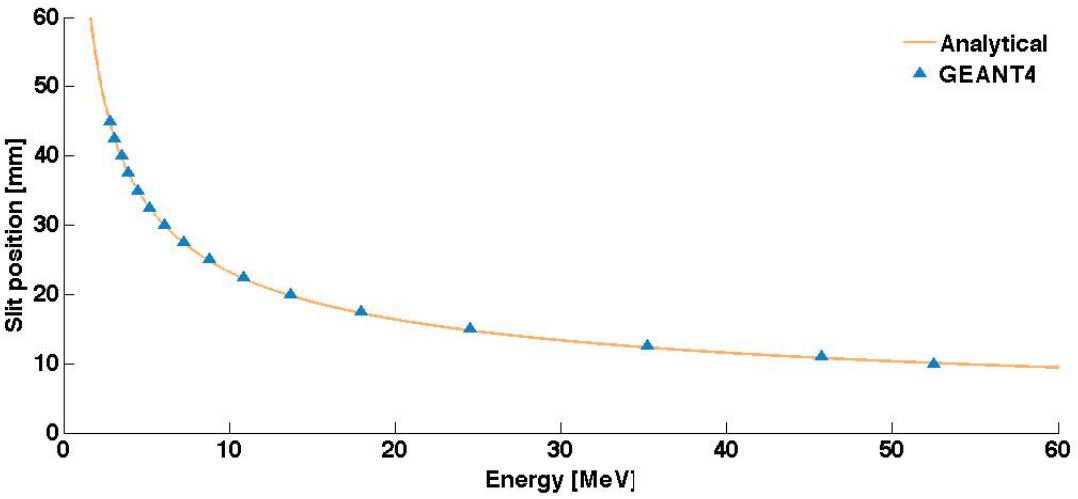

FIGURE 4.14: Comparison between the analytical calculation and the MC simulation on the correspondence between the slit positions and the energies selected.

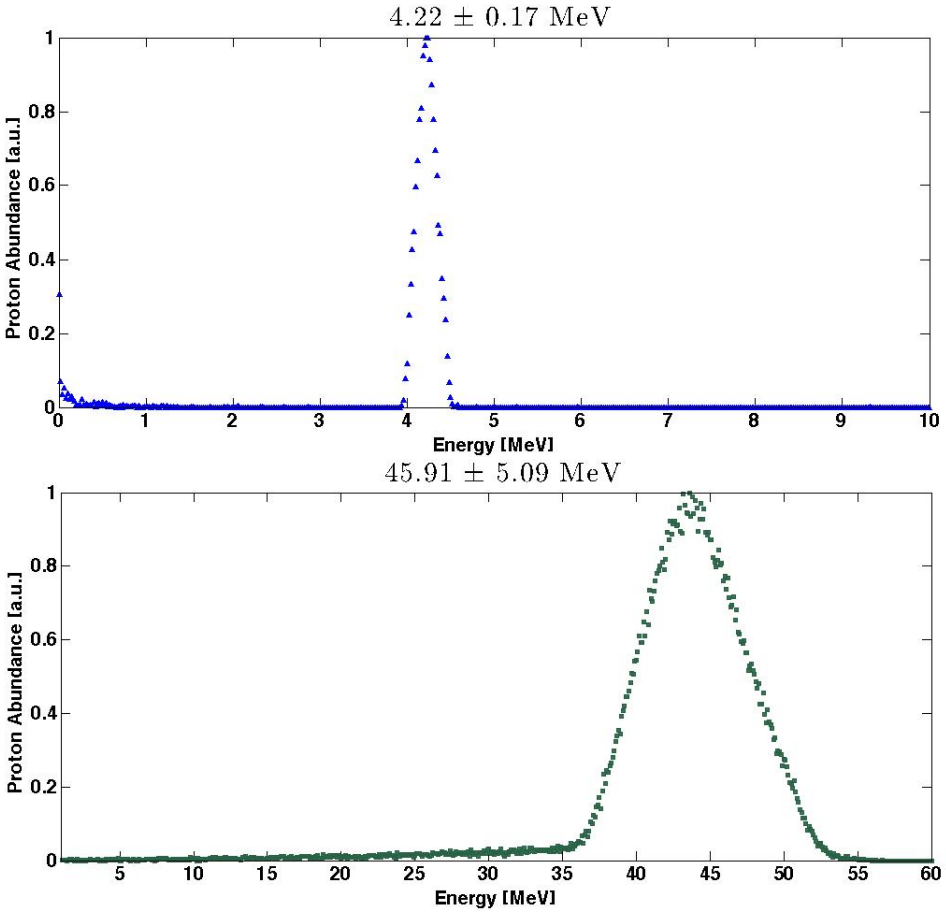

FIGURE 4.15: Proton beams evalauted at the ESS exit point with the 3 mm diameter for the first collimator and 1 mm hole for the slit and the final collimator.

slit aperture decreases the transmission efficiency through the device. A study of the transmission efficiency dependence on the slit aperture sizes has been also carried out.

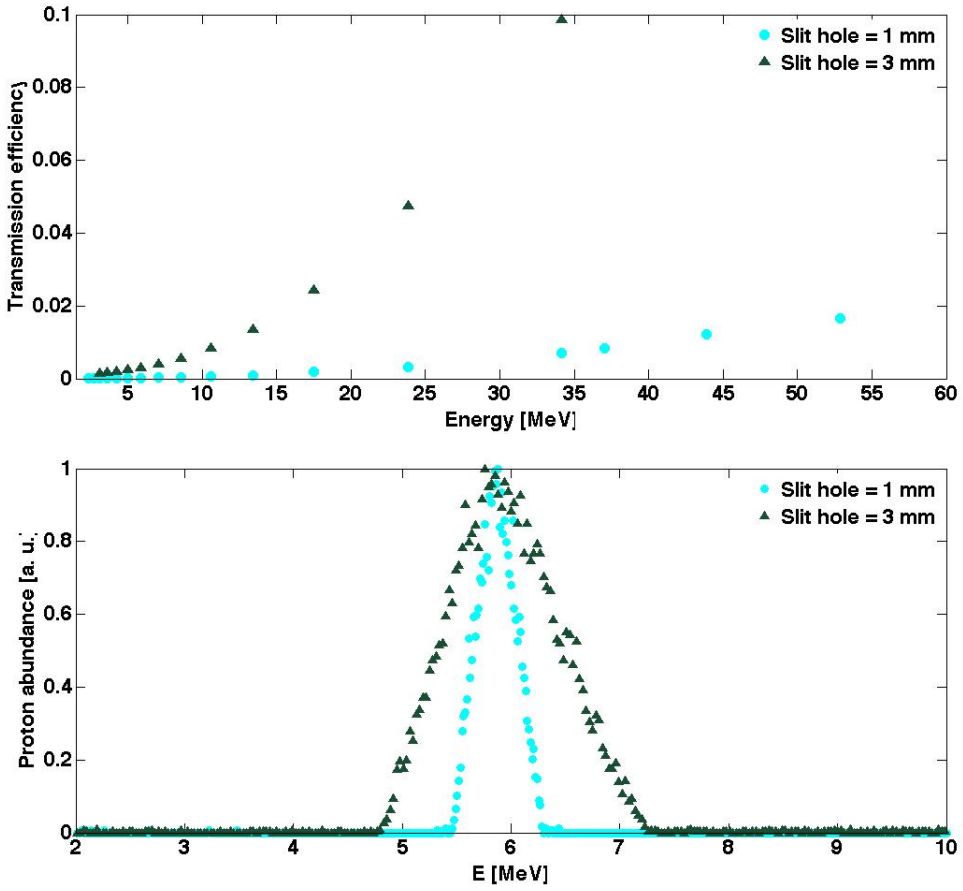

FIGURE 4.16: On the top the ESS transmission efficiency and on the bottom the data comparison between output spectra for 1 mm (5.9 ± 0.2 MeV) and 3 mm (5.9 ± 0.5 MeV) as slit hole aperture.

Figure 4.16 (up) shows the transmission efficiency obtained using two different collimation configurations for the slit, 1 × 1 mm^2 and 3 × 3 mm^2 aperture size, and 3 mm diameter for the first collimator in both cases. The transmission efficiency has been calculated as the ratio between the number of particles recorded after the first collimator and the one recorded at the ESS exit point. As expected, the use of a larger slit aperture allows to increase the transmission efficiency. On the other hand, a larger slit aperture size results in a larger energy spread as it can be observed in figure 4.16 (down) that shows the proton energy spectra obtained by selecting particles within an energy interval around 6 MeV using the two different slit configurations. Spread values of about 3 and 8.5 % are obtained if 1 × 1 mm^2 and 3 × 3 mm^2 hole slit are used, respectively.

Summing up, the slit dimensions have to be properly chosen depending on the desired applications and considering that the energy spread and the transmission efficiency are strictly correlated to them.

The developed code has been also used to choose the proper thickness and material for the slit in order to minimize secondary particles production, crucial for radioprotection assessments and for the design of the shielding elements. Different slit materials have been taken into account and compared in terms of photons and neutrons yields, evaluated after the final collimator as a function of the slit thickness for different materials. According to this study, aluminium and brass represent good choices for secondary neutron emission. Moreover, as expected, the material with higher

atomic number, as tungsten and lead, minimize the yield of photons at the ESS exit point.
In conclusion, this preliminary set of MC simulations has shown that the ESS prototype is able to select proton beams with energies ranging from few MeV up to about 60 MeV with an energy spread ranging from few per cent up to tens of percent. Moreover, according to transmission efficiency and energy spreads required, the collimation system has to be conveniently varied.

4.3.2.1 Test with conventional proton beams: experimental vs simulation data

The ESS prototype has been successfully tested and calibrated using conventional pure mono-energetic proton beams at the Laboratori Nazionali di Legnaro (LNL) in Padova and at the LNS in Catania.
At LNL the beam optics has been investigated using a 5 MeV proton beam with no divergence, as input, and GafChromic films, type EBT-3, as detectors (see appendix A). In detail, for this measurement, no slit and no final collimator have been mounted, the first collimator was 3 mm in diameter and the relative distance between the third and fourth dipole was 67 mm (typical distance is 85 mm). The beam input axis was fixed 42 mm on the left (beam view) from the central dipole axis. Figure 4.17 shows the obtained gafs irradiated during the experimental session for 10 seconds, considering that the input proton beam current was 16 nA. They have been placed at the exit of each dipole.

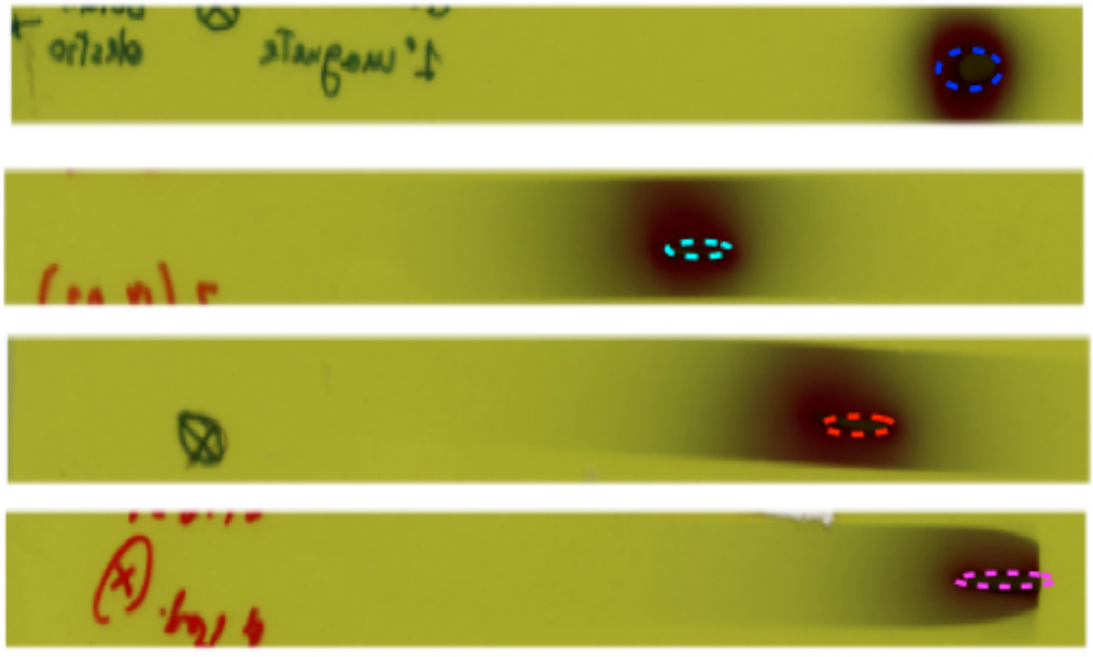

FIGURE 4.17: Beam optics inside the energy selector for a 5 MeV proton beam. Data are related to the exit point of each dipole.

The simulation of this experimental setup has been also performed, implementing a third-fourth dipole relative distance of about 60 mm. The beam spots, evaluated at the exit plane of each dipole, are shown in figure 4.18.

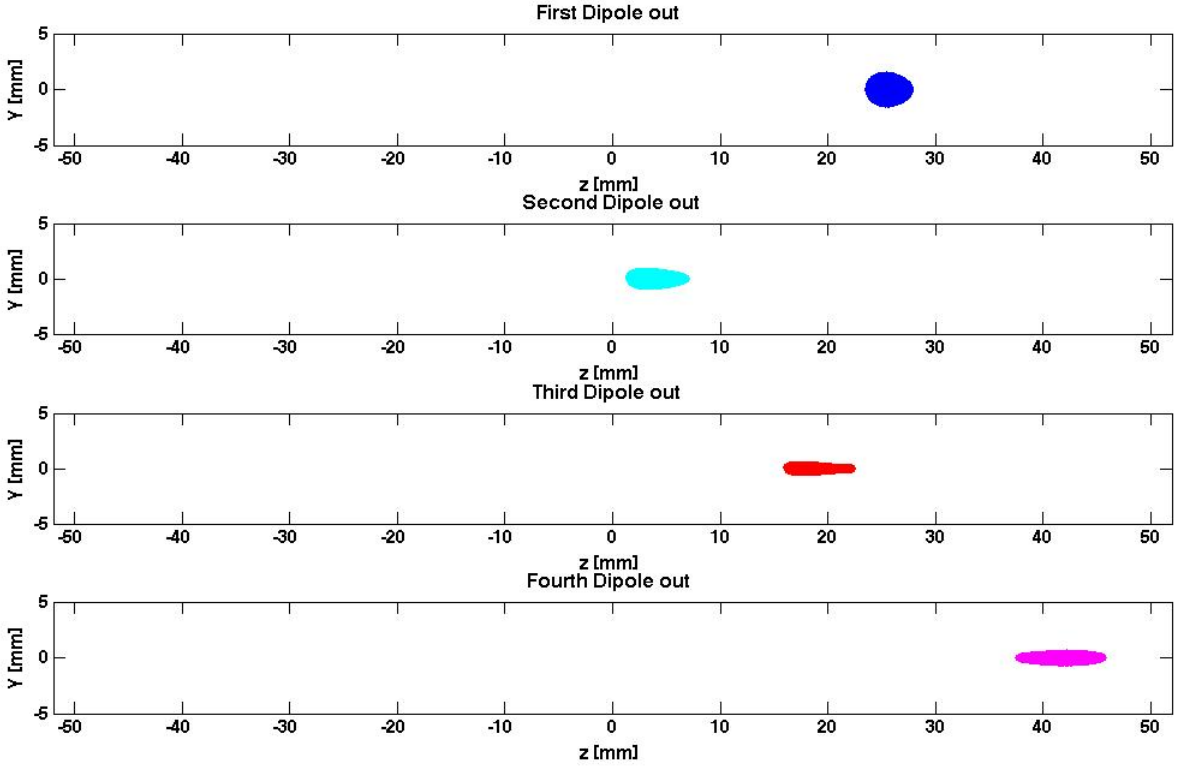

FIGURE 4.18: Simulated beam optics inside the energy selector for a 5 MeV proton beam with no input divergence. Data are related to the exit point of each dipole.

TABLE 4.1: Beam spot dimensions (D_y and D_z) and distance d of the beam spot centre from the input axis: experimental and simulated data.

Position	Simulation output	Experimental data
1° dipole exit	D_y= 2.5 mm, D_z= 3.8 mm, d= 16.3 mm	D_y= 2.3 mm, D_z= 3.8 mm, d=16.0 mm
2° dipole exit	D_y= 1.3 mm, D_z= 5.3 mm, d= 37.8 mm	D_y= 1.4 mm, D_z= 5.4 mm, d=37.5 mm
3° dipole exit	D_y= 0.5 mm, D_z= 6.0 mm, d= 22.7 mm	D_y= 1.0 mm, D_z= 7.4 mm, d= 22.3 mm
4° dipole exit	D_y= 0.7 mm, D_z= 7.8 mm, d= 0.3 mm	D_y= 2.3 mm, D_z= 8.8 mm, d=-3.8 mm

From a qualitative point of view, there is a quite good agreement between experimental and simulated data. A more quantitative analysis has been also performed, as reported in table 4.1. The experimental spot dimensions (vertical D_y and horizontal D_z) have been referred to the signal saturated part and the distance d to the gap between the input beam axis and the centre of the signal saturated part. Similarly for the simulated output, the spot dimensions and the distance d have been evaluated, but referring to the 50 % of the beam spot.

The experimental and simulated beam features are quite similar. The main differences are related to the fourth spot, because of the different third-fourth dipole relative distance. Its optimal value, that is the simulated one, allows, indeed, to have an output beam leaving the selector system maintaining the straight direction (input beam axis).
Also the vertical (y) beam spot dimensions have a quite significant difference, probably due to a small degree of divergence in the input experimental beam. For a non divergent beam, a focusing

effect of the dipoles magnetic field on the beam is indeed expected [141].
An MC study has been performed using, as input, also 3.5, 4 and 4.5 MeV protons, with no divergence, to understand the effect of the y magnetic field component on the beam features.

During the second test performed at LNS in Catania, an accurate knowledge of the slit position corresponding to a given energy has been obtained. The calibration was performed using proton beams in the energy range between 4.5 and 12 MeV, delivered by the TANDEM accelerator. They were collimated by a 4 $\times$ 4 mm^2 slit, placed 154 cm upstream the prototype. The used ESS collimation system consists of a 2 mm thick, Al initial collimator with a 3 mm diameter hole, placed 42 mm on the left (beam view) from the central dipole axis, and an 8 mm thick, Al slit with a 1 mm $\times$ 10 mm (WH) aperture, placed between the second and the third dipole. No final collimator has been used. The selected proton beam has been detected using a 500 μm Si surface barrier detector, placed 40 mm downstream the fourth dipole along the initial beam direction and properly collimated. The measurement of the proper third-fourth dipole relative distances and of the slit positions for each energy represents another important goal of this experimental test.
As already reported, the proper relative distance between the third and the fourth dipole (D_{T-F}) allow to compensate the field asymmetry and to correct any possible misalignment of the beam direction with respect to the incoming one. In particular, the D_{T-F} for each energy has been measured acquiring the detector counting rate for different fourth dipole positions and with a stable input beam current, using no slit.

Once the D_{T-F} has been measured for the energies of interest, the selection slit has been placed back in its position and the detector counts have been registered varying the slit positions with a 0.5 mm step. A roller guide allows, indeed, the radial displacement of the central slit with a precision of 100 μm.
Registered data have been, then, fitted using a Gaussian function. The results for the 4.5 MeV case are shown in figure 4.19. Fit parameters for each data set, i.e. the centroid and the sigma values for each energy, have been finally assumed as *the slit positions* with the corresponding uncertainties. The results are listed in table 4.2 together with the corresponding Geant4 simulation predictions.

The whole experimental setup used in the calibration has been simulated with the Geant4 toolkit. A Gaussian spatial distribution with a 4 mm FWHM at 154 cm upstream the ESS and no divergence has been implemented as simulation input for each energy of interest. Moving the slit aperture on the radial plane, '*the slit position*' corresponding to a given energy has been determined maximizing the number of particles at the third dipole entrance. The uncertainty on '*the slit position*' has been evaluated considering the experimental error of $\pm$ 50 gauss in the magnetic field measurement. Several simulations have been also performed considering a beam divergence of $\pm 0.065°$, which corresponds to the maximum divergence value permitted from the beamline constraints (4 $\times$ 4 mm^2 slit @154 cm upstream the first ESS collimator). According to the simulation results, *the slit position* variation due to such divergence is negligible.
The obtained values are listed in table 4.2.

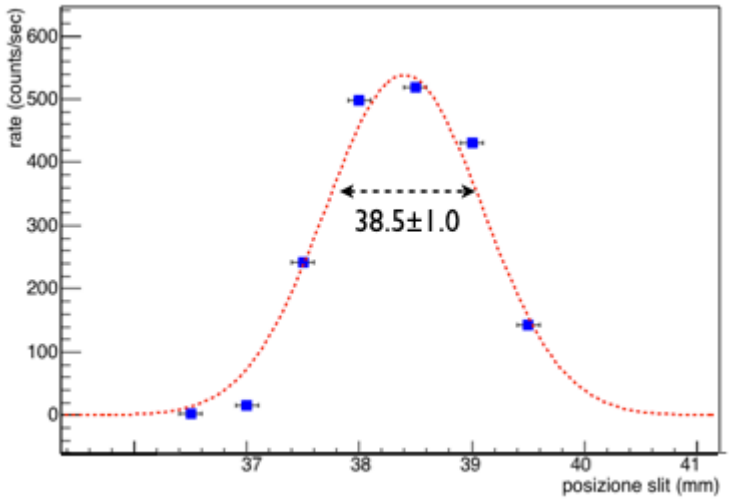

FIGURE 4.19: Detector counts versus slit position, with 0 as the input beam axis. The data set is referred to a 4.5 MeV proton beam delivered by the TANDEM with a fixed beam rate.

TABLE 4.2: Simulated and experimental slit positions corresponding to 4.5, 5.0, 6.0, 10.0 and 12.0 MeV energy.

Energy [MeV]	Experimental Slit Position [mm]	Geant4 Slit Position [mm]
4.5	38.5 ± 1.0	39.0 ± 1.0
5.0	37.0 ± 1.5	37.0 ± 0.9
6.0	34.0 ± 1.5	34.0 ± 0.8
10.0	26.3± 1.0	26.0 ± 0.6
12.0	24.5 ± 1.5	23.5 ± 0.6

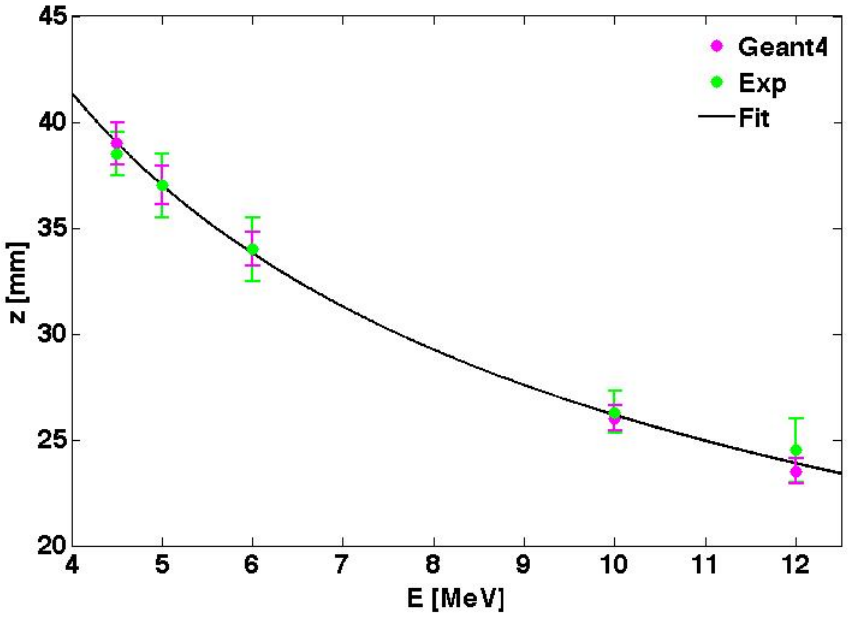

FIGURE 4.20: Protons energy versus slit position, with 0 as the input beam axis. Magenta and green dots are referred to the simulation and the experimental data, respectively, black line to the fit curve.

Figure 4.20 shows the comparison between the measured slit positions as a function of the protons energy and the Geant4 results. As one can see, a rather good agreement between experimental and simulated data is observed.

The found out slit position (z) *versus* energy (E) curve can be approximated using a function like $y[mm] = C/\sqrt{E[MeV]}$. Considering no fringing fields and a setup cointaining only the first and the second ESS dipoles, the following relation can be indeed derived for a particle of charge ze, mass m and kinetic energy E_{kin}:

$$y = \frac{(zeB_2L_2^2)/2 + zeB_1L_1L_2 + zeB_1L_1(D + L_1/2)}{\sqrt{2mE_{kin}}} \tag{4.6}$$

where B_i and L_i are the magnetic field value and the length of the i-dipole (i=1, 2), respectively, and D the length of the drift sector between the two dipoles.

Fitting the experimental data, $C = 82.7$ is obtained. Deriving the 4.6 function, the ESS energy resolution can be calculated. In figure 4.21 there are reported the resolution curves for a slit radial dimention of 1 mm and 3 mm.

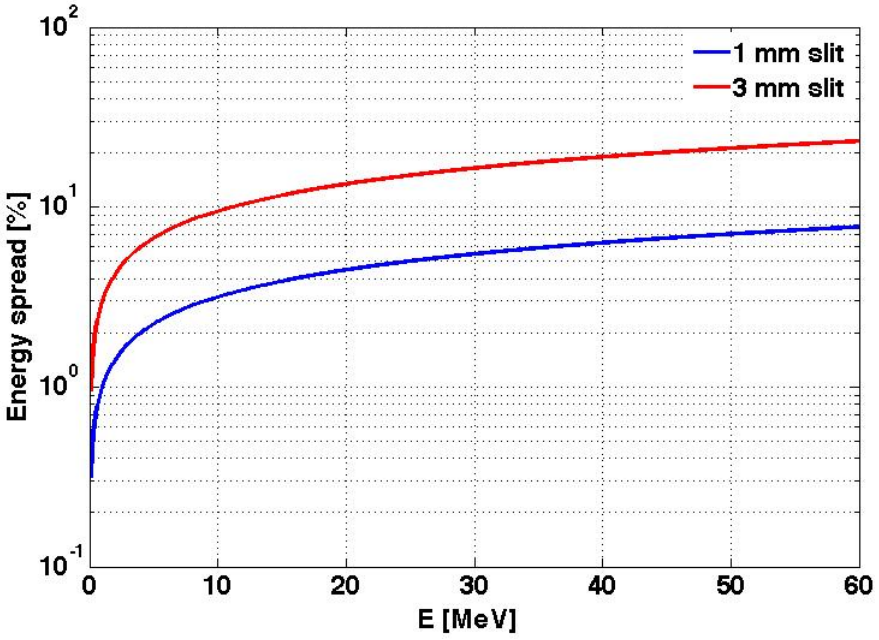

FIGURE 4.21: ESS energetic resolution: energy spread as a function of the selected energy for a slit radial dimension of 1 mm and 3 mm.

As shown, fixing the slit radial dimension, the energy spread increases with the selected energy and, for a given energy, with the slit radial aperture. In particular, if the selected proton energy goes from 4 to 60 MeV, the energy spread ranges from 2 to 8 % for the 1 mm slit option and from 6 to 23 % for the 3 mm one.

Chapter 5

Test of the energy selector system with laser-driven beams

As already pointed out in this thesis, optically accelerated particle beams are characterised by some extreme features, therefore, they have to be specifically handled to be used for multidisciplinary applications. Indeed, ion beams accelerated in the TNSA regime are characterised by a broad energy spectrum, ranging from few keV up to a maximum cutoff value depending on the laser intensity and on the target shape/material [142, 143].
In order to investigate the feasibility of using optically accelerated ion beams for multidisciplinary application, a lot of efforts have been therefore recently devoted to develop new strategies and advanced techniques for the beam transport. In this context, the ESS and PMQs prototypes, described in chapter 4, were realised. After their preliminary characterisation with conventionally accelerated beams (chapter 4), the main task was to test them with laser-driven protons, in order to verify their performances.
An experimental shift dedicated to the ESS prototype has been carried out at the Center for Plasma Physics of the Queen's University in Belfast (UK), where there is the TARANIS (Terawatt Apparatus for Relativistic And Nonlinear Interdisciplinary Sciences) laser system.
The proton source was produced within the TNSA regime by irradiating 10 μm thick Au foil targets with a high-power, short-pulse laser. Using the beam accelerated from the non-irradiated target surface, as input, and knowing the calibration curve, protons of 4.5 and 7 MeV have been selected and studied in terms of energy spread and fluence. Several simulations have been also performed and obtained outputs compared with the experimental data.

In this chapter the experiment is carefully described together with the simulation study.

5.1 Laser system

The experimental run was performed at the Queen's University of Belfast (UK), where the TARANIS laser system is installed since 2006. It is a hybrid Ti:Sapphire-Nd:glass system operating in

the chirped pulse amplification mode. It can simultaneously deliver two 1053 nm beams for each of the two existing target areas, in different combinations of ∼700 fs/1 ns pulse and with intensities up to about 10^{19} W/cm^2 in the short pulse mode and up to 30 J on target with the ns laser beam [146].
The detailed optical layout of the laser is shown in Figure 5.1. There is a Ti:Sapphire oscillator, followed by a folded all-reflective stretcher and by a Ti:Sapphire regenerative amplifier.
The oscillator provides a train of Fourier transform-limited 120 fs long pulses at a wavelength of 1053 nm, with repetition frequency of 76 MHz. The wavelength is chosen to match the peak of the Nd-Glass amplifiers gain curve in the glass amplification chain, and, although the gain of the Ti:Sapphire crystal is not peaked at 1053 nm, the oscillator delivers an average power of 400 mW. Pulse stretching, up to a factor of 10^4, is then achieved in the double-pass stretcher, equipped with a 1740 lines/mm diffraction grating and a f = 1524 mm spherical mirror, arranged in an inverting telescope configuration.
A three stage Nd:Glass amplification chain optically pumped with flash lamps, finally provides the amplification to multi-TW levels. The first two stages consist of phosphate glass rods of increasing diameter of 9 mm and 25 mm, respectively. The third stage is made of two parallel couples of rods (50 mm in diameter) to amplify two separate pulses up to peak energies of about 30 J per pulse at a repetition rate of 1 shot every ten minutes in the full power mode.
When a programmable acousto-optic modulator is additionally employed, a minimum pulse duration of 560 fs can be achieved, (700 fs is the typical average) with an energy transmission through the compressors of about 60%.

During the run, the laser pulse has been focused using an f/3, f = 300 mm off-axis parabola, that has been protected from the debris, produced during the laser-target interaction, using a SiO_2 sheet. The pulse energy was monitored on each shot, by means of several diagnostics detectors, placed at different locations along the laser chain. On average the laser pulse features were 7 J and 700 fs, with a focal spot of about 6 μm, as FWHM, for a corresponding laser intensity value of about 2×10^{19} W/cm^2.

5.2 Experimental setup and used detectors

Considering the geometrical constrains of the different mirrors and of the laser diagnostics detectors placed inside the target chamber, the ESS prototype has been placed 8.2 cm downstream the target position. In order to reduce the beam angular divergence entering the ESS and to control the ingoing and outgoing beam spot size, both collimators have been mounted. They were made of 2 mm thick Al plate (able to stop up to 20 MeV protons) with a circular 3 mm diameter aperture. As done during the calibration section, the centre of the collimators apertures was positioned 42 mm far from the central dipole axis.
The movable slit, placed between the second and the third dipole, it was made of an 8 mm thick Al plate characterised by a 3 mm × 6 mm (HW) aperture, chosen in order to have a good compromise between the achievable transmission efficiency and the spatial mixing effect, due the input beam

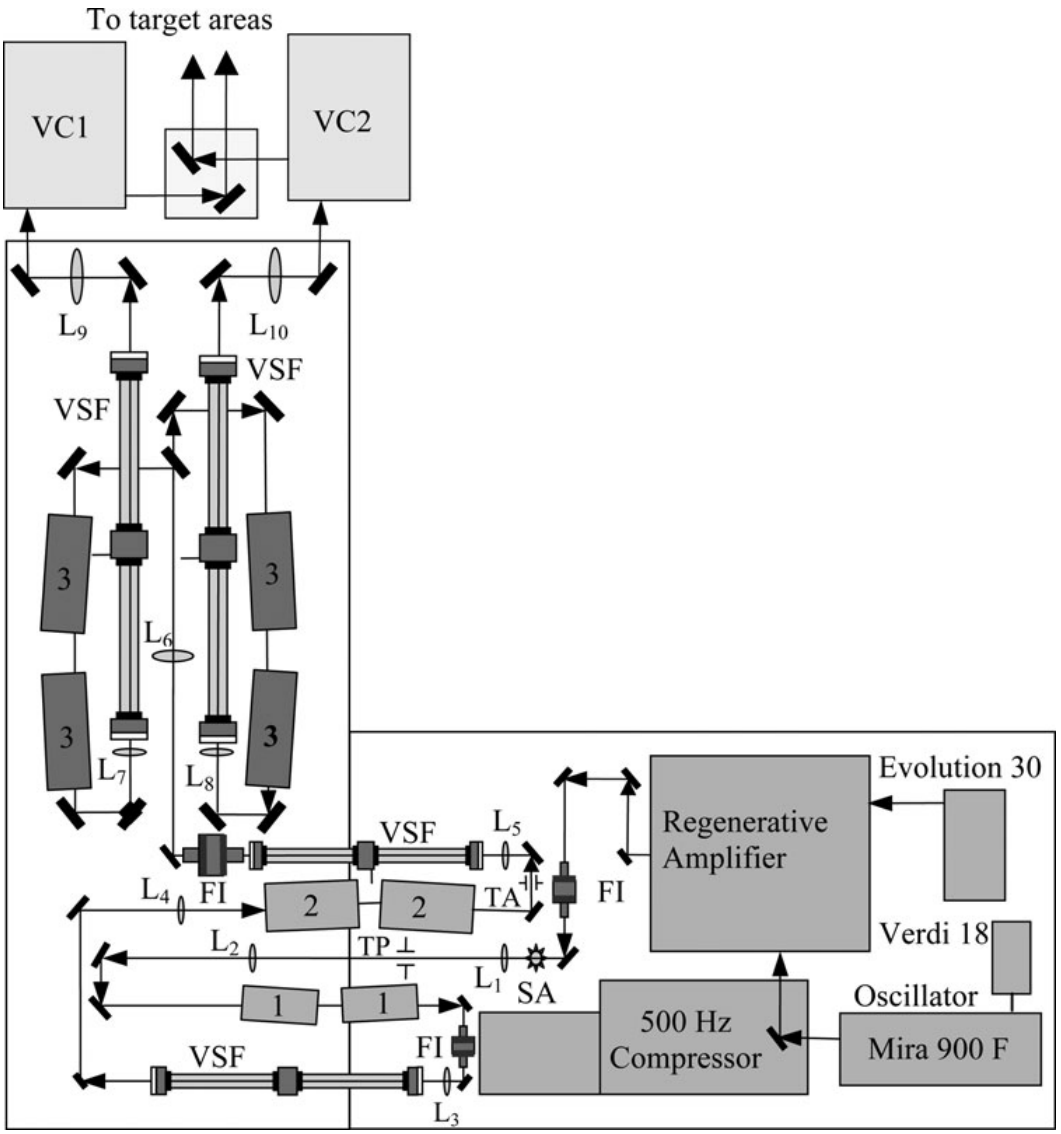

FIGURE 5.1: Optical layout of TARANIS laser. FI - Faraday isolator; VSF - vacuum spatial filter; TA - Teflon aperture; TP - Teflon pinhole; SA - serrated aperture; 1, 2, 3 - laser heads with Nd:Glass rods of 9 mm, 25 mm, and 50 mm diameter, respectively; L1L2, L3L4, L5L6, L7L9, L8L10 - relay imaging telescopes, VC1, VC2 - vacuum compressors.

divergence.

A schematic layout of the experimental setup is shown in figure 5.2.

As first step of the experimental run, beam fluence and divergence measurements were performed by means of Imaging Plates (IP) and CR-39 detectors, mounted on the rear side of the final collimator and at different distances d downstream it (d = 16.0, 22.0, 30.0 and 42.0 cm).

Regarding the measurement of the output energy spread, a 0.92 T, 10 cm long magnet (*spectrometer*) with a 500 μm slit aperture was placed 30 cm downstream the final collimator. As shown in figure 5.3, the output beam, dispersed by the spectrometer, has been then detected using an IP, placed 16.5 cm downstream this fifth dipole.

In other words, protons selected by the 500 μm slit were deflected from the magnetic field according to their energies. Therefore measuring the deflections along the radial plane, from the IP signals,

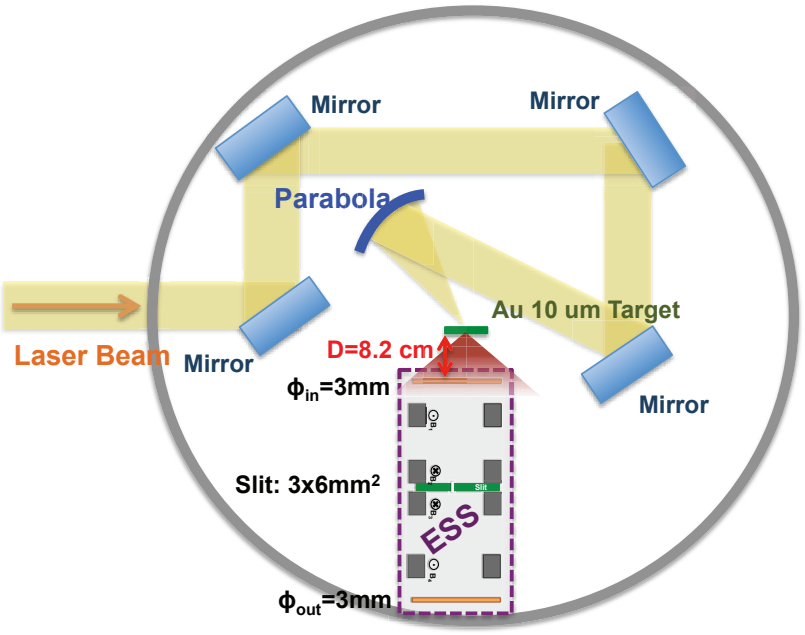

FIGURE 5.2: Schematic not-scale layout of the experimental setup at one of the TARANIS target area.

and knowing the magnetic field intensity, it was possible to reconstruct the energy interval of the beam coming out from the ESS.

During the experimental run, the following detectors were used: CR-39, Gaf-chromic films (HD-810) and IPs, of the type BAS-TR 2025 from Fuji Photo Film Co. Ltd, together with a scanner FUJI FILM FLA-7000, as IP reader. Since the signal obtained from the IPs decreases with time, they were always scanned right after the exposure to the proton source. Moreover, for the measurements, Gaf-chromic films and IPs were wrapped in the 12 μm thin Al foil, as a filter to shield detectors from soft X-rays, heavy ions and target debris, allowing a minimum detectable proton energy of about 1 MeV.
In order to analyse the tracks created inside the CR39s by the protons, a 30 min etching procedure has been performed with a NaOH solution at 80°C. An optical inverted microscope has been then used to analyse the particle tracks.

5.3 Input beam features

A complete study of laser-driven proton beams, accelerated using the TARANIS laser system, has been performed by Dzelanis et al. in [146]. Figure 5.4 reports the energetic spectra extracted from the RCF data, for different Al target thicknesses. Typically, the proton spectrum resembles a truncated Boltzmann-like distribution, with a temperature of 2.3 $\pm$ 0.1 MeV, however the highest maximum proton energy and conversion efficiency of the laser energy are obtained for the 10 μm thick targets.

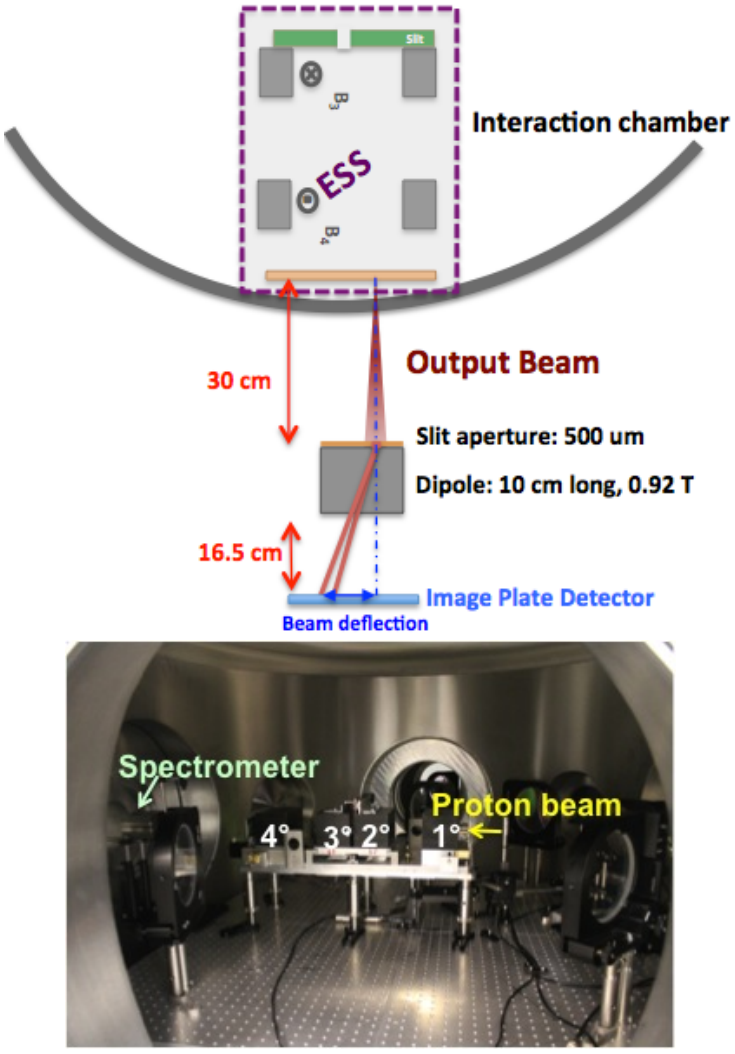

FIGURE 5.3: On the top a schematic not-scale layout of the experimental setup dedicated to the energy spread measurement. On the bottom a picture of the experimental setup.

During the experimental run, the used targets were gold, 10 μm thick. This choice was the consequence of a preparatory phase, when several kinds of targets have been irradiated and compared in terms of output beam features, i. e. energetic and angular distributions as well as beam uniformity and abundance.

For the measurement of these input beam characteristics, RCFs have been used, thanks to their relatively small energy dependence, high spatial resolution and dose rate independence [147]. In particular, stacks of 10 layers (3 cm $\times$ 3 cm), wrapped in a 12 μm Al foil, have been placed 2.7 cm downstream the target holder. Due to the high beam intensity, the HD-810 RCF type has been chosen thanks to its wide operational dose range, from 10 Gy up to 400 Gy.

Figure 5.5 shows, a RCF stack composed of 7 layers obtained using the Au, 10 μm thick target.

The corresponding energetic spectrum is shown in figure 5.6. It was extracted from the RCF stack reported in figure 5.5 applying the spectroscopic method [148, 149] developed and tested also at INFN-LNS [150] (see appendix A). Data related to the first layer has not been considered since it is significantly affected by photon, electron and other ion contributions.

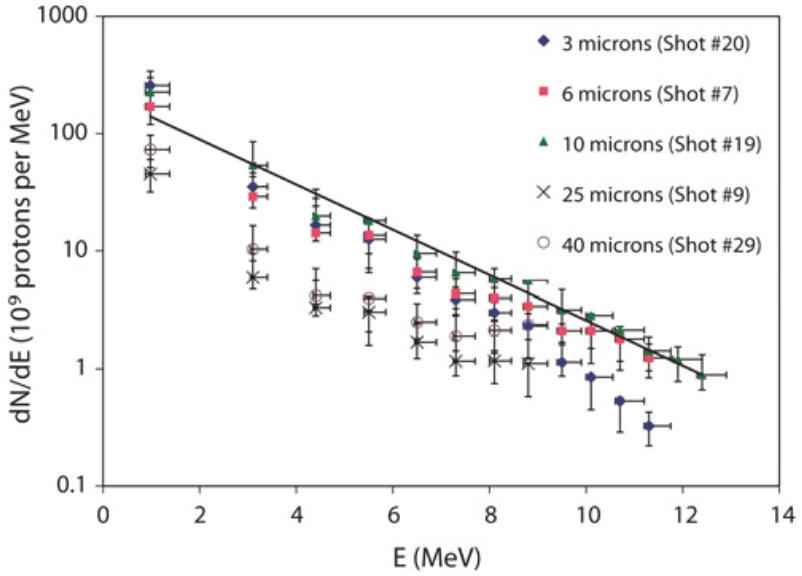

FIGURE 5.4: Typical proton spectra obtained for different target thicknesses.

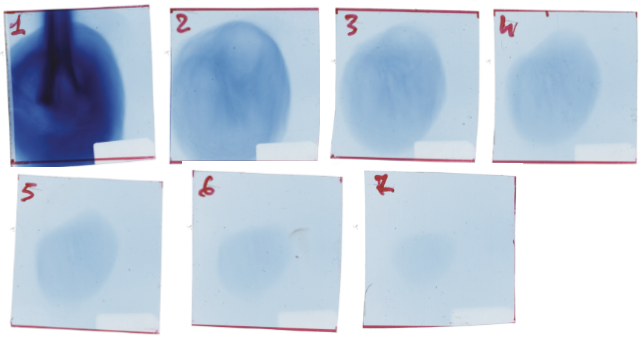

FIGURE 5.5: Protons signal on a stack of 7 films (HD-810 model), wrapped in a 12 μm Al foil and placed @ 2.7 cm from the 10μm thick Au target.

As shown in figure 5.6, the energy cut-off value is about 8.0 MeV, moreover the total number of particles with E>3 MeV is about 2×10^{10} ppb.

Measured data have been also fitted using an exponential function $dN/dE = Ae^{bE}$, typical for a particles beam produced in the TNSA regime. The obtained value for b is -0.5 and it is in a good agreement with the value found by Dzelzainis et al. in [146] ($b = -0.44$).

RCF stack of figure 5.5 has been also used to extract the angular distribution of the input beam. For each layer, the distance from the target, the beam spot size and the proton energy at the given layer, i. e. the Bragg peak at the corresponding depth, have been considered. For example protons of about 3.1 and 7.3 MeV, that have a projected range corresponding to the second and the sixth RCF active layer, have a spot radius of about 12.8 and 5.6 mm (average value between the two semi axis of the ellipse shaped beam spot). These values, considering the distance target-films, are equivalent to a maximum emission angle of $\pm$ 25.3° and $\pm$ 11.7°, respectively.

Such evaluations have been performed for each film and results are listed in table 5.1.

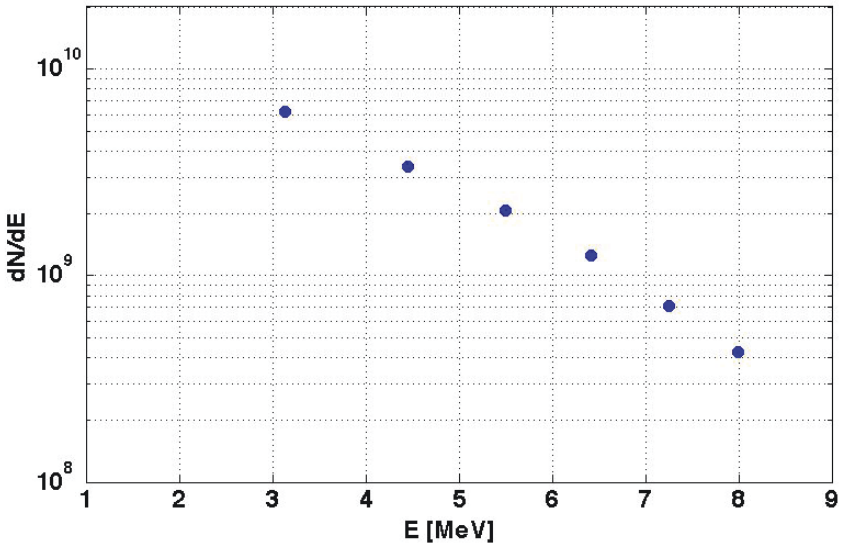

FIGURE 5.6: The input energy spectrum obtained using the spectroscopic method on the films stack of fig. 5.5.

TABLE 5.1: Angular distribution for the proton beam generated in the laser-target interaction.

Energy [MeV]	1.1	3.1	4.5	5.5	6.4	7.3	8.0
Theta [deg]	28.1	25.3	21.7	17.9	14.2	11.7	7.2

5.3.1 Simulated input

The proton beam characteristics measured using the RCF stack of figure 5.5 have been implemented, as input parameters, in the Geant4 simulation. A circular spot with a radius of 6 μm has been used to describe the source spatial distribution. This is the value of the measured laser spot size on the target surface, also reported in section 5.1.
The proton beam energy distribution has been simulated in the energy range [1-8.2] MeV, using the exponential function $dN/dE = e^{-0.5E}$, as shown in figure 5.7. Protons with energies lower than 1 MeV have not been considered in the simulation since they are deflected back by the ESS magnetic field.

As one can see from the experimental data extracted from the RCF and listed in table 5.1, the angular distribution is strongly dependent from the proton energy, therefore it has to be taken into consideration in the simulations. It was, indeed, implemented using the step function, shown in figure 5.8.

In order to verify the simulation input parameters, a stack of 7 HD-810 type RCF films, wrapped in 12 μm Al foil and placed at 2.7 cm from the source point was simulated. The beam spot area and the dose values, extracted from each simulated layer of the stack, have been then compared with the experimental data, showing a quite good agreement with an error less than 10 %, mainly due to the homogeneity level of the experimental input beam.

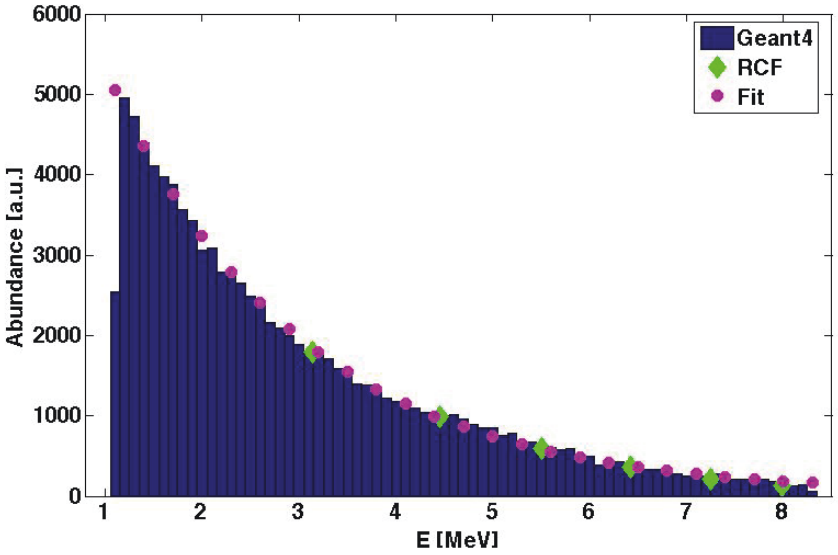

FIGURE 5.7: The energy spectrum implemented as input in the Geant4 simulations, together with the exponential fit (magenta dots) and the RCF data (green diamonds).

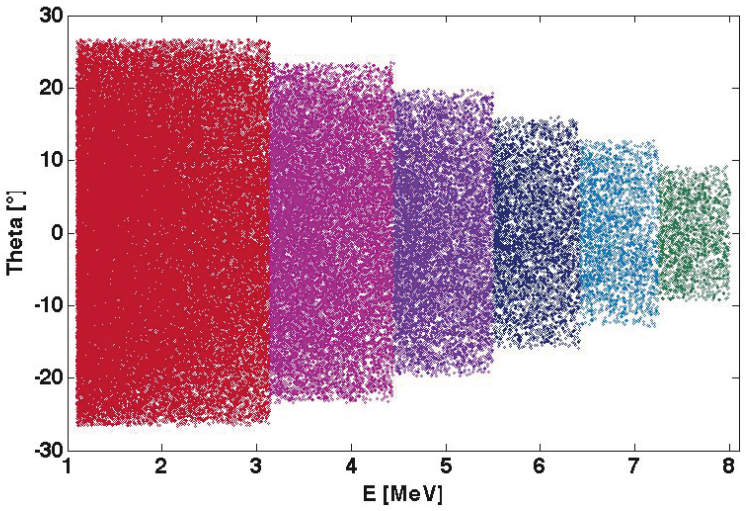

FIGURE 5.8: The angular-energy dependent distribution implemented as input in the Geant4 simulations.

5.4 Output

The main goal of the presented experiment was to characterise the proton beam selected by the ESS prototype in terms of fluence, divergence and energy spread.

Preliminary to these measurements, CR-39s and IPs have been used to qualitative study the beam shape on the slit plane, due to the dispersion effect of the first two dipoles. Figure 5.9 shows the results. As reported, the beam radial dimension is about 74 mm. Considering the exponential energy spectrum of the TARANIS laser-driven proton beam and taking into account the simulation prediction on the particle transmission through the ESS prototype, two energies, 4.5 and 7 MeV, have been chosen for the selection. The slit and the fourth dipole positions were those determined

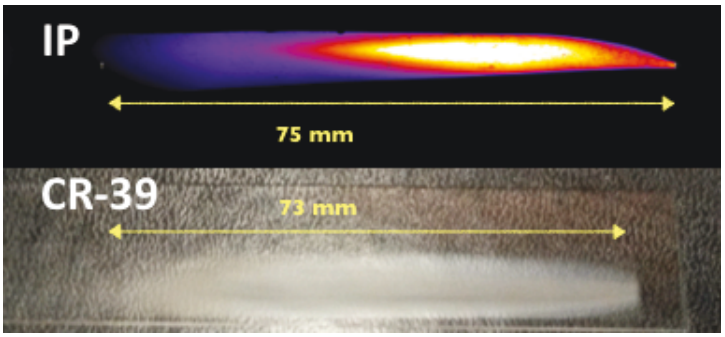

FIGURE 5.9: Beam shape detected using an IP and a CR-39, both placed on the slit plane.

during the calibration run performed at the INFN-LNS (see section 4.3.2.1). For both the selected beams, measurements of fluence and energy spread have been performed.
The particle fluence, i.e. the number of particles per cm^2, was measured using CR-39 solid state plastic detectors [151–153], placed just behind the final collimator.
An example of CR-39, irradiated and read, after the etching procedure, using the inverted microscope with a magnification of 32x, is shown in figure 5.10.

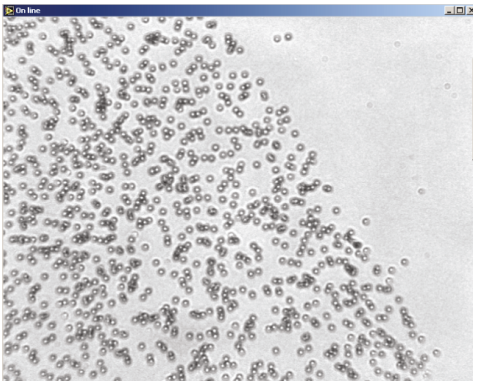

FIGURE 5.10: CR-39 detector mounted on the rear side of the final collimator. Proton tracks are visualized using an optical inverted microscope with a magnification of 32x.

The irradiated regions of the different CR-39 detectors have been analysed by sampling several areas of $2.72 \times 10^{-4} \pm 5 \times 10^{-6}$ cm^2, with a 63x microscope magnification.
When selecting protons at 4.5 MeV, the average value of the measured fluence was of about 1.2×10^6 p/cm^2 with an uncertainty of 20%, estimated as the standard deviation of the experimental data.
As regarding the 7 MeV case, the fluence average value was of about 0.8×10^6 p/cm^2 with an uncertainty of about 20%.
Several detectors have been also irradiated at different distances from the final collimator, showing a beam droplet shape. This data is in agreement with the beam optics study performed at INFN-LNF (see section 4.3.2.1). Figure 5.11 shows the IP and CR-39 signals, obtained when they are placed at 30.0 cm downstream the final collimator and when 4.5 MeV was the selected energy.

As reported in figure 5.11, the beam dimensions are about 7.6 mm and 1.7 mm on the radial and vertical axis, respectively. Considering the 3 mm circular aperture of the final collimator, the

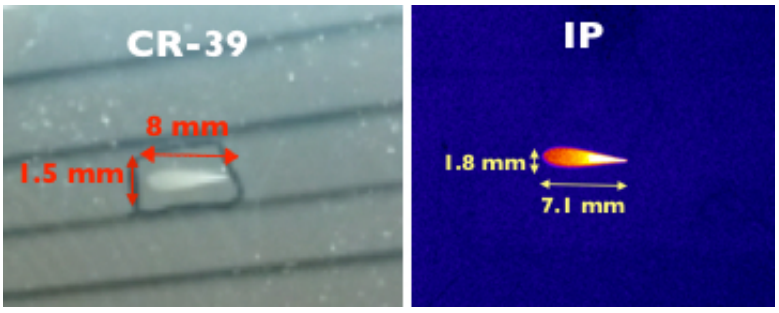

FIGURE 5.11: Beam shape detected using an IP and a CR-39, both placed 30.0 cm downstream the final collimator. The selected energy was 4.5 MeV.

beam horizontal divergence could be calculated: its value is about 0.8°. Concerning the vertical dimension, there is a focusing effect due to the ESS magnetic field and in particular to its vertical component [141].

The second main task of the experiment was to measure the energy spread of the selected proton beams. It has been done using an additional magnet dipole with a 500 μm aperture slit, i. e. the setup shown in figure 5.3.

In order to identify the initial direction of the beam selected by the ESS, necessary to reconstruct the beam deflection measured with the IP, a shot has been taken mounting only the 500 μm slit, downstream the ESS, without the additional magnet. This direction has been considered as the "zero" direction with respect to the fixed reference position (i.e. a *alignment laser* position marked for each shot on the detector), as shown in figure 5.12, part *a*. Several shots, for both energies of interest, have been, then, carried out after the fifth magnet has been mounted, as one can see in fig. 5.12), part *b* for the 4.5 MeV case.

Finally, the open-source ImageJ program has been used to analyse the IP images and reconstruct the lowest and the highest energy components present in the energy bandwidth selected by the ESS, as shown in figure 5.12, part *c*.

The energy bandwidths extracted for the two selected energies are listed in table 5.2. As shown from the different values obtained for different shots, a rather good shot-to-shot reproducibility of the energy intervals selected by the ESS can be observed.

TABLE 5.2: Experimental energy spread measurements. Data are obtained for both selected energies, 4.5 and 7 MeV.

Slit position	Energy [MeV]
1	4.0 → 4.6
2	4.1 → 4.7
3	4.2 → 4.8
4	6.3 → 7.3
5	6.6 → 7.9

Knowing the input proton energy distribution, from the RCF stack, and the output fluence for a given energy interval selected by the ESS, thanks to the CR-39 measurements, the transmission efficiency was estimated as the ratio between the selected and incoming protons number in the

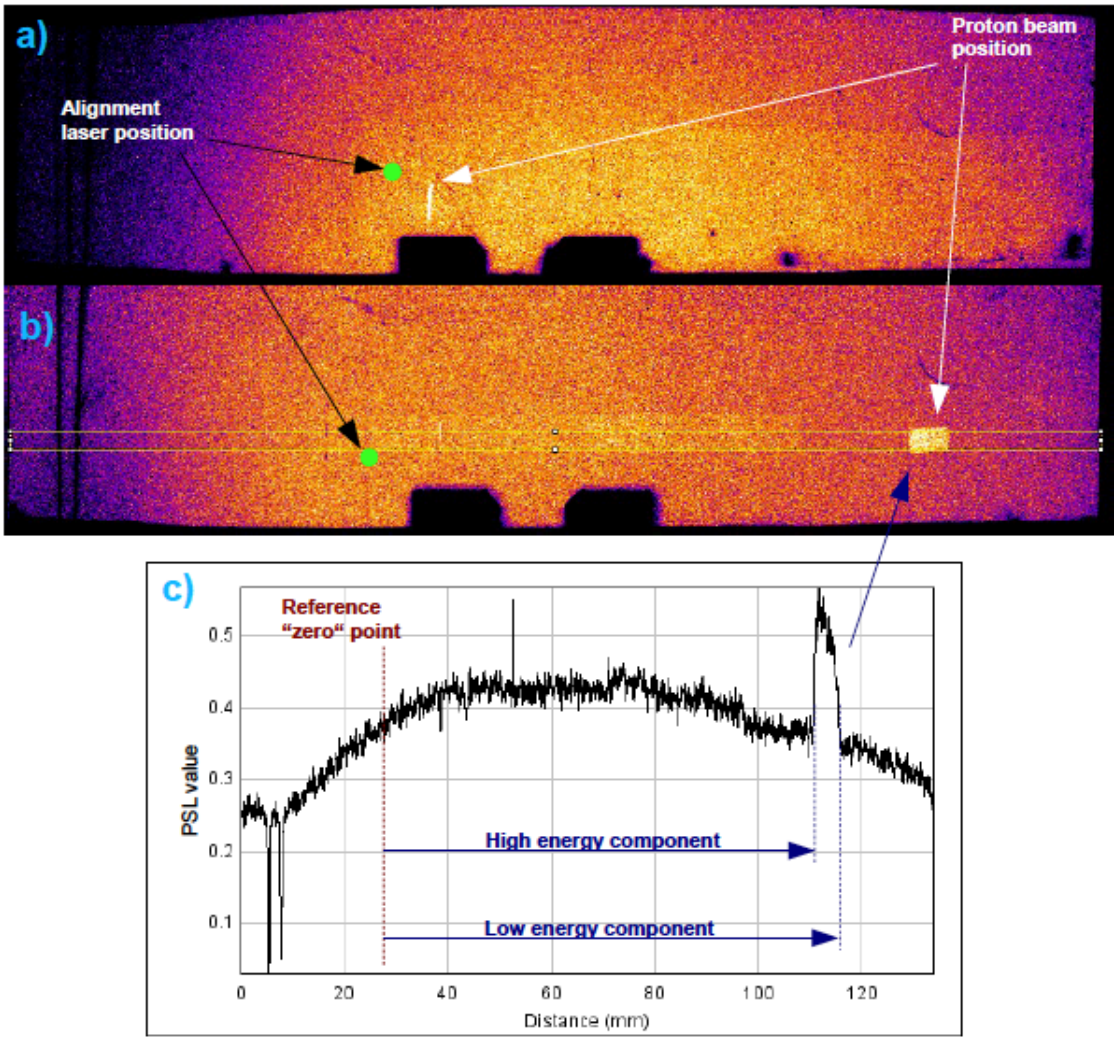

FIGURE 5.12: Measurement of: a) the zero point of the output beam respect to a fixed reference position (the *laser alignment* is the green point); b) the energy spread through the proton deflection due to the additional magnet. c) The IP signal analysis performed with the ImageJ tool. These data are obtained when 4.5 MeV was the selected energy.

energy range of interest. In particular, the obtained transmission efficiency in the energy range between 4.0 and 4.8 MeV is of about 3.4×10^{-3} % and between 6.3 and 7.9 MeV of about 1.1×10^{-3} %.

5.4.1 Simulation Results

The TARANIS experimental setup has been simulated in order to compare and benchmark the simulation predictions with the experimental results.

As first step, similar to the experiment, a qualitative study of the beam shape on the slit plane has been performed, obtaining a beam radial dimension of about 73 mm, that is in a good agreement with the corresponding experimental value.

Thanks to the simulations, it was also possible to investigate the effect of the initial beam divergence on the energy selection, due to the spatial mixing effect inside the magnetic field. Figure 5.13 shows the energy distribution $E[MeV]$ on the central slit plane along the radial direction $z[mm]$. The particle fluence is represented by means of the colour index: blue and red are, respectively, for low

and high fluence values. As shown, low energetic particles have higher fluence value, in agreement with the input energy spectrum.

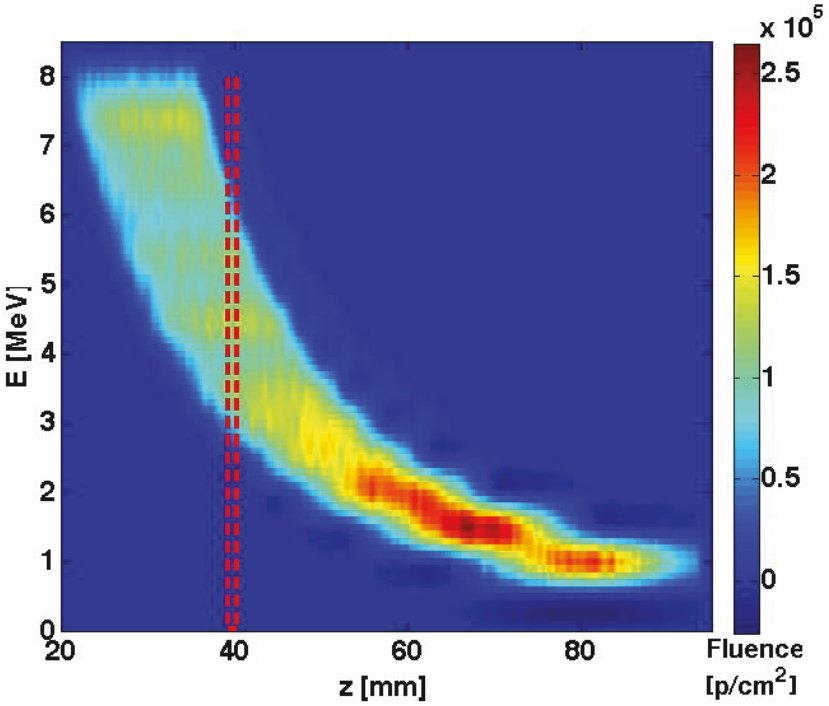

FIGURE 5.13: Protons energy ($E[MeV]$) *vs* radial position ($z[mm]$) on the slit plane, with the fluence distribution described by the colour index. The red dashed lines centered in z = 39.0 mm represents the slit aperture, placed in order to select 4.5 MeV.

The E *vs* z distribution of figure 5.13 has the same trend of the calibration curve, obtained using monoenergetic, no-divergence input beam and reported in figure 4.20. However, now the function is not 'univocal', i. e. fixing the z value, there is not only one corresponding value of E. The broad distribution observed in figure 5.13 is actually due to the spatial mixing effect. Indeed, due to the large energy-dependent angular distribution of the particle accelerated in the TNSA, protons with different energies may be deflected to the same radial position on the slit plane. For example, by considering a 3 mm × 6 mm (HW) slit in the position to select 4.5 MeV (red dashed lines in figure 5.13), protons in the energy range between about 3 and 6.5 MeV are actually selected. Figure 5.14 shows, indeed, the energy distribution, obtained on the final collimator plane, when the slit position is fixed to select 4.5 MeV.

In order to select only protons included in a narrower energetic range, centred at the desired energy, the third-fourth dipole relative distance has a crucial importance. Using, indeed, the optimised third-fourth dipole relative distance, an output energy range of [3.9:4.8] MeV is obtained just behind the last collimator, as reported in figure 5.15. Moreover, if a Gaussian fitting is applied, there are 4.5 MeV as centroid and 12.5% as FWHM.

The proton fluence distribution, obtained just behind the last collimator, has been also evaluated. It is reported in figure 5.16, when 4.5 MeV was the selected energy.

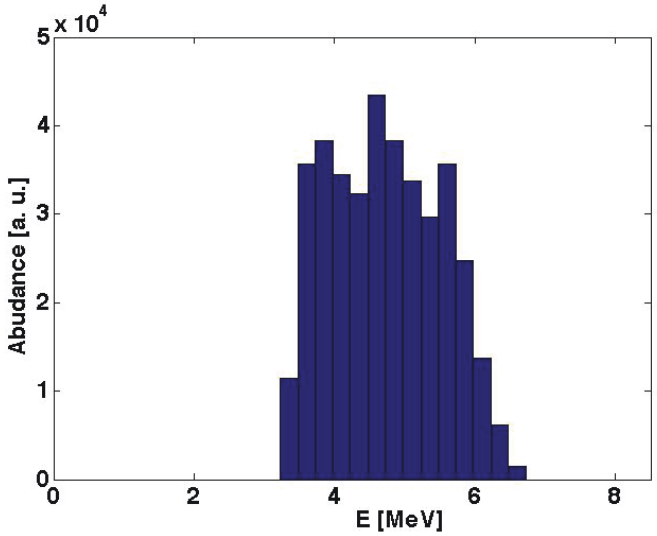

FIGURE 5.14: Energy distribution obtained on the final collimator plane, when 4.5 MeV is the selected energy.

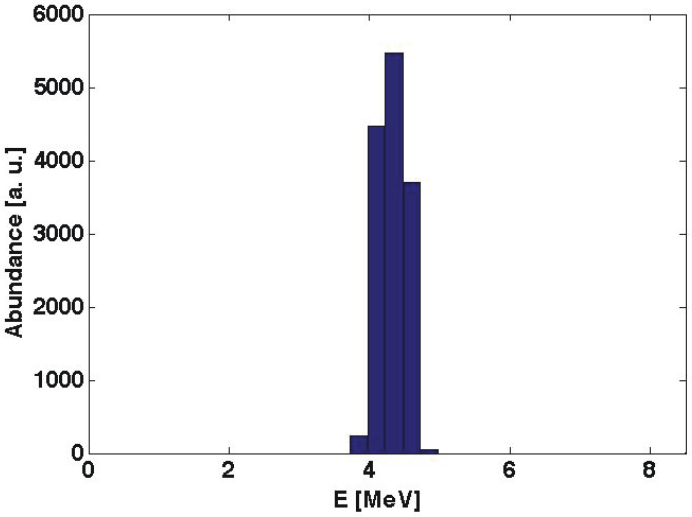

FIGURE 5.15: Energy distribution obtained just behind the final collimator plane, when 4.5 MeV is the selected energy.

In order to calculate the fluence average value with the relative uncertainty, pixels of 165 μm $\times$ 165 μm, i. e. with the same experimental area of the 63x microscope magnification used for the CR-39 analysis, have been considered. The mean value with the standard deviation of the different fluence values, evaluated for each pixel, has been finally used as fluence average value and relative uncertainty. It values $1.3 \times 10^6 \mathrm{p/cm^2} \pm 15\%$.

The same simulation set has been performed with 7 MeV as desired output energy, obtaining just after the final collimator an energy range of [6.0:7.7] MeV and an average fluence value of about $1.5 \times 10^6 \mathrm{p/cm^2} \pm 19\%$.

Knowing the input proton energy distribution and the output fluence for a given selected energy range, the transmission efficiency was estimated as the ratio between the selected and incoming protons number in the energy range of interest. In particular, the transmission efficiency in the

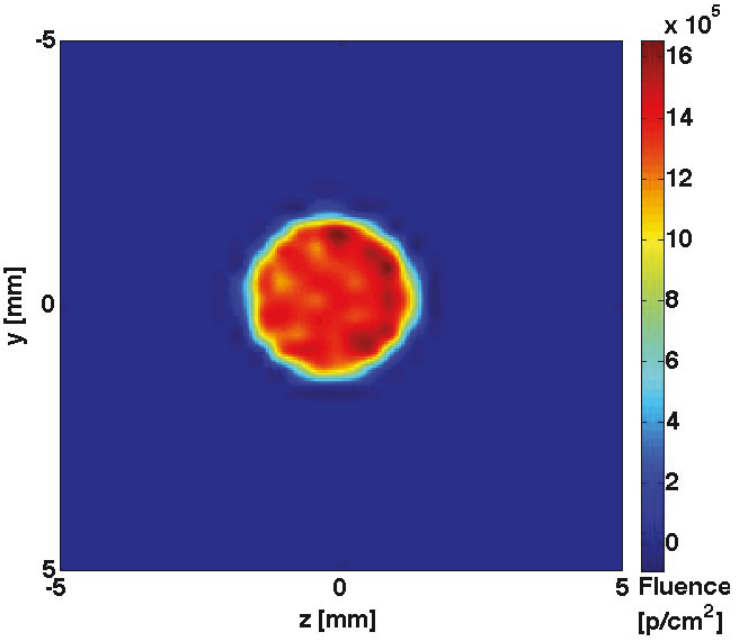

FIGURE 5.16: Fluence distribution, obtained just behind the final collimator plane, when 4.5 MeV is the selected energy.

energy range between 3.9 and 4.8 MeV is about 3.4×10^{-3} % and between 6.0 and 7.7 is about 1.9×10^{-3} %. In tables 5.3 and 5.4 are summed up the experimental and simulated energetic range, fluence average values and transmission efficiencies, obtained when 4.5 and 7 MeV were the selected energies, respectively.

TABLE 5.3: Experimental and simulated energetic range, fluence average values and transmission efficiencies when 4.5 MeV was the selected energy.

	Experimental data	Simulated data
Energy range [MeV]	$4.0 \rightarrow 4.8$	$3.9 \rightarrow 4.8$
Fluence [p/cm^2]	$1.2 \times 10^6 \pm 20$ %	$1.3 \times 10^6 \pm 15$ %
Transmission efficiency [%]	3.4×10^{-3}	3.4×10^{-3}

As reported, there is a quite good agreement between experimental and simulated data. The main differences are related to the 7 MeV case, maybe due to the a lower statistics. Only few shots have been indeed performed to obtain the 7 MeV results.

A quite good agreement is also obtained comparing the simulated and experimental beam shape, evaluated at 30.0 cm downstream the ESS, when 4.5 MeV is the selected energy. Radial and vertical

TABLE 5.4: Experimental and simulated energetic range, fluence average values and transmission efficiencies when 7 MeV was the selected energy.

	Experimental data	Simulated data
Energy range [MeV]	$6.3 \rightarrow 7.9$	$6.0 \rightarrow 7.7$
Fluence [p/cm^2]	$0.8 \times 10^6 \pm 20$ %	$1.5 \times 10^6 \pm 19$ %
Transmission efficiency [%]	1.1×10^{-3}	1.9×10^{-3}

dimensions of about 6.2 and 1.9 mm, respectively, have been revealed and positively compared with the corresponding experimental values of 7.6 and 1.7 mm.
A systematic study of the beam shape has been performed at different distances d downstream the ESS. Figure 5.17 summarizes the experimental and simulated beam radial dimension obtained for d = 16.0, 22.0, 30.0 and 42.0 cm.

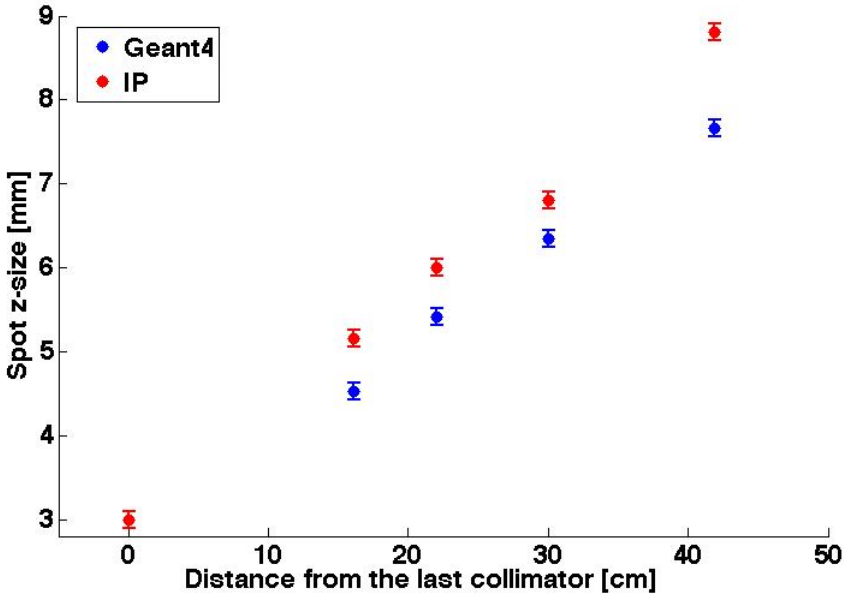

FIGURE 5.17: Beam radial (z) dimensions: simulated (blue dots) *vs* experimental data (red dots).

Results have permitted the calculation of the output beam radial divergence. Considering that the experimental value is about 0.8° and the simulated one 0.6°, a quite good agreement could be deduced.

5.4.1.1 The 1 mm slit case

In order to investigate the role of the first collimator aperture, placed upstream the ESS, on both the spatial mixing and on the energy selection, a simulation set considering 1 mm circular aperture as the initial collimator has been performed, allowing to change the proton angular distribution accepted by the ESS.
A comparison of the energy distributions obtained along the radial direction on the central slit plane considering 1 mm (red points) and 3 mm (blue points) initial apertures is shown in figure 5.18. As one can see, the E *vs* z distribution in the 1 mm case is narrower than in the 3 mm case. Indeed, using a smaller entrance collimator, a smaller solid angle is accepted by the ESS. Particles going through the selector will be therefore characterised by a narrower angular distribution and the spatial mixing effect will be limited.
As an example, considering a 3 mm × 6 mm (HW) slit in the position to select 4.5 MeV, the obtained proton energy ranges actually from 3.5 to 5 MeV, when the 1 mm initial aperture is used. This energy bandwidth is smaller than the one obtained in the 3 mm initial aperture case ([3-6.5]

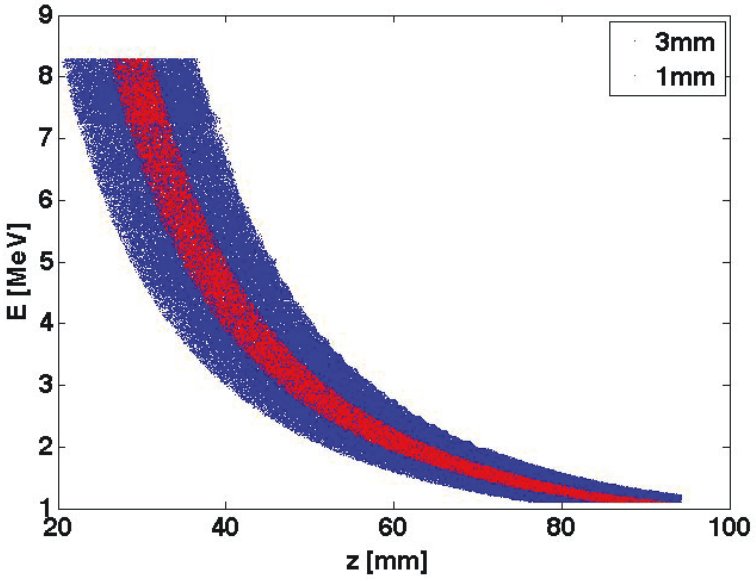

FIGURE 5.18: Protons energy ($E[MeV]$) *versus* radial position ($z[mm]$) on the slit plane for a choice of 3 and 1 mm circular aperture for the first collimator.

MeV). At the same time, fixing the slit position to select 4.5 MeV and evaluating the average fluence and the energy range just behind the final collimator, values of about $1\times\ 10^6$ p/cm^2 $\pm$ 14 % on an energy range from 3.9 to 4.7 MeV are obtained. These results are not significant different respect to the data obtained using the 3 mm initial aperture.

Considering the output beam features and the energy range evaluated for both apertures before the last collimator plane, it seems that the 1 mm case is more performing then the 3 mm one. A more controlled beam is indeed produced just using the central slit, without a significant variation in the output number of particles.

However in the 1 mm case, the shot-to-shot reproducibility represents a critical element. For instance if the conical angular distribution (beam axis) is not centred on the alignment axis, the most populated component of the beam is lost, with a consequently poor output.

The choice of the collimators diameter is therefore one of the main element, that has to be carefully investigated before any experimental run and considering the shot-to-shot beam instabilities.

Chapter 6

A simulation study with the whole transport beamline

As already described, ion acceleration driven by ultra intense lasers represents a very promising field but produced beams are characterised by extreme features, such as wide angular and energy distributions and high peak current, making them not directly suitable for several potential applications. In order to overcome these intrinsic limitations, many researches and technological initiatives have been proposed to accelerate controlled, reliable and reproducible laser-driven ion beams.
This chapter is based on the conceptual solution and on the corresponding Monte Carlo simulation of a transport beamline, composed by the described prototypes. It was designed for laser-driven ions with kinetic energy up to 30 MeV and composed by a collection system and an energy selector device. Considering the shot-to-shot beam instabilities, due to the laser beam fluctuations, to the target inhomogeneities or to the interaction regime fluctuations, together with the beam collection and selection, another important task of a transport beamline is also to compensate for these instabilities, obtaining a controlled and reliable output beam, in terms of energy and angular distribution as well as beam spot size and fluence.
Considering these purposes, a set of simulations has been performed, using, as input, a typical laser-driven proton beam with different angular distributions, implemented in order to treat the beam instabilities.
Results show that only the proper combined use of the collection system with the energy selector allows to obtain a controlled and reliable output beam, mainly considering the input beam fluctuations. In detail, the best beamline configuration for the maximum transmission of a 5 MeV proton beam with, as final features, a FWHM of about 7% and a divergence of about $\pm 0.5^{\circ}$ is presented.
A feasible radiobiological application of the transported beam has been also considered. In particular, the use of scattering foils, placed at different distances from the beam exit point, has been evaluated mainly in terms of absolute 2-dimensional dose distributions at the irradiation point. The ultrashort duration of laser-driven multi-MeV ion bursts offers, indeed, the possibility of innovative investigations at extremely high dose rates. In this proof-of-principle experiment, respect to the preliminary one reported in chapter 3, the beam energy spread is narrower, the dose incertainty

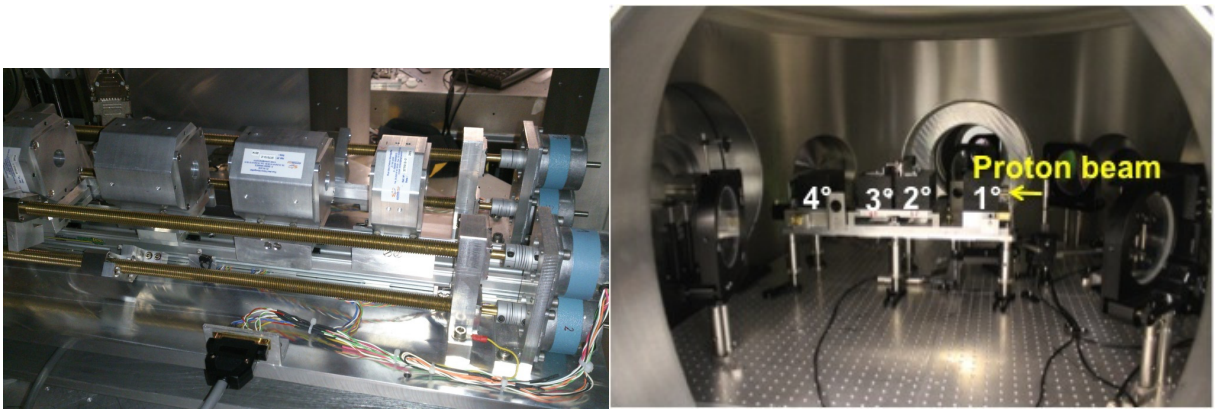

FIGURE 6.1: On the left the collection system prototype at the LOA facility (Fr) during the test with laser-driven proton beams. On the right the energy selector system prototype placed in the interaction chamber at the TARANIS facility (Queen's University of Belfast, UK) during its characterisation with laser-driven proton beams.

smaller and the dose rate comparable (about 10^{10} Gy/min per shot).
Finally a preliminary study for a 24 MeV protons selection is reported, in order to briefly exploit the whole operational energy range of the transport beamline.

6.1 The Transport Beamline

The prototype transport beamline is composed by two main sections, as described in chapter 4. The first part is the set of four NdFeB permanent magnetic quadrupoles (PMQs), located just downstream the target. Its main function is to reduce the divergence of the primary beam and to perform its collection and preliminary energy selection. The second part of the beamline is an energy selection system (ESS), composed by four magnetic permanent dipoles and designed for the final energy selection.
Each prototype has carefully been studied, calibrated and tested with different experimental runs and simulation sets. The good agreement between the experimental data with the simulated one, observed in chapter 4 and 5, has confirmed their correct implementation in the code. Figure 6.1 shows the PMQs and the ESS prototypes during their test with laser-driven proton beams, respectively, at LOA laboratory (still ongoing) and the TARANIS facility (see chapter 5).

The final step is represented by the test of the whole transport beamline, with the two prototypes properly coupled (collection system and energy selector). Experimental campaigns could be planned for the next months, at the TARANIS facility (Belfast, UK) and at LOA laboratory (Paris, Fr). Preliminarily, having a reliable code, a simulative study has to be performed, in order to study how optimise the coupling of PMQs and ESS for the 5 MeV proton selection. This energy has been chosen considering the energy distributions available in many laser facilities [31, 154] and especially the spectra of the input proton beams available at the TARANIS facility and at LOA laboratory, where the experimental runs could be planned.
Two different codes were used: the analytical TraceWin code and the Geant4 Monte Carlo toolkit. In particular TraceWin has been used to optimise the quadrupole configuration for the 5 MeV proton

beam selection and Geant4 to perform the detailed beam transport for the evaluation of the beam interaction effects, the accurate estimation of the fluence, energy, angular and dose distributions as well as the beam spot size along the transport beamline and at the final interaction point.
The Geant4 code, as described in chapter 2, was based on the *Hadrontherapy advanced example*, freely released inside the Geant4 distribution. Figure 6.2 shows the Geant4 simulation of the whole transport beamline with its main elements set for the 5 MeV proton selection.

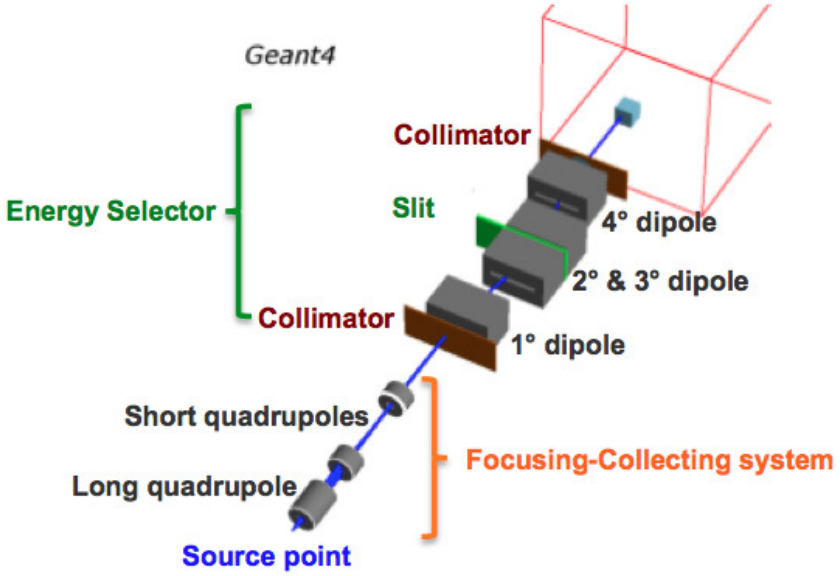

FIGURE 6.2: The simulated transport beamline for laser-driven charged particles with its main elements set for the 5 MeV proton selection.

6.2 Monte Carlo simulations

Monte Carlo simulations have been carried out with the described beamline, in order to study the transport and the handling of a typical laser-driven protons beam, considering the poor experimental reproducibility of the beam generated by the laser-target interaction.
In particular, I have chosen, as energetic spectrum, the decreasing exponential shaped function reported in Fig. 6.3, with 8.2 MeV as energy cutoff, 3.4 $\times 10^{11}$p as total number of input particles, which corresponds to the energy spectrum measured at the TARANIS facility during the experimental run reported in chapter 5. Protons with energy lower than 1.0 MeV are not simulated as they are deflected back, due to the magnetic field intensity.

The angular input divergence has been implemented using different *angle vs energy* functions. They were also obtained during the experimental run at Queen's University of Belfast (indeed, it is represented by the 29° case). Experimental data have been fitted with a second order polynomial function and the correspondent parameters found. Then, changing the parameters we were able to rescale the curves and finally to obtain the other cases (5° - 25°), related to a different laser-target interaction condition or different shaped target, in order to partially reproduce the shot-to-shot

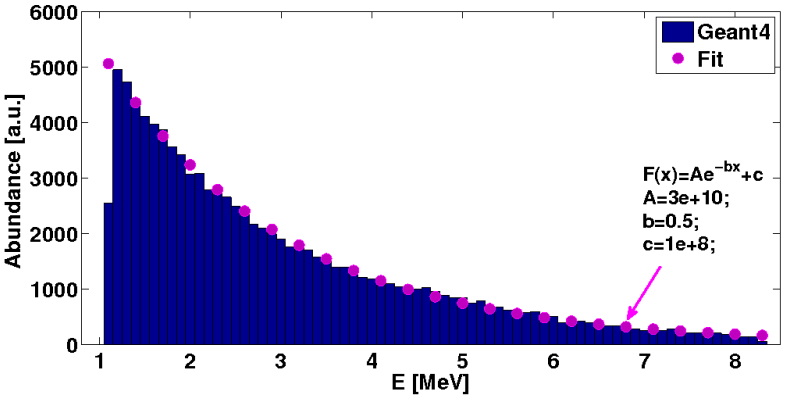

FIGURE 6.3: Typical laser-driven proton spectrum, used as simulation input.

instabilities [1, 31–33, 146, 155].

The different implemented curves are reported in figure 6.4 and will be hereafter identified with the angle value for Energy=0. If we select one of the curves in the plot (which represents a specific case of particle emission after the laser-target interaction), fixing an energy value on X axis, protons will be emitted with an isotropic distribution in an angular range limited by the value of function itself.

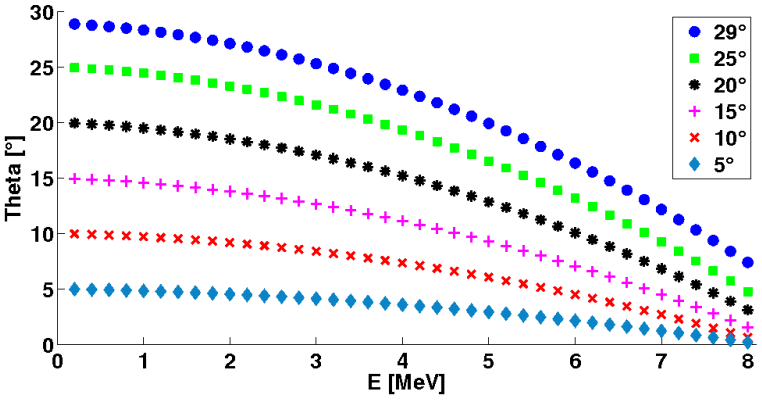

FIGURE 6.4: Energy-dependent angular distributions used as input for the simulations.

The different energy-dependent angular distributions of figure 6.4 have been approximated with equivalent step functions, as for instance the '15°' case reported figure 6.5.

This simulation study has been focused on the 5 MeV output selection. However this study could be carried out for any energy value included in the beamline operational range ([1-30] MeV).

As a first step, the beamline setup, i. e. the injection of the beam coming from the collection system in the energy selector, has been optimised. A mono energetic 5 MeV proton beam with an isotropic divergence of $\pm$ 10° and a spot size comparable with a typical laser beam spot size on the target (Gaussian profile with σ=0.06 mm) has been implemented.

In this preliminary phase the energy selector was not simulated, therefore the beamline was considered only as the collection system with two collimators (Φ_{In}=8 mm and Φ_{out}=8 mm, as in the

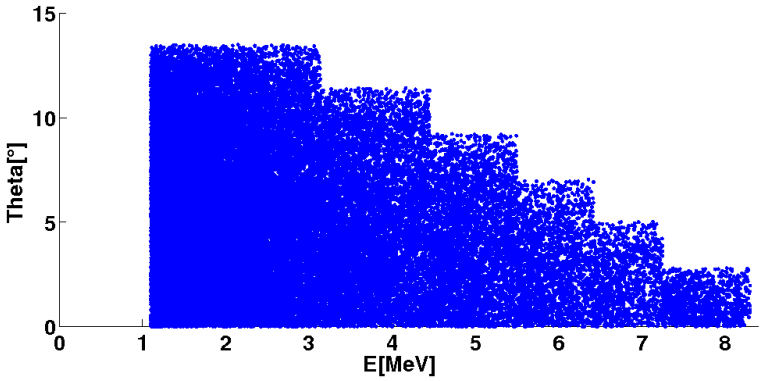

FIGURE 6.5: Step function for the '15°' case of fig. 6.4.

third case. See section 6.2.3 (III Case) for more details.) and the 1 mm × 8 mm (HW) central slit. Different available setups have been studied and evaluated in terms of transmission efficiency and total divergence of the output beam. In particular the final setup was chosen because of the small output angular divergence of ±0.5°, the low particle losses of about 95% and the quite big acceptance angle of ± 17°, even if the downstream beam spot does not show an high degree of uniformity, as reported in Figure 6.6.

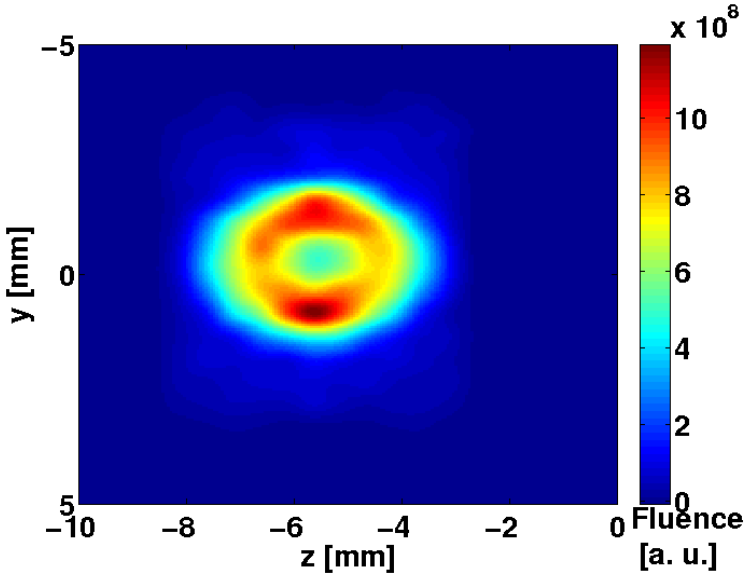

FIGURE 6.6: Fluence distribution obtained after the final collimator, without the ESS dipoles simulation. The input protons energy and divergence are 5 MeV and ± 10 °, respectively.

Details of the relative quadrupoles distances are reported in figure 6.7.

As regarding the ESS setup, in order to minimise the beam optics distortion due to the no-zero gradient field region, the two ESS central dipoles were shifted of 32 mm and the centre of the two collimators apertures positioned 11 mm far from the central dipole axis. Thanks to these shiftings, a 5 MeV proton beam will pass through the uniform regions of the magnetic field and the droplet shape of the output beam, observed in chapter 4 and 5, will became an approximately spherical one.

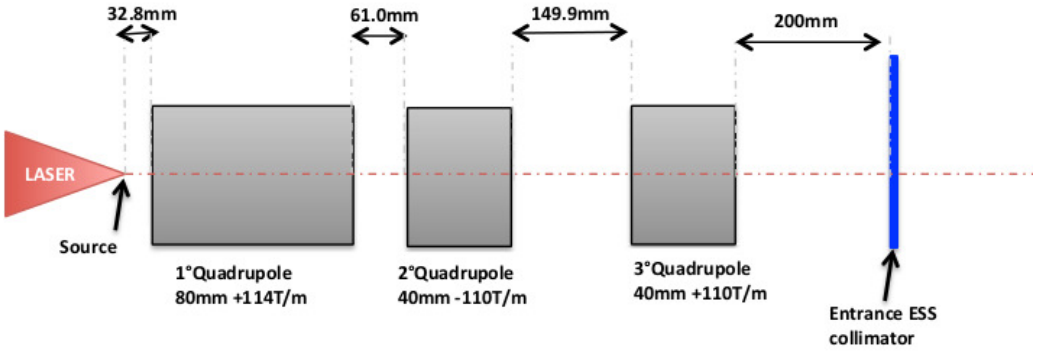

FIGURE 6.7: Details of the final PMQs setup, optimised for a 5 MeV proton beam transmission.

The beamline setup optimisation was performed only once, for an input beam (5 MeV, ± 10 °), whose features could be found in the 5 MeV component of the '15°' case (fig. 6.5). We have indeed decided to maintain the same configuration for all the angle distributions in order to consider the possible experimental shot-to-shot instabilities.
Next sections will show step-by-step that the whole transport beamline allows to obtain a reproducible output beam, comparing the final energy and fluence distributions with other two cases: (I) only collection system and (II) only energy selector.
Also the transmission efficiency values will be evaluated, as the ratio between the number of output and input protons considered in the selected energy window, at 1σ when a Gaussian fitting was applied.

6.2.1 I Case: collection system

In this first case, only the collection system and the two energy selector collimators (Φ_{In}=8 mm and Φ_{out}=8 mm) were simulated. The diameters as well as the position of both collimators were fixed in order to have the ESS dipoles simulation, as unique difference respect to the III case. Regarding the collimator sizes, this choice has been done in order to find the best compromise between the transmission efficiency and the coupling with the ESS, which is characterised by a specific gap dimension (10 mm). The size of 8 mm, indeed, represents the maximum possible dimension to avoid the non-uniform region of the field near the magnet and, on the other side, to have a reasonable abudance.
The output analysis has shown how this configuration does not allow the compensation of the shot-to-shot input beam instabilities, mainly influencing the reproducibility of the output energy spectrum. Particles emitted from the source with low divergence are, indeed, not affected by the quadrupole field and are transported undisturbed throughout the whole system.
As an example, Figure 6.8 shows the energy distributions after the last collimator for the two extreme cases ('5°' and '29°') of the input beam.

It is evident as the output energy spectrum has a strong dependence on the input beam characteristics. The main energetic component, indeed, is centred at 5 MeV, but the FWHM (FWHM as 2.35 σ) value increases from 8.2% to 11.6% when the input divergence decreases from '29°' to

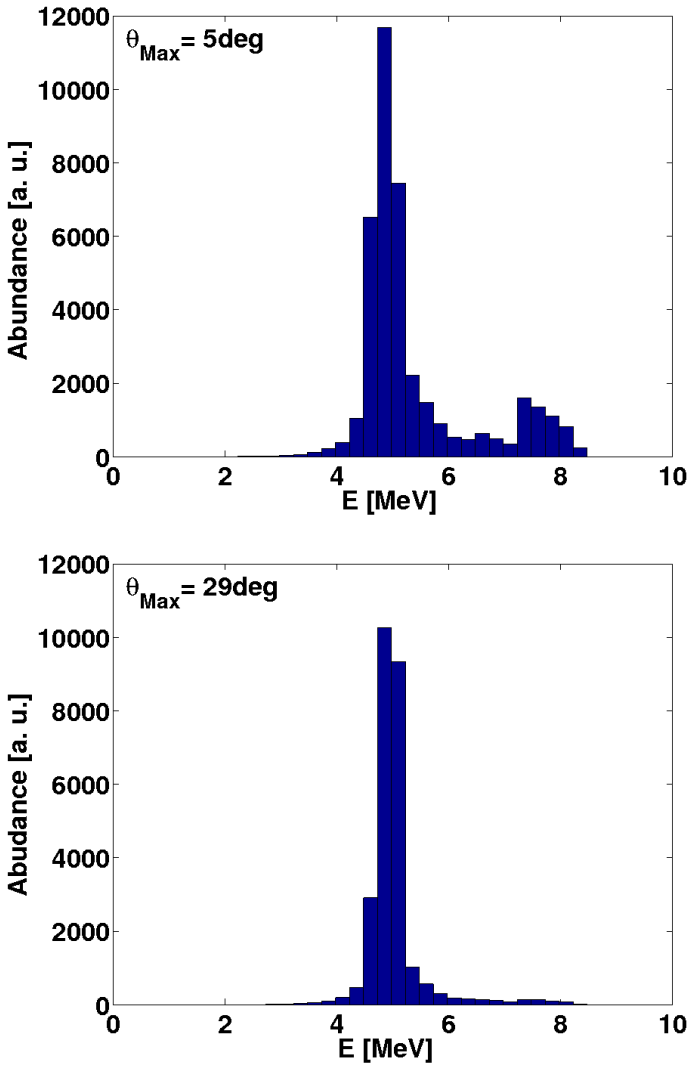

FIGURE 6.8: Proton beam energetic spectra after the ESS final collimator for the I case. The input angle distributions are the '5°' case on the top and the '29°' case on the bottom.

'5°'. Also a tail at higher energies becomes significant for lower angles. This is due, as above reported, to the fact that particles emitted by the source with low emission angle are not affected by the quadrupole field and therefore they are transported undisturbed up to the exit point of the beamline. For instance, for the '5°' case, particles with energy higher then 6 MeV represents the 19% of the whole spectrum.

In this case the transmission efficiency evaluation is related only to the main peak at 1σ. Obtained data are reported in table 6.1, however they cannot be compared to the other cases because of the tail presence and of the significant energy spread variation.

TABLE 6.1: Collection system: transmission efficiency values for different input angle distributions, from 5° up to 29°

Input angle distribution	5°	10°	15°	20°	25°	29°
Transmission efficiency	47.6%	21.6%	11.9%	6.0%	3.7%	2.8%

6.2.2 II Case: Energy Selector System

In this second case, only the energy selector (Φ_{In}=3 mm and Φ_{out}=3 mm) with the slit (1×8 mm^2 - HW) positioned in order to permit the 5 MeV protons selection, were simulated. The source was placed 8.2 cm far from the system in order to reproduce the experimental setup used during the ESS test performed at the Center for Plasma Physics of the Queen's University in Belfast (UK). The diameter value of collimators and the source position were chosen in order to maximise the transmission efficiency and to partially limit the spatial mixing of the different energy protons, due to the input beam divergence (i.e. to reduce the output energy spread). As an example, the '5°' case is reported. As shown in figure 6.9, the fluence distribution appears uniform. Moreover, the energy spectrum is characterised by a centroid at 5.0 MeV and a FWHM of about 10.0 %, when a Gaussian fitting is applied.

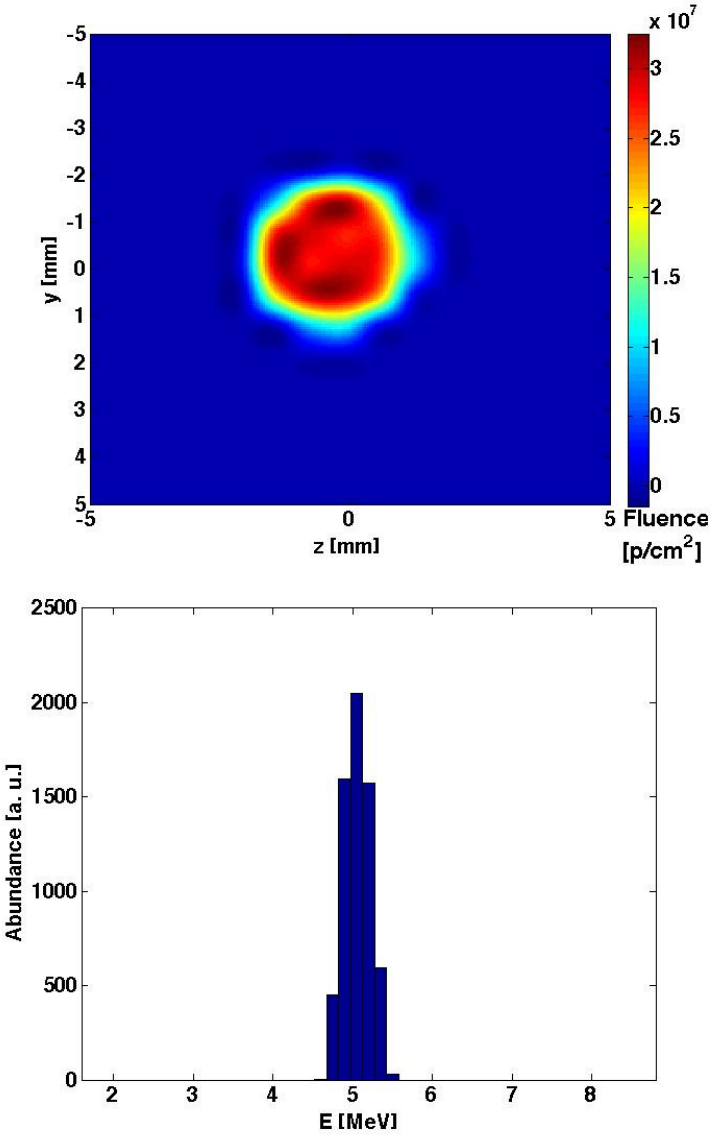

FIGURE 6.9: Proton beam after the ESS final collimator for the II case: fluence distribution on the top and energy spectrum on the bottom. The input angle distribution is the '5°' case.

The beam output characteristics seem to be very stable, also considering the different input divergences. Nevertheless, the overall particles transmission is not yet sufficient to be usable for common applications, as can be argued from table 6.2, where the transmission efficiency values are listed for the different input angle distributions.

TABLE 6.2: Energy Selector: transmission efficiency values for different input angle distributions, from 5° up to 29°

Input angle distribution	5°	10°	15°	20°	25°	29°
Transmission efficiency	0.16%	0.037%	0.016%	0.008%	0.005%	0.003%

6.2.3 III Case: Transport Beamline

The last investigated case is related to the simulation of the whole transport beamline, i.e. the collection system proper coupled to the energy selector. The ESS collimators diameter has been fixed to 8 mm in order to avoid the inhomogeneous part of the field, close to the iron walls of the magnets.
As reported in figures 6.10 and 6.11, the output beam shows a narrow energy distribution, peaked at 5 MeV, but with a FWHM that has the same dependence of the first case. However, the energy spread is 5 % for the '29°' case (fig. 6.11) and increases only up to 7 % for the '5°' case (fig. 6.10). Also the same trends for the beam spots and fluence distributions are here observed, even if the spatial symmetry is now lost because of the paths differences of protons with different energy inside the selection system.

Summarising, this setup clearly permits to fulfil the requirements of a stable, reproducible beam, with no significant difference in the energetic spectrum on varying the input angle distribution, and still maintaining a good transmission efficiency, two orders of magnitude bigger than before (table 6.2), as shown in table 6.3.

TABLE 6.3: Whole transport beamline: transmission efficiency values for different input angle distributions, from 5° up to 29°

Input angle distribution	5°	10°	15°	20°	25°	29°
Transmission efficiency	23.2%	8.9%	4.3%	2.5%	1.7%	1.26%

6.2.4 Comparing the three cases

Once the TBL has been optimised for the transmission of a 5 MeV proton beam, several simulations were performed using different laser-driven proton beams, as input. As the energy spectrum was described using a decreasing exponential function with a cutoff value of 8.2 MeV, several energy-dependent angular distributions (θ_0 is the angle value for E=0) were implemented in order to

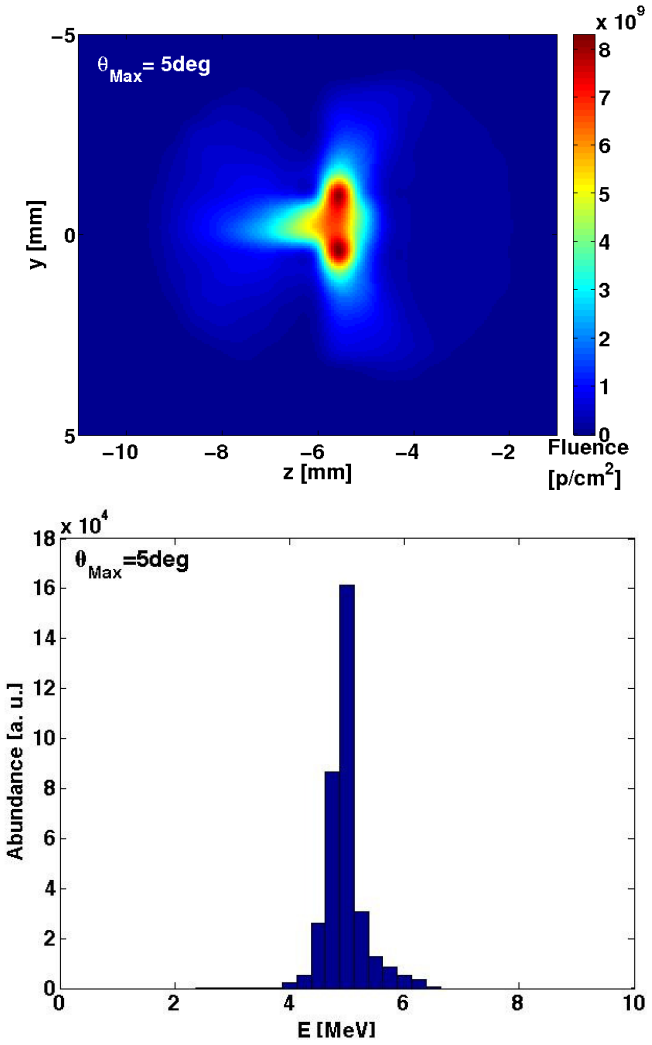

FIGURE 6.10: Proton beam after the ESS final collimator for the III case: fluence distribution on the top and energy spectrum on the bottom. The input angle distribution is the '5°' case.

consider the beam shot-to-shot instabilities.
Three different cases were studied and compared in terms of downstream spatial, energy, fluence and dose distributions.

- (I) case: only collection system → a non-uniform beam spot and a non-reproducible energy spectrum are obtained. The centroid value of the energy distribution is controlled, but for lower θ_0 values, the FWHM increases up to 11.6% and a tail at higher energy becomes not negligible, up to the 19% of the whole spectrum. The transmission efficiency has been calculated, but only considering the contribution of the main peak. For this reason it cannot be compared with the other cases.

- (II) case: only energy selector → a uniform beam spot and a controlled energy distribution with a FWHM of about 10% are obtained. The transmission efficiency goes from 0.003% up to 0.16% for decreasing θ_0 values.

- (III) case: whole transport beamline → a non-uniform beam spot and a controlled energy distribution are obtained. The FWHM of the energy spectrum increases for lower θ_0 values,

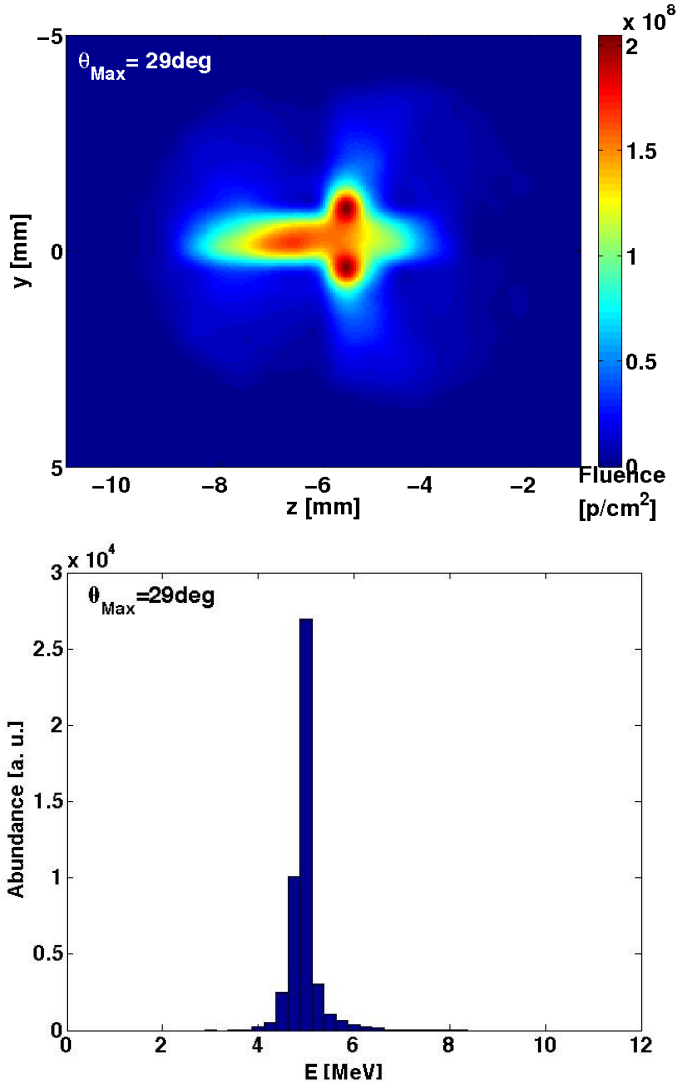

FIGURE 6.11: Proton beam after the ESS final collimator for the III case: fluence distribution on the top and energy spectrum on the bottom. The input angle distribution is the '29°' case.

but in the worst case it is only 7%. The transmission efficiency, that increases for lower θ_0 values, is about two orders of magnitude bigger than the (II) case.

Figure 6.12 sums up the transmission efficiency of the last two cases as a function of the input beam divergence.

As shown, the whole transport beamline is more performing respect to the only ESS choice. Moreover, the transmission efficiency for bigger θ_0 values has a decreasing trend.
The comparison between these three cases has shown that only the proper combined use of the collection system with the energy selector allows to obtain a controlled and reliable output beam, considering the input beam fluctuations. Using the two systems in a separate configuration a compromise between transmission efficiency and energy spread is not reached, as it is in case of coupling the systems. Indeed, for the ESS alone the number of transmitted protons is lower, on the other side for the quadrupole system alone the energy spectrum has significant undesired contaminations. However, the relative distances of the different elements are crucial parameters, that have to be

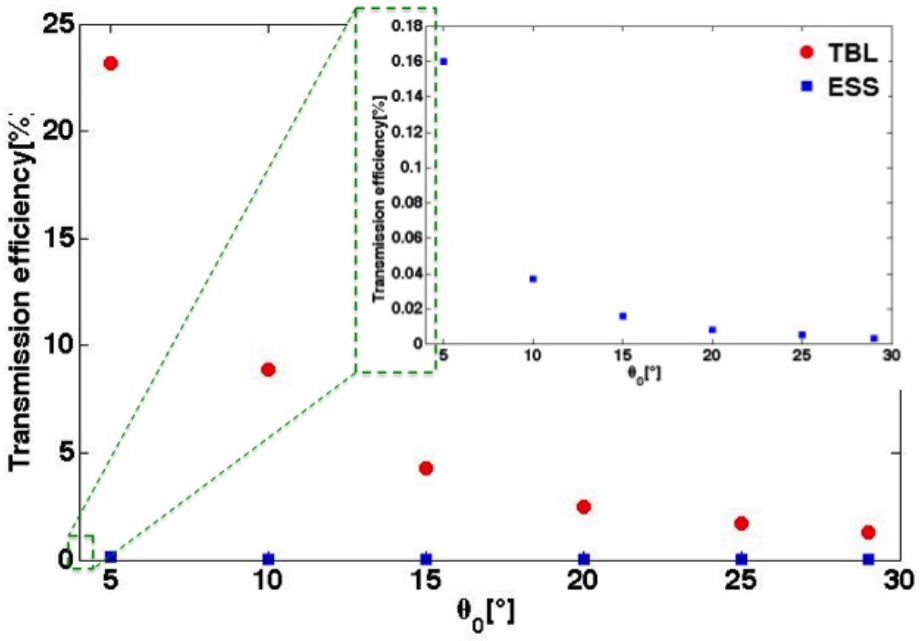

FIGURE 6.12: The plot shows the transmission efficiency as a function of the input beam divergence, identified with the different θ_0 values. The II (only ESS) and III (whole TBL) are reported. The subplot shows the II case in detail.

optimised for the best injection of the beam, coming from the collection system, in the energy selector.

6.3 Feasible controlled cell irradiation with laser-driven proton beams

There are many potential applications for the optically accelerated beams [4]. In particular, the possibility to irradiate cell samples with controlled dose distributions represents one of the most interesting fields. The ultrashort duration of laser-driven multi-MeV ion bursts offers the possibility to perform radiobiological studies at dose rates of about 10^{10} Gy/min per shot, which are much higher in comparison to the conventional values of about 1-10 Gy/min [101]. Preliminary measurements and evaluations have already been performed accumulating dose over several laser shots as well as isolating effects associated to a single short burst deposition [86, 87, 90, 92, 93]. As already reported in chapter 3, more investigations, especially for single shot effects and with controlled beams, are still necessary in order to understand if the ultra-short nature of the dose deposition influences the biological end-points.

Considering that, the dynamics of the beam described in sec 6.2.3 were studied at different distances d from the ESS final collimator, in order to perform proof-of-principle radiobiological experiments. Figure 6.13 reports the dose distributions at d=0-10-20-40-60 and 100 cm from the final collimator.

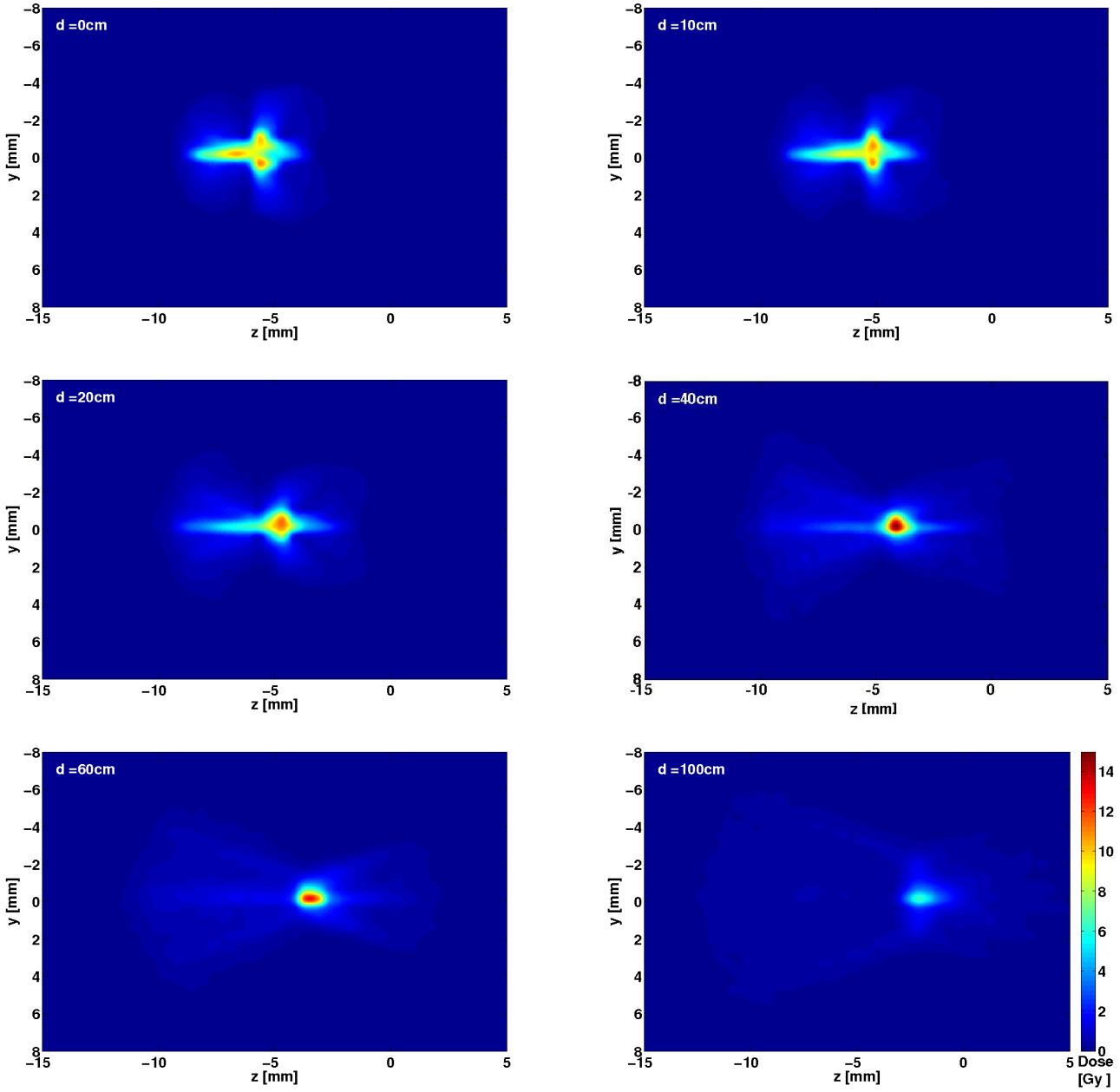

FIGURE 6.13: Dose distributions at different distances form the ESS final collimator for the III case. The distance values are reported in each plot, while the colour bar is shown only in the last subfigure.

As shown, the beam spot is not big enough to irradiate a significant cell sample area with a quite uniform dose distribution, necessary for a cellular irradiation [156–159]. For this reason, several configurations with different scattering foils placed at different distances d from the final collimator were investigated. The dose distributions were then evaluated at different distances from the foil position, from 5 up to 40 cm. In detail, a water phantom was simulated, with $0.4 \times 40 \times 40$ mm^3 as dimensions.

In order to quantitatively compare the different scattering configurations, the x and y dose profiles on the beam centroid axis were considered. In detail, the widths Δx and Δy at the 80% of the maximum dose value was evaluated and, therefore, a cell irradiation with a maximum dose inhomogeneity of 20 % was supposed, as shown in figure 6.14.

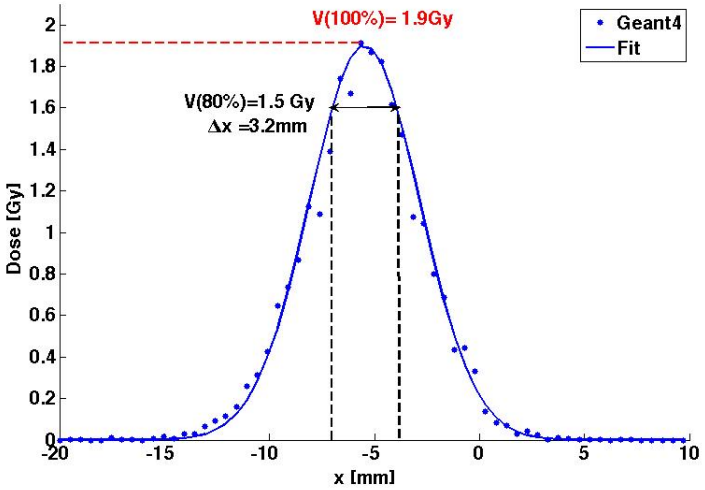

FIGURE 6.14: The plot shows the x dose profile on the beam centroid axis with the widths Δx at the 80% of the maximum dose value. Ta, 1.5 μm placed at 40 cm from the final ESS collimator is the used scattering foil.

Ta and Au, 1.5 and 3 μm thick foils, placed at d=10 cm and 40 cm from the final collimator are presented here. Figure 6.15 displays the x and y dose distribution profiles evaluated at 10 cm from the foil position, when the different scattering leafs are placed 10 and 40 cm far from the final collimator. As shown, the scattered beam spot is broader than before (fig. 6.13), even if it has a Gaussian and not flat profile. Moreover, considering the output beam energetic spectrum centred at 4.8 MeV with a FWHM of about 7 %, a dose rate of about 10^{10} Gy/min was calculated.

In table 6.4 the obtained results are reported, evaluated at 10 cm from the foil position, where there is the best compromise between dose distribution and area value for a possible single shot cells exposure.

TABLE 6.4: Area and dose values per shot, evaluated at 80% of the maximum value for different scattering configurations.

Foil	@10cm Dose [Gy]	@10cm Δx × Δy [mm^2]	@40cm Dose [Gy]	@40cm Δx × Δy [mm^2]
Ta1,5μm	1.2	4.9×3.2	1.5	3.2×3.4
Ta3μm	0.8	5.3×4.0	0.84	4.9×3.7
Au1,5μm	1.2	4.7×3.4	1.24	1.24×2.9
Au3μm	0.64	5.5×3.9	0.72	5.1×4.7

If the dose maximisation is the main goal, Ta 1.5 μm thick foil placed 10 cm far from the final collimator represents the best option. On the other hand, if the irradiated cell spot should be maximised, Au 3 μm thick foil placed 10 cm far from the final collimator should be chosen. If both parameters (dose and cell spot dimension) should be maximised Ta 1.5 μm thick foil placed 40 cm far from the final collimator is the best choice. This position actually corresponds to the beam focus (Figure 6.13).

The dose distributions are also interesting for a proof-of-principle experiment, if evaluated 20 cm

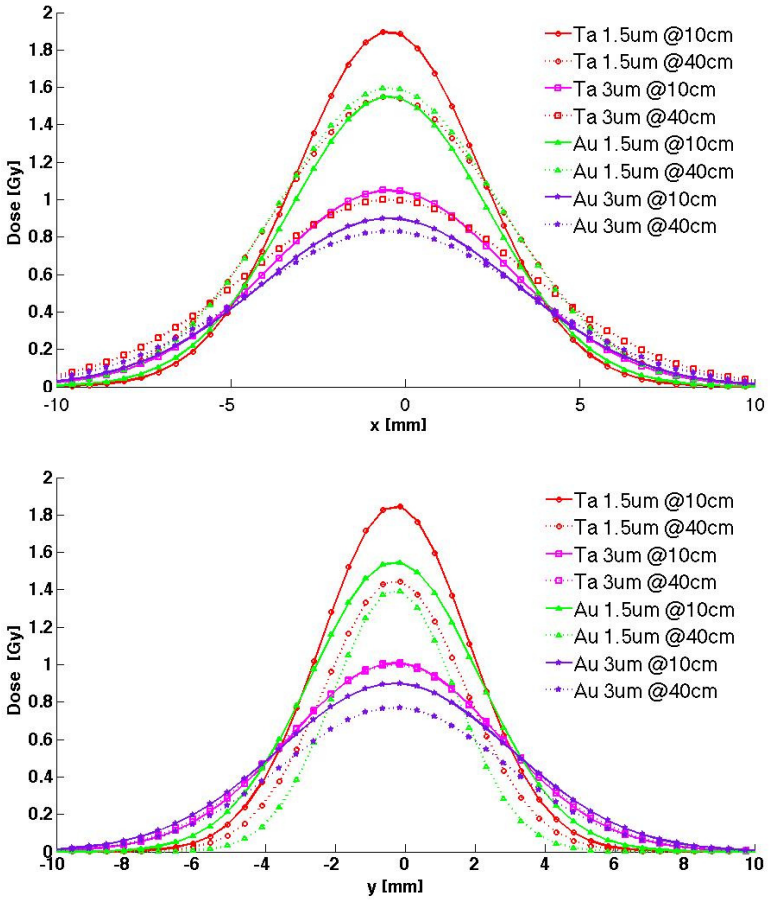

FIGURE 6.15: X (up) and Y (bottom) dose distribution profiles, evaluated at 10 cm from the foil position, when the different scattering leafs are placed 10 and 40 cm far from the final collimator.

far from the foil position. Obtained doses are about 60% less and cell spots 40% bigger as respect to the values reported in table 6.4. Dose evaluated at other distances from the scattering foil position has not reported here. Considering that 1-0.5 Gy is the desired dose, higher values on a smaller area or too low value on a broader area are, indeed, obtained if estimated at 5 cm and 30-40 cm from the foil, respectively.

Summing up, using the optimised transport beamline and the Ta 1.5 μm foil placed 40 cm far from the last ESS collimator, a cellular sample of 3.2 $\times$ 3.4 mm^2 can be irradiated with a dose of about 1.7 $\pm$ 10 %, a dose rate of about 10^{10} Gy/min and a proton beam of 4.7 MeV $\pm$ 3 %. With these parameters, significantly different respect to the features used in the experimental run described in chapter 3, a proof-of-principle radiobiological experiment can be accurately performed and considered as a relaible pre-clinical study, to understand the biological effects of the laser-driven beams structure.

6.4 An ideal case: 5 and 24 MeV selected energies

Considering the operational energy range [1-30] MeV of the presented transport beamline, a preliminary set of Monte Carlo simulations have been performed using, as input, a typical laser-driven proton beam, with an exponential shaped energy spectrum defined in [0-55] MeV (see fig. 6.17) and an energy-dependent angular function. In order to reproduce the real experimental data observed in chapter 5, higher energy particles have been simulated with a narrower angular distribution, for instance 5 and 25 MeV protons have been described with an angular divergence of 20 deg and 5 deg, respectively. The setup has been optimised in order to have 5 MeV, like before, and 24 MeV as selected output energies. As first step, a set of simulations has been performed using only the ESS (Φ_{in}=8mm, Φ_{out}=6mm, 1×8 mm^2 slit aperture), placed 60 mm far from the source point. As second step the collection system has been added to the energy selector. Figure 6.16 reports the two different configurations, preliminary optimised for the two desired energies.

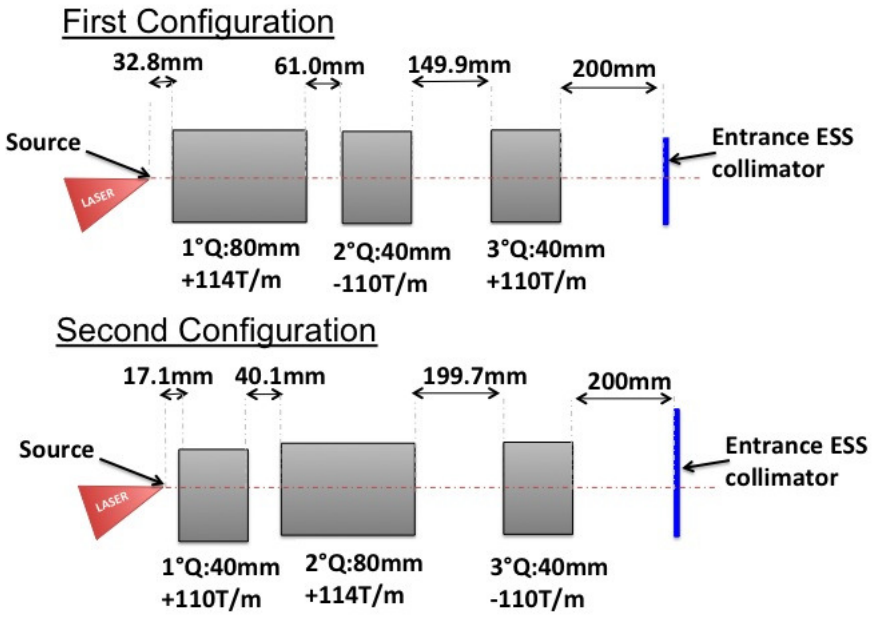

FIGURE 6.16: Details of the final PMQs setups, optimised for a 5 MeV (top) and 24 MeV (bottom) proton beam transmission.

The obtained output beams have been then evaluated downstream the second ESS collimator, in terms of energy spectrum, fitted with a Gaussian function, and transmission efficiency, as ratio between the output and the input number of particles considered in the same energetic window. Figure 6.17 shows the output energy spectra, obtained when only the ESS or the whole transport beamline (TBL) have been simulated. In the same plot, the input spectrum has been reported in an appropriate log scale, as well. A quantitative evaluation of the output beams characteristics is reported in table 6.5.

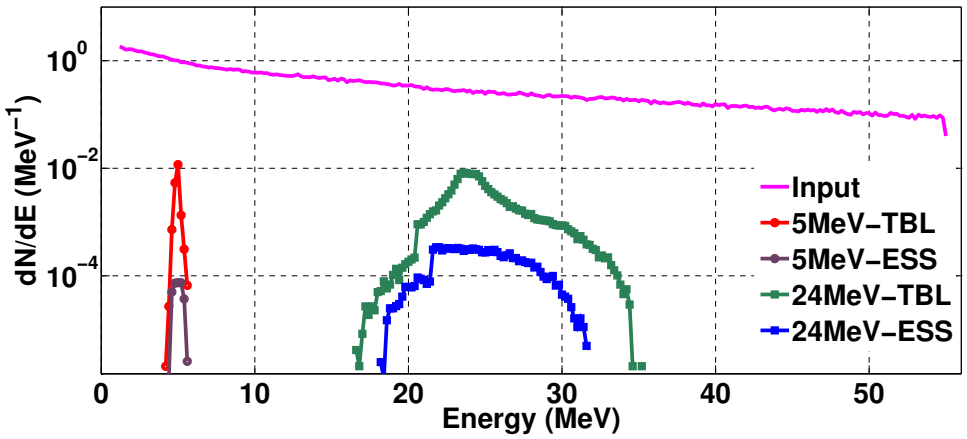

FIGURE 6.17: Input and output energy spectra, obtained when only the ESS or the whole transport beamline (TBL) have been simulated.

TABLE 6.5: Output beam characteristics for the two selected energies.

	E [MeV]	**FWHM**	**Transmission Efficiency**
ESS	5	14.1 %	0.007 %
TBL	5	5.2 %	1.2 %
ESS	24	25.9 %	0.1 %
TBL	24	13.5 %	2.3 %

Obtained results show that only the energy selector system conveniently coupled to the collection system (TBL) allows to select output beams with defined energy spectra and transmission efficiencies in the whole TBL operational energy range.

More detailed investigations should be performed. The reported study at high energy is, indeed, preliminary.

Conclusions and future perspective

Cancer rank is the second biggest cause of death in developed countries, behind cardiovascular diseases. It is estimated that one-third of the population will develop a tumour within their lifetime. These statistics single out cancer prevention and treatment as one of the major societal challenges worldwide, and motivate research into novel, more effective ways of fighting cancer.
Radiotherapy is a broadly used approach for the cancer treatment. However, although energetic photons are widely used, ion beams are much more effective thanks to their physical dose deposition pattern. The tumour control probabilities are indeed comparable to, or exceed, those achieved with conventional radiotherapy, moreover the side effects are considerably reduced, which, for example makes this type of treatment particularly suitable for pediatric tumours.
Unfortunately only about 42 centres have been already realised worldwide to perform treatments with protons and heavier ions (i.e. carbon). The large cost of conventional accelerators (synchrotron, cyclotron or linac) represents indeed the main limiting factor for a wider availability of this kind of treatment, when compared for example with X-ray radiotherapy, virtually available in any large hospital. In this background, the idea of future facilities based on laser-driven ion accelerators has been proposed as a way of reducing complexity and cost.
Hadrontherapy represents only one of the possible applications of laser-driven beams. It is chosen as demonstration-case of this thesis, considering that it is the most demanding in terms of beam handling and control.
Significant effort, at laser/target level as well as by means of customised transport beamlines, is currently ongoing in several facilities world wide in order to demonstrate the possible clinical application of laser-driven beams.
Moreover, also pre-clinical studies were performed to understand if the biological effectiveness of laser-driven beams is different in respect to the conventional ones. The temporal structure and therefore the dose rates per pulse are indeed completely different: 10^9 Gy/s and 1-10 Gy/min for laser-driven and conventional beams, respectively. In literature, some papers already report preliminary results in this field, but more investigations are still necessary with more controlled beams and dose distributions.
For instance, in chapter 3, an experimental campaign dedicated to pre-clinical studies is described. In particular the clonogenic assay and the sublethal cytogenetic damage were investigated irradiating Human Umbilical Vein Endothelial Cells (HUVEC). During the run, CR-39s, Image Plates and Radiochromic films were used to study the beam features on the cells plane. Simultaneously several simulation sets have been also performed, using the Geant4 Monte Carlo toolkit.
Thanks to a simple transport beamline, based on a dipole and on a drift sector, protons of 6, 9 and 14 MeV with an energetic spread of about $\pm$ 9% and dose values of about 4.5 $\pm$ 0.8, 1.8$\pm$ 0.5 and 0.6$\pm$ 0.2 Gy were used for the cellular irradiation (dose rate of about 3×10^9 Gy/sec per shot).
The analysis of the investigated biological end-points was then performed and compared with respect to the corresponding measurements obtained with conventional beams, showing no significant differences. It seems that laser-driven protons have the same biological effectiveness of conventional

beams. However, considering the significant energy spreads and dose uncertainty, the obtained results have demonstrated that the irradiation conditions need to be improved. Therefore, to reach the required accuracy for radiobiology experiments, it is desirable to better handle and control the transported beam.

According to this requirement, a new transport beamline solution has been proposed and already realised at INFN-LNS. As described in chapter 4, it is based on two main elements. The first part is composed by a set of four NdFeB permanent magnetic quadrupoles (PMQs), located just downstream the target to reduce the divergence of the primary beam and to perform its collection and preliminary energy selection. The second part is an energy selection system (ESS), composed by four magnetic permanent dipoles with alternate polarity and designed for the final energy selection. In addiction to a precise description of the transport beamline prototypes, in chapter 4, 5 and 6 results from their tests are reported together with different simulative studies. Monte Carlo simulations have been indeed preliminary performed to support the design procedure and after to study the particle transport and dose distributions along the beamline. In particular, as described in chapter 2, the Geant4 (GEometry ANd Tracking) Monte Carlo toolkit has been used. It is written in the C++ language and it takes advantage from the object oriented software technology, which allows writing a clearer and more partitioned code. Geant4 is a toolkit, i. e. a collection of libraries, with no ready-to-use default program. Indeed, the source code consists of a kernel containing all libraries and tools that the user has to include, according to the specific requirements of his application.

Using the potentiality of the Geant4 toolkit, the beamline has been simulated. The code has been based on the *hadrontherapy advanced example*, where a specific module for the laser-driven beamline was recently official added in the 10.1 Geant4 release.

The beamline was implemented with its specific geometric and magnetic features. In order to check and set some simulation parameters for the best compromise between accuracy and CPU time, particle tracking and beam emittance have been compared with three reference codes outputs (COMSOL, OPERA & TraceWin). Benchmarks have been also performed for each magnetic element, using the experimental data coming from tests with conventional and laser-driven beams. The PMQs has been indeed tested with a 10 MeV conventional proton beam delivered by the TANDEM accelerator at LNS, and the ESS has been fully characterised and calibrated using conventional pure monoenergetic proton beams in the energy range [4.5-12] MeV at the Laboratori Nazionali di Legnaro (LNL) in Padova and at the LNS in Catania (see chapter 4). For these tests, simulations have been performed as well, and output data compared with the experimental results. The good agreement demonstrated the reliability of the developed code and provided a validation of the magnetic element implementation.

After this preliminary characterisation with conventionally accelerated beams, the second step was the characterization of ESS and PMQs prototypes with laser-driven protons to verify their performance in their final configuration.

The test of PMQs is ongoing at LOA laboratory in Paris, while the ESS characterisation was already performed at the Taranis facility, in the Queen's University of Belfast (UK). The proton source was produced with the TNSA regime by irradiating 10 μm thick Au foil targets with a 2

$\times$ 10^{19} W/cm^2, short-pulse (700 fs) laser. Using the beam accelerated from the non-irradiated target surface, as input, and knowing the calibration curve from the test with conventional beams, protons of 4.5 and 7 MeV have been selected and studied in terms of energy spread and fluence, as described in chapter 5. In particular energy spreads of about $\pm$ 10% and fluence values of about 1.0 $\times$ 10^6 p/cm^2 have been measured for both energies. A good agreement has been obtained between experimental and simulated data. Some discrepancies have been found for 7 MeV, maybe due to a lower statistics.

After the mentioned characterisations of the single elements with both conventional and laser-driven beams, the final goal is represented by the test of the whole transport beamline, composed by the two prototypes, properly coupled. At this aim, experimental campaigns could be planned for the next months, at the TARANIS facility (Belfast, UK) and at LOA laboratory (Paris, Fr).

To realistically study the configuration to be used in future experimental campaigns, Monte Carlo simulations of the whole transport beamline was performed, as presented in chapter 6. The purpose was to optimise the coupling of PMQs and ESS for the 5 MeV proton selection. This energy has been chosen considering the energy distributions available in many laser facilities and especially the spectra of the input proton beams available at the TARANIS facility and at LOA laboratory, where the experimental runs could be planned. Moreover, in order to take into account the shot-to-shot instabilities, several input angular distributions have been implemented. Three different setups were then compared: only energy selector, only collection system and the whole transport beamline, optimised for the best injection of the beam, coming from the collection system, in the energy selector. The main task was to obtain a controlled output beam in terms of energy and angular distributions with the highest transmission efficiency.

This study showed that, using the two systems in a separate configuration, a compromise between transmission efficiency and energy spread cannot be reached, as it is in case of coupling the two systems. Indeed, for the ESS alone the number of transmitted protons was lower, on the other side for the quadrupole system alone the energy spectrum had significant undesired contributions. Only the optimised transport beamline allowed to obtain a 5 MeV proton beam with, as final features, a FWHM of about 7% and a divergence of about $\pm 0.5^\circ$, independently from the shot-to-shot instabilities. Moreover, values two orders of magnitude bigger were obtained for the transmission efficiency if the two coupled systems are used.

The produced beam was finally used to perform a a simulation reproducing a proof-of-principle radiobiological experiment, that could be carried out to investigate different radiobiological end-points with high dose-rate, small energy spread and well controlled dose distribution.

Indeed, using the proposed transport beamline and the Ta 1.5 μm foil placed 40 cm far from the last ESS collimator, a cellular sample of 3.2 $\times$ 3.4 mm^2 could be irradiated with a dose of about 1.7 $\pm$ 10 %, a dose rate of about 10^{10} Gy/min per shot and a proton beam of 4.7 MeV $\pm$ 3 %. With these parameters a radiobiological experiment could be performed to futher study the biological effects of laser-driven beams.

Thanks to experimental and simulative studies reported in this thesis, the control of laser-driven beams thanks to a compact transport beamline was demonstrated. Even if the obtained results are not sufficient yet for an extended feasibility study related to hadrontherapy applications, they

represent an important step towards future and more systematic studies. Indeed the presented beamline solution was considered as a prototype of a new transport beamline that will be installed at the ELI-Beamlines facility in Prague (Cz), which is one of the four sites of the Extreme Light Infrastructure (ELI) project.

ELI is a new Research Infrastructure, part of the European ESFRI Roadmap. Its aims are to host the most world-wide intense lasers (up to 10 PW), with few femtoseconds (10-15 fs) pulse duration and to carry on new interdisciplinary research activities based on these lasers and on the secondary radiations derived from them, finally making them available to an international scientific user community.

In particular, the ELI-Beamlines facility, that is currently under construction near Prague (Czech Republic), will mainly focus on the development of short-pulse secondary sources of radiation and particles and on their multidisciplinary applications in molecular, biomedical and material sciences, physics of dense plasmas, warm dense matter and laboratory astrophysics.

In 2014 the FZU (ELI-Beamlines) launched a public tender to realise the beam transport, the dosimetric and the irradiation section of the ELIMAIA beamline, representing the ELI-Beamlines areas specifically dedicated to the ion acceleration and their applications. The INFN-LNS has been officially appointed through a three years contract for this delivery. ELIMED will represent the section of ELIMAIA addressed to the transport, handling and dosimetry of laser-driven ion beams and to the achievement of stable, controlled and reproducible beams that, in the future, will be available for users interested in multidisciplinary and medical applications of such innovative technology. The transport beamline that will be installed at ELIMAIA will be made of three main elements: a collection system, namely a set of permanent magnet quadrupoles that will be placed close to the laser-interaction point, an energy selection system (ESS) based on four resistive dipoles, and a set of conventional electromagnetic transport elements. The beam-line will be working for laser-produced beams up to 60 AMeV, offering, as output, a controllable beam in terms of energy spread (varying from 5% up to 20% for the highest energies), angular divergence and hence, manageable beam spot size in the range 0.1-10 mm and acceptable transmission efficiency (namely 10^6-10^{11} ions/pulse). Studies are currently ongoing to fullfil these requirements and to finalise the design of this new, more performant transport beamline.

The multidisciplinary and medical applications of controlled laser-driven beams seem to be now a real possibility for the future and accurate feasibility studies can be done in the next years. Thanks to the recent improvements, both on the technological and scientific side, further and systematic studies will be indeed performed with these non-conventional beams: fields currently unknown will be investigated and new ideas could rise.

Appendix A

Detectors

In this appendix I give an overview of the different detectors used during the experimental campaigns together with the spectroscopic method, crucial for the input energy spectrum measurements. In particular, the working principles for the following detectors are described: CR39 solid detectors, Imaging Plate detectors and Radiochromic film.

A.1 CR-39

CR-39s are solid state nuclear track detectors for protons and heavy ions [58, 151]. Respect to other types of detectors, CR39s have the particular advantage of being sensitive to single ion events and, at the same time, relatively insensitive to other forms of radiation, such as gamma rays, x rays and electrons. For these reasons, they have therefore been a preferred ion detector and has even been combined with the other types of detectors in many recent high energy, laser accelerated ion beam experiments.

CR-39s are clear, colourless, rigid plastics, with a density of 1.30 g/cm^3, chemical formula $C_{12}H_{18}O_7$, and are made out of the polyallyl diglycol carbonate (PADC) resin. They have been widely used since the 1980s as solid state nuclear track detectors. Heavy nuclei, as well as light particles, such as protons or α particles, with energy greater than 100 keV, damage the bulk material leaving etchable tracks.

Tracks are caused by the breaking of the polymeric bonds in the plastic matrix along the particle path, due to its linear energy transfer. In this case, the electrons are removed from their initial position in the bulk material (electron defect), leaving a "narrow cylinder, which is densely filled with excess positive ions." These ions "strongly repel one another and are ejected into interstitial positions surrounding a now depleted core region." [100]

Considering particles with a given nuclear atomic number Z, the penetration depth gets larger with increasing particle energy. On the other hand, for a given particle energy, the penetration depth gets larger as Z decreases. For the same nuclear charge, the track diameter gets bigger as the mass increases, especially for light particles, where the heavier isotopes will leave larger tracks.

The created particle tracks are made visible by chemical etching in hot, concentrated alkali solutions

(mainly NaOH or KOH). The average diameter of the tracks left on the surface of the plastic will depend on the incident mean energy of the particles as well as on the CR-39s processing. For instance the size of tracks gets larger with increased etching durations and, fixing the etching time, for lower energy, as shown in figure A.1 [151].

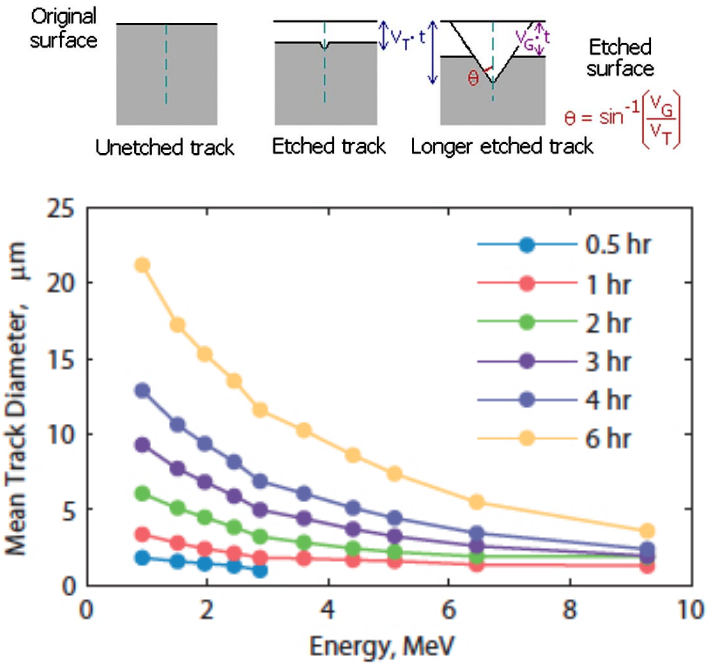

FIGURE A.1: On the top: progressive effects of etching a track detector [160]. On the bottom: proton track diameters as a function of incident mean energy for various etch times, from 30 minutes up to 6 hours in a 6 N NaOH solution at 80°C [151].

Also the temperature of the solution is crucial for the track diameter as well as for its uniformity, as shown in figure A.2.

Typically, the CR-39 plates are etched in time steps of 10-20 minutes. After each step, images are taken under the microscope to reveal tracks corresponding to different energies. The etching and controlling of the detectors in several steps are necessary, particularly for protons with higher energies since they require longer etching time for their pits to become large enough to be counted. However the right etching time is also a crucial parameter in order to avoid the signal saturation, as reported in figure A.3 where the maximum detectable fluence value is reported as a function of the track diameter that, as known, increases with the etching time [100].

Optimised the etching procedure and knowing the response of CR-39s to a given particle for a given energy range, spectral information, fluence value and spatial distribution about the particles incident on the surface of the plastic detector can be obtained. In this thesis the CR-39s were used only to perform fluence measurements.

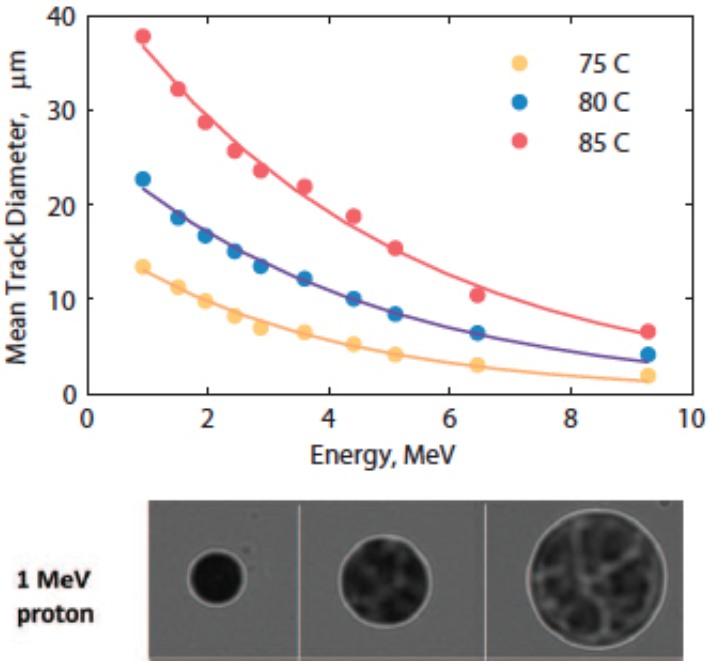

FIGURE A.2: On the top: proton track diameter as a function of incident mean energy for various etchant temperatures, in a 6 N NaOH solution for 6 hours. On the bottom: microscope images (at 40x magnification) of 1 MeV proton tracks on CR-39, illustrating the non-uniformity of track contrast with increasing etchant temperature from 75 to 80 and 85 °C, respectively [151].

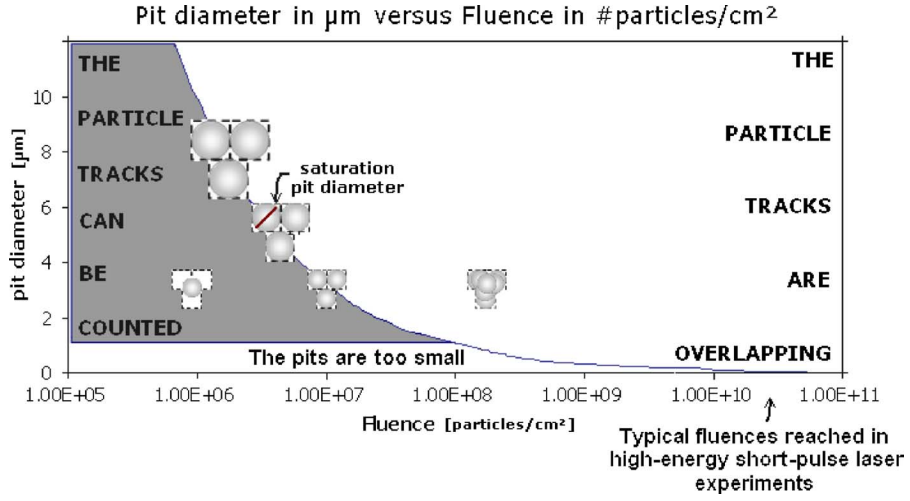

FIGURE A.3: This graph shows, as a function of track diameter vs fluence, when the tracks are separated (can therefore be individually counted) and when they are overlapping [100].

A.2 Image Plate (IP)

Image Plates (IPs) are mostly used as x-ray imaging detector for medical applications. However, they can also reveal different particles, such as ions and electrons. They are sensitive to a wide range of particle energies, can be reused, are insensitive to electromagnetic noise and have a good spatial resolution, which is limited by the scanner, typically 25 or 50 μm. For all of these reasons, recently they are also widely used in laser-matter interactions field, like in the experiments described in this thesis.

IPs, originally developed by Fuji and Kodak, have the form of a flexible plastic sheet with a layer of active material on one side. In particular, depending on their type, IP detector consists of 3 or 4 layers: a protective layer, a phosphor layer (active layer), a support and a magnetic layer. The standard IP phosphor composition is $BaF(Br_{0.85}I_{0.15}) : Eu^{2+}$.
When particles pass through the phosphor layer, Eu^{2+} is ionised in Eu^{3+}. The photoelectron is ejected into the conduction band of the phosphor crystals, where it becomes trapped in a lattice defect, called an F centre and created by the absence of halogen ions (F, Br, or I). These states are metastable and the spontaneous recombination of the trapped electron and the Eu^{3+} can occur, if thermally activated. This is called $fading$ and the fade rate is described by an exponential decay function.
After exposure, therefore after the energy storing of the considered input beam, the plates are placed in a reader, where they are scanned with a narrow $HeNe$ laser beam. The laser excites the trapped photoelectron from the F centre into the conduction band where it recombines with the Eu^{3+}, releasing a photon characterized by $\lambda \approx 390nm$.
A photomultiplier tube (PMT) finally collects this photostimulated luminescence (PSL). The output is therefore processed, i.e. amplified and digitized, leading to a PSL-value for each scanned pixel. The total read signal is proportional to the amount of stored energy from the primary beam interaction with the IP. The described reading process is shown in figure A.4.

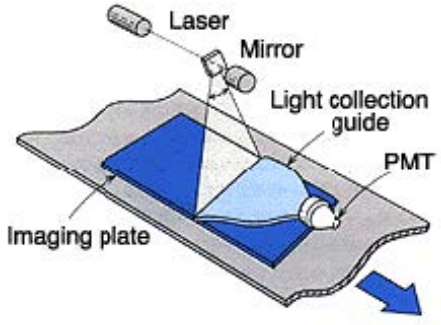

FIGURE A.4: Principle of reading the radiation image from the Imaging Plate: the exposed IP, while being conveyed, is scanned with a focused laser beam. The PSL released upon the laser is collected into the photomultiplier tube (PMT) through the light collection guide and is converted to electric signals.

The de-excitation procedure is done using a commercial scanners designed for medical imaging. Measurements should be carried out in the dark room in order to minimize the loss of the signal caused by ambient light. After the readout process, 60%-90% of the stored image, depending on the model of IP reader used, is removed. The residual image on the IP can be completely erased by exposure to visible light for 10-15 minutes. The plate is then ready for reuse [161–164].
Considering the working principle, for a fixed particle, IP has an energy-dependent response function. For instance, protons with different energy release a different amount of energy in the IP. Figure A.5 shows the experimental calibration curve of PSL value (per proton) as a function of the energy [163].

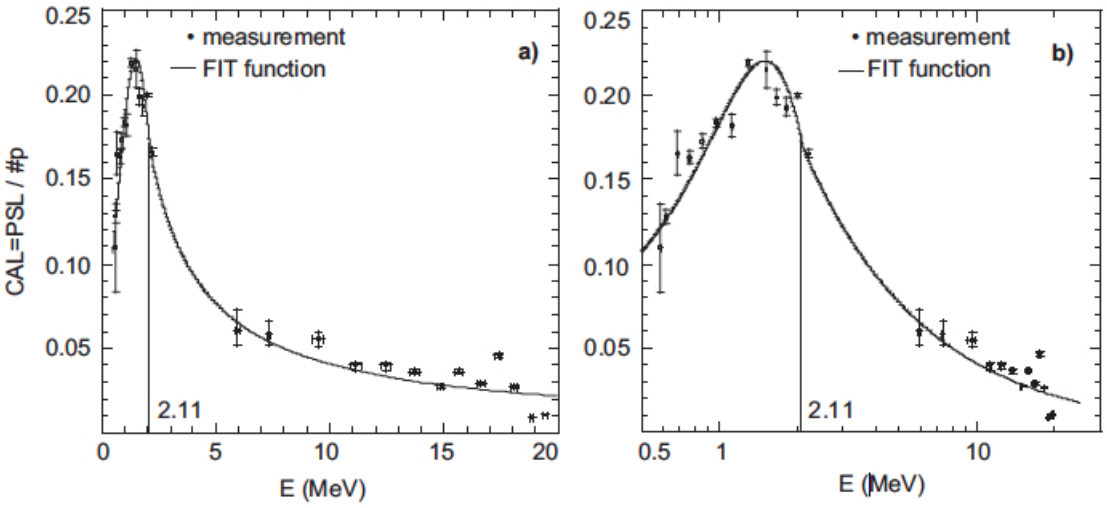

FIGURE A.5: Calibration curve that vertically relates the PSL signal to the number of protons detected by the IP and horizontally represents the proton energy in MeV a) in regular scale and b) in logarithmic scale. Dots represent the measured data that were fitted with two different functions: for energy less than 2.11 MeV and for energies in the range [2.11-20] MeV. Different fitting regions are separated by a vertical line [163].

A.3 Radiochromic film

Radiochromic films are widely used for dosimetry measurements in clinical radiation oncology [165], thanks to their small energy dependence, high spatial resolution (of the order of tens microns) and water-equivalence.

The film sensitivity is based on a solid solution of colourless crystalline diacetylene monomer (sensitive component) coated on a flexible film base. When the active component is exposed to any kind of radiation, it reacts to form a blue coloured polymer (self-developing films). This self-developing film has a spatial resolution of more than 10^4 dots per inch (dpi) or less than 2.54 μm according to the manufacturer, even though it is limited by the scanner up to 50-200 μm.

The change in optical density (OD), following a dose deposition in the gafchromic films, may be measured with transmission densitometers, film scanners or spectrophotometers. A simple analysis of the irradiated film can be obtained by using flatbed RGB scanners in the red channel [166]. Attention should be paid to the time of reading. Nearly complete dyeing of the film (90%) appears within milliseconds. However, during the first 24 hours after irradiation, an increasing dyeing cannot be neglected. It is therefore recommended to read films at the earliest of 2 days after exposure, as it was done for the data reported in this thesis.

Recent experimental studies have demonstrated a clear independence of Gafchromic response from the dose rate [167]. This characteristic is obviously essential, especially for the highly pulsed laser-driven proton beams. In detail, for the experimental measurements reported in chapters 3 and 5, EBT3, HD-810 and HD-V2 types have been used, according to their different operational ranges: [0.01-40]Gy for EBT3, [10-400]Gy for HD-810 and [10-1000]Gy for HD-V2 [168].

Structures and compositions of the used RCF types are reported in figures A.6, A.7 and A.8 respectively, together with their calibration curves obtained at INFN-LNS with 60 MeV proton beams,

using an ionization Markus chamber as reference.

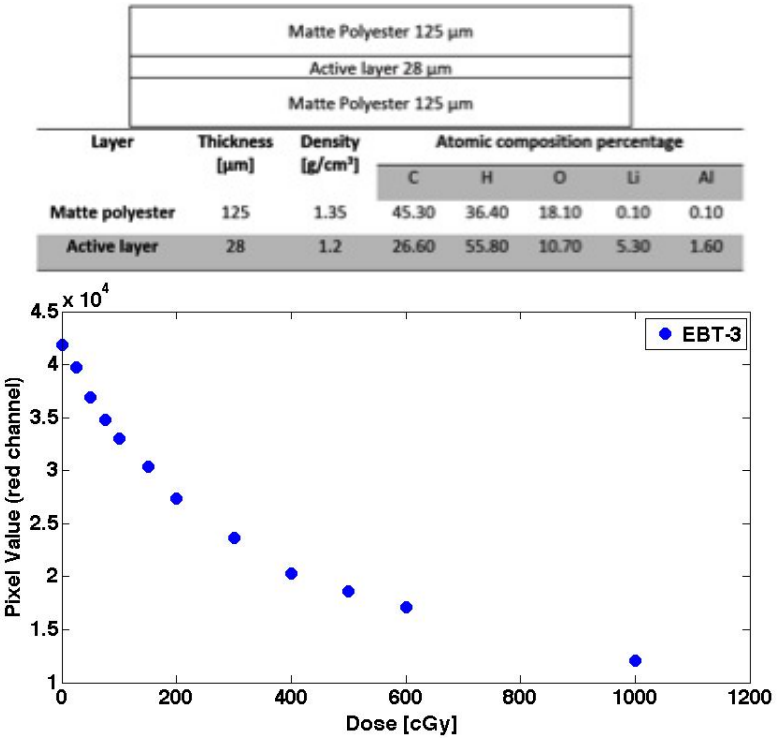

Layer	Thickness [µm]	Density [g/cm³]	Atomic composition percentage				
			C	H	O	Li	Al
Matte polyester	125	1.35	45.30	36.40	18.10	0.10	0.10
Active layer	28	1.2	26.60	55.80	10.70	5.30	1.60

FIGURE A.6: On the top: structure, relative dimensions of layers and nominal atomic abundances of GafChromic film EBT3 are reported. On the bottom: calibration curve OD in red channel vs Dose value, measured at INFN-LNS, is shown.

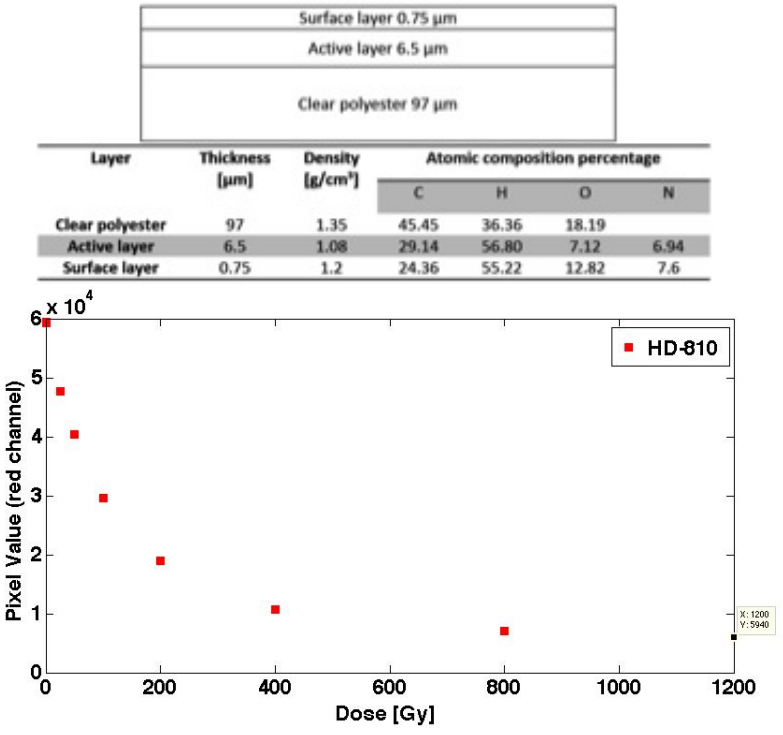

Layer	Thickness [µm]	Density [g/cm³]	Atomic composition percentage			
			C	H	O	N
Clear polyester	97	1.35	45.45	36.36	18.19	
Active layer	6.5	1.08	29.14	56.80	7.12	6.94
Surface layer	0.75	1.2	24.36	55.22	12.82	7.6

FIGURE A.7: On the top: structure, relative dimensions of layers and nominal atomic abundances of GafChromic film HD-810 are reported. On the bottom: the calibration curve OD in red channel vs Dose value, measured at INFN-LNS, is shown.

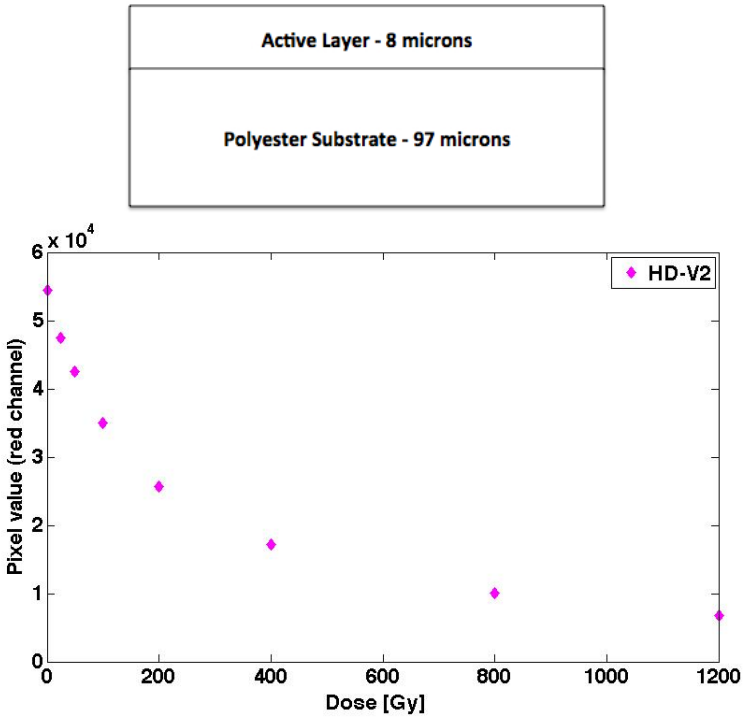

FIGURE A.8: On the top: relative dimensions of layers of GafChromic film HD-V2 is reported. On the bottom: calibration curve OD in red channel vs Dose value, measured at INFN-LNS, is shown.

For both the calibration and the experimental runs the same lot numbers have been used. There could be, indeed, some differences in the film manufacturing among different lots and therefore different responses.

A.4 Spectroscopic method

Due to the particular characteristics (broad energy spectra and extremely high dose per pulse) of the optical-accelerated beams available nowadays in the laser facilities, the dosimetry is extremely challenging. RCF and CR-39 can be used as single detector or in stack configuration in order to have quantitative information on the energy spectrum of the accelerated protons [92, 147, 149]. Indeed, an accurate measurement of the energy spectrum is necessary.

In the experimental run reported in this thesis, RCF films in stack configuration have been used to measure the proton beam generated by the laser-target interaction. A full characterization of their response was performed and a spectroscopic method developed and tested in a preparatory phase at INFN-LNS.

For the spectroscopic method development, one of the main drawbacks is the dependence of their response from the ion beam energy. In fact, when the proton beam energy decreases, the higher LET (Linear Energy Transfer) values results in a saturation of the film output, probably related to local saturation processes at the track level [169]. Taking into account these LET effects, by means of a correction factor (experimentally checked at INFN-LNS with respect to the Markus Chamber dose measurement), the deconvolution procedure has been finalized and tested, and obtained results have been finally successful compared with the Monte Carlo simulations outputs (Geant4 toolkit).

In particular, the spectroscopic method has been tested with a polychromatic spectrum coming from a wheel modulator, which is a typical clinical device used in proton therapy to achieve Spread Out Bragg Peaks (SOBPs). The proton depth dose distributions in water, reproduced using HD-810 films, Advanced Markus chamber and Geant4 simulations, are shown in figure A.9. RCF data are reported without taking into account the correction factor. From the plot is clear the agreement between the experimental measures and the Monte Carlo simulations.

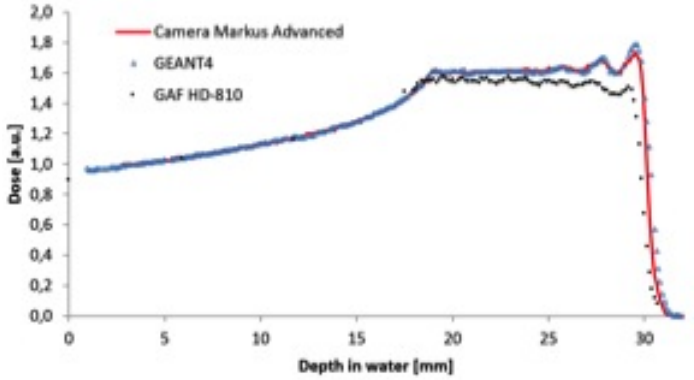

FIGURE A.9: A comparison among the proton depth dose distributions in water reproduced using HD-810 films (no correction factor is applied), the Advanced Markus chamber and the Geant4 simulations [150].

The stack of HD-810 has been then used to reconstruct the energy spectrum, exploiting the developed spectroscopic procedure. Figure A.10 shows the proton energy spectrum relative to the depth dose distribution of figure A.9. Dots represent the experimental measurements obtained from the gafchromic analysis while the line represents the simulation results. As shown, the agreement

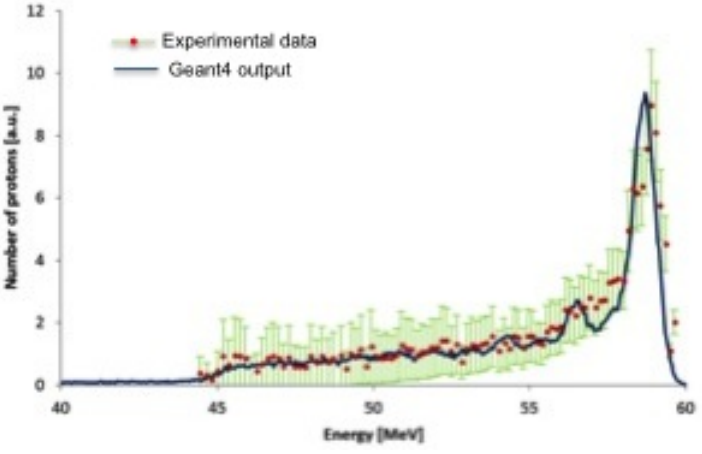

FIGURE A.10: Comparison between the energy spectrum obtained from the HD-810 films analysis (dots) and the simulation results (line) [150].

appears quite good and within the experimental uncertainties [150].

The developed deconvolution method, widely used during each experimental run reported in this thesis, has been based on [15, 113, 170].

Bibliography

[1] K. Flippo D. Umstadter A. Maksimchuk, S. Gu and V. Y. Bychenkov. Forward ion acceleration in thin films driven by a high-intensity laser. *Phys. Rev. Lett.*, 84:4108, 2000.

[2] E. L. Clark et al. Measurements of energetic proton transport through magnetized plasma from intense laser interactions with solids. *Phys. Rev. Lett.*, 84:670, 2000.

[3] R. A. Snavely et al. Intense high-energy proton beams from petawatt-laser irradiation of solids. *Phys. Rev. Lett.*, 85:2945, 2000.

[4] M. Borghesi A. Macchi and M. Passoni. Ion acceleration by superintense laser-plasma interaction. *Rev. Mod. Phys.*, 85:751, 2013.

[5] K W D Ledingham and W Galster. Laser-driven particle and photon beams and some applications. *New Journal of Physics*, 12:045005, 2010.

[6] *Short Pulse Laser Interaction with Matter.* 2005.

[7] A. Tramontana. Produzione di plasmi-laser e monitoraggio con spettrometro di thomson per applicazioni medicali. Master's thesis, Universitá degli studi di Messina, 2012.

[8] F. Schillaci. Modellizzazione e diagnostica di fasci di ioni accelerati otticamente. Master's thesis, Universitá degli studi di Catania, 2012.

[9] *The Physics of Plasma.* 2011.

[10] *A Superintense Laser–Plasma Interaction Theory Primer.* 2013.

[11] M. Zakova. Handling and transport of laser-driven ion beams. Master's thesis, Czech Technical University in Prague, 2013.

[12] P. Sprangle E. Esarey and J. Krall. Laser acceleration of electrons in vacuum. *Phys. Rev. E*, 52:5443–5453, 1995.

[13] Marius S. Schollmeier. *Optimization and control of laser-accelerated proton beams.* PhD thesis, Technische Universitat Darmstadt, 2008.

[14] M. Sc. Simon Busold. *Construction and characterization of a laser-driven proton beamline at GSI.* PhD thesis, Technische Universitat Darmstadt, 2014.

[15] Frank Nurnberg. *Laser-Accelerated Proton Beams as a New Particle Source*. PhD thesis, Technische Universitat Darmstadt, 2010.

[16] P. Drude. Ueber fernewirkungen. *Ann. Phys*, 298 (12), 1897.

[17] *Fundamentals of Plasma Physics*. 2008.

[18] *The Interaction of High-Power Laser with Plasmas*. 2002.

[19] E. Lefebvre et al. Nonlinear electron heating in ultrahigh-intensity-laser-plasma interaction. *Phys. Rev. E*, 55:1011, 1897.

[20] M. I. Santala et al. Effect of the plasma density scale length on the direction of fast electrons in relativistic laser-solid interactions. *Phys. Rev. Lett.*, 84:1459, 2000.

[21] K. Adumi et al. Characterization of preplasma produced by an ultrahigh intensity laser system. *Phys. Plasmas*, 11:3721, 2004.

[22] F. N. Beg et al. A study of picosecond laser-solid interactions up to 10^{19} w/cm2. *Phys. Plasmas*, 4:447, 2004.

[23] S.C. Wilks et al. Energetic proton generation in ultra-intense laser-solid interactions. *Phys. Plasmas*, 8:542, 2001.

[24] S. A. Gaillard et al. Nearly 70 mev laser-accelerated-proton beams from micro-cone targets via laser grazing. *Phys. Rev. Lett.*, 2010.

[25] P. McKenna et al. Characterization of proton and heavier ion acceleration in ultrahigh-intensity laser interactions with heated target foils. *Phys. Rev. E*, 70:036405, 2004.

[26] J. J. Santos et al. Fast electron transport in ultraintense laser pulse interaction with solid targets by rear-side self-radiation diagnostics. *Phys. Rev. Lett*, 89:025001, 2002.

[27] K. L. Lancaster et al. Measurements of energy transport patterns in solid density laser plasma interactions at intensities of $5\text{x}10^{20}$ w/cm2. *Phys. Rev. Lett.*, 98:125002, 2007.

[28] L. Bertagna M. Passoni and A. Zani. Target normal sheath acceleration: theory, comparison with experiments and future perspective. *New J. Phys.*, 12:045012, 2010.

[29] J. Fuchs et al. Laser-driven proton scaling laws and new paths towards energy increase. *Nature Physics*, 2:48, 2006.

[30] T. Burris-Mog et al. Laser accelerated protons captured and transported by a pulse power solenoid. *PHYSICAL REVIEW SPECIAL TOPICS-ACCELERATORS AND BEAMS*, 14: 121301, 2011.

[31] K. Zeil et al. The scaling of proton energies in ultrashort pulse laser plasma acceleration. *New Journal of Physics*, 12:045015, 2010.

[32] M. Roth et al. Energetic ions generated by laser pulses: A detailed study on target properties. *Physical Review Special Topics-Accelerators and Beams*, 5:061301, 2002.

[33] L. Laska et al. Angular distributions of ions emitted from laser plasma produced at various irradiation angles and laser intensities. *Laser and Particle Beams*, 26:555, 2008.

[34] Strickland D and Mourou G. Compression of amplified chirped optical pulses. *Opt. Commun.*, 56:219, 1985.

[35] Barty C P J Mourou G A and Perry M D. Ultrahigh-intensity lasers: physics of the extreme on a tabletop. *Phys. Today*, 1998.

[36] M. Allen et al. Direct experimental evidence of back-surface ion acceleration from laser-irradiated gold foils. *Phys. Rev. Lett.*, 93:265004, 2004.

[37] V. Malka et al. Practicability of protontherapy using compact laser systems. *Med. Phys*, 31: 1587, 2004.

[38] J. Fuchs et al. Comparison of laser ion acceleration from the front and rear surfaces of thin foils. *Phys. Rev. Lett.*, 94:045004, 2005.

[39] S. Bahk et al. Generation and characterization of the highest laser intensities (10^{22} w/cm2). *Opt. Lett.*, 29:2837, 2004.

[40] S. V. Bulanov et al. Laser ion acceleration for hadron therapy. *Physics - Uspekhi*, 57 (12): 1149–1179, 2014.

[41] T. Elsasser D. Schardt and D. Schulz-Ertner. Heavy-ion tumor therapy: Physical and radiobiological benefits. *REVIEWS OF MODERN PHYSICS*, 82:383 –417, 2010.

[42] R. Orecchia et al. Clinical and research validity of hadrontherapy with ion beams. *Critical Reviews in Oncology/Hematology*, 51 (2):81–90, 2004.

[43] Schulz-Ertner D. and Tsujii H. J. Particle radiation therapy using proton and heavier ion beams. *Critical Reviews in Oncology/Hematology*, 25:953, 2007.

[44] R. R. Wilson. Radiological use of fast protons. *Radiology*, 47:487, 1946.

[45] J. H. Lawrence. Proton irradiation of the pituitary. *Cancer Res.*, 10:795, 1957.

[46] . URL http://ptcog.web.psi.ch/ptcentres.html.

[47] J. Ferlay et al. Cancer incidence and mortality patterns in europe: Estimates for 40 countries in 2012. *European Journal of Cancer*, 49:1374–1403, 2013.

[48] G. J. Caporaso et al. A compact linac for intense modulated proton therapy based on a dielectric wall accelerator. *Phys. Med.*, 98:24, 2008.

[49] Schippers J M and Lomax A J. Emerging technologies in proton therapy. *Acta Oncol.*, 50: 838, 2011.

[50] U. Linz and J. Alonso. What will it take for laser driven proton accelerators to be applied to tumor therapy? *PHYSICAL REVIEW SPECIAL TOPICS - ACCELERATORS AND BEAMS*, 10:094801, 2007.

[51] Ludewigt B A Chu W T and Renner T R. Instrumentation for treatment of cancer using proton and light ion beams. *Rev. Sci. Instrum.*, 64:2055, 1993.

[52] E. Pedroni et al. The 200-mev proton therapy project at the paul scherrer institute: conceptual design and practical realization. *Med. Phys.*, 22:37–53, 1995.

[53] G. Kraft. What we can learn from heavy ion therapy for radioprotection in space. *Physica Medica*, 17 (1):13–20, 2001.

[54] URL http://www.icru.org.

[55] URL http://www.aapm.org.

[56] R. F. Service. Laser labs race for the petawatt. *Science*, 154:301, 2003.

[57] S. Sinigardi et al. High quality proton beams from hybrid integrated laser-driven ion acceleration systems. *NIM A*, 740:99–104, 2014.

[58] B. M. Hegelich et al. *Nature*, 439:441, 2006.

[59] G.A.P. Cirrone et al. Transport and dosimetric solutions for the elimed laser-driven beam line. *NIM A*, 796:99–103, 2015.

[60] C. Richter et al. A dosimetric system for quantitative cell irradiation experiments with laser-accelerated protons. *Phys. Med. Biol*, 56:1529–1543, 2011.

[61] *Monte Carlo: concepts, algorithms and applications*. New York: Springer, 1995.

[62] N. Metropolis. The beginning of the monte carlo method. *Los Alamos Science, Special Issue*, pages 125–130, 1987.

[63] Stan Ulam R. Eckhardt and John von Neumann. *Los Alamos Science, Special Issue*, 15: 131–137, 1987.

[64] F. Romano. *Monte Carlo simulations of carbon ions fragmentation in hadronterapy*. PhD thesis, Universita' degli Studi di Catania, 2009.

[65] S. Guatelli et al. Transferring advanced physics research tools to education: how to teach simulation tools used in radiation physics research to university students. *Proceeding Records, International Technology, Education and Development Conference (INTED2010), Valencia, Spain*, 2010.

[66] H. Hirayama W. R. Nelson and D. W. O. Rogers. The egs4 code system. *SLAC-256. Stanford Linear Accelerator Center, Stanford, California*, 1985.

[67] F. Salvat et al. Penelope, a code system for monte carlo simulation of electron and photon transport. *Proceedings of a Workshop/Training Course, OECD/NEA*, 2001.

[68] *MCNPX User's Manual, Version 2.3.0.*

[69] S. Agostinelli et al. Geant4 - a simulation toolkit. *NIM A*, 506:250–303, 2003.

[70] J. Allison et al. Geant4 developments and applications. *IEEE Transactions on Nuclear Science*, 53 (1):270–278, 2006.

[71] www.geant4.cern.ch, .

[72] https://twiki.cern.ch/twiki/bin/view/geant4/quickmigrationguideforgeant4v10, .

[73] Gene Cooperman Xin Dong and John Apostolakis. Multithreaded geant4: Semi-automatic transformation into scalable thread-parallel software. *Euro-Par 2010 - Parallel Processing Lecture Notes in Computer Science*, 6272:287–303, 2010.

[74] *Geant4 User's Guide for Application Developers.* .

[75] *Physics Reference Manual.* .

[76] G.A.P. Cirrone et al. *NUCLEAR SCIENCE and TECHNOLOGY*, 2:207–212, 2011.

[77] G. Cuttone et al. *THE EUROPEAN PHYSICAL JOURNAL PLUS*, 126:65, 2011.

[78] https://www.comsol.it.

[79] http://operafea.com.

[80] D. Uriot and N. Pich0. New implement in tracewin/partran codes: integration in external field map. *Particle Accelerator Conference, PAC*, 5:3491–3493, 2003.

[81] M. Durante and J. S. Loeffler. Charged particles in radiation oncology. *Nat. Rev. Clin. Oncol*, 7:37–43, 2010.

[82] *http://ptcog.web.psi.ch/ptcentres.html*, .

[83] et al. S.V. Bulanov. Oncological hadrontherapy with laser ion accelerators. *Phys. Lett. A*, 299:240–247, 2002.

[84] E. Fourkal et al. Intensity modulated radiation therapy using laser-accelerated protons: a monte carlo dosimetric study. *Phys. Med. Biol.*, 48:3977–4000, 2003.

[85] M. S. Kreipl et al. Interaction of ion traks in spatial and temporal proximity. *Radiat. Environ Biophysics*, 48:349–359, 2009.

[86] S. Auer et al. Survival of tumor cells after proton irradiation with ultra-high dose rates. *Radiation Oncology*, 6:139, 2011.

[87] S. D. Kraft et al. Dose-dependent biological damage of tumour cells by laser-accelerated proton beams. *New Journal of Physics*, 12:085003, 2010.

[88] A. Yogo et al. Measurement of relative biological effectiveness of protons in human cancer cells using a laser-driven quasimonoenergetic proton beamline. *Appl. Phys. Lett.*, 94:181502, 2009.

[89] A. Yogo et al. Measurement of dna double-strand break yield in human cancer cells by high-current, short-duration bunches of laser-accelerated protons. *Japanese Journal of Applied Physics*, 50:053701, 2011.

[90] D. Doria et al. Biological effectiveness on live cells of laser driven protons at dose rates exceeding 109 gy/s. *AIP Advances*, 2:011209, 2012.

[91] S. Kar et al. First results on cell irradiation with laser-driven protons on the taranis system. *AIP Conf. Proc*, 87:1546, 2013.

[92] F. Fiorini et al. Dosimetry and spectral analysis of a radiobiological experiment using laser-driven proton beams. *Phys. Med. Biol.*, 56:6969–6982, 2011.

[93] K. Zeil et al. Dose-controlled irradiation of cancer cells with laser-accelerated proton pulses. *Appl. Phys. B*, 110:437–444, 2013.

[94] *http://www.luli.polytechnique.fr/accueil/lesinstallations/luli2000/.*

[95] M. Suzuki and D. A. Boothman. Stress-induced premature senescence (sips) - influence of sips on radiotherapy-. *J. Radiat. Res.*, 48:105–112, 2008.

[96] K. Itabana et al. Methods to detect biomarkers of cellular senescence: the senescence-associated beta-galactosidase assay. *J. Radiat. Res.*, 371:21–31, 2007.

[97] R.J. Sabin and R. M. Anderson. Cellular senescence - its role in cancer and the response to ionizing radiation. *Genome Integrity*, 2:2–9, 2011.

[98] G. Schettino et al. Low-dose studies of bystander cell killing with targeted soft x rays. *Radiat Res.*, 160(5):505–11, 2003.

[99] A. Szydlowski et al. Application of solid-state nuclear track detectors of the cr-39/pm-355 type for measurements of energetic protons emitted from plasma produced by an ultra-intense laser. *Radiation Measurements*, 44:881–884, 2009.

[100] S. Gaillard et al. Study of saturation of cr39 nuclear track detectors at high ion fluence and of associated artifact patterns. *REVIEW OF SCIENTIFIC INSTRUMENTS*, 78:013304, 2007.

[101] J. B. Farr et al. Clinical characterization of a proton beam continuous uniform scanning system with dose layer stacking. *Med. Phys.*, 35 (11):4945, 2008.

[102] G. Cuttone et al. Use of 62 mev proton beam for medical applications at infn-lns: Catana project. *Physica Medica*, 17, 2001.

[103] M. Folkard et al. Inactivation of v79 cells by low-energy protons, deuterons and helium-3 ions. *Int. J. Radiat. Biol.*, 49:729–738, 1996.

[104] P. Wilson et al. Revisiting the ultra-high dose rate effect: implications for charged particle radiotherapy using protons and light ions. *Br. J Rad.*, 85:933, 2012.

[105] C-M Ma E. Fourkal, I. Veltchev and J. Fan. Linear energy transfer of proton clusters. *Phys. Med. Biol*, 56:3123, 2011.

[106] S. V. Bulanov et al. Oncological hadrontherapy with laser ion accelerators. *Phys. Lett.*, 299: 240–247, 2002.

[107] P. R. Bolton et al. Toward integrated laser-driven ion accelerator systems at the photo-medical research center in japan. *Nuclear Instruments and Methods in Physics Research A*, 620:71–75, 2010.

[108] J. Bin et al. A laser-driven nanosecond proton source for radiobiological studies. *Appl. Phys. Lett*, 101:243701, 2012.

[109] K. Krushelnick et al. Ultrahigh-intensity laser-produced plasmas as a compact heavy ion injection source. *IEEE Trans. Plasma Sci.*, 28:1184, 2002.

[110] M. Roth et al. Fast ignition by intense laser-accelerated proton beams. *Phys. Rev. Lett.*, 86: 436, 2001.

[111] A. J. Mackinnon et al. Enhancement of proton acceleration by hot-electron recirculation in thin foils irradiated by ultraintense laser pulses. *PHYSICAL REVIEW LETTERS*, 88(21): 215006, 2002.

[112] S. A. Gaillard et al. Increased laser-accelerated proton energies via direct laser-light-pressure acceleration of electrons in microcone targets. *Phys. Plasmas*, 18:056710, 2011.

[113] K. A. Flippo et al. Increased efficiency of short-pulse laser-generated proton beams from novel flat-top cone targets. *Phys. Plasmas*, 15:056709, 2008.

[114] J. Badziak et al. Fast proton generation from ultrashort laser pulse interaction with double-layer foil targets. *Phys. Rev. Lett.*, 87:215001, 2001.

[115] K. A. Zigler et al. 5.5-7.5 mev proton generation by a moderate-intensity ultrashort-pulse laser interaction with h2o nanowire targets. *Phys. Rev. Lett.*, 106:134801, 2011.

[116] S. M. Pfotenhauer et al. Spectral shaping of laser generated proton beams. *New J. Phys*, 10: 033034, 2008.

[117] B. Shen et al. High-quality monoenergetic proton generation by sequential radiation pressure and bubble acceleration. *PHYSICAL REVIEW SPECIAL TOPICS - ACCELERATORS AND BEAMS*, 12:121301, 2009.

[118] T. Bartral et al. Focusing of short-pulse high-intensity laser-accelerated proton beams. *Nature Physics*, 8:139–142, 2012.

[119] T. Toncian et al. Ultrafast laser-driven microlens to focus and energy-select mega-electron volt protons. *Science*, (3)12:410, 2006.

[120] T. Toncian et al. Properties of a plasma-based laser-triggered micro-lens. *AIP ADVANCES*, 1:022142, 2011.

[121] E. Foulkal et al. Particle selection for laser-accelerated proton therapy feasibility study. *Med. Phys.*, 30:1660, 2003.

[122] W. Luo et al. Particle selection and beam collimation system for laser-accelerated proton beam therapy. *Med. Phys.*, 32:794, 2005.

[123] I. Hofmann et al. Controlled transport and focusing of laser-accelerated protons with miniature magnetic devices. *Physical Review Special Topics-Accelerators and beams*, 14:031304, 2011.

[124] M. Roth et al. Proton acceleration experiments and warm dense matter research using high power lasers. *Plasma Phys. Control Fusion*, 51:124039, 2009.

[125] S. Busold et al. Focusing and transport of high-intensity multi-mev proton bunches from a compact laser-driven source. *PHYSICAL REVIEW SPECIAL TOPICS-ACCELERATORS AND BEAMS*, 16:101302, 2013.

[126] K. Harres et al. Beam collimation and transport of quasineutral laser-accelerated protons by a solenoid field. *Physics of Plasmas*, 17:023107, 2010.

[127] S. Ter-Avetisyan et al. First demonstration of collimation and monochromatisation of a laser accelerated proton burst. *Laser and Particle Beams*, 26:637–642, 2008.

[128] M. Nishiuchi et al. Focusing and spectral enhancement of a repetition-rated, laser-driven, divergent multi-mev proton beam using permanent quadrupole magnets. *Applied Physics Letters*, 94:061107, 2009.

[129] M. Schollmeier et al. Controlled transport and focusing of laser-accelerated protons with miniature magnetic devices. *Physical Review Letters*, 101:055004, 2008.

[130] I. Hofmann. Performance of solenoids versus quadrupoles in focusing and energy selection of laser accelerated protons. *PHYSICAL REVIEW SPECIAL TOPICS-ACCELERATORS AND BEAMS*, 16:041302, 2013.

[131] M. Nishiuchi et al. Measured and simulated transport of 1.9 mev laser-accelerated proton bunches through an integrated test beam line at 1 hz. *PHYSICAL REVIEW SPECIAL TOPICS-ACCELERATORS AND BEAMS*, 13:071304, 2010.

[132] *Focusing of charged particles.* New York : Academic Press, 1967.

[133] *Optics of charged particles.* Academic Press Inc., 1987.

[134] F. Schillaci et al. Errors and optics study of a permanent magnet quadrupole system. *JNIST*, 10:T05001, 2015.

[135] M. Maggiore et al. Innovative handling and transport solutions for laser-driven ion beams. *AIP Conf. Proc.*, 1546:34–43, 2013.

[136] V. Scuderi et al. Development of an energy selector system for laser-driven beam applications. *NIM A*, 740:87, 2014.

[137] A. Tramontana. A transport beamline solution for laser-accelerated proton beams at eli-beamlines. *Il Nuovo Cimento C*, accepted, 2015.

[138] P. Castro. Beam trajectory calculations in bunch compressors. *DESY TECHNICAL NOTE*, 2003-01.

[139] L. P. Chau et al. Bunch compressor for intense proton beams. *Proc. LINAC*, 2010.

[140] A. Tramontana. The energy selection system for the laser-accelerated proton beams at eli-beamlines. *Journal of Instrumentation*, 9:C05065, 2015.

[141] M. A. Preger. First and second order closed orbit effects in short dipoles. *Frascati Physics Series*, 10:221–226, 1998.

[142] A.V. Kuznetsov et al. Efficiency of ion acceleration by a relativistically strong laser pulse in an underdense plasma. *Plasma Phys. Rep.*, 27:211–220, 2011.

[143] D. Haberberger et al. Collisionless shocks in laser-produced plasma generate monoenergetic high-energy proton beams. *Nature Phys.*, 8:95–99, 2012.

[146] T. Dzelzainis et al. The taranis laser: A multi-terawatt system for laser-plasma investigations. *Laser and particles beams*, 28:451–461, 2010.

[147] D. S. Hey et al. Use of gafchromic film to diagnose laser generated proton beams. *Rev. Sci. Instrum.*, 79:053501, 2008.

[148] F. Fiorini et al. Dosimetry and spectral analysis of radiobiological experiment using laser-driven proton beams. *Phys. Med. Biol.*, 56:6969–6982, 2011.

[149] D. Kirby et al. Radiochromic film spectroscopy of laser-accelerated proton beams using the fluka code and dosimetry traceable to primary standards. *Laser and Particle Beams*, 29: 231–239, 2011.

[150] GAP. Cirrone et al. Absolute and relative dosimetry for elimed. *AIP Conf. Proc*, 1546:70–80, 2013.

[151] N. Sinenian et al. The response of cr-39 nuclear track detector to 1-9 mev protons. *Review of Scientific Instruments*, 82:7103303, 2011.

[152] S. Gaillard et al. Study of saturation of cr39 nuclear track detectors at high ion fluence and of associated artifact patterns. *Review of Scientific Instruments*, 78:013304, 2007.

[153] A. Szydlowski et al. Application of solid-state nuclear track detectors of the cr-39/pm-355 type for measurements of energetic protons emitted from plasma produced by an ultra-intense laser. *Radiation Measurements*, 44:881–884, 2009.

[154] M. Nishiuchi H. Daido and A.S. Pirozhkov. Review of laser-driven ion sources and their applications. *Rep. Prog. Phys.*, 75:056401, 2012.

[155] J. Badziak et al. Generation of highly collimated high-current ion beams by skin-layer laser-plasma interaction at relativistic laser intensities. *Applied Physics Letters*, 89:061504, 2006.

[156] R. Al et al. Dna damage intensity in fibroblasts in a 3-dimensional collagen matrix correlates with the bragg curve energy distribution of a high let particle. *New Journal of Physics*, 83(3): 194, 2010.

[157] L. Manti et al. Chromosome aberrations in human lymphocytes from the plateau region of the bragg curve for a carbon-ion beam. *NIM B*, 259:884, 2007.

[158] H. Wu et al. Induction of micronuclei in human fibroblasts across the bragg curve of energetic heavy ions. *Radiat. Res.*, 166(4):583, 2006.

[159] L. Manti et al. Development of a low-energy particle irradiation facility for the study of the biological effectiveness of the ion track end. *Journal of Physics: Conference Series*, 373: 012019, 2012.

[160] R. L. Fleisher. Absolute calibration of photostimulable image plate detectors used as (0.5–20 mev) high-energy proton detectors. *REVIEW OF SCIENTIFIC INSTRUMENTS*, 79:073301, 2008.

[161] Z. Dauter and K. S. Wilson. Imaging plates in sinchrotron and conventional x-ray crystallographic data collection. *Acta Physica Polonica A*, 86 (4):477, 1994.

[162] S. G. Gales and C. D. Bentley. Image plates as x-ray detectors in plasma physics experiments. *REVIEW OF SCIENTIFIC INSTRUMENTS*, 75 (10):4001, 2004.

[163] A. Mancic et al. Absolute calibration of photostimulable image plate detectors used as (0.5–20 mev) high-energy proton detectors. *REVIEW OF SCIENTIFIC INSTRUMENTS*, 79:073301, 2008.

[164] URL http://home.fujifilm.com/products/science/ip/feature.html.

[165] G.F.Dempsay. Validation of a precision radiochromic film dosimetry system for quantitative two-dimensional imaging of acute exposure dose distributions. *Med Phys.*, 27(10):2462–75, 2000.

[166] S.T. Chiu-Tsao. Dose response characteristics of new models of gafchromic films: Dependence on densitometer light source and radiation energy. *Med Phys.*, 31(9):2501–8, 2004.

[167] L. Karsch et al. Dose rate dependence for different dosimeters and detectors: Tld, osl, ebt films and diamond detectors. *Med. Phys.*, 39(5):2462–75, 2012.

[168] URL http://www.ashland.com/products/gafchromic-radiotherapy-films.

[169] Jirasek A and Duzenli C. Relative effectiveness of polyacrylamide gel dosimeters applied to proton beams: Fourier transform raman observations and track structure calculations. *Med. Phys.*, 29:569–77, 2002.

[170] F. Nurnberg et al. Radiochromic film imaging spectroscopy of laser-accelerated proton beams. *Rev. Sci. Instrum.*, 80:033301, 2009.